ABSTRACT

High-resolution Age Constraints and Fluvial Sedimentology of Late Cretaceous to Early Paleocene Terrestrial Deposits of the Southwestern USA

Caitlin E. Leslie, Ph.D.

Mentor: Daniel J. Peppe, Ph.D.
Mentor: Stacy C. Atchley, Ph.D.

A well-constrained age model is a critical piece of information in geologic studies. This dissertation focuses on two successions of fossiliferous fluvial strata within the southwestern US that prior to this work were lacking high-resolution geochronologic control: the Dawson Creek section of Big Bend National Park, Texas and the upper Nacimiento Formation of the San Juan Basin, New Mexico. Establishing age control facilitates interpretations regarding the timing of climatic events, ages of faunas and timing of turnovers, and basin evolution through time. The first case study involves using magnetostratigraphy, biostratigraphy, and detrital sanidine ages to construct the first independent, high-resolution age model for the Late Cretaceous to early Paleocene Dawson Creek section. The generated age model indicates eustatic sea level was the primary driver of deposition, documented warming events represent rapid changes in climate, and the Javelina Formation dinosaur fauna is equivalent in age to the Hell Creek fauna supporting the hypothesis of dinosaur provinciality in the latest Cretaceous. The second case study focuses on the upper Nacimiento Formation of the San Juan Basin, New Mexico and presents a detailed lithostratigraphy and high-resolution age model for the strata using magnetostratigraphy and a detrital sanidine age to constrain the age of Torrejonian mammal localities. Findings from this study indicate the faunal turnover between the Torrejonian 2 – Torrejonian 3 North America Land Mammal age interval zones occurred over ~120 kyr. Comparisons of calculated mean sediment accumulation rates indicate that sedimentation equalized across the basin, suggesting an accommodation minimum in the basin. The last study uses the distributive fluvial system model to evaluate the position of four upper Nacimiento sections within a fan and assess whether the strata were deposited by a prograding system. Results from characterizing pedotypes, paleosol maturity and drainage, fluvial facies, and floodplain location indicate the Kutz Canyon and Escavada Wash sections represent medial deposits and the Torreon West and East sections represent distal deposits. The study interval appears to capture autocyclic migration and aggradation, suggesting the interval is too fine to capture progradation. This work provides improves the chronology of regions important to mammalian and climatic studies in North America.

High-resolution Age Constraints and Fluvial Sedimentology of Late Cretaceous to Early Paleocene Terrestrial Deposits of the Southwestern USA

by

Caitlin E. Leslie, B.S.

A Dissertation

Approved by the Department of Geosciences

____

Stacy C. Atchley, Ph.D., Chairperson

Submitted to the Graduate Faculty of
Baylor University in Partial Fulfillment of the
Requirements for the Degree
of

Doctor of Philosophy

Approved by the Dissertation Committee

____

Daniel J. Peppe, Ph.D., Chairperson

____

Stacy C. Atchley, Ph.D., Chairperson

____

Lee C. Nordt, Ph.D.

____

Steve I. Dworkin, Ph.D.

____

Kenneth T. Wilkins, Ph.D.

Accepted by the Graduate School
May 2018

____

J. Larry Lyon, Ph.D., Dean

Page bearing signatures is kept on file in the Graduate School.

TABLE OF CONTENTS

LIST OF FIGURES

LIST OF TABLES

ACKNOWLEDGMENTS

First, the work presented in this dissertation would not have been possible without the patience and support of my two advisors: Drs. Dan Peppe and Stacy Atchley. Both provided invaluable direction, career guidance, and encouragement to see me through this process and enable my success. Dr. Peppe has introduced me to and steered me through the wonderful world of paleomagnetism. Dr. Atchley has provided me opportunities to expand my knowledge base and pushed me to perform to my fullest. It has been a privilege to work with both.

This work was also supported by numerous collaborators whose contributions elevated the quality of this work: Thomas Williamson, Ross Secord, Lee Nordt, Mike Jackson, Dario Bilardello, Matt Heizler, Tyler Leggett, Steve Brusatte, and Barbara Standhardt. I would like to extend my gratitude to Dr. Steve Dworkin and Dr. Kenneth Wilkins for providing feedback on this work. I owe a special thanks to those who assisted me in the field: Ashley Ramsey, Andrew Flynn, Aly Baumgartner, Joe Milligan, Adam Davis, and Michaela Donahoo. The Geosciences Department has provided me generous support and the work from Paulette Penney, Janelle Atchley, and Jamie Ruth is greatly appreciated.

Financial support for this study was provided by the National Science Foundation, American Chemical Society Petroleum Research Fund, Society for Sedimentary Geology, Fort Worth Geological Society, University of Minnesota Institute for Rock

Magnetism visiting student fellowship, Colorado Scientific Society, and Baylor University Department of Geosciences' Dixon Fund.

My fellow graduate students have pushed me to become a better scientist and I thank all for the laughs we have shared.

Last, my family and friends have supported me through this journey. Above all, my partner, Luke, has given the encouragement to see me to the finish line.

CHAPTER ONE

Introduction

This dissertation contains three manuscripts corresponding to three separate chapters. These studies were conducted with collaborators whose contributions aided in the completion of each chapter. For each chapter, I collected and analyzed all data and samples, produced all figures and tables, and wrote the corresponding manuscript with the exceptions outlined below.

This dissertation focuses on constraining the age of geologic regions that are important to understanding the climate and mammalian faunal dynamics of the Late Cretaceous and early Paleocene in western North America. The first study area of this dissertation is the Dawson Creek section of Big Bend National Park where extensive previous research has documented warming events in the Late Cretaceous and characterized the dinosaur and mammalian faunas that represent the southernmost faunas in North America during this time period. Chapter Two contains the high-resolution age model generated for this section which was previously lacking. The San Juan Basin of New Mexico, the second study area of this dissertation, contains extensive early Paleocene mammalian fossils and the fluvial deposits of the Nacimiento Formation and represents the type location for the Puercan and Torrejonian North American Land Mammal ages. Although extensive work has been done previously characterizing the mammalian faunas, less work has been done precisely constraining the deposits relative to the mammalian fossil localities or creating a detailed lithostratigraphy for the sections.

Chapter Three contains the age constraints produced for the upper Nacimiento Formation and Chapter Four covers the work documenting the detailed sedimentology and stratigraphy of the deposits.

In Chapter Two, titled "Revised age constraints for Late Cretaceous to early Paleocene strata from the Dawson Creek section, Big Bend National Park, west Texas", we use a combination of magnetostratigraphy, biostratigraphy, and detrital sanidine ages to construct the first independent, high resolution age model for the Dawson Creek section that documents the duration of deposition as well as multiple unconformities in the section. Using the age model, we evaluate the timing of warming events and hiatuses within the section in comparison with global isotope and sea level records. D. Peppe and S. Atchley helped design the study. D. Peppe also aided in collection of the paleomagnetic samples and fieldwork for the study. M. Jackson aided in interpretation of the rock magnetism data. M. Heizler performed analyses and calculated detrital sanidine ages. S. Atchley and L. Nordt documented the paleosols through the section and provided detailed notes on the stratigraphy to guide sampling and data interpretation. T. Williamson and B. Standhardt conducted the reevaluation of the vertebrate fauna.

In Chapter Three, titled "High-resolution magnetostratigraphy of the upper Nacimiento Formation, San Juan Basin, New Mexico, USA: implications for basin evolution and mammalian turnover", we use magnetostratigraphy to construct a high-resolution age model for four measured sections across the basin that include the Torrejonian 2-Torrejonian 3 faunal turnover event. Using magnetostratigraphy, we calculate sedimentation rates for each section, which allows us to determine the duration of each section and to assign an age to mammalian localities. D. Peppe, T. Williamson, and R. Secord assisted in the design of the study. T. Leggett, and D. Peppe helped collect the paleomagnetic samples, measure sections, and assisted with fieldwork for the study. T. Leggett assisted in the analysis of sample paleomagnetic properties. D. Bilardello aided in interpretation of the rock magnetism data. T. Williamson and R. Secord identified and measured mammalian localities. M. Heizler performed analyses and calculated detrital sanidine ages.

In Chapter Four, titled "Modeling the upper Nacimiento Formation, San Juan Basin, New Mexico as a distributive fluvial system", we use the distributive fluvial system (DFS) model to assess the position of the four sections within a depositional fan and then test whether these deposits accumulated as a prograding distributive fluvial system. D. Peppe and S. Atchley helped design the study and provided critical feedback on the manuscript.

CHAPTER TWO

Revised Age Constraints for Late Cretaceous to Early Paleocene Terrestrial Strata from the Dawson Creek Section, Big Bend National Park, West Texas

This chapter published as: Leslie, C.E., Peppe, D.J., Williamson, T.E., Heizler, M., Jackson, M., Atchley, S.C., Nordt, L., and Standhardt, B., *in press*, Revised age constraints for Late Cretaceous to early Paleocene terrestrial strata from the Dawson Creek section, Big Bend National Park, west Texas: *GSA Bulletin.*

Abstract

We analyzed samples for paleomagnetism, $^{40}Ar/^{39}Ar$ detrital sanidine ages, and mammalian fauna to produce a precise chronostratigraphic framework for the Upper Cretaceous to lower Paleocene Dawson Creek section of Big Bend National Park. Prior to this work, the absolute age and duration of the Upper Cretaceous Aguja and Javelina Formations and Paleocene Black Peaks Formation were relatively poorly constrained. The documented polarity zones can be correlated to C32n-C31n, C29r, and C27r of the geomagnetic polarity time scale (GPTS) with three hiatuses spanning more than 1.5 myr each. Rock magnetic analyses indicate that the dominant magnetic carrier in the Aguja and Black Peaks Formations is titanomagnetite while the Javelina Formation has varying magnetic carriers including hematite, magnetite, and maghemite. An overprint interval surrounding the K-Pg boundary suggests the primary magnetic carrier, titanohematite, was likely reset by burial and/or overlying basaltic flows. These are the first independent age constraints for the Cretaceous-Paleocene strata at the Dawson Creek section that determines the age and duration of deposition of each formation in the section, as well as the age and duration of multiple unconformities through the succession. As a result, these

age constraints can be used to reassess biostratigraphic and isotopic correlations between the Big Bend area and other Cretaceous-Paleogene (K-Pg) basins across North America. Based on this new data, we reassign the age of the mammalian fauna found in the Black Peaks Formation from the Puercan to the Torrejonian North American Land Mammal age. Our age constraints show that the dinosaur fauna in the Javelina Formation in the Dawson Creek area is latest Maastrichtian and restricted to C29r. Thus, the Javelina dinosaur fauna is correlative to the Hell Creek Formation dinosaur fauna from the Northern Great Plains, indicating differences between the faunas are not due to differences in age and providing support for the hypothesis of provinciality and endemism in dinosaur communities in the late Maastrichtian. Further, the age constraints indicate that the previously documented mid-Maastrichtian and late Maastrichtian greenhouse events were rapid (<200 k.y.) and correlate closely with climate events documented in the marine record.

Introduction

The Dawson Creek section within Big Bend National Park, Texas documents a series of Cretaceous though lower Paleocene alluvial deposits that accumulated along a passive continental margin within the Tornillo Basin of west Texas (Fig. 1.1). This coastal plain succession has been the focus of several lithostratigraphic, cyclostratigraphic, paleopedologic, magnetostratigraphic, and paleontologic studies (e.g., Lawson, 1972; Standhardt, 1986; Lehman, 1989a, 1990; Nordt et al., 2003; Atchley et al., 2004). The Cretaceous dinosaur and early Paleocene mammalian faunas from Big Bend, and particularly from the Dawson Creek area, are key for understanding regional patterns in dinosaur and mammal community diversity and biostratigraphy. Dawson Creek is the

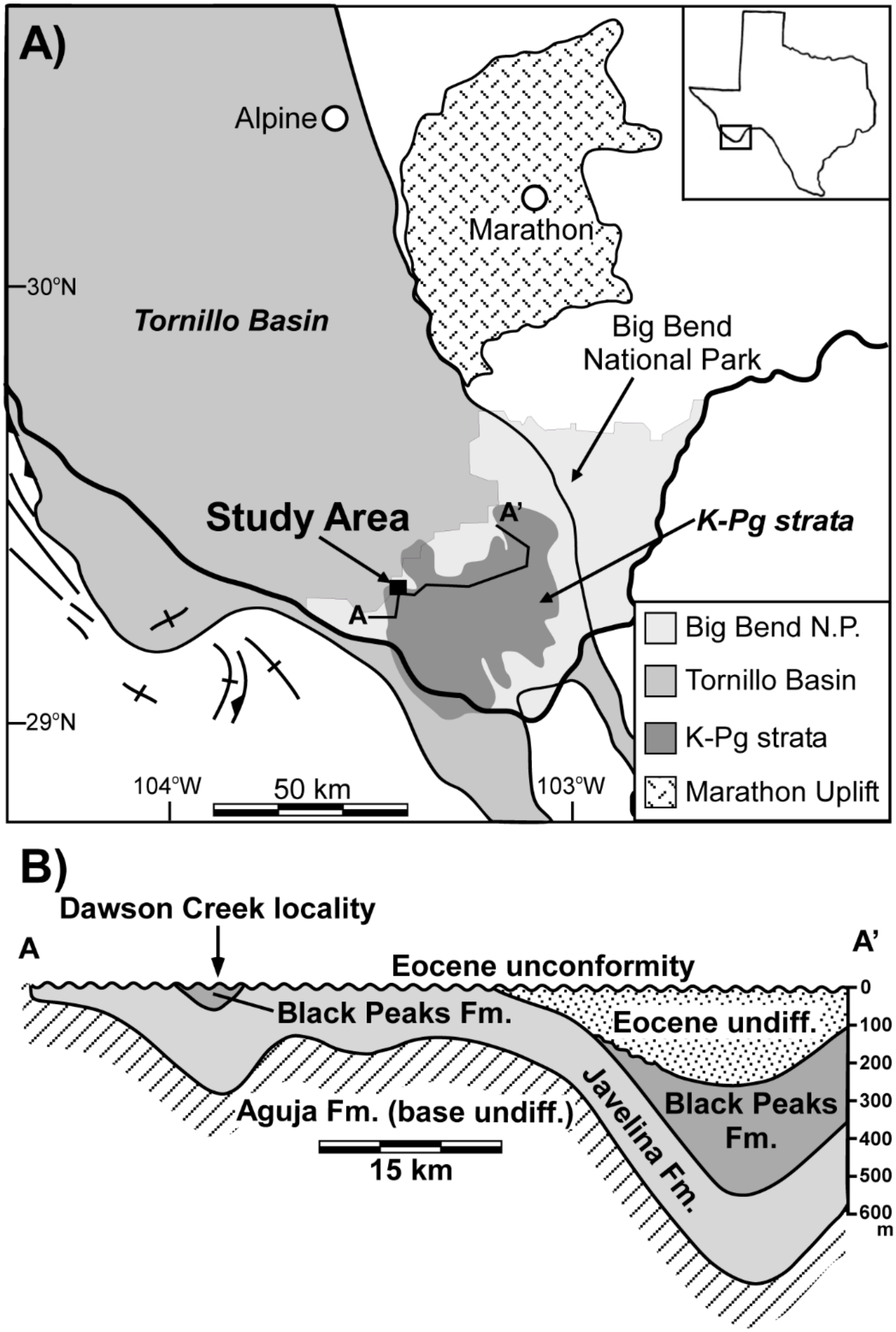

Figure 1.1. (A) Location of study area (highlighted with box) within Big Bend National Park modified from Lehman (1991). (B) Cross section A-A' through the Tornillo Basin modified from Lehman (1986).

southernmost latest Cretaceous (late Maastrichtian) terrestrial vertebrate fossil site in North America. Therefore, it forms a critical data set necessary for assessing patterns of endemism in Campanian and Maastrichtian dinosaur faunas across North America (e.g., Standhardt, 1986; Lehman, 1997, 2001; Lofgren et al., 2004; Sampson et al., 2010; Lucas et al., 2016). Additionally, analyses of paleosols at the Dawson Creek section have been used to argue for two short-lived greenhouse events during the Maastrichtian (Nordt et al., 2003; Dworkin et al., 2005). Despite the importance of Dawson Creek record for understanding Cretaceous and Paleocene paleoclimate and the composition of vertebrate communities, the absolute age and duration of the Upper Cretaceous Aguja and Javelina Formations and Paleocene Black Peaks Formation are relatively poorly constrained.

In this study, we develop a precise chronostratigraphic framework for the Dawson Creek section using magnetostratigraphy, $^{40}Ar/^{39}Ar$ detrital sanidine geochronology, and biostratigraphy based on a reevaluation of the vertebrate fauna. From these analyses, we determine the age and duration of deposition of each formation in the section, as well as the age and duration of multiple unconformities through the succession. Finally, we use these new age constraints to assess the implications for biostratigraphic and isotopic correlations between the Big Bend area and other Cretaceous-Paleogene (K-Pg) basins across North America and the global marine record.

Previous Work

Geochronology

Previous studies used a combination of biostratigraphy, estimates of sedimentation rates based on paleosol maturity, and correlations of local isotope stratigraphy to marine isotope curves to produce a chronostratigraphic framework for the

Dawson Creek area (e.g., Lehman, 1990; Nordt et al., 2003; Atchley et al., 2004). The existing age determinations indicate the section spans from the latest Campanian through the early Paleocene (Nordt et al., 2003) when adjusted to reflect the most recent age of the K-Pg boundary (e.g., Renne et al., 2013; Clyde et al., 2016). The Aguja Formation elsewhere in the park is interpreted to be stratigraphically equivalent to the base of the Dawson Creek section and contains a late Campanian vertebrate fauna (Rowe et al., 1992; Lehman, 1985; Wick and Lehman, 2013). Based on this correlation, the base of the Dawson Creek section has been interpreted to be close to the Campanian-Maastrichtian boundary (Lehman and Busbey, 2007). Based on the last occurrence of dinosaur fossils and the first occurrence of Paleocene mammals, the K-Pg boundary has traditionally been identified in the Dawson Creek section to be at approximately the contact between the Javelina and Black Peaks Formations (Lehman, 1990). However, recent ichnological work documents an abrupt decrease in adhesive meniscate burrow diameter within a sandstone channel of the Javelina Formation at 172 m in the Dawson Creek section, interpreted to represent the post-extinction recovery community, and thus the stratigraphic position of the K-Pg boundary (Fig. 1.2; Wiest et al., 2018). Lehman (1990) used preliminary magnetostratigraphy (MacFadden in Standhardt, 1986) to argue that the Black Peaks Formation correlated to C29r-C28r meaning that the top of the section is older than 64.6 Ma, which is the end of C28r (Ogg, 2012). Correlations between stable isotopic trends from pedogenic carbonate nodules through the Dawson Creek section and carbon isotopes from marine deposits combined with the location of cyclostratigraphic boundaries, were used to indicate the presence of multiple hiatuses in the section (Nordt

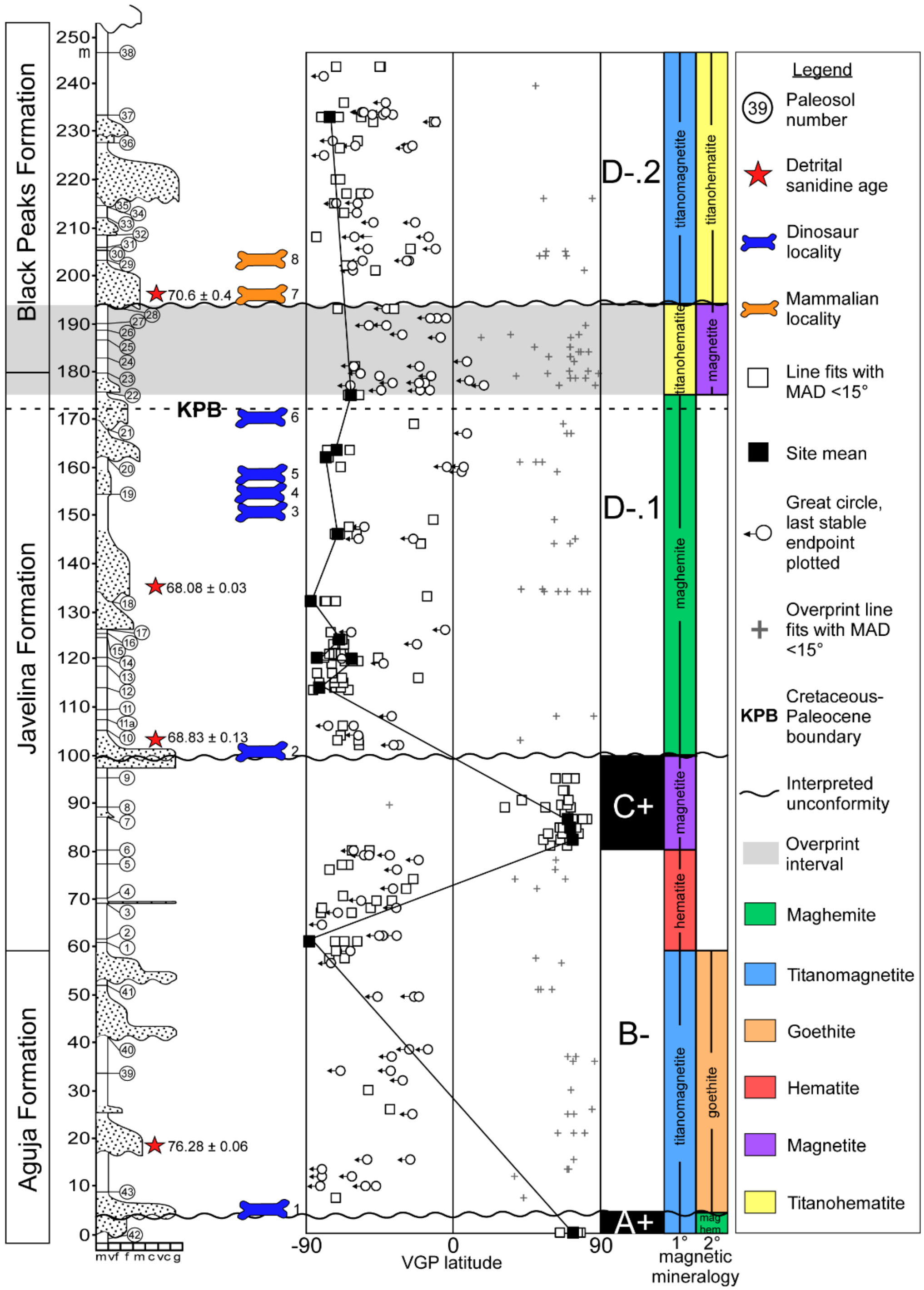

Figure 1.2. VGP latitude, interpreted polarity zonations, and primary (1°) and secondary (2°) magnetic mineralogies for the section. Location of detrital sanidine samples shown. Faunal localities: 1. LSU VL-110; 2. LSU VL-149; 3. TMM 41450 (LSU VL-106); 4. LSU VL-112 5. LSU VL-145; 6. TMM 41501; 7. TMM 41400, "Tom's Top" (LSU VL-111); 8. LSU VL-109 (Lehman, 1990). Unconformities are placed based on sedimentological indicators, faunal interpretations, and detrital age dates. MAD - mean angle of deviation.

et al., 2003; Atchley et al., 2004). However, the duration of these unconformities or their exact age is uncertain.

There was a preliminary attempt to use magnetostratigraphy at Dawson Creek by B.J. MacFadden (*in* Standhardt, 1986) to determine the age of the section. In this work, the local polarity stratigraphy that was developed was correlated to C30n through C28r. However, MacFadden (*in* Standhardt, 1986) noted that large parts of the section were overprinted and as a result this magnetostratigraphic framework has not been accepted, though it was used by Lehman (1990) to estimate an approximate minimum age for the top of the section.

In other areas of the park, volcanic deposits within the upper portion of the Aguja Formation have been dated to 76.9 ± 1.2 Ma (Befus et al., 2008) and 72.6 ± 1.5 Ma (Breyer et al., 2007) using U-Pb dating, suggesting the Aguja Formation is Campanian. A monazite U-Pb age of 69.0 ± 0.9 Ma for a tuff occurring within the Javelina Formation, 90 m stratigraphically below the K-Pg boundary, from the northern part of Big Bend National Park indicates that all or at least the majority of the Javelina Formation was deposited during the Maastrichtian (Lehman et al., 2006).

Paleoclimate and Depositional Environments

Previous geochemical research focused on paleosols through the succession documented two Late Cretaceous greenhouse events using isotopic composition of pedogenic carbonate nodules, referred to as the mid-Maastrichtian event and late Maastrichtian event (Nordt et al., 2003). This work used correlations of the local isotope stratigraphy with marine isotope curves to adjust the ages of these events. When adjusted to reflect the most recent age of the K-Pg boundary (Ogg, 2012; Renne et al., 2013), the mid-Maastrichtian event occurs from ~71–70 Ma and the late Maastrichtian event occurs from ~66.2–66.3 Ma. Work done by Lehman (1990) on the Paleocene paleosols found a transition toward increased rainfall and cooler temperatures using paleosol macromorphology.

Alluvial stacking pattern analyses of the Aguja, Javelina, and Black Peaks Formations indicate that deposits in the Dawson Creek area were deposited cyclically (Atchley et al., 2004). Changes in stacking pattern thicknesses were interpreted to represent the rate of change of base level rise and fall and suggest that the primary control on stratigraphic cyclicity in the Dawson Creek section was eustatic sea level change, despite the succession being deposited exclusively in the continental realm (Atchley et al., 2004). Interestingly, despite evidence for shifts in climate through the section, there does not appear to be evidence for climate change strongly influencing deposition (Atchley et al., 2004), which differs from evidence from other parts of the Big Bend area (Bataille et al., 2016).

Vertebrate Paleontology

Fossil vertebrates have been collected from the Big Bend National Park area for over 70 years and the Dawson Creek area contains a record of terrestrial vertebrate fossil localities throughout the Javelina and Black Peaks Formations. These faunas are of particular interest because they represent the southernmost latest Cretaceous and early Paleocene faunas of North America, and thus are important for understanding terrestrial vertebrate biogeographic patterns across the K-Pg boundary.

Disagreement on the placement of the formational boundaries between these units has resulted in differences in the taxa reported from each of the formations (e.g., Standhardt, 1986; Lehman, 1990; Rowe et al., 1992). For example, Standhardt (1986) considered the Javelina and Black Peaks members of the Tornillo Formation and placed the Javelina-Black Peaks boundary to be above the mammal-bearing localities discussed here. Herein, we use the stratigraphic nomenclature and position of formational contacts of Lehman (1990), Nordt et al. (2003), and Atchley et al. (2004). Thus, we place all Paleocene mammal localities within the Black Peaks Formation, and all dinosaur faunas within the Javelina and Aguja Formations.

Aguja Formation. The Aguja Formation contains a rich vertebrate fauna that includes microvertebrate fossils collected through screenwashing techniques. These include chondrichthyan and actinopterygian fish (Rowe et al., 1992; Sankey, 1998; Standhardt, 1986), amphibians (Rowe et al., 1992; Lehman, 1985; Sankey, 1998; Standhardt, 1986), squamates (Rowe et al., 1992; Sankey, 1998; Standhardt, 1986; Nydam et al., 2013), turtles (Rowe et al., 1992; Sankey, 2008; Standhardt, 1986; Tomlinson, 1997), crocodylians (Colbert and Bird, 1954; Lehman, 1985; Rowe et al., 1992; Sankey, 2008; Standhardt, 1986), pterosaurs (Rowe et al., 1992), dinosaurs (Davies, 1983; Forster et al., 1993; Larson and Currie, 2013; Lehman, 1982, 1985, 1989b, 2010; Longrich et al., 2010, 2013; Prieto- Márquez, 2014; Rivera-Sylva et al., 2016; Rowe et al., 1992; Sankey, 1998, 2001, 2008; Sankey et al., 2005; Standhardt, 1986; Wagner, 2001; Wagner and Lehman, 2009; Wick et al., 2015), and mammals (Cifelli, 1995; Rowe et al., 1992; Weil, 1992).

Nearly all the seemingly valid dinosaur taxa identified from the Aguja Formation appear to be endemic. Several of the taxa such as *Texacephale* (see Jasinski and Sullivan, 2011) are probably not valid. Several small theropod taxa that are based on isolated teeth (e.g., *Saurornitholestes langstoni, Richardoestesia gilmorei*, and *R. isosceles*; Sankey, 2001, 2008) have been identified in temporally and geographically wide-ranging faunas throughout western North America, though it is likely that many, if not most of these, are not correctly identified as small theropod taxa were probably exclusive to discrete time intervals and geographic areas (Larson and Currie, 2013).

Mammals from the Aguja Formation include several genera that are typical of Late Cretaceous faunas of western North America (e.g., *Alphadon*, *Turgididon*, *Pediomys*; Rowe et al., 1992). One species, the multituberculate *Cimolomys clarki*, indicates the Aguja mammalian fauna correlates to the Judithian North American Land Mammal age (NALMA; Cifelli et al., 2004).

Javelina Formation. In the Dawson Creek area, a relatively small vertebrate fauna has been reported from the middle and upper Javelina Formation and fossil specimens tend to be fragmentary, though bone beds containing multiple dinosaurs have been documented within the Javelina Formation in other areas of Big Bend National Park (Hunt and Lehman, 2008). The Javelina fauna includes the giant pterosaur Quetzalcoatlus from TMM 41501 in Dawson Creek (Table 1.1 and Fig. 1.2) (Lawson, 1975), and a number of dinosaurs, detailed below.

At least one chasmosaurine ceratopsian, *Bravoceratops polyphemus,* is present in the Javelina Formation of the Big Bend area, based on fragmentary specimens (Wick and Lehman, 2013) and this was regarded as being near in age to the Edmontonian-Lancian boundary. Fragmentary skulls and partial skeletons from the middle and upper Javelina Formation have been referred to, or tentatively referred to, *Torosaurus utahensis* (Lawson, 1976; Lehman, 1996; Hunt and Lehman, 2008), a taxon originally described

Table 1.1. Dawson Creek Fossil localities.

Locality	*Taxa*	Age
1. LSU VL-110	*Odontaspis* tooth, fish,crocodile,dinosaur	Judithian
2. LSU VL-149	*tyrannosaur* femur	Lancian
3. LSU VL-106, TMM 41450	*Alamosaurus sanjuanensis*	Lancian
4. LSU VL-112	fish, turtle, crocodile	Lancian
5. LSU VL-145	scraps of dinosaur bone	Lancian
6. TMM 41501	giant pterosaur, *Quetzalcoatlus northropi*	Lancian
7. TMM 41400 "Tom's Top" (LSU VL-111)*	*Bryanictis*	Torrejonian
	Mixodectes malaris	Torrejonian 2
	Plesiolestes nacimienti	Torrejonian
	Promioclaenus cf. P. lemuroides	Torrejonian
8. LSU VL-109	turtle remains	Torrejonian

Note. *Taxa reclassified in this paper.

from the North Horn Formation of Utah (see Sullivan et al., 2005). At least one taxon of a large titanosaurian sauropod has been identified from the Javelina Formation. Many of the sauropod specimens lack diagnostic characters to allow generic identification, but at least some can be confidently referred to *Alamosaurus sanjuanensis* (Lehman and Coulson, 2002; Fronimos and Lehman, 2014; Tykoski and Fiorillo, 2016). Some specimens of a large titanosaurian sauropod, probably representing *Alamosaurus,* have been described from the TMM 41450 (LSU VL-106) locality within the Javelina Formation in the Dawson Creek section (Table 1.1 and Fig. 2.1) (Lawson, 1972;

Standhardt, 1986), as well as near the top of the Cretaceous part of the section of the Rough Run area, which is near Dawson Creek (Fronimos and Lehman, 2014). A large tyrannosaurid, referred to *Tyrannosaurus rex* (Carr and Williamson, 2000, 2004), is present based on isolated postcranial bones (Wick, 2014) and on a partial maxilla (Lawson, 1975; Wick, 2014). At least two small theropod dinosaurs have been documented based on isolated teeth: *Saurornitholestes* cf. *S. langstoni* and *Sauronitholestes* n. sp.? (Sankey et al., 2005). Other dinosaurs reported from the Javelina Formation, but not well documented, are indeterminate hadrosaurs, ankylosaurs, and ornithomimids (Lawson, 1972; Lehman, 1985, 1990).

Several workers have reported that Lancian age mammals and herpetofaunas are present in the Javelina Formation, citing Standhardt (1986). Standhardt (1986) reported a small microfauna from LSU locality VL-113 ("Running Lizard") in the Dawson Creek area, which she described as being from the upper Aguja Formation; however, based on its stratigraphic position it is more likely from the Javelina Formation. She indicated a Lancian age for the fauna based on the presence of a fragmentary tooth that she referred to *Alphadon marshi*, a taxon restricted to the Lancian NALMA (Cifelli et al., 2004). However, we find that the tooth fragment is too incomplete to be diagnostic to genus or species.

The Javelina dinosaur fauna has been included in the latest Cretaceous "*Alamosaurus* community" (Sloan, 1969) or "*Alamosaurus* fauna" (Lehman, 1987), based primarily on the presence of the titanosauriform sauropod *Alamosaurus*, which is absent from contemporaneous latest Cretaceous faunas of the northern Rocky Mountain Region. Lehman (1987) argued that *Alamosaurus* was confined to seasonal, semi-arid intermontane basins south of ~35°N latitude, unlike the contemporaneous "*Triceratops* fauna", which was not environmentally restricted (Lehman, 1987). However, other workers have argued that the distribution of *Alamosaurus* does not reflect latitudinal faunal provinciality, but instead may be related to differences in ages between the *Alamosaurus* fauna of southern North America and the *Triceratops* fauna from the Northern Great Plains or due to other environmental factors such as distance from the shoreline with *Alamosaurus* restricted to more "inland" environments (e.g., Mannion and Upchurch, 2011; Lucas et al., 2016). Therefore, given the limited extent of the *Alamosaurus* fauna, determining the precise age of the Javelina Formation is of interest to further understanding possible latitudinal faunal provinciality or environmental heterogeneity during the latest Cretaceous of North America.

Black Peaks Formation. The Black Peaks Formation contains a diverse vertebrate fauna that includes a ray, a gar, amphibians, lizards, a champsosaur, turtles, crocodiles, and mammals (Schiebout, 1974; Schiebout et al., 1987; Standhardt, 1986; Brochu, 2000; Lehman and Barnes, 2010; Cobb, 2016).

The mammalian fauna found in the Black Peaks Formation has long been recognized as being Paleocene in age (e.g., Schiebout, 1974; Schiebout et al., 1987; Standhardt, 1986), based on the presence of diagnostic Torrejonian, Tiffanian, and possibly Clarkforkian NALMA taxa. In the Dawson Creek area there are two mammalian faunas within the Black Peaks Formation: TMM 41400 (LSU VL-111; "Tom's Top"; Fig. 1.2) in Dawson Creek and TMM 42327 (LSU VL-108; "Dogie") from nearby Rough Run Amphitheater ~5 miles (8 km) east of the Dawson Creek section (Lehman and Busbey, 2007; Cobb, 2016). TMM 41400 and TMM 42327 have both yielded diverse microvertebrate assemblages that are 20 m and 80 m above the highest occurrence of dinosaur bones in those areas, respectively (see Lehman and Busbey, 2007; Cobb, 2016). Standhardt (1986) and Schiebout et al. (1987) described or provided a faunal list of several mammalian taxa recovered from low in the Black Peaks Formation that included a combination of Puercan and Torrejonian genera and species, leading them to conclude that these faunas are late Puercan. However, some workers have argued that those faunas are not Puercan, but Torrejonian in age (Williamson, 1996; Lehman and Busbey, 2007).

Methodology

Paleomagnetism

Four paleomagnetic block samples were collected from paleosols and fine-grained sandstones at ~1 m intervals (0.3 m minimum and 2 m maximum sample spacing), through the section. A total of 121 localities were sampled. A flat face was shaved onto the samples in situ using a hand rasp and the orientation was measured using a Brunton compass. In the laboratory, the samples were cut into ~2 cm^3 cubes using a diamond-bit saw.

Three hundred and sixty samples were measured at Baylor University using a 2G cryogenic DC-SQuID magnetometer located in a 2-layer magnetostatic shielded room with a background field typically less than 300 nT. A dip correction was applied to the section based on field measurements ranging from 14°-36°. All samples were demagnetized using a combined alternative-field (AF) and thermal demagnetization strategy following the methods of Peppe et al. (2009). Samples were first given a low-AF pre-treatment (50 and 100 MT steps) to remove any low-coercivity viscous or isothermal remanence. Thermal demagnetization steps were performed in 20–50° increments up to the maximum unblocking temperature or until samples became erratic and unstable (between 250 and 600 °C). Thermal demagnetization was performed using a nitrogen atmosphere using ASC controlled atmosphere thermal demagnetizer to minimize oxidation reactions.

The characteristic remanence for samples was isolated using principal-component analysis (PCA) (Kirschvink, 1980). A best-fit line was calculated from a minimum of three demagnetization steps that trended toward the origin and had a maximum angle of deviation (MAD) <20° (Figs. 1.3A, 1.3B, 1.3C). Specimens that were analyzed by great circles were used if they had a MAD <20° (Fig. 1.3D). Virtual geomagnetic pole directions for circles were calculated using their last stable end point used in the great circle calculation. Data from specimens that had erratic demagnetization behaviors were excluded from analysis (Fig. 1.3E). A site mean direction was calculated for all sites with three samples with statistically significant directions using Fisher statistics (Fisher, 1953). Only sites that pass the Watson test for randomness (Watson, 1956) were used. Reversal boundaries were placed at the stratigraphic midpoints between samples of opposing polarity. The local polarity stratigraphy was then correlated to the geomagnetic polarity time scale (GPTS) (Ogg, 2012).

Rock Magnetism

Rock magnetic analyses were performed at the Institute for Rock Magnetism at the University of Minnesota. High temperature susceptibility measurements were collected on 8 rock samples using a Geofyzika KLY-2 Kappabridge AC Susceptibility meter in air. Measurements were recorded on warming from room temperature to 650 °C and cooling back to room temperature. The first derivative of the measurements was used

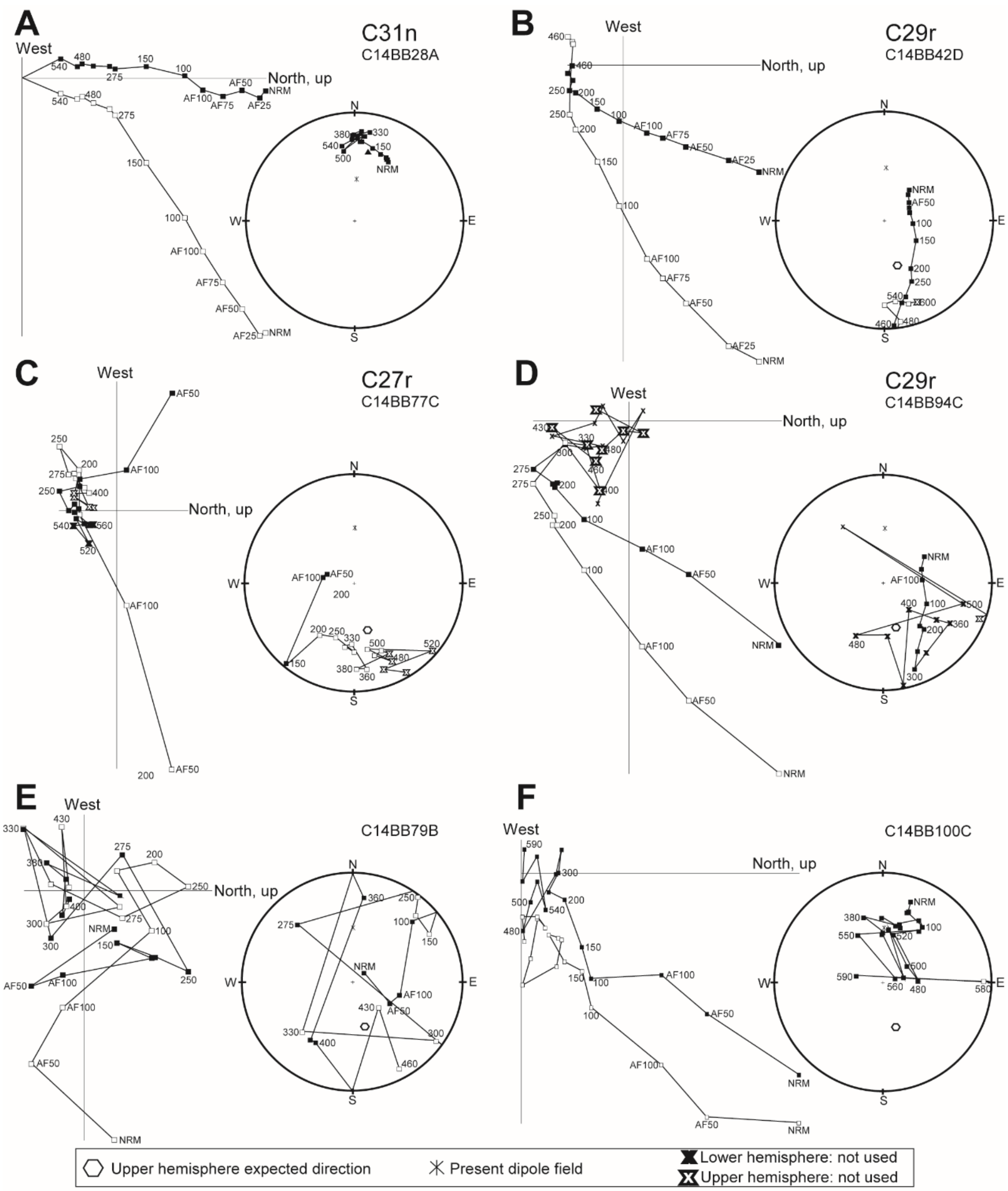

Figure 1.3. Representative Zijderveld diagrams and equal-area plots for each subset of data. (A) Demagnetization trajectory of a normal polarity sample from C31n where a line was calculated (36% of data). (B) Demagnetization trajectory of reversed polarity sample from C29r where a line was calculated. (C) Demagnetization trajectory of a reversed polarity sample from C27r where a line was calculated. (D) Reversed polarity sample with demagnetization trajectory best characterized by a great circle from C27r, direction calculated from last stable endpoint (28% of the data). Sample is located in overprinted interval. (E) Representative sample of erratic data that was not used for interpretations (11% of data). (F) Representative overprinted sample where calculated direction overlaps with modern (25% of data).

to determine the Curie temperatures. Hysteresis loops were measured on a MicroMag Princeton Measurements vibrating sample magnetometer (VSM) on eight samples at temperatures ranging from 30 °C to 600 °C.

The Quantum Design Magnetic Properties Measurement System (MPMS) was used for low-temperature remanence measurements on eight samples. The protocol included field-cooled (FC) remanence, zero-field-cooled (ZFC) low-temperature saturation isothermal remanent magnetization (LTSIRM), and room temperature saturation isothermal remanent magnetization (RTSIRM) following the methods of Sprain et al. (2016). This method involves initially applying a sustained DC field of 2.5 T on a sample as it cools from 300 K to 20 K (FC). The field is then turned off and remanence is measured while the sample warms to 300 K. The sample is cooled back down to 20 K with no field applied (ZFC) after which a 2.5 T LTSIRM applied. Remanence is measured while the sample warms back to 300 K. While at 300 K, a 2.5 T SIRM (RTSIRM) is applied and the remanence is measured while cooling down to 20 K then warming to 300 K.

Detrital Sanidine Dating

Four **s**amples were collected in the field from channels within the Aguja, Javelina, and Black Peaks Formations. Sample SS02 was taken at the base of the channel above paleosol 23 (Fig. 1.2). Samples SS07 and SS08 were taken within the Javelina Formation from the top of the channel below P10 and from the base of the channel below paleosol 19, respectively (Fig. 1.2). Sample SS13, from the Black Peaks Formation, was taken at the base of the channel above paleosol 28.

All processing and mineral separations were done at the New Mexico Geochronology Research Laboratory (NMGRL). Sample separation included: crushing and grinding whole rocks, cleaning with H_2O and HF acid, and sieving to appropriate grain size. Magnetic and heavy liquid density separation was used to concentrate the K-feldspar grains. Sanidine was hand-picked from the bulk feldspar separate based on optical clarity as viewed under a binocular microscope. As shown later by the argon analyses, the picked clear grains contained significant plagioclase and quartz.

The sample crystals were irradiated at the TRIGA reactor in Denver, Colorado for 16 h in the NM-276 package along with Fish Canyon Sanidine interlaboratory standard FC-2 with an assigned age of 28.201 Ma (Kuiper et al., 2008). Ages are calculated with a total ^{40}K decay constant of 5.463e-10 /a (Min et al., 2000).

After irradiation, six crystals of FC-2 from each monitor hole and ~100 sample crystals were loaded into copper trays, evacuated and baked at 140 °C for 4 h. Sample crystals were fused with a CO_2 laser and the extracted gas was cleaned with a NP 10 getter operated at 1.5 A for 30 seconds. The gas was analyzed for argon isotopes using an ARGUS VI multicollector mass spectrometer equipped with five Faraday cups, and one ion counting multiplier (CDD). The configuration had ^{40}Ar, ^{39}Ar, ^{38}Ar, ^{37}Ar and ^{36}Ar on the H1, AX, L1, L2, and CDD detectors, respectively. All data acquisition was accomplished with NM Tech Pychron software and data reduction used Mass Spec (v. 7.875) written by Al Deino at the Berkeley Geochronology Laboratory. Extraction line blank plus mass spectrometer background data are given in Table DR3.

Minimum age populations are generally defined by choosing the youngest dates that form a normal distribution as defined by the MSWD value of the distribution. The minimum age is the inverse variance weighted mean of the selected crystals and the error is the square root of the sum of $1/\sigma^2$ values. The error is also multiplied by the square root of the MSWD for MSWD greater than 1. J-error is included for all weighted mean ages and all errors are reported at 1σ unless otherwise noted.

Vertebrate Paleontology

A description and reevaluation of the therian component of the mammalian faunas, which is primarily on isolated and often fragmentary teeth, was undertaken by detailed examination of the specimens collected by Schiebout, Standhardt, and collaborators from the TMM 41400 (LSU VL-111; Tom's Top; Fig. 1.2), TMM 42327 (LSU VL-108; Dogie), and other localities from Big Bend (Schiebout, 1974; Schiebout et al., 1987; Standhardt, 1986). We also reevaluated the taxonomy of the Cretaceous dinosaur faunas from the Javelina and Aguja Formations.

Results

Magnetostratigraphy

Three hundred and sixty samples were analyzed from 121 sampling horizons. The samples can be divided into four subsets based on demagnetization behavior. The demagnetization trajectory of 36% of samples began with a strong north and moderately downward overprint that was mostly removed by ~275 °C (Fig. 1.3A) up to 450 °C (Figs. 1.3B, 1.3C), after which the stable endpoint was reached. The second subset, encompassing 28% of samples, had a demagnetization trajectory that was best characterized by a great circle. For these samples, the VGP latitude and longitude was calculated using the last coherent direction along a great circle trajectory (Fig. 1.3D), which was usually not a stable endpoint but which was sufficient to define polarity. The third subset of samples, 11% of samples, had an erratic demagnetization trajectory where a good direction could not be calculated (Fig. 1.3E). These samples were not used for polarity interpretation. The fourth subset comprised of the remaining 25% of samples had a stable direction between 100 and 300 °C, which then became erratic (Fig. 1.3F). The VGPs of these samples consistently overlaps with the modern direction and they have been interpreted to be completely overprinted. Consequently, these samples were not used for polarity interpretation.

In total, 235 samples from 121 sampling horizons composed the first and second subsets above and were used to calculate directions (Fig. 1.4; Table 1.2, A4, A5). Site mean directions were calculated from fifteen sample horizons that had three samples with statistically significant directions and passed the Watson test for randomness (Watson, 1956) (Table A6). The mean VGP latitude and longitude for Late Cretaceous reversed samples (local polarity B-) is −88°N, 274.7°E (n = 23; a_{95} = 12.1) and normal samples (local polarity A+, C+) is 76.4°N, 26.7°E (n = 30, a_{95} = 7.3). The mean VGP latitude and longitude for K-Pg samples (D-.1) is −79.5°N, 288.2°E (n = 57, a_{95} = 6.3). The mean VGP latitude and longitude for early Paleocene samples (D-.2) is −76.9 °N, 191.6°E (n = 21, a_{95} = 12.8). These pole locations are significantly distinct from the Cretaceous and Paleocene reference paleomagnetic pole for North America (Fig. 4) (Torsvik et al., 2008). There is also a small but consistent clockwise directional offset from the expected direction, which has no effect on our polarity interpretations. The origin of the directional offset and the difference between our calculated VGPs and the Cretaceous and Paleocene reference poles is likely due to variability in dip throughout the section, which may have

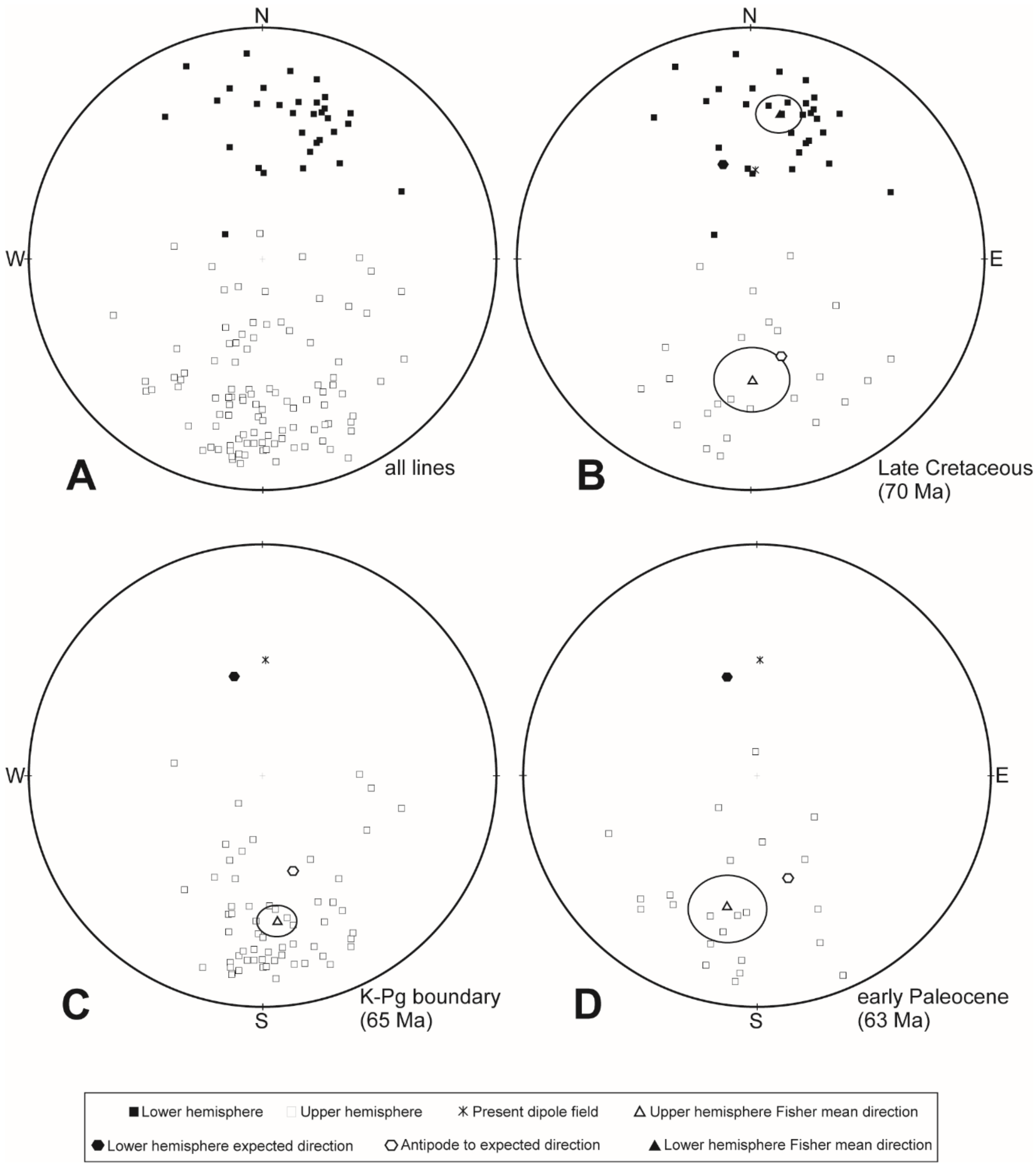

Figure 1.4. Equal area plot of characteristic magnetization directions calculated from: A) all lines B) all lines from Late Cretaceous interval C) all lines from K-Pg boundary interval D) all lines from early Paleocene interval.

been overcorrected for, and syndepositional/early post-deposition inclination shallowing, with a flattening factor of ~10%.

Table 1.2. Mean paleomagnetic directional data from the Dawson Creek section.

Subset	*n*	D (°)	I (°)	k	a95 (°)	Pole (°N)	Pole (°E)	K	A95 (°)
C32n - lines	*3*	13.3	31.5	96.2	12.6	72.9	28.4	107.2	12.0
C31r - lines	*23*	179.3	-46.0	7.3	12.1	87.6	226.2	5.6	14.0
C31n - lines	*27*	11.4	36.8	12.4	8.2	77.3	19.0	11.1	8.7
C31n - sites	*3*	358.4	29.5	27.5	24.0	76.5	83.2	24.1	25.7
C29r - lines	*58*	173.1	-36.6	9.5	6.4	80.8	118.4	8.2	7.0
C29r - sites	*9*	178.7	-30.8	23.2	10.9	77.7	81.7	24.2	10.7
C27r - lines	*21*	192.9	-40.6	7.2	12.8	78.4	354.1	6.0	14.2

Note. n – number of lines or sites included in the mean; D – declination; I – inclination; k – Fisher's (1953) precision parameter; a95 – radius of 95% confidence cone around mean (Fisher, 1953); pole N and E – mean of virtual geomagnetic poles calculated from each line or site mean; K and A95 – Fisher statistics of paleomagnetic pole.

The local polarity stratigraphy shows each sample direction and site means (Fig. 1.2). Polarity zones A- through D-.2 are highlighted along with interpreted hiatuses. An overprint interval is present at the top of the Javelina Formation and the base of the Black Peaks Formation from 177 to 194 m (Fig. 1.2). In this interval, there is a high proportion of overprint line fits and great circles where the direction was calculated from the last stable endpoint.

Detrital Sanidine Dating

The detrital sanidine dates in this study are used to correlate the deposits to the GPTS and to constrain the maximum deposition age. The age probability plots for all samples and associated analytical results are provided in Figure 1.5. Figure 1.2 shows the stratigraphic position of each detrital sanidine sample.

The Aguja Formation sample, SS02, has a minimum age population (= maximum depositional age) of 76.28 ± 0.06 Ma. Two samples were dated from the Javelina

Formation, SS07 and SS08. Sample SS07 recorded a minimum age population of 68.83 ± 0.13 Ma whereas, sample SS08 has a well-defined minimum age population at 68.08 ± 0.03 Ma. The sample from the Black Peaks Formation, SS13, has a minimum age population of 70.6 ± 0.4 Ma. However, the maximum depositional age is defined by a single grain dated to 65.9 ± 0.4 Ma.

Rock Magnetism

The dominant magnetic mineralogy in the Aguja Formation is a low-Ti titanomagnetite indicated by a 525 °C Curie temperature in high temperature hysteresis loops and a Verwey transition at ~110 K, lower than expected for pure magnetite (Figs. 1.6A, 1.6B). High temperature hysteresis loops for a normal polarity sample from the A+ interval of the Aguja Formation show a 600 °C Curie temperature suggesting the presence of maghemite as well. Field-cooled/zero field-cooled curves from low temperature rock magnetometry for a reversed polarity sample from the B- interval of the Aguja Formation converge at 300 K suggesting goethite is also a magnetic carrier.

Throughout the Javelina Formation, the dominant magnetic mineralogy varies. For the basal portion of the formation, samples with statistically significant reversed directions (B- interval) have >600 °C Curie temperatures measured from high temperature susceptibility and hysteresis loops, which indicates hematite is the primary magnetic mineral (Figs. 1.6C, 1.6D). In the overlying C+ interval, low temperature rock magnetometry measurements for a representative normal polarity sample show a pronounced Verwey transition at 120 K, with $M_{FC}>M_{ZFC}$, suggesting single domain magnetite is the dominant magnetic carrier (Figs. 1.6E, 1.6F). Both high temperature susceptibility measurements and hysteresis loops demonstrate a 600 °C Curie

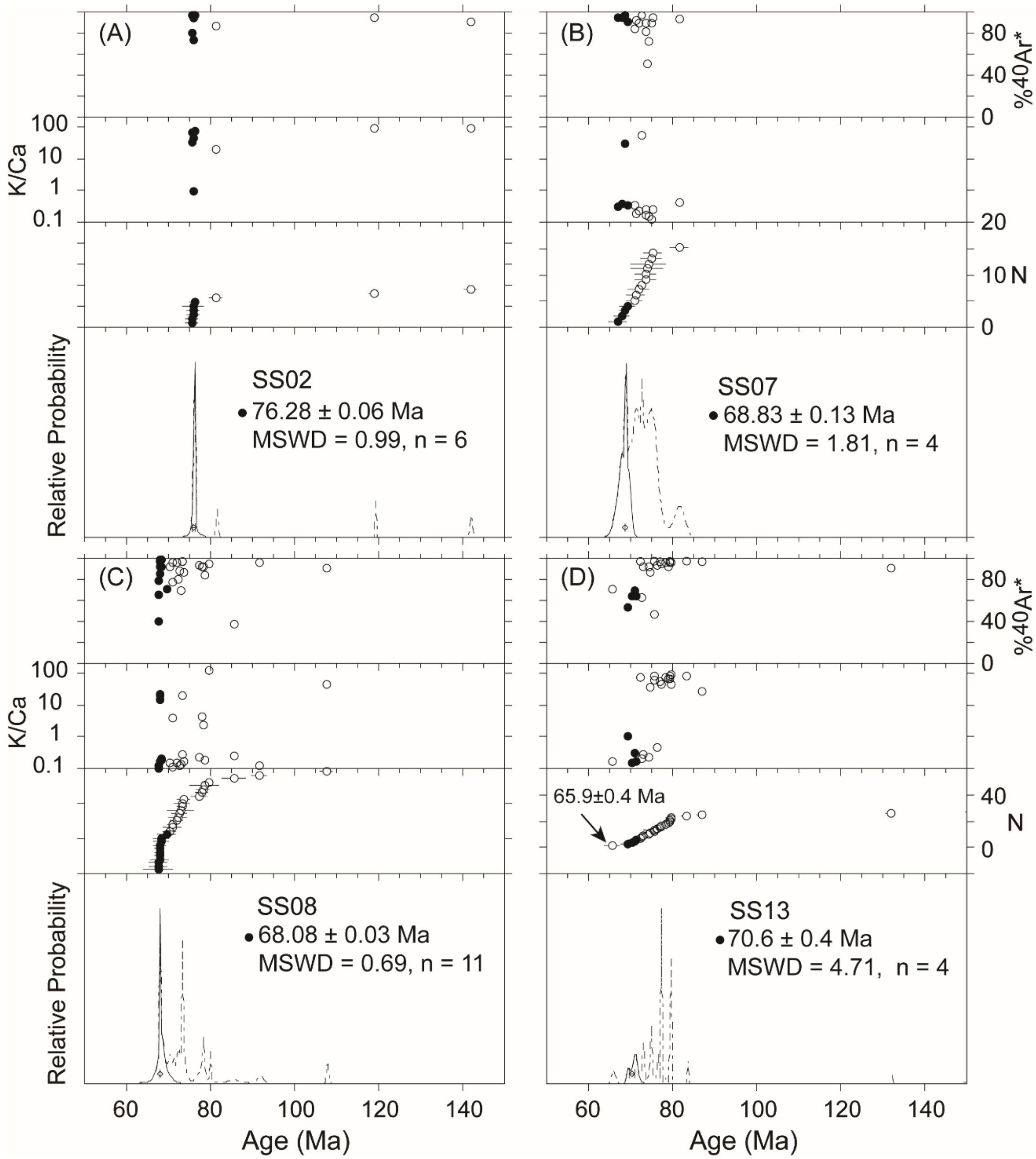

Figure 1.5. Age probability diagrams for the four analyzed samples. The plots show, from bottom to top, the age probability distribution spectrum where the dashed line represents the probability curve for all of the data whereas the solid line is for the data shown with solid circles, distribution of individual single-crystal ages with 2σ errors, K:Ca ratios, and percentage of radiogenic ^{40}Ar.

temperature signaling maghemite is the dominant magnetic mineralogy over the D-interval of the Javelina Formation (Figs. 1.6G, 1.6H).

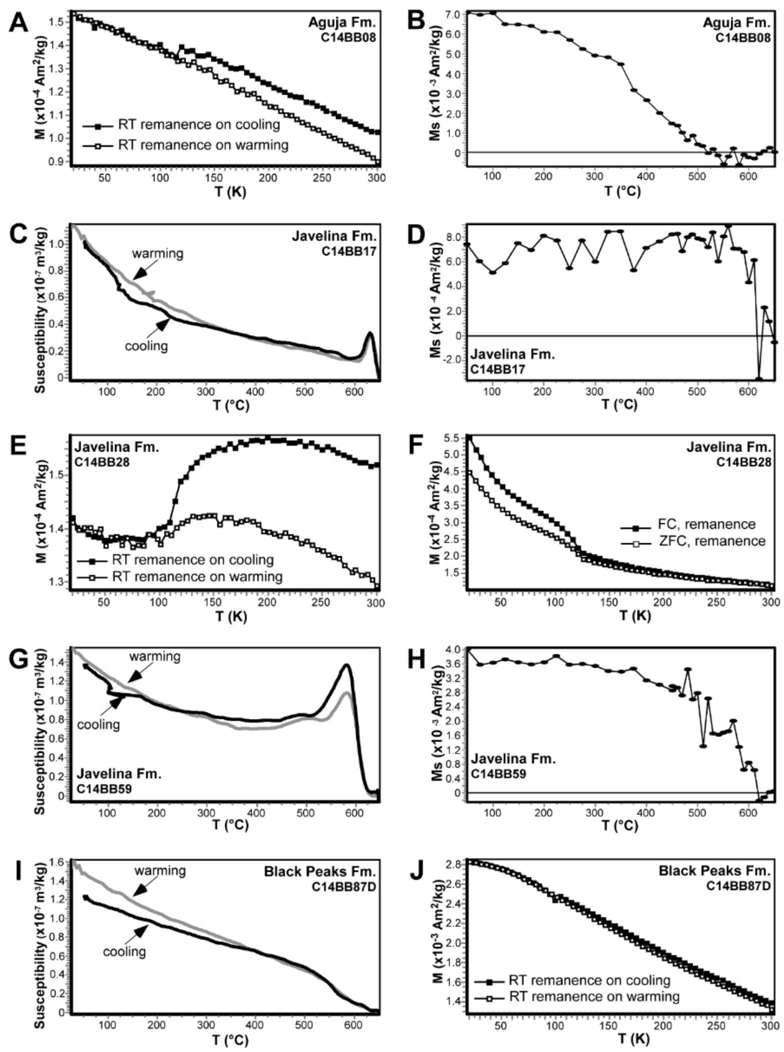

Figure 1.6. Rock magnetic analysis results including low temperature magnetization curve of representative samples, high temperature VSM (vibrating sample magnetometer) curves of bulk magnetic susceptibility, and high temperature heating and cooling curves of bulk magnetic susceptibility in air. Room temperature (RT) plots show magnetization measurements at room temperature following the application of saturation isothermal remanent magnetization (SIRM). FC (field-cooled) and ZRC (zero field-cooled) plots show magnetization during warming following a sustained direct current field of 2.5 T during cooling (FC) and during warming following a SIRM imparted at low temperature (ZFC). (A) RT curves for a B- polarity zone reversed polarity sample from the Aguja Fm. indicating titanomagnetite. (B) High temperature VSM curve for a B- polarity zone reversed polarity sample from the Aguja Fm. indicating titanomagnetite. (C) High temperature susceptibility curves for a B- polarity zone reversed sample in the Javelina Fm. indicating hematite. (D) High temperature VSM curve for a B- polarity zone reversed sample in the Javelina Fm. indicating hematite. (E) RT curves for a C+ polarity zone normal sample in the Javelina Fm. indicating magnetite. (F) FC/ZFC curves for a C+ zone polarity zone normal sample in the Javelina Fm. indicating magnetite. (G) High temperature susceptibility curves for a D-.1 polarity zone reversed sample in the Javelina Fm. indicating maghemite. (H) High temperature VSM curve for a D-.1 polarity zone reversed sample in the Javelina Fm. indicating maghemite. (I) High temperature susceptibility curves for a D-.2 polarity zone reversed sample in the Black Peaks Fm. indicating titanomagnetite. (J) RT curves for a D-.2 polarity zone reversed sample in the Black Peaks Fm. indicating titanomagnetite.

A large number of samples are interpreted to be overprinted in the upper portion of the Javelina Formation and lower portion of the Black Peaks Formation (Fig. 1.2). Rock magnetic analysis for a representative overprinted sample and representative reversed sample within this interval indicates that titanohematite is the dominant magnetic carrier with minor amounts of magnetite. RTSIRM curves indicate an approximate twofold increase in remanence which could suggest either goethite or titanohematite (Figs. 1.7A, 1.7C) (Dekkers, 1989; France and Oldfield, 2000). However, FC-ZFC-LTSIRM curves also show little to no separation between FC and ZFC curves, which would be expected with goethite (Figs. 1.7B, 1.7D). Consequently, titanohematite is the most likely magnetic carrier. This interpretation is further supported by the similar character of the curves to those interpreted as titanohematite by Sprain et al. (2016). Overprinted samples were differentiated from a K-Pg normal polarity based on the presence of titanohematite and VGPs that overlapped with modern.

Titanomagnetite is the dominant magnetic carrier in the Black Peaks Formation above the overprinted interval as indicated by a 560 °C Curie temperature and 110 K Verwey transition in high temperature susceptibility, low temperature magnetometry, and high temperature hysteresis loops (Figs. 1.6I, 1.6J). Titanohematite also appears to be a secondary magnetic carrier in this interval.

Vertebrate Paleontology

The results of a reevaluation of the lower Black Peaks Formation faunas of the Dawson Creek, Rough Run, and possibly correlative areas of Big Bend National Park are summarized in Figures 1.8 and 1.9, Table 1.3, and the Appendix. Mammals originally identified as Puercan NALMA taxa (i.e., *Eoconodon*, *Periptychus coarctatus* [=

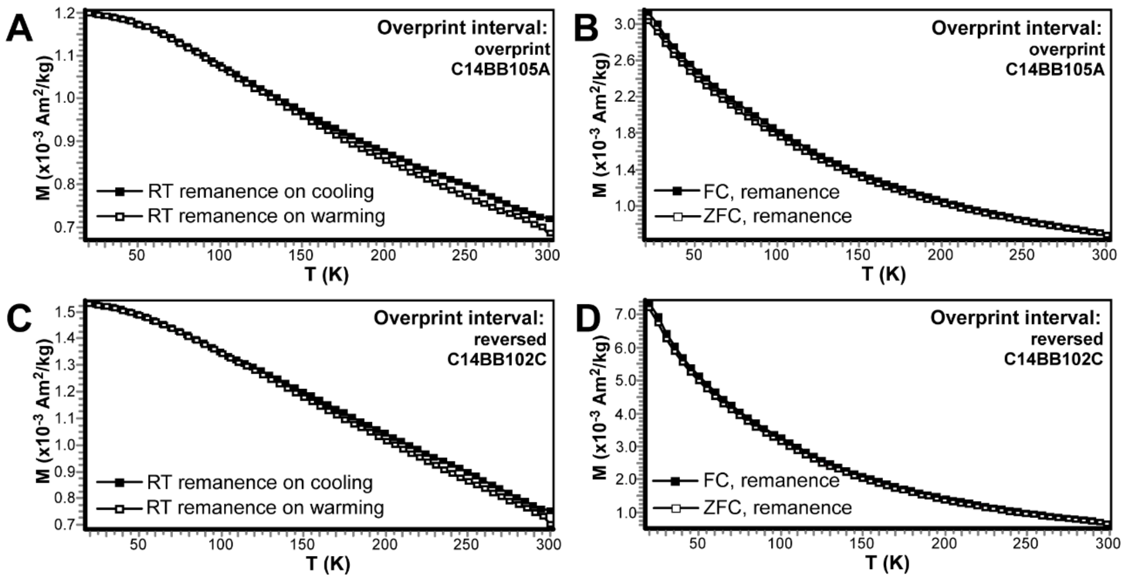

Figure 1.7. Rock magnetic analysis for the overprint interval in the upper Javelina and lower Black Peaks Formations indicating titanohematite. (A) RT curves for an overprinted sample in the overprint interval. (B) FC/ZFC curves for an overprinted sample in the overprint interval. (C) RT curves for a reversed sample in the overprint interval. (D) FC/ZFC curves for a reversed sample in the overprint interval.

Carsioptychus coarctatus], and *Ellipsodon priscus*) were misidentified and instead represent typical and in some cases defining Torrejonian taxa (*Triisodon coryphaeus*, *Periptychus carinidens*, and *Ellipsodon* cf. *E. inaequidens*) (Table 1.3). In addition, we describe two new species that are endemic to the Black Peaks Formation of Big Bend National Park (see Appendix).

The fauna from low in the Paleocene of the Dawson Creek section (TMM locality 41400 [LSU VL-111]; Tom's Top) can be confidently placed within the Torrejonian NALMA based on the presence of several characteristic Torrejonian taxa (see Lofgren et al., 2004): the genera *Bryanictis*, *Mixodectes*, *Plesiolestes*, and *Promioclaenus*. Moreover, two of these taxa are represented by species known only from the middle Torrejonian (To2), *Mixodectes malaris* and *Plesiolestes nacimienti*. *M. malaris* is an index taxon for the middle Torrejonian and is restricted to chron C27r of the Nacimiento

Formation (Williamson, 1996), and is also present in the Swain Quarry fauna of the Fort Union Formation of Wyoming (Rigby, 1980). *Promioclaenus lemuroides* is also tentatively identified in the fauna and is restricted to the Torrejonian of western North America where it is present in Montana, Wyoming, Utah, and New Mexico.

The fauna from TMM 42327 (LSU VL-108; Dogie) of Rough Run Amphitheater is also firmly established to be Torrejonian because it contains the defining taxon for the Torrejonian: *Periptychus carinidens*. That fauna also contains a number of other taxa including *Bryanictis*, *Ellipsodon*, and *Mioclaenus* that are elsewhere restricted to the Torrejonian. *Ellipsodon* is from the middle Torrejonian (To2), and the species *E. inaequidens*, which is tentatively identified in the Dogie fauna, is restricted to the lower part of chron C27r in the Nacimiento Formation, in the *Protoselene opisthacus* – *Ellipsodon granger* [Tj2] and *E. granger* – *Arctocyon ferox* [Tj3] zones (after Williamson, 1996).

Following the reevaluation of the Tom's Top and Dogie faunas, we find that no fossil therian mammals that are restricted to the Puercan are present in the Black Peaks Formation, and instead the fauna is comprised of Torrejonian taxa. Thus, we ca confidently correlate these fossil localities to the Torrejonian NALMA (Table 1.3; a complete description of the therian mammals from these localities is contained in the Appendix). Further, given the occurrence of taxa in both localities that are restricted to the middle Torrejonian in the San Juan Basin in New Mexico, we tentatively correlate both TMM 41400 (Tom's Top) and TMM 42327 (Dogie) to the Torrejonian 2 NALMA. The reidentification of taxa from localities low in the Black Peaks Formation and reevaluation of the resulting biochronology of the Aguja, Javelina, and Black Peaks

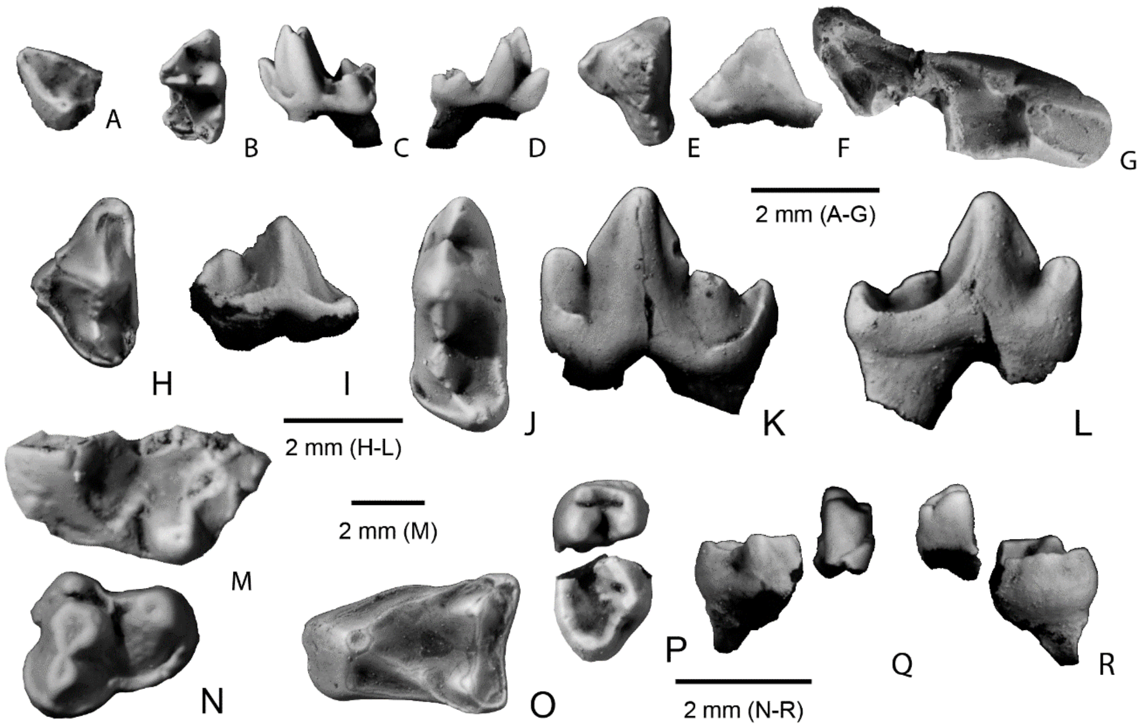

Figure 1.8. Metatheria, Cimolesta, Carnivoramorpha, and Euarchonta from the Dawson Creek and Rough Run areas, Big Bend National Park, Texas. A-D, *Peradectes* sp.: A, partial right M1 (LSU V-895) in occlusal view; B-D, left m2 or m3 (LSU V-705), in occlusal (B), buccal (C), and lingual (D) views; E-G, Cimolestidae indeterminate: E-F, left P3 (LSU V-708) in occlusal (E) and buccal (F) views; G, partial right M2 (LSU V-841) in occlusal view; H-I, *Bryanictis* new sp.: H-I, left P3 (LSU V-709) in occlusal (H) and buccal (I) views; J-L, left p4 (TMM 41400–10, holotype) in occlusal (J), buccal (K), and lingual (L) views; M, *Mixodectes malaris*, partial left M3 (LSU V-924) in occlusal view; N-R, *Plesiolestes nacimienti*; N, right P4 (LSU V-921) in occlusal view; O, left M2 (TMM 41400–17) in occlusal view; P-R, partial right m3 (LSU V-923) in occlusal (P), buccal (Q), and lingual (R) views. Specimens have been dusted with magnesium oxide to increase visibility of surface features.

Formations indicates that the Aguja fauna correlates to the Judithian NALMA, the Javelina fauna to the Lancian NALMA, and the Black Peaks fauna to the Torrejonian. Therefore, there is likely a significant hiatus between the vertebrate localities in the Aguja Formation and the Javelina Formation and another major hiatus between the vertebrate localities in Javelina Formation and the Black Peaks Formation.

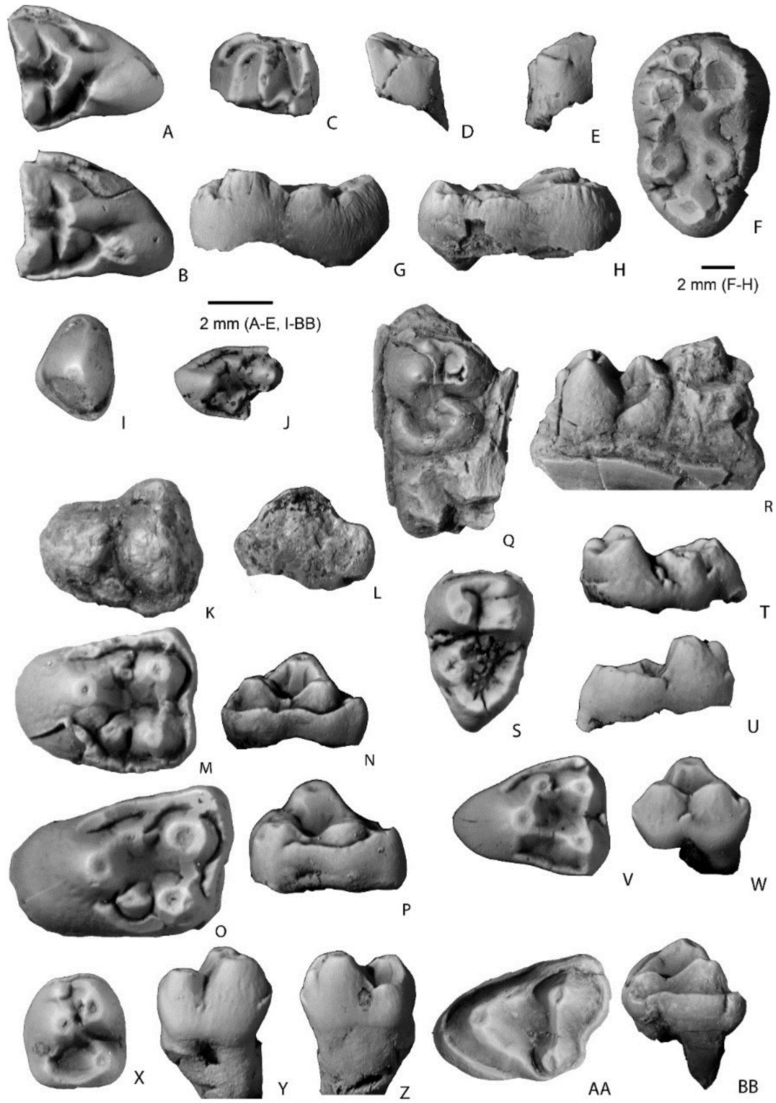

Figure 1.9. ‘Condylarthra’ from the Dawson Creek and Rough Run areas, Big Bend National Park, Texas. A-E, *Haploconus* sp.: A, partial right M1 (LSU V-711) in occlusal view; B, partial right M2 (LSU V-710) in occlusal view; C-E, partial left m1 (LSU V-835) in occlusal (C), lingual (D), and buccal (E) views; F-H, *Periptychus carinidens*: nearly complete m3 (LSU V-888) in occlusal (F), lingual (G), and buccal (H) views; I-J, *Promioclaenus* cf. *P. lemuroides*: I, left P3 (LSU-875) in occlusal view; J, partial left M3 (LSU V-920) in occlusal view; K-U, *Mioclaenus* new sp.: K-L, left P4 (LSU V-833) in occlusal (K), and buccal (L) views; M-N, left M1 (LSU V-891) in occlusal (M) and buccal (N) views; O-P, left M2 (LSU V-890, holotype) in occlusal (O) and buccal (P) views; Q-R, partially erupted right m2 (LSU V-703) in occlusal (Q) and lingual (R) views; S-U, left m3 (LSU V-881) in occlusal (S), buccal (T), and lingual (U) views; V-Z, *Ellipsodon* cf. *E. inaequidens*: V-W, left M1 (LSU V-706) in occlusal (V) and buccal (W) views; X-Z, right m1 (LSU V-701) in occlusal (X), buccal (Y), and lingual (Z) views; AA-BB, cf. *Goniacodon levisanus*: AA-BB, left M3 (LSU V-704) in occlusal (AA) and buccal (BB) views. Specimens have been dusted with magnesium oxide to increase visibility of surface features.

Table 1.3. Therian mammals.

Standhardt (1986)	This paper
TMM locality 41400, "Tom's Top"	
Carnivora	Carnivoramorpha
Didymictidae	Viverravidae
Bryanictis terlinguae new species	*Bryanictis* new species
Insectivora	Euarchonta
Mixodectidae	Mixodectidae
Mixodectes malaris	*Mixodectes malaris*
?Primates	Primates
Microsyopidae	"Palaechthonidae"
Palaechthon nacimienti	*Plesiolestes nacimienti*
"Condylarthra"	"Condylarthra"
Mioclaenidae	Mioclaenidae
Promioclaenus sp.	*Promioclaenus* cf. *P. lemuroides*
TMM locality 42327, "Dogie"	
Marsupialia	Metatheria
Didelphidae	Peradectidae
Peratherium sp.	*Peradectes* sp.
Cimolesta	Cimolesta
Palaeoryctidae	Cimolestidae
Gelastops sp.	Cimolestidae indeterminate
Carnivora	Carnivoramorpha
Didymictidae	Viverravidae
Bryanictis terlinguae new species	*Bryanictis* new species
"Condylarthra"	"Condylarthra"
Arctocyonidae	"Triisodontidae"
Eoconodon sp.	cf. *Goniacodon levisanus*
Periptychidae	Periptychidae
Carsioptychus coarctatus	*Periptychus carinidens*
Haploconus inopinatus	*Haploconus* sp.
Mioclaenidae	Mioclaenidae
Ellipsodon priscus	*Ellipsodon* cf. *E. inaequidens*
Nexus plexus new genus and species	*Mioclaenus* new species

Discussion

Magnetic Mineralogy

The dominant magnetic mineralogy of the Aguja and Black Peaks Formations is titanomagnetite. The Javelina Formation contains various magnetic mineralogies including hematite, single domain magnetite, maghemite, and titanohematite. The presence of titanohematite as a magnetic carrier can explain much of the overprint signal in the upper portion of the Javelina Formation and lower portion of the Black Peaks. Titanohematite is likely detrital and has a relatively low Curie temperature ranging from 150 to 200 °C; consequently, the grains could easily be viscously reset with modest burial heating. Additionally, the Black Peaks Formation in the section is overlain by basaltic flows which plausibly heated the underlying deposits above the Curie temperature of titanohematite, causing these grains to be reset, which could also have resulted in the overprinted interval.

All reversed polarity samples in the section have a natural remanent magnetization (NRM) that overlaps with the modern direction suggesting all samples have a modern overprint. In samples where titanohematite is the primary magnetic carrier, remanence is lost at low temperatures during the stepwise thermal demagnetization process. In most of these samples, low temperature magnetometry curves also indicate a minor presence of magnetite that could hold remanence beyond the Curie temperature of titanohematite. The demagnetization behavior of samples with titanohematite as the primary magnetic carrier behaved in two ways. The samples demagnetization behavior was either (1) too erratic for a statistically significant reversed direction to be calculated (Fig. 1.3F); or (2) was measurable to ~300 °C such that a reversed direction could be calculated using a great circle (Fig. 1.3D). We interpret samples that we were able to calculate a reversed direction to have had a larger proportion of magnetite than samples that behaved erratically. Given that we calculated several lines and great circles indicating a reversed direction within this interval, we interpret that entire interval to be reversed with a strong normal overprint (Fig. 1.2).

Relationship of Polarity Stratigraphy to GPTS

We correlated the local polarity stratigraphy to the GPTS using a combination of vertebrate paleontology, $\delta^{13}C$ values of carbonate nodules (Nordt et al., 2003), detrital sanidine ages, and stratigraphic thickness (Fig. 1.10). Using these methods, we correlate our polarity stratigraphy to the GPTS as follows: A+ to >C32n, B- to C31r, C+ to C31n, D-.1 to C29r, and D-.2 to C27r.

The B- and C+ intervals were correlated to C31r and C31n respectively based on the presence of dinosaur faunas and stratigraphic thickness. The change from reversed polarity to normal polarity in the section was pinned to the boundary between C31r and C31n (Ogg, 2012). Given that the strata are a series of stacked paleosols over this interval, there is assumed to be no significant amount of time missing. It is possible that the B- and C+ intervals could correlate to C30r and C30n; however, C30r only spans 173 k.y. (Ogg, 2012) and the B- interval corresponds to 77 m of section. Deposition over such a short time interval seems unlikely (see discussion of sedimentation rates below). The detrital age of 76.28 ± 0.06 Ma from SS02, near the base of the B- interval, suggests the sandstone bodies represent reworked older sediments.

Because the B- interval was correlated to C31r, the underlying A+ interval was correlated to C32n. However, there is only one stratigraphic locality associated with this interval and no fossils from Dawson Creek to constrain its age further. The mammalian fauna of the Aguja correlated to the Judithian, which occurs from ~79–74 Ma (Cifelli et al., 2004), suggests the Aguja is likely older than C32n. Additionally, geochronologic studies on the Aguja Formation in other areas of the park also indicate that the age may be older (Befus et al., 2008; Breyer et al., 2007). Thus correlation to C32n represents the minimum age for the Aguja. The detrital age of 76.28 ± 0.06 Ma in the overlying B- interval also suggests that the A+ interval could be older.

We interpret the D-.1 interval to correlate to C29r for two reasons. First, the detrital sanidine ages support correlation to C29r. At the base of the D-.1 interval, the SS07 detrital age of 68.83 ± 0.13 Ma corresponds to C31n and the SS08 detrital age of 68.08 ± 0.03 Ma, from the middle of the D-.1 interval, corresponds to C30n. Since the deposits in this interval are reversed, these detrital ages constrain the interval to either C29r or C30r. Second, the K-Pg boundary, which occurs within C29r (Ogg, 2012), is within the D-.1 polarity interval (Lehman, 1990; Wiest et al., 2018), indicating D-.1 is correlative to C29r and not C30r.

There is a significant sandstone body with an erosive base indicating an unconformity between D-.1 and D-.2 (Fig. 1.2) (Atchley et al., 2004). The occurrence of Torrejonian mammals, which first appear in C28n (Lofgren et al., 2004), above this sandstone means that the D-.2 interval cannot correlate to C29r. The identification of To2 mammals, which occur in C27r in the San Juan Basin (Lofgren et al., 2004; Williamson, 1996), allows us to correlate the D-.2 interval to C27r (Fig. 1.10). The maximum depositional age of sample SS13 located in the sandstone overlying P28 is defined by a single grain dated to 65.9 ± 0.4 Ma, which supports an early Paleocene age. Because we

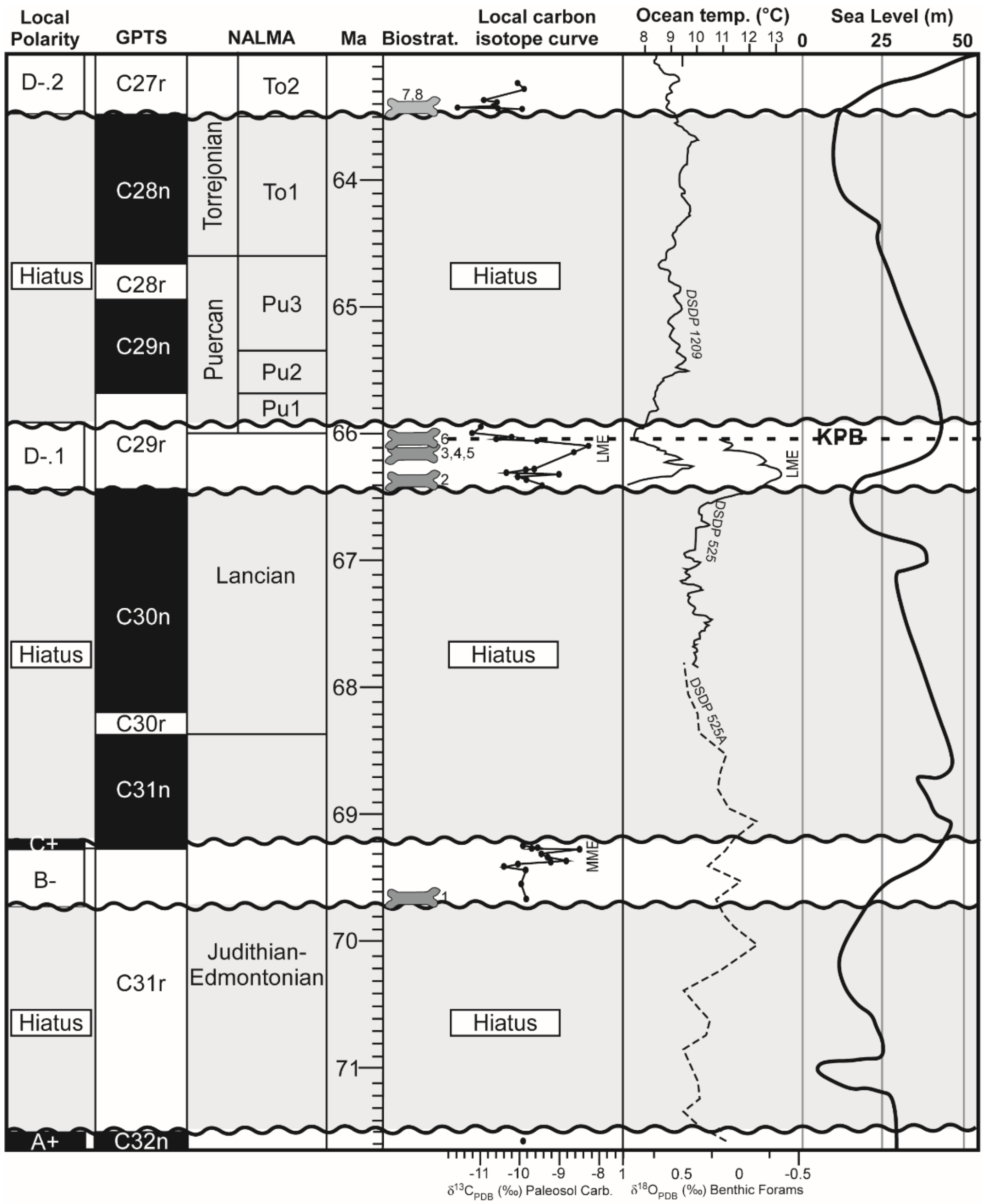

Figure 1.10. Summary chart for the Dawson Creek section showing correlation of local polarity stratigraphy, GPTS (Ogg, 2012), NALMA (Woodburne, 2004), time scale (Gradstein et al., 2012), and local fossil localities. Fossil localities: 1. LSU VL-110; 2. LSU VL-149; 3. TMM 41450, LSU VL-106; 4. LSU VL-112; 5. LSU VL-145; 6. TMM 41501; 7. TMM 41400, "Tom's Top" (LSU VL-111); 8. LSU VL-109 (Lehman, 1990). Gray boxes highlight hiatuses in the record, KPB: K-Pg boundary. $\delta^{13}C_{PDB}$ isotopic values from pedogenic carbonate modified from Nordt et al. (2003), MME: mid-Maastrichtian Event and LME: late Maastrichtian Event. Marine temperature curves calculated from stable O isotopes using Erez and Luz (1983) equation assuming a −1.2‰ ice-free standard mean ocean water (SMOW): DSDP 1209 in the North Pacific (Westerhold et al., 2011), and DSDP 525A (Li and Keller, 1998a) and DSDP 525 (Li and Keller, 1998b) in the South Atlantic. Global sea level curve from Miller et al. (2005).

do not have any other age constraints for this interval, we assumed the base of the D-.2 interval starts at the base of C27r, but note that this is a maximum age for this interval.

Sedimentation Rate Calculations

There are multiple chronostratigraphic tie points within the D-.1 local polarity interval, and therefore we used that interval to develop a sedimentation rate model for the Dawson Creek section. To determine the sedimentation rates for C29r, we first used the K-Pg boundary (66.043 Ma, Renne et al., 2013), which occurs at 172 m in the section (Wiest et al., 2018), and late Maastrichtian event, which occurs at 154 m in the section (Nordt et al., 2003) as known tie points. The late Maastrichtian event has been estimated to occur ~250 k.y. before the boundary (Li and Keller, 1998a, 1998b; Westerhold et al., 2011; Tobin et al., 2012), thus we used an age of 66.25 Ma (C29r) for it (Fig. 1.10). Using these tie points, the resulting sedimentation rate is 87 m/myr. Extrapolation of this sedimentation rate throughout the underlying portion of the reversed D-.1 interval would put the base of the polarity zone at 66.77 Ma, which is well within C30n (Ogg, 2012). Given that this interval is of reversed polarity, the age estimate is impossible, thus, we interpret the sedimentation rate of 87 m/myr to be too slow.

Second, we assumed the maximum depositional age for the base of the D-.1 interval correlates to the base of C29r or 66.398 Ma (Ogg, 2012). A sedimentation rate was then calculated from the base of the D-.1 local polarity zone to the K-Pg boundary at 172 m, resulting in a rate of 203 m/myr. This sedimentation rate estimates an age of 66.157 Ma for the onset of the late Maastrichtian event, which is similar to age estimates from the marine record (Li and Keller 1998a, 1998b; Westerhold et al., 2011; Tobin et al., 2012). Thus, we favor the second interpreted sedimentation rate, and extrapolated it to the remainder of the section to estimate the durations of deposition (Fig. 1.10). The B-interval spans 379 k.y., the C+ interval spans 54 k.y., the D-.1 interval spans 459 k.y., and the D-.2 interval spans 280 k.y.

Unconformities

The magnetostratigraphy from B.J. MacFadden (*in* Standhardt, 1986) correlated the section to C30n to C28r with no recognized unconformities. Atchley et al. (2004) documented unconformities in the section, but concluded that they did not span any significant amount of time. Our new age constraints indicate the Dawson section spans from C32n to C27r (71.6 Ma to 63.2 Ma) with significant hiatuses (Fig. 1.10), which supports the suggestion in Nordt et al. (2003) that considerable time is missing from the section. The hiatuses in the section correspond with amalgamated sandstone channel complexes suggesting incision into the landscape. Based on our chron assignments and sedimentation rate estimates, the minimum duration for the hiatuses between A+ and B-intervals spans ~1.75 myr, between C+ and D-.1 spans ~2.82 myr, and between D-.1 and D-.2 spans ~2.4 myr. Mammalian biostratigraphy from the Javelina and Black Peaks Formations supports the duration of the unconformity between D-.1 and D-.2 because the last occurrence of Lancian dinosaurs near the top of the Javelina Formation and the lowest occurrence of Torrejonian mammals suggests a hiatus of ~2.5 Ma (66.04 Ma for the K-Pg boundary to 64.49 for base of C27r [Ogg, 2012]). The occurrence of Judithian mammals in the Aguja (~79–74 Ma [Cifelli et al., 2004]) and the Lancian dinosaur assemblage of the Javelina (~69–66 Ma [Cifelli et al., 2004]) suggests that the unconformity between the A+ and B- intervals is likely longer than ~1.75 myr.

Relating the section and associated hiatuses to the global sea level curve from Miller et al. (2005) in Figure A demonstrates the hiatuses are associated with falling stage and lowstand tracts while intervals of deposition occurred during transgressive and highstand tracts. Increases in accommodation due to relative sea level rise could have resulted in deposition along the coastal plain while relative sea level fall resulted in loss of accommodation and non-deposition and/or erosion (e.g., Wright and Marriott, 1993; Shanley and McCabe, 1994). The detrital ages also suggest that the sediment deposited in the section represents recycled material from the missing time intervals. These results support the conclusion in Atchley et al. (2004) that the deposition of the section was controlled by eustatic sea level; however, at a different time scale than previously suggested. The trend of deposition during transgressive and highstand system tracts and non-deposition/erosion during falling stage and lowstand tracts provides an independent check on the reasonability of the calculated sedimentation rate, as deposition throughout the section is internally consistent.

Biostratigraphic Implications

A Lancian biostratigraphic age for the middle and upper part of the Javelina Formation (which also includes the base of the Black Peaks Formation of some workers [e.g., Lehman and Busbey, 2007; Cobb, 2016]) is based on the presence of three dinosaurs: *Alamosaurus*, *Tyrannosaurus rex*, and *Torosaurus,* which have been regarded as part of its distinctive *Alamosaurus* fauna (Lehman, 2001; Lehman et al., 2006). *Alamosaurus sanjuanensis* has been reported from several latest Cretaceous faunas restricted to the American Southwest: the North Horn Formation of central Utah, the Naashoibito Member, Kirtland Formation of the San Juan Basin northwestern New

Mexico, the McRae Formation of central New Mexico, and the Javelina Formation of west Texas. In all the faunas where *Alamosaurus*, *Tyrannosaurus rex* or cf *T. rex,* and the large ceratopsian *Torosaurus utahensis* or a similar taxon (identified as either *Torosaurus* cf. *T. utahensis* [Big Bend National Park] or *Ojoceratops*, a taxon considered by some workers to be synonymous with *Triceratops* [e.g., Longrich, 2011] or *Torosaurus utahensis* [see Wick and Lehman, 2013]) are present. None of these taxa are known from pre-Lancian age faunas and *Tyrannosaurus* is restricted to Lancian faunas of the northern Rocky Mountain region, supporting a Lancian assignment for the faunas of the Javelina Formation. Additionally, our age constraints indicate that the dinosaur fauna in the Javelina Formation is confined to C29r. Thus it is contemporaneous to the dinosaur fauna of the Hell Creek Formation in the Northern Great Plains. The Hell Creek Formation dinosaur fauna is the most complete, continuous end-Cretaceous North American record and has been well studied with respect to dinosaur diversity prior to the boundary (e.g., Sheehan et al., 1991; Pearson et al., 2002; Fastovsky and Sheehan, 2005; Fastovsky and Bercovici, 2016). Our age constraints for the Dawson Creek section indicate that differences between the Javelina and Hell Creek faunas are not the result of them being different ages as suggested by Lucas et al. (2016). Instead, the differences in the faunas are likely driven by other factors such as isolation between populations and/or environmental conditions leading to endemism and provinciality in the Latest Cretaceous as suggested by Lehman (1987, 2001). Additionally, it suggests that the magnitude of Brusatte et al., 2015), because these taxa restricted to the American Southwest also likely went extinct at the boundary. Future work comparing the Javelina and Hell Creek dinosaur faunas will be valuable for evaluation of dinosaur endemism, provinciality, and extinction.

The mammalian fauna in the Black Peaks Formation has been reassigned as age equivalent to Torrejonian 2 fauna found elsewhere in western North America. Any difference between the mammals found in Dawson Creek and other Torrejonian localities would reflect environmental or biogeographic variability rather than temporal. Thus, the Black Peaks fauna is an important addition to evaluate North American early Paleocene mammalian diversity and biostratigraphy across other basins.

Paleoclimate Implications

Our age constraints suggest that the two warming events presented in Nordt et al. (2003) document rapid (<200 k.y.) changes in climate within the Maastrichtian. At the top of the B- interval, the pedogenic carbonate $\delta^{13}C$ values previously identified as the mid-Maastrichtian Event occur (Nordt et al., 2003). The age constraints in this paper assigns the mid-Maastrichtian event an age between 69.35–69.30 Ma. The mid-Maastrichtian Event observed in the marine record contains multiple peaks in isotopic values, one that occurs from ~69.0–69.4 Ma (Li and Keller, 1998a, 1998b), suggesting a possible correlation (Fig. 1.10). Using the sedimentation rate that was calculated independent of the marine record late Maastrichtian event chemostratigraphic correlation, the onset of the late Maastrichtian event in paleosol 19 is at 66.157 Ma with the peak excursion value occurring at 66.092 Ma. These ages are in general agreement with the marine record where the peak excursion values occur at 66.25 Ma (Li and Keller, 1998a, 1998b; Westerhold et al., 2011). However, it should be noted that there is likely a sedimentation rate change associated with the late Maastrichtian event in the Dawson

Creek section suggested by the much lower sedimentation rate calculated between the K-Pg boundary and the late Maastrichtian event onset (87 m/myr) compared to the sedimentation rate calculated for the entire D-.1 interval from the K-Pg boundary and the assumed base of C29r at the base of the D-.1 zone (203 m/myr). Thus, it is possible that the age estimated here for the late Maastrichtian event from the calculated sedimentation rate is too young. Nonetheless, the age estimate supports the correlation between the terrestrial late Maastrichtian event greenhouse event (Nordt et al., 2003) and the greenhouse event recorded in the marine record (Li and Keller, 1998a, 1998b; Westerhold et al., 2011; Tobin et al., 2012).

Our age constraints demonstrate that the Dawson Creek section correlates differently to strata in Big Bend National Park and western North America than previously thought. The Dawson Creek C27r strata correlate with the lower portion of the west Tornillo Flat section in the northern area of Big Bend where pedogenic carbonate carbon and oxygen isotopes have also been characterized through the Eocene (Bataille et al., 2016). They observe a correlation between early Paleogene global temperature trends and the sediment accumulation rates and lithostratigraphy, concluding climate was the dominant control on deposition rather than global sea level as we suggest. However, the Tornillo Flats and Dawson Creek sections are not age equivalent. The Dawson Creek section is predominantly Cretaceous while the Tornillo Flat section is predominately Paleogene, which suggests the primary controls on deposition in the Big Bend region changed from eustatic sea level in the late Cretaceous and early Paleocene to climate in the middle Paleocene and Eocene, possibly reflecting the retreat of the Western Interior Seaway in the Paleogene (Davidoff and Yancey, 1993). The Dawson Creek C27r strata also correlate to terrestrial deposits of the San Juan Basin, New Mexico where work is ongoing reconstruction paleosol bulk carbon $\delta^{13}C$ values and climate trends from paleosol geochemical proxies (e.g., Secord et al., 2016; Leslie et al., 2016). The age model for Dawson Creek presented here constrains the timing of climate trends from the Late Cretaceous through early Paleocene, bolstering the significance of the Dawson Creek section as part of the North American terrestrial record.

Conclusions

Paleomagnetic analysis of the Dawson Creek Section in Big Bend National Park combined with reexamination of the fauna indicates the section correlates to C32n-C31n, C29r, and C27r of the GPTS with three large hiatuses that are longer than 1.5 myr each. These hiatuses correspond to falling stage and lowstand tracts of the global sea level curve, while deposition correlate to transgressive and highstand tracts (Miller et al., 2005), indicating that eustatic sea level change was the primary driver of environments of deposition within the Dawson Creek section. Rock magnetic analyses indicates that the dominant magnetic carrier in the Aguja and Black Peaks Formations is titanomagnetite, while the Javelina Formation has varying magnetic carriers including hematite, magnetite, and maghemite. We conclude that the overprint interval surrounding the K-Pg boundary was likely a result of titanohematite that was reset by burial or overlying basaltic flows.

This new age model has implications for biostratigraphic and isotopic correlations between the Big Bend area and other Cretaceous-Paleogene (K-Pg) basins across North America. The Javelina Formation dinosaur fauna is limited to C29r and age equivalent to the dinosaur fauna of the Hell Creek Formation in the Northern Great Plains, which supports the concept of provinciality. Additionally, it implies the K-Pg extinction of non-avian dinosaurs was larger than previously suggested because all non-avian dinosaur taxa endemic to the Big Bend area also went extinct at the boundary. The mammalian fauna previously identified as Puercan by Standhardt (1986) is reidentified as Torrejonian taxa and allows for future diversity comparisons to other basins. This is one of only a few Torrejonian faunas in North America, which makes it important for understanding mammalian evolution following the K-Pg boundary on both local and regional scales. Lastly, our findings show the mid-Maastrichtian and late Maastrichtian greenhouse events documented by Nordt et al. (2003) represent rapid (<200 k.y.) changes in climate during the end-Cretaceous and correlate closely with the marine record. This work contributes to ongoing work developing a more complete late Cretaceous through Paleogene chronology for southern North America through a combination of detrital sanidine dates, magnetostratigraphy, and biostratigraphy, and suggests the application of the method to others areas in Big Bend would significantly improve the chronology of this important region.

Acknowledgments

This work was conducted in Big Bend National Park on research permit BIBE-2014-SCI-005 to CL. This work was supported by SEPM, National Science Foundation EAR-132552, 0207750 and 1325544, American Chemical Society Petroleum Research Fund (PRF#52822-DN18), and Baylor University Department of Geosciences' Dixon Fund. We thank two anonymous reviewers for their helpful comments and B. Pratt and B. Singer for the editorial assistance. Thanks to A. Ramsey for assistance with sample collection and section measuring, L. Peters for assistance with sanidine separation, J.

Schiebout and S. Ting of the LSU and M. Brown and C. Sagebiel of the TMM for providing access and loan of fossil specimens, and J. Feinberg for helpful discussions.

Appendix

Therian mammals from the lower Black Peaks Formation

Vertebrate fossils are found within the Javelina and Black Peaks formations in the Dawson Creek section (Fig. 1.8). Fossil mammals from two localities TMM locality 41400 (LSU VL-111), Tom's Top in Dawson Creek and TMM locality 42327 (LSU VL-108), Dogie, were originally described by Schiebout (1974). LSU VL-109 ("Hot White") (locality 8, Fig. 1.2) yielded turtle, lizard, and crocodilian fossils (Standhardt, 1986). Additional fossils were later collected by Standhardt (1986) using screenwashing methods and described in an unpublished dissertation. The fauna has appeared primarily in faunal lists (Schiebout et al., 1987; Standhardt, 1995) and briefly evaluated by Williamson (1996). The only mammal previously described in the published literature is a single specimen of a multituberculates mammal from Tom's Top, *Stygimys vastus*, was described by Lofgren et al. (2005). *Stygimys* is known from the Puercan through the Torrejonian of western North America and the species *S. vastus* is endemic to the Tom's Top locality and therefore does not aid in refining its biostratigraphic correlation. The therian mammals from these faunas are illustrated and briefly described here.

Standhardt (1986) reported the presence of *Eoconodon coryphaeus* from locality LSU VL-107 ("Glen Eleven"), a locality is from outside the study area from the near Glen Draw, 3.4 km southeast of Glenn Springs. Standhardt (1986) was not able to precisely place this locality into any regional stratigraphic section because it is within faulted sediments in a syncline. We included a reassessment of this specimen because it was identified as a mammal known elsewhere only from the Puercan.

Included in this Appendix is the systematic paleontology and a brief description of the reidentified material. A more complete description and discussion is available in the Appendix A beginning on page 127.

Systematic Paleontology

Infraclass METATHERIA Huxley, 1880

Family PERADECTIDAE Trouessart, 1879

Genus PERADECTES Matthew and Granger, 1921

Peradectes sp.

Figure 1.8A-D

Peratherium sp. Standhardt, 1986, p. 210, fig. 68.

Material.—LSU V-895, right partial M?; and LSU V-705, left m? from TMM locality 42327.

Description.—A small metatherian mammal is represented by a partial upper molar (LSU V-895; Fig. 1.8A) and a lower molar (LSU V-705; Figure 1.8B-D).

Order CIMOLESTA McKenna, 1975

Family CIMOLESTIDAE Marsh, 1889

Genus and Species indeterminate

Figure 1.8E-G

Gelastops sp. Standhardt, 1986, p. 213, fig. 69.

Material.—LSU V-708, left P3; and LSU V-841, partial right M2 from TMM locality 42327.

Description.—A small cimolestid is represented by a complete crown of a poorly preserved and abraded left P3 (LSU V-708; Figure 1.8E-F) and a partial M2 (LSU V-841; Fig. 1.8G) that includes the mesial and lingual portion of the tooth including part of the paracone and a complete parastylar lobe and the protocone and talon basin.

Legion CARNIVORAMORPHA Wyss and Flynn, 1993

Family VIVERRAVIDAE Wortman and Matthew, 1899

Genus BRYANICTIS MacIntyre, 1966

Bryanictis new species

Figure 1.8H-L

Protictis (Bryanictis) terlinguae Standhardt, 1986, p. 218, figs. 71, 72. [nomen nudum]

Material.—TMM 41400–10, left p4 from TMM locality 41400, and LSU V-709, incomplete P3 from TMM locality 42327.

Description.—A small viverravid carnivoramorph representing a new species of *Bryanictis* is represented by at least two isolated teeth, an incomplete P3 (LSU V-709; Figure 1.8H-I) and a p4 (TMM 41400–10; Figure 1.8J-L). Standhardt (1986) referred an additional specimen to this taxon consisting of an isolated p2 (LSU V-960). However, this specimen could not be located for this study.

Order DERMOPTERA Illiger, 1811

Family MIXODECTIDAE Cope, 1883

Genus MIXODECTES Cope, 1883

Mixodectes malaris Cope, 1883

Figure 1.8M

Indrodon malaris Cope, 1883, p. 60.

Mixodectes malaris Cope, 1883 [see Szalay, 1969 for synonymy]; Rigby, 1980, p. 63, Table 16; Taylor, 1984, p. 147, Table 10; Standhardt, 1986, p. 222, fig. 73; Williamson, 1996, p. 38.

Material.—LSU V-924, partial left M3; and LSU V-928, partial left M2 from TMM locality 41400.

Description.—The mixodectid *Mixodectes malaris* is represented by two fragmentary upper molars, a partial left M3 (LSU V-924; Fig. 1.8M) and a partial left M2 (LSU V-928). Unfortunately, the partial left M2 was not available for this study. The partial left M3 consists of the distal half of the crown.

Order PRIMATES Linnaeus, 1758

Family 'PALAECHTHONIDAE' Szalay, 1969

Genus PLESIOLESTES Jepsen, 1930

Plesiolestes nacimienti Wilson and Szalay, 1972

Figure 1.8N-R

Palaechthon nacimienti Wilson and Szalay, 1972, p. 5, figs. 2–9; Taylor, 1984, p. 164, Table 13; Standhardt, 1986, p. 225, fig. 74; Williamson and Lucas, 1993, p. 121, Williamson, 1996, p. 39.

Plesiolestes nacimienti (Wilson and Szalay, 1972). Gunnell, 1989, p. 24; Silcox and Williamson, 2012, p. 810, fig. 4.

Material.—LSU V-921, right P4; TMM 41400–17, left M2; and LSU V-923, right m3 from TMM locality 41400.

Description.—*Plesiolestes nacimienti* is represented by three isolated teeth including a right P4 (LSU V-921; Fig. 1.8N), left M2 (LSU V-923; Fig. 9O), and right partial m3 (LSU V-923; Figure 1.8P-R).

Order 'CONDYLARTHRA' Cope, 1881b

Family PERIPTYCHIDAE Cope, 1882b

Genus HAPLOCONUS Cope, 1882a

Haploconus sp.

Figure 1.9A-E

Haploconus inopinatus Standhardt, 1986, p. 248, fig. 82.

Material.—LSU V-710, partial right M1; LSU V-711, partial right M2; and LSU V-835, left m2 from TMM locality 42327.

Description.—The periptychids "condylarth" *Haploconus* is represented by three partial teeth. Two isolated teeth represent a partial M1 (LSU V-710; Fig. 1.9A) and a partial M2 (LSU V-711; Fig. 1.9B) that likely come from a single individual.

Genus PERIPTYCHUS Cope, 1881a

Periptychus carinidens Cope, 1881a

Figure 1.9F-H

Periptychus carinidens Cope, 1881a, p. 337 [see Taylor, 1984 for synonymy], Rigby, 1980, p. 111, pl. XIV, figs. 7–9, Table 42, Archibald, 1998, p. 312, fig. 20.3c; Williamson and Lucas, 1992, fig. 15i-k; Williamson and Lucas, 1993, p. 125; Williamson, 1996, p. 45.

Periptychus gilmorei Gazin, 1939, p. 272, fig. 3; Archibald, 1998, p. 313.

Carsioptychus coarctatus Standhardt, 1986, p. 243, fig. 81.

Material.—LSU V-888, right m3; LSU V-873, right dentary fragment with partial m?; and LSU V-1554, right partial M? from TMM locality 42327.

Description.— *Periptychus carinidens* is represented by a dentary fragment with a partial and highly abraded lower molar, an isolated partial right upper molar (LSU V-1554), and a nearly complete m3 (LSU V-888; Figure 1.9F-H).

Family MIOCLAENIDAE Osborn and Earle, 1895

Genus PROMIOCLAENUS Trouessart, 1904

Promioclaenus cf. *P. lemuroides* Matthew, 1897

Figure 1.9I-J

Promioclaenus sp. Standhardt, 1986, p. 256, fig. 84.

Ellipsodon priscus Standhardt, 1986, (in part), p. 251, fig. 83a.

Material.— LSU V-875, right P3; and LSU V-920, partial left M3 from TMM locality 41400.

Description.— *Promioclaenus* cf. *P. lemuroides* is represented by an isolated P3 (LSU V-875; Fig. 1.9I) and a partial M3 (LSU V-920; Fig. 1.9J).

Genus MIOCLAENUS Cope, 1881d

Mioclaenus new species.

Figure 1.9K-U

Nexus plexus Standhardt, 1986, p. 258, fig. 85. [nomen nudum]

Material.—LSU V-890, left M2; LSU V-891, left M1; LSU V-833, left P4; LSU V-703, right partial dentary with erupting m2; LSU V-839, V-840, partial right m2; and LSU V-881, left m3 from TMM locality 42327.

Description.—A small mioclaenid "condylarth" represents a new species of *Mioclaenus,* which represents the most complete taxon reported from TMM locality 42327. The new species is represented by an isolated, poorly preserved P4 (LSU V-833; Figure 1.9K-L), an isolated M1 (LSU V-891; Figure 1.9M-N), an isolated left M2 (LSU V-890; Figure 1.9O-P), an m2 (LSU V-703; Figure 1.9Q-R), a partial right m2 (LSU V-839, V840), and a left m3 (LSU V-881; Figure 1.9S-U).

Genus ELLIPSODON Scott, 1892

Ellipsodon cf. *E. inaequidens* Cope, 1884

Figure 1.9V-Z

Ellipsodon priscus Standhardt, 1986, p. 251, (in part), fig. 83B-H.

Material.—LSU V-706, left M1; and LSU V-701, right m1 from TMM locality 42327.

Description.—*Ellipsodon inaequidens* is represented by two teeth: a left M1 (LSU V-706; Figure 10V-W), and a right m1 (LSU V-701; Figure 1.9X-Z).

Family 'TRIISODONTIDAE' Scott, 1892

Genus GONIACODON Cope, 1888

cf. *Goniacodon levisanus* Cope, 1883

Figure 1.9AA-BB

Eoconodon sp. Standhardt, 1986, p. 238, fig. 84.

Material.—LSU V-704, left M3 from TMM locality 42327.

Description.— cf. *Goniacodon levisanus* is represented by an isolated left M3 (LSU V-704; Figure 1.9AA-BB).

Genus TRIISODON Cope, 1881c

Triisodon quivirensis Cope, 1881c

Fig. A1

Triisodon quivirensis Cope, 1881c, p. 485; Van Valen, 1978, p. 58; Williamson and Lucas, 1993, p. 123; Williamson, 1996, p. 41.

Triisodon antiquus Cope, 1882, p. 193 [see Taylor, 1984 for synonymy]; Tomida, 1981, p. 230, pl. 10.2, figs 1–2.

Eoconodon coryphaeus Standhardt, 1986, p. 232, fig. 77.

Material.—LSU V-1156, partial right M2; and LSU V-1157, partial left m1 or m2 from LSU locality VL-107.

Description.—The taxon *Triisodon quivirensis* is represented by fragments of two teeth (Fig. A1), portions of a dentary, and postcranial fragments. These were found in close association and likely represent a single individual. However, some of the individual fragments were given different specimen numbers.

CHAPTER THREE

High-resolution Magnetostratigraphy of the Upper Nacimiento Formation, San Juan Basin, New Mexico, USA: Implications for Basin Evolution and Mammalian Turnover

This chapter published as: Leslie, C.E., Peppe, D.J., Williamson, T.E., Bilardello, D., Heizler, M., Secord, R., and Leggett, T., *in press*, High-resolution magnetostratigraphy of the upper Nacimiento Formation, San Juan Basin, New Mexico, USA: implications for basin evolution and mammalian turnover: *American Journal of Science.*

Abstract

Lower Paleocene deposits in the San Juan Basin document one of the best records of mammalian change and turnover following the Cretaceous-Paleogene mass extinction and is the type area for the Puercan (Pu) and Torrejonian (To) North America Land Mammal age (NALMA) interval zones. One of the largest mammalian turnover events in the early Paleocene occurs between the Torrejonian 2 (To2) and Torrejonian 3 (To3) NALMA interval zones. The Nacimiento Formation contains the only deposits in North America where the To2-To3 mammalian turnover can be constrained, however, the precise age and duration of the turnover is poorly understood due to the lack of a precise chronostratigraphic framework. We analyzed paleomagnetic samples, produced a $^{40}Ar/^{39}Ar$ detrital sanidine age, and developed a detailed lithostratigraphy for four sections of the upper Nacimiento Formation in the San Juan Basin, New Mexico (Kutz Canyon, Escavada Wash, Torreon West and East) to constrain the age and duration of the deposits and the To2-To3 turnover. The polarity stratigraphy for the four sections can be correlated to chrons C27r-C26r of the geomagnetic polarity time scale (GPTS). Using the local polarity stratigraphy for each section, we calculated a mean sediment accumulation

rate and developed a precise age model, which allows us to determine the age of important late Torrejonian mammalian localities. Using the assigned ages, we estimate the To2-To3 turnover was relatively rapid and occurred over ~120 kyr (-60/+50 kyr) between 62.59 and 62.47 Ma. This rapid duration of the mammalian turnover suggests that it was driven by external forcing factors, such as environmental change driven by the progradation of the distributive fluvial system across the basin and/or changes in regional or global climate. Additionally, comparisons of the mean sediment accumulation rates among the sections that span from the basin margin to the basin center indicate that sediment accumulation rates equalized across the basin from the end of C27r through the start of C26r, suggesting an accommodation minimum in the basin associated with the progradation of a distributive fluvial system into the basin. This accommodation minimum also likely led to the long hiatus of deposition between the Paleocene Nacimiento Formation and the overlying Eocene San Jose Formation.

Introduction

The Nacimiento Formation outcrops in the San Juan Basin of northwestern New Mexico (Fig. 2.1) and is composed primarily of terrestrial fluvial rocks. The Nacimiento Formation contains one of the most continuous records of lower Paleocene terrestrial evolution in North America and documents the early Paleocene radiation of mammals when mammals rapidly diversified following the Cretaceous-Paleogene (K-Pg) mass extinction (Williamson, 1996). The San Juan Basin is the “type” area for the early Paleocene Puercan (Pu) and Torrejonian (To) North American Land Mammal age interval zones (NALMAs) which were first defined based on mammalian assemblages from the Nacimiento Formation (Wood et al., 1941). These mammal assemblages

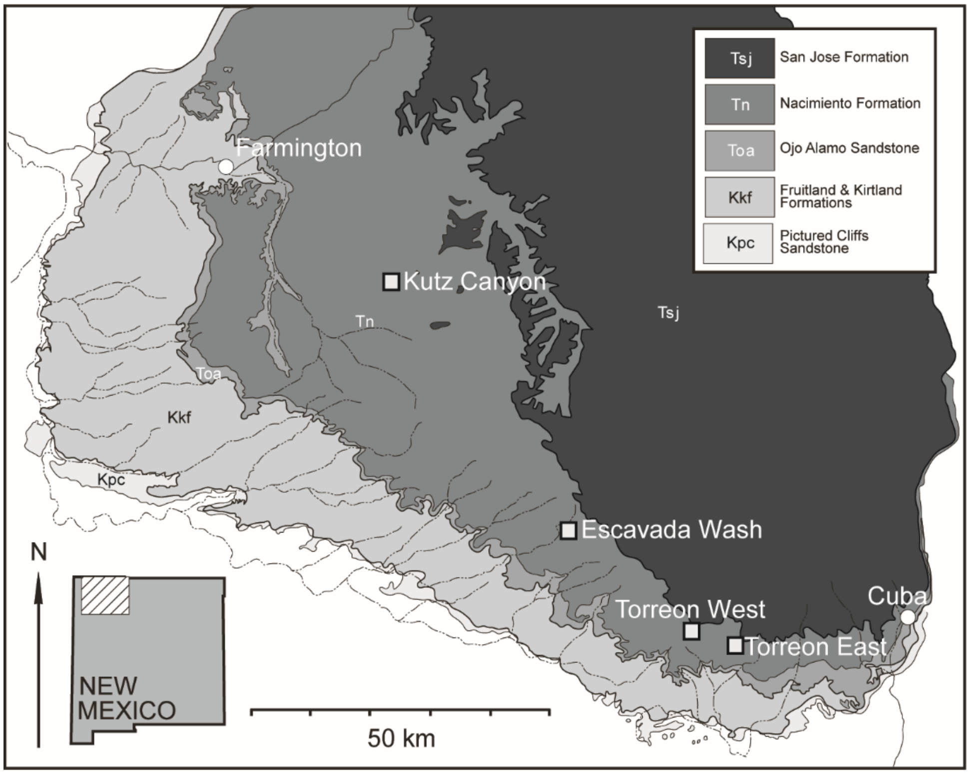

Figure. 2.1. Geologic map of the San Juan Basin, New Mexico showing the Cretaceous through Eocene sediments and the locations of the four sections collected in this study, Kutz Canyon, Escavada Wash, Torreon West, and Torreon East, indicated by white squares (modified from Williamson et al., 2008).

continue to be critical for the characterization and definition of early Paleocene NALMAs and their subdivisions (Archibald et al., 1987; Lofgren et al., 2004).

Matthew (1937) provided the first comprehensive review of the long history of fossil mammalian collections from the Nacimiento Formation. Williamson (1996) documented two significant intervals of mammalian turnover within the formation, between Puercan 2 (Pu2) and Puercan 3 (Pu3) and between Torrejonian 2 (To2) and Torrejonian 3 (To3) that exhibit high rates of turnover. However, the precise timing of these turnovers and their contemporaneous nature across the basin is uncertain. The Nacimiento Formation is the only continuous record of the To2-To3 turnover interval in

North America, therefore a more precise geochronologic framework is needed to better evaluate biotic change through this critical interval of time.

Magnetostratigraphy has been used to develop a chronostratigraphic framework for the Nacimiento Formation with the aim of providing a geochronologic framework for study of vertebrate evolution and evaluating the timing of mammalian faunal change for much of the early Paleocene (Butler et al., 1977; Taylor, ms, 1977; Taylor and Butler, 1980; Butler and Taylor, 1978; Lindsay et al., 1978, 1981; Butler and Lindsay, 1985). However, a high-resolution age model in conjunction with detailed stratigraphy is still lacking for portions of the formation, and particularly for the To2-To3 interval.

In this study, we focus on developing a high-resolution age model for mammalian turnover between the To2 and To3 interval zones across the San Juan Basin. We develop a detailed lithostratigraphy in conjunction with the Torrejonian mammal localities and determine the magnetostratigraphy of four sections across the basin that span the To2-To3 boundary. These sections are: Kutz Canyon, Escavada Wash, Torreon West, and Torreon East (Fig. 2.1). We then correlate the polarity stratigraphy of each section to the global geomagnetic polarity time scale (GPTS) (Ogg, 2012) with the help of a $^{40}Ar/^{39}Ar$ detrital sanidine age to constrain the timing and duration of sediment deposition in each section. Using calculated sediment accumulation rates, we assign an age to each fossil locality within the sections to correlate the Torrejonian mammal localities across the basin and constrain the age of the To2-To3 mammalian turnover. Finally, we use comparisons of sediment accumulation rates among the four sections to assess the evolution of deposition in the upper Nacimiento Formation.

Previous Work

Lithostratigraphy

The San Juan Basin of northwestern New Mexico is a Laramide foreland basin containing Upper Cretaceous through lower Eocene deposits (Fig. 3.1) (Chapin and Cather, 1983). Cather (2004) documents three phases of subsidence in the San Juan basin: an early phase during the late Campanian-early Maastrichtian, a medial phase during the latest Maastrichtian-early Paleocene, and a last phase during the Eocene. The medial phase (~74-67 Ma) was responsible for the deposition of the Nacimiento Formation composed of alluvial deposits that are subdivided into three members: the Arroyo Chijuillita, the Ojo Encino, and the Escavada members (Williamson and Lucas, 1992; Williamson, 1996). The Ojo Alamo Sandstone underlies the Nacimiento Formation, representing earliest Paleocene deposition in the basin, and the lower Eocene San Jose Formation unconformably overlies the Nacimiento Formation. This study focuses on the Ojo Encino Member of the Nacimiento Formation which contains variegated red and drab paleosols, sheet and channel sandstone units, and three persistent "black" paleosols that we refer to as the "lower black", "middle black", and "upper black". These black beds are useful marker beds as they can be traced across the basin. The abundant red beds in the Ojo Encino Member distinguish it from the drab colored mudstone and sandstone beds of the underlying Arroyo Chijuillita Member and the high proportion of sandstones and silcretes of the overlying Escavada Member (Williamson and Lucas, 1992; Williamson, 1996; Davis et al., 2016).

The four sections investigated in this study are spread along a northwest-southeast transect through the basin and span from basin center to basin margin (Fig. 2.1). Kutz

Canyon, the northernmost section, is near the center of the basin, Escavada Wash is near the basin margin approximately 48 km southeast of Kutz Canyon, and Torreon West and East, the southernmost sections, are approximately 32 km southeast of Escavada Wash near the basin margin. Torreon West and East are separated by about 10 km. Taylor (ms, 1977) produced the first stratigraphic sections, collected paleomagnetic samples, and documented the stratigraphic position of fossil mammal localities for Torreon West, Torreon East, and the Big Pocket fossil locality in Kutz Canyon. In the measured sections, lithologies were generalized and lumped into siltstone, sandstone, volcanic ash, and coal intervals. Taylor (ms, 1977) also identified lower, middle, and upper "carbonaceous" clay beds that outcrop as distinct black intervals, referred to the lower, middle, and upper blacks in this paper. Williamson (1996) subsequently produced more detailed measured sections for Torreon West, Torreon East, Kutz Canyon, and Escavada Wash by documenting pedogenic features and reporting Munsell colors for mudstones. However, his sections are not tied directly to magnetostratigraphic sections, and thus are not well constrained geochronologically.

Paleomagnetism and Rock Magnetism

Taylor and Butler (1980) constructed the magnetic polarity stratigraphy of a 185 m section at Torreon West, a 62 m section at Torreon East, and a 420 m section at Kutz Canyon. The *Deltatherium* mammalian zone (equivalent to Torrejonian 2, *sensu* Lofgren et al., 2004) was recognized at all three sections and the "*Pantolambda* mammalian zone" (*sensu* Osborn, 1929, see below; equivalent to Torrejonian 3, *sensu* Lofgren et al., 2004) at Torreon West and Kutz Canyon. The two zones were estimated to be separated by about 500 kyr. The section at Kutz Canyon, measured at the Big Pocket fossil locality, includes approximately 100 m of strata below the *Deltatherium* zone. The paleomagnetic sample spacing for all sections was approximately 3 meters. The Torreon West, Torreon East, and upper portion of the Kutz Canyon sections were correlated to C26r to C25r based on previous work correlating the Upper Cretaceous through middle Paleocene San Juan Basin deposits to the geomagnetic polarity time scale (GPTS) (Lindsay et al., 1978; Taylor, ms, 1977). Following the work of Taylor and Butler (1980), Butler and Lindsay (1985) recognized magnetic overprinting in the lower part of the section and revised correlation of the polarity zones to C27r to C26r rather than C26r to C25r. Despite the numerous mammalian localities identified at Escavada Wash, a polarity stratigraphy has not been constructed until now.

Taylor and Butler (1980) identified the persistent black mudstones at Torreon West and East which function as excellent marker beds to reference the stratigraphic position of reversals in each section. The C27r-C27n reversal was reported near the base of the middle black at Torreon West and near the top of the middle black at Torreon East and the C26r-C27n reversal was reported at the base of the upper black at Torreon West and 9 m below the base at Torreon East. These findings suggest that the blacks are diachronous despite the proximity of the two sections.

A rock magnetic study of the San Juan Basin deposits was also conducted by Butler and Lindsay (1985) who analyzed magnetic separates from nine stratigraphic levels through Upper Cretaceous to middle Paleocene deposits; however, the exact sample locations are unclear and therefore it is unknown whether any sample overlap exists with the new sections presented here. Butler and Lindsay (1985) determined that titanohematite of intermediate composition was the dominant magnetic mineral based on microprobe and X-ray analyses, supported by Curie temperatures ranging from 180-300°C. These findings indicate the sediments were likely sourced from volcanic rocks of the San Juan Mountain region to the north, based on the presence of titanohematite. Kodama (1997) measured the anisotropy of remanence on samples of the Nacimiento Formation collected from Kutz Canyon to conduct an inclination shallowing correction and found support for a primary detrital magnetization for the formation.

Mammalian Biostratigraphy

Mammalian interval zones in the San Juan Basin have a long and complicated history. Sinclair and Granger (1914) established the presence of two zones of distinct mammalian assemblages at Torreon Wash, the *Deltatherium* and *Pantolambda* zones, which are separated by approximately 30 m of non-fossiliferous deposits. Osborn (1929) treated the two zones as separate life zones representing different ages and formally named and characterized the *Deltatherium* zone by the presence of *Deltatherium fundaminis*, *Mioclaenus turgidus*, and *Haploconus angustus* and the *Pantolambda* zone by the presence *of Pantolambda cavirictum* and *Arctocyon ferox*. However, others considered these two zones to be a facies effect, sampling bias, or inaccurate due to the presence of the same species in both zones (Granger, 1917; Matthew, 1937; Wilson, 1956; Russell, 1967). Using magnetostratigraphy, Taylor and Butler (1980) demonstrated that the *Deltatherium* and *Pantolambda* zones represent different ages at Torreon Wash. Taylor (1984) renamed the *Deltatherium* and *Pantolambda* zones *Deltatherium – Tetraclaenodon* (D-T) and *Pantolambda bathmodon – Mixodectes pungens* (P-M) after the discovery of *Pantolambda cavirictum* in other localities in the basin within the upper portion of the "*Deltatherium* zone".

Archibald et al. (1987) updated the Paleocene NALMAs and divided the Torrejonian into three zones, To1-To3, using the San Juan Basin mammalian assemblages to establish the To2 and To3 mammal ages. The *Deltatherium* and *Pantolambda* zones established by Sinclair and Granger (1914) are equivalent to To2 and To3, respectively, of Archibald et al. (1987). Archibald et al. (1987) defined To2 as the *Tetraclaenodon-Pantolambda* zone and To3 as the *Pantolambda-Plesiadapis praecursor* zone, placing the boundary between the two zones within the upper part of the *Deltatherium* zone of Sinclair and Granger (1914). Williamson (1996) further subdivided the To2 and To3 interval into five biostratigraphic zones within the San Juan Basin: P-E zone (lowest occurrence of *Protoselene opisthacus* and lowest occurrence of *Ellipsodon granger*), E-A zone (lowest occurrence of *Ellipsodon granger* and first occurrence of *Arctocyon ferox*), A-P zone (lowest occurrence of *Arctocyon ferox* and lowest occurrence of *Pantolambda cavirictum*), P-M zone (lowest occurrence of *Pantolambda cavirictum* and first occurrence of *Mixodectes pungens*), and M zone (first and last occurrence of *Mixodectes pungens*). Williamson (1996) defined the A-P zone exclusively from Kutz Canyon and the P-M zone from Torreon West, Kutz Canyon, and two other locations in the basin, Kimbeto and Betonnie-Tsosie washes. The M zone was defined from Torreon East and West and Escavada Wash.

In their revision of Paleocene NALMAs, Lofgren et al. (2004) redefined the To2 interval zone as the *Protoselene opisthacus-Mixodectes pungens* interval zone, based primarily on the faunal succession observed at Kutz Canyon and the To3 interval zone as the *Mixodectes pungens-Plesiadapis praecursor* interval zone based primarily on the faunal record at Torreon Wash. With these revisions, To2 is approximately equivalent to the duration of the local San Juan Basin biozones P-E through P-M (Williamson, 1996), and approximately equivalent to the *Deltatherium* zone (Sinclair and Granger, 1914). To3 is nearly equivalent to the duration of the M biozone (Williamson, 1996) and the *Pantolambda* zone (*sensu* Sinclair and Granger, 1914).

Using the Torrejonian zonation of Lofgren et al. (2004), there are significant changes in therian mammals across the To2-To3 boundary in the San Juan Basin. The changes observed between the last two San Juan Basin biozones in To2, the A-P and P-M zones, and To3, the M zone are locally considerable (Williamson, 1996). Intense collecting efforts over the last twenty years have resulted in modifications of the San Juan Basin biozones of Williamson (1996), including the movement of several localities from the P-M zone to the older A-P zone (Table 2.1). Despite this extensive collecting, collection biases remain among the fossil zones. For example, the A-P and P-M zones contain few microvertebrate sites, but several are present in the M zone. Additionally, the A-P and P-M zones are generally less fossiliferous and have significantly fewer fossil sites than the M zone.

Despite potential issues with collection biases, there are notable differences between the P-M and M zones in species occurrences and abundance. Several taxa found in the P-M zone, but not the M zone represent medium- to large-bodied taxa that are abundant in P-M zone faunas, making their disappearance across the To2-To3 boundary particularly significant. These are the ‘triisodontid’ ‘condylarth’ *Triisodon quivirensis*, the periptychid ‘condylarth’ *Haploconus angustus*, and the enigmatic ‘condylarth’? *Deltatherium fundaminis*. The taeniodont *Huerfanodon torrejonius* and the mioclaenid ‘condylarth’ *Ellipsodon yotankae* are uncommon in the P-M zone and do not appear in

Table 2.1. Selected mammal localities and calculated ages.

Mammal Localities	NALMA biozone (Lofgren et al., 2004)	San Juan Basin biozone (Williamson, 1996)	Stratigraphic position (m)	Calculated age (Ma)
Kutz Canyon				
Sedimentation rate: 119.9 (-16.3, +18.7) m/myr				
1: L-00400	To2	A-P zone	1-6	62.76-62.71 (-0.04, +0.05)
2: L-06419	To2	A-P zone	1-6	62.76-62.71 (-0.04, +0.05)
3: L-09907, L-09908, L-09909	To2	A-P zone	10	62.68 (-0.00, +0.00)
4: L-08234	To2	P-M zone	16	62.63 (-0.00, +0.01)
Escavada Wash				
Sedimentation rate: 115.7 (-30.3, +34.7) m/myr				
5: L-10453	To2	P-M zone	6.5	62.80 (-0.09, +0.11)
6: L-09187	To2	P-M zone	15.25	62.72 (-0.08, +0.08)
7: L-09985	To2	P-M zone	15.25	62.72 (-0.08, +0.08)
8: L-10554	To2	P-M zone	15.25	62.72 (-0.08, +0.08)
9: L-10350	To2	P-M zone	16.5	62.71 (-0.07, +0.08)
10: L-09981	To3	M zone	59	62.35 (-0.10, +0.05)
11: L-10444	To3	M zone	59	62.35 (-0.10, +0.05)
12: L-10556	To3	M zone	61	62.33 (-0.10, +0.06)
13: L-09982	To3	M zone	62	62.32 (-0.10, +0.06)
14: L-10415	To3	M zone	63	62.31 (-0.11, +0.06)
15: L-10660	To3	M zone	63.25	62.31 (-0.11, +0.06)
16: L-10414	To3	M zone	64.5	62.30 (-0.11, +0.06)
17: L-10403	To3	M zone	65	62.29 (-0.11, +0.06)
18: L-09197	To3	M zone	65.15	62.29 (-0.11, +0.06)
Torreon West				
Sedimentation rate: 119.9 (-10.1, +11.6) m/myr				
19: L-08182	To2	A-P zone	19.75	62.66 (-0.03, +0.04)
20: L-08178	To2	A-P zone	23.25	62.63 (-0.03, +0.03)
21: L-08180	To2	P-M zone	27.5	62.59 (-0.02, +0.03)
22: L-09173	To3	M zone	43	62.46 (-0.02, +0.03)
23: L-08183	To3	M zone	45	62.45 (-0.02, +0.03)
24: L-10500	To3	M zone	48	62.42 (-0.03, +0.03)
25: L-06898	To3	M zone	50.5	62.40 (-0.03, +0.03)
26: L-10490	To3	M zone	55.5	62.36 (-0.03, +0.04)
27: L-07108	To3	M zone	57	62.35 (-0.03, +0.04)
28: L-07582	To3	M zone	57	62.35 (-0.03, +0.04)
29: L-10493	To3	M zone	57.75	62.34 (-0.03, +0.04)
30: L-10494	To3	M zone	57.75	62.34 (-0.03, +0.04)
31: L-10495	To3	M zone	57.75	62.34 (-0.03, +0.04)
32: L-01121	To3	M zone	58.5	62.33 (-0.03, +0.04)
33: L-10534	To3	M zone	59.25	62.33 (-0.04, +0.04)
34: L-10558	To3	M zone	59.25	62.33 (-0.04, +0.04)
35: L-10561	To3	M zone	59.25	62.33 (-0.04, +0.04)

Table 2.1. Selected mammal localities and calculated ages.

Mammal Localities	NALMA biozone (Lofgren et al., 2004)	San Juan Basin biozone (Williamson, 1996)	Stratigraphic position (m)	Calculated age (Ma)
36: L-07848	To3	M zone	59.75	62.32 (-0.04, +0.04)
37: L-08205	To3	M zone	59.75	62.32 (-0.04, +0.04)
38: L-10506	To3	M zone	61.5	62.31 (-0.04, +0.04)
39: L-10535	To3	M zone	61.5	62.31 (-0.04, +0.04)
40: L-10512	To3	M zone	63.5	62.29 (-0.04, +0.04)
41: L-10560	To3	M zone	63.5	62.29 (-0.04, +0.04)
42: L-10505	To3	M zone	66	62.27 (-0.04, +0.04)
Torreon East				
Sedimentation rate: 87.0 (-8.0, +9.0) m/myr				
43: L-07725	To2	A-P zone	18.5	62.66 (-0.03, +0.04)
44: L-08227	To2	A-P zone	18.5	62.66 (-0.03, +0.04)
45: L-08228	To2	A-P zone	18.5	62.66 (-0.03, +0.04)
46: L-07583	To2	A-P zone	21.25	62.63 (-0.02, +0.04)
47: L-04954	To2	A-P zone	21.25	62.63 (-0.02, +0.04)
48: L-04950	To2	A-P zone	21.25	62.63 (-0.02, +0.04)
49: L-10013	To3	M zone	35	62.47 (-0.02, +0.03)
50: L-10432	To3	M zone	35	62.47 (-0.02, +0.03)
51: L-09166	To3	M zone	39	62.43 (-0.02, +0.03)
52: L-09167	To3	M zone	39	62.43 (-0.02, +0.03)
53: L-01079	To3	M zone	52	62.28 (-0.04, +0.05)
54: L-09169	To3	M zone	52	62.28 (-0.04, +0.05)
55: L-10454	To3	M zone	52	62.28 (-0.04, +0.05)
56: L-09172	To3	M zone	52	62.28 (-0.04, +0.05)

the M zone. Considering the difference in collection size and localities between the P-M and M zones, the disappearance of these taxa appears to be significant. Several taxa reported from the M zone, but not from the P-M zone (*Picrodus calgariensis,* the palaeanodont? *Escavadodon zygus,* the hyopsodontid 'condylarth' *Haplaletes* sp., and the arctocyonid 'condylarth' *Colpoclaneus procyonoides* are rare in the M zone, and thus their absence from the P-M zone could be due to sampling biases between the zones.

In addition to differences in taxonomic occurrences, there are notable differences in the morphology of the mammalian taxa between the P-M and M zones. Several of the changes in mammal taxa between the two zones may reflect anagenic changes within a lineage as they represent two species, usually included within a single genus, distinguished primarily by a significant difference in size, for example: *Swaindelphys johansoni* and *S. encinensis*, *Mixodectes malaris* and *M. pungens* (contra Tsentas, 1981 and Szalay and Lucas, 1996, *M. malaris* is not present in the M. zone), *Anasazia williamsoni* and *Torrejonia wilsoni*, and *Pentacodon inversus* and *P. occultus*. Interestingly, for all these "species pairs", the M zone taxon is larger than the P-M zone taxon.

Although the mammalian turnover between To2 and To3 is well defined, the fossils come from different locations and the exact timing of the To2-To3 turnover is uncertain. This demonstrates the need for a robust age model for the To2-To3 intervals in the Nacimiento Formation to allow for correlations of the San Juan Basin mammalian assemblages to other contemporaneous assemblages across North America and to other continents, and to precisely constrain the age of the To2-To3 turnover. For the purposes of this paper, we use the definition of Lofgren et al. (2004) for the To2 and To3 interval zones.

Methodology

Measured Sections

A total of four sections were measured: a 70 m section at Kutz Canyon, a 87 m section at Escavada Wash, a 79 m section at Torreon West, and a 76 m section at Torreon East (Figs. 2.2, 2.3). At Torreon West and Torreon East, the base of the lithostratigraphic and magnetostratigraphic sections was the lower black marker bed. The Escavada Wash section contains multiple middle black marker beds so the section began at the lowest black marker bed present at that locality. Kutz Canyon does not contain the lower or middle black marker beds, so this section was measured from a known late To2 mammal locality (Bab's Basin) to ensure overlap with the other sections.

At each section, the outcrop was trenched to remove weathered material and document the lithologic contacts. The paleosols were described at the centimeter scale. The texture, color, ped structure, and shrink-swell features of each paleosol were documented using the guidelines of Soil Survey Staff (1999). For sandstones, the grain size and relationship to underlying strata was characterized.

The stratigraphic positions of mammal localities that occur within each measured section were documented in the field (Figs. 2.2, 2.3). Some mammal localities occur lateral to the measured sections and these localities were placed into each section using measurements from marker beds. Here we recognize A-P zone localities at Torreon West and Torreon East for the first time. Table 3.1 shows each selected mammal locality (localities that contain multiple taxa and can be precisely placed into the section), the numeric code it has been given for this paper, the associated NALMA interval zone, San Juan Basin biozone, and stratigraphic position.

Paleomagnetism

Four paleomagnetic block samples were collected from paleosols, mudstone, and fine grained sandstone beds at ~1 m intervals (0.25 m minimum and 7 m maximum sample spacing) in each section, defining a study site. Lithologies coarser than fine grained sandstones were avoided. Site spacing was primarily dictated by stratigraphic exposure and lithology. When sampling, a flat face was shaved onto the samples *in situ* using a hand rasp and its orientation was measured using a Brunton Pocket Transit

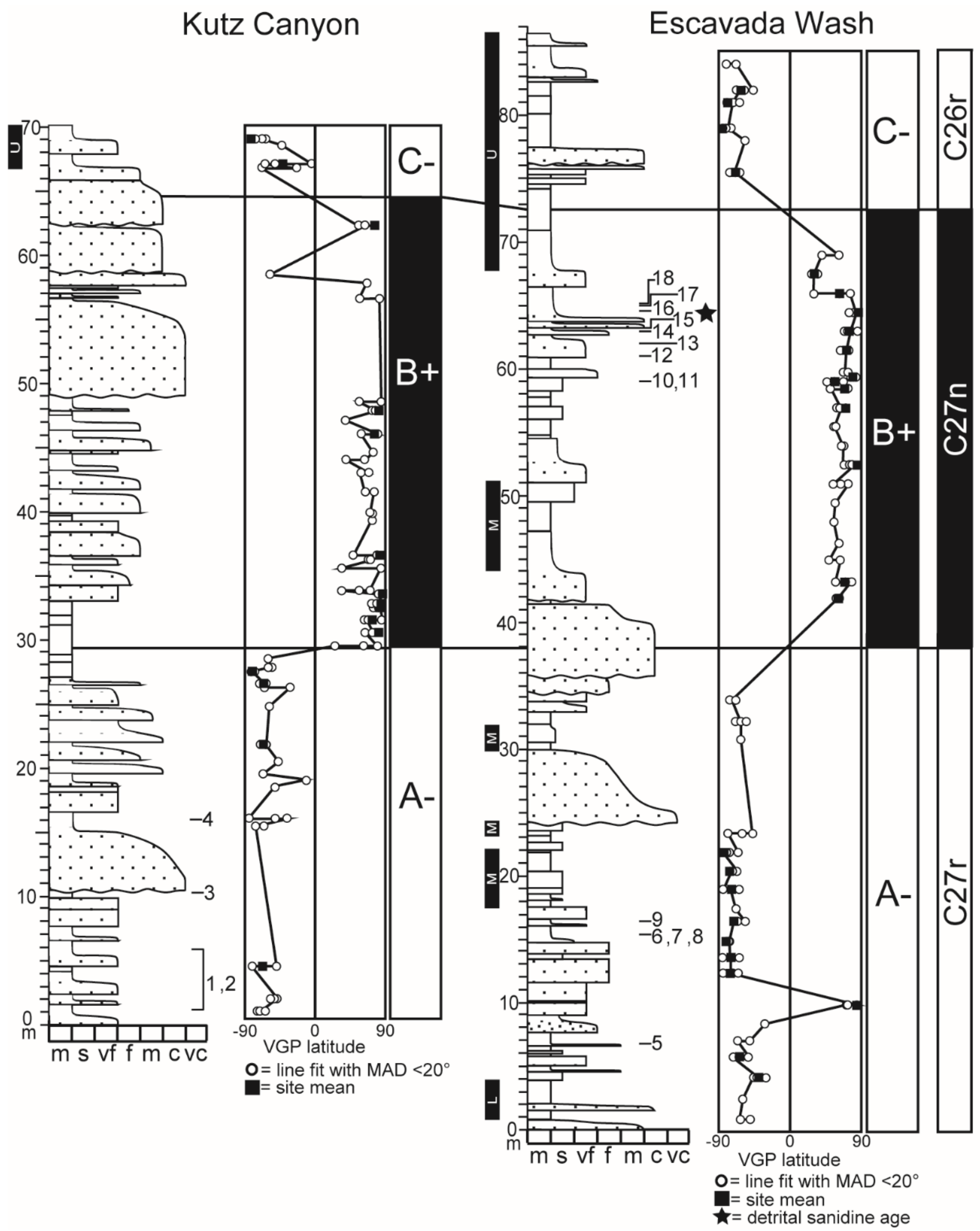

Figure. 2.2. Measured sections with fossil localities, VGP latitude, and interpreted polarity zonations for the Kutz Canyon and Escavada Wash sections. Note the presence of the black beds highlighted and labeled L (lower), M (middle) and U (upper). The base of the B+ magnetozone is used as the datum. Fossil localities 1-4 from Kutz Canyon and 5-18 from Escavada Wash are described in Table 2.1.

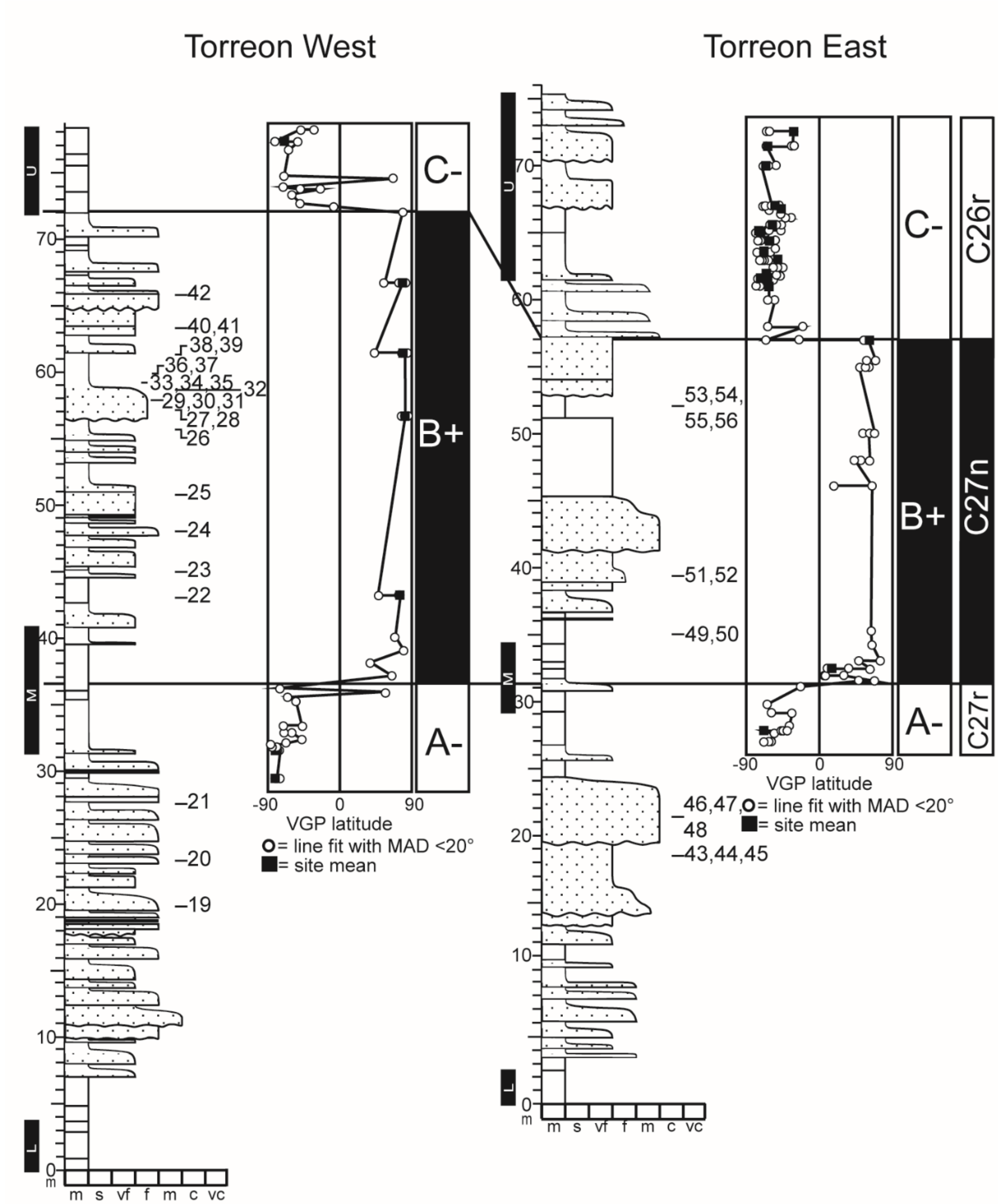

Figure 2.3. Measured sections with fossil localities, VGP latitude, and interpreted polarity zonations for the Torreon West and Torreon East sections. Note the presence of the black beds highlighted and labeled L (lower), M (middle) and U (upper). The base of the B+ magnetozone is used as the datum. Fossil localities 19-42 from Torreon West and 43-56 from Torreon East are described in Table 2.1.

Compass. In the laboratory, the samples were cut into approximately 4 cm^3 cubes using a diamond-bit saw. Each sample yielded one cubic specimen.

At Kutz Canyon and Escavada Wash, the entire sections spanning from late To2 through To3 strata were sampled. A total of 48 sites were sampled at Kutz Canyon and 50 sites at Escavada Wash. At Torreon West and East, the position of reversals had been reported by Taylor and Butler (1980) for the entire late To2-To3 succession. Consequently, full sections were not sampled but rather the deposits surrounding the approximate reversal positions were densely sampled to better constrain each reversal. A total of 38 sites were sampled at Torreon West and 44 sites at Torreon East.

Specimens were measured at Baylor University using a 2G Enterprises (Mt. View, Ca) cryogenic DC-SQuID magnetometer located in a 2-layer magnetostatic shielded room with a background field typically less than 300 nT. All specimens were demagnetized using a thermal demagnetization strategy. Rock magnetic analyses determined the magnetic carriers in the samples had relatively low unblocking temperatures (see below), therefore thermal demagnetization steps were performed in 25° increments up to the maximum unblocking temperature or until the magnetizations became erratic and unstable, ranging between 225°-400°C. To minimize oxidation reactions, thermal demagnetization was performed using a nitrogen atmosphere using ASC (Carlsbad, Ca) controlled atmosphere thermal demagnetizer.

Principal-component analysis (PCA) was used to isolate the characteristic remanence for each demagnetized specimen (Kirschvink, 1980). A best-fit line was calculated from at least three demagnetization steps that trended toward the origin and had a maximum angle of deviation (MAD) <20°. Data from specimens that had erratic demagnetization behaviors were excluded from further analysis. A site mean direction was calculated for all sites with three specimens with statistically significant directions using Fisher statistics (Fisher, 1953). If site means had a 95% confidence circle (α_{95}) >35°, which exceeds cut-off values based on the randomness criteria of Watson (1956), they were not used. Reversal boundaries were placed at the stratigraphic midpoints between samples of opposing polarity. The local polarity stratigraphy was then correlated to the geomagnetic polarity time scale (GPTS) (Ogg, 2012). The polarity stratigraphy of the Torreon West and East deposits coarsely resolved by Taylor and Butler (1980) determined the base and top of each section was reversed, therefore the deposits below and above the sampling intervals in this study were interpreted to be reversed.

Rock Magnetism

Rock magnetic analyses were performed at the Institute for Rock Magnetism at the University of Minnesota. To characterize the full suite of magnetic mineralogies present within the study interval, representative samples were chosen that captured the range of lithologies present. The lithologies were categorized into the following categories: black slickensided paleosols, red calcareous paleosols, brown to gray slickensided paleosols, drab-colored slickensided paleosols, and silty weakly-developed paleosols. Saturation magnetization was measured on a MicroMag Princeton Measurements Corporation (Princeton, NJ) vibrating sample magnetometer (VSM) on 11 specimens at temperatures ranging from 30°C to 600°C.

A Quantum Design (San Diego, Ca) Magnetic Properties Measurement System (MPMS) was used for low-temperature remanence measurements on 18 specimens. The protocol included field-cooled (FC) remanence, zero-field-cooled (ZFC) low-temperature saturation isothermal remanent magnetization (LTSIRM), and room temperature saturation isothermal remanent magnetization (RTSIRM). The method involves applying a sustained DC field of 2.5 T as a specimen is cooled from 300 K to 20 K (FC) and its magnetic remanence is measured upon warming back to room temperature (300 K). Subsequently the specimen is cooled to 20 K with no applied field (ZFC) and a 2.5 T LTSIRM is applied. The magnetic remanence is measured while the specimen warms back to 300 K. A 2.5 T room temperature SIRM (RTSIRM) is then applied at 300K and the magnetic remanence is measured upon cooling to 20 K and warming back to room temperature.

An additional goethite test was performed on four specimens to determine whether goethite was present. The method, similar to that of Guyodo et al. (2006), involves heating a sample up to 400 K and then applying a thermal remnant magnetization (TRM) as the sample cools from 400 to 300 K, magnetizing any goethite through its Néel temperature. The applied field is then turned off and the remanence is measured as the specimen is cooled to 20 K and warmed back up to 300 K, allowing the specimens to cycle through the magnetite structural phase transition temperature of ~120 K (the Verwey transition, e.g. Dunlop and Ozdemir, 1997) resulting in loss of remanence if any magnetite is present. The specimen is then heated to 400 K again in zero field, demagnetizing goethite through its Néel ordering temperature. Remanence is measured while the sample cools to 20 K and warms to 300 K to determine which, if any, magnetic phases remain after the contribution of goethite is removed.

A triaxial-IRM Lowrie test was performed at Baylor University on 11 samples to determine the primary magnetic carrier on mixed mineralogy samples (Lowrie, 1990). 11

cubic specimens were imparted with a 1T, 300 mT, and 100 mT field along the X, Y, and Z axes respectively with an ASC pulse magnetizer. Samples were thermally demagnetized in 50°C increments from 100-650°C in an ASC controlled atmosphere thermal demagnetizer. Samples were measured using the 2G cryogenic DC-SQuID magnetometer.

Detrital Sanidine Dating

One sample, H16-SJ-11, was collected from a sandstone body at 64 m in Escavada Wash (Fig. 2.2). Processing and mineral separation was done at the New Mexico Geochronology Research Laboratory (NMGRL). Sample separation included: crushing & grinding the rock sample, cleaning with H_2O and 5% HF acid, and sieving grain size between 40 and 80 mesh. Magnetic and heavy liquid density separation was used to concentrate the K-feldspar grains. Sanidine was hand-picked from the bulk K-feldspar separate based on optical properties indicative of sanidine as viewed while immersed in wintergreen oil under a polarizing binocular microscope. Approximately 100 grains were selected and then washed in acetone to remove the wintergreen oil.

The crystals were irradiated at the TRIGA reactor in Denver, Colorado for 8 hours in the NM-291 package along with Fish Canyon Sanidine interlaboratory standard FC-2 with an assigned age of 28.201 Ma (Kuiper et al., 2008). Ages are calculated with a total ^{40}K decay constant of 5.463e-10 /a (Min et al., 2000).

After irradiation, six crystals of FC-2 from each of 8 monitor holes from a 24-hole irradiation tray, along with 89 sample crystals were loaded into a copper tray, evacuated and baked at 140°C for 2 hours. Sample crystals were fused with a CO_2 laser and the extracted gas was cleaned with a NP 10 getter operated at 1.6 A for 30 seconds. The gas was analyzed for argon isotopes using an ARGUS VI multicollector mass spectrometer equipped with five Faraday cups, and one ion counting multiplier (CDD). The configuration had ^{40}Ar, ^{39}Ar, ^{38}Ar, ^{37}Ar and ^{36}Ar on the H1, AX, L1, L2, and CDD detectors, respectively. H1, AX and L2 utilized Faraday detectors equipped with $1x10^{13}$ Ohm resistors whereas L1 had a Faraday with a $1x10^{14}$ Ohm resistor. The CDD is an ion counting detector with a dead time of 14 nS. All data acquisition was accomplished with NM Tech Pychron software and data reduction used Mass Spec (v. 7.875) written by Al Deino at the Berkeley Geochronology Laboratory. Extraction line blank plus mass spectrometer background values are averages of numerous measurements interspersed with the unknown measurements. These values are 3±12%, 0.16±12%, 0.05±11%, 0.3±4%, 0.03±2.5%, x 10^{-17} moles from masses 40, 39, 38, 37, and 36, respectively.

The minimum age population is defined by choosing the youngest dates that form a near Gaussian distribution as defined by the MSWD value of the distribution. The minimum age is the inverse variance weighted mean of the selected crystals and the error is the square root of the sum of $1/\sigma^2$ values. The error is also multiplied by the square root of the MSWD for MSWD greater than 1. J-error (0.03%) is included for the weighted mean age error and all errors are reported at 1σ.

Results

Magnetostratigraphy

One hundred and forty-four samples were analyzed from 48 sampling horizons from Kutz Canyon, 150 samples from 50 sampling horizons from Escavada Wash, 114 samples from 38 sampling horizons from Torreon West, and 132 samples from 44 sampling horizons from Torreon East. The demagnetization trajectory of most specimens trended towards the origin after a few steps and were fully demagnetized by 200° to 400°C (Figs. 2.4A, 2.4B, 2.4C). All specimens with coherent demagnetization trajectories and stable endpoints were characterized by line fits. In total, reliable paleomagnetic directions were obtained for 353 specimens from 160 sampling horizons (Fig. 2.5A): 96 specimens (27% of total specimens) from 46 sampling horizons from Kutz Canyon, 114 specimens (32% of total specimens) from 47 sampling horizons from Escavada Wash, 53 specimens (15% of total specimens) from 31 sampling horizons from Torreon West, and 90 specimens (25% of total specimens) from 36 sampling horizons from Torreon East.

Of these sampling horizons, sixty-six (41% of total sampling horizons) had at least three samples with statistically significant directions that could be used to calculate site-mean directions with α_{95}s <35°: 15 from Kutz Canyon, 26 from Escavada Wash, 8 from Torreon West, and 17 from Torreon East (Fig. 2.5B). The remaining 187 samples (35% of the data) had erratic demagnetization trajectories and coherent directions could not be obtained (Fig. 2.4D).

The site-mean directions were averaged by section according to their polarity (Fig. 2.5C), and also averaged at the formation-level, yielding normal (chron 27n) and reversed (chrons 26r and 27r) Upper Nacimiento Formation-mean directions (Fig. 2.5D), and were used to calculate mean VGP latitude and longitude (Table 2.2). The average Upper Nacimiento Formation direction for all the normal site-mean directions is oriented 352.8°, 56.1° (α_{95}= 4.9°, n= 28), whereas that of all the reversed polarity site-mean directions is oriented 164.4°, -55° (α_{95}= 5°, n= 38). The reversal test of McFadden and McElhinny (1990) returned a positive, class A test, indicating that these directions share a common mean at the 95% confidence level. These directions plot close to the expected

Paleocene (62.5 Ma) direction of 341.8°, 60.1° recalculated from Torsvik et al. (2008) and our mean sampling location. In addition, these directions also agree with the mean characteristic remanent direction of 342.1°, 49.6° (α_{95}=7.1°, n= 20) for the Nacimiento Formation reported by Kodama (1997) after reversing all site-mean directions to normal polarity.

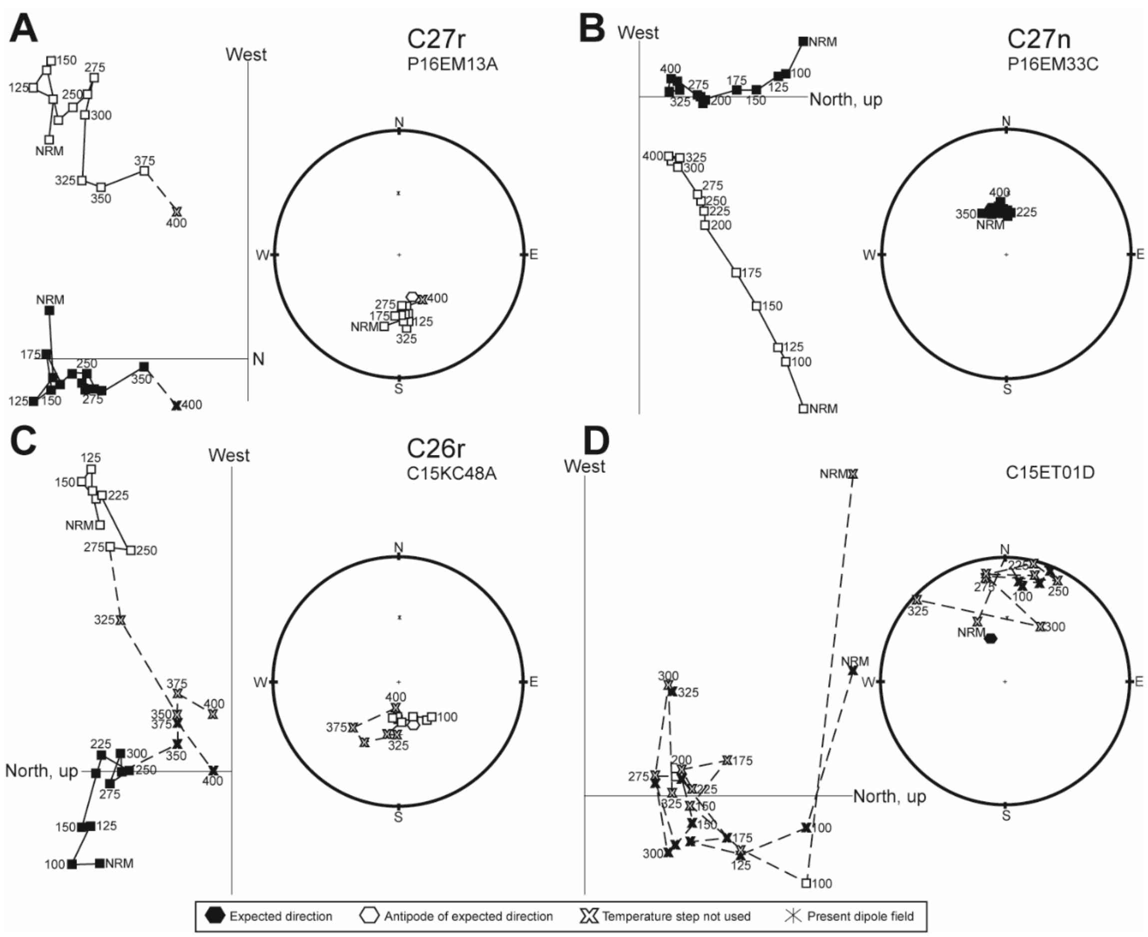

Figure 2.4. Representative orthogonal end vector demagnetization diagrams and equal-area plots for each subset of data. (A) Demagnetization trajectory of a reversed polarity sample from C27r that allowed line-fitting to determine a characteristic direction (21% of data). (B) Demagnetization trajectory of a normal polarity sample from C27n where a line was calculated (27% of data). (C) Demagnetization trajectory of a reversed polarity sample from C26r where a line was calculated (17% of data). (D) Representative sample of erratic data that was not used for interpretations (35% of data).

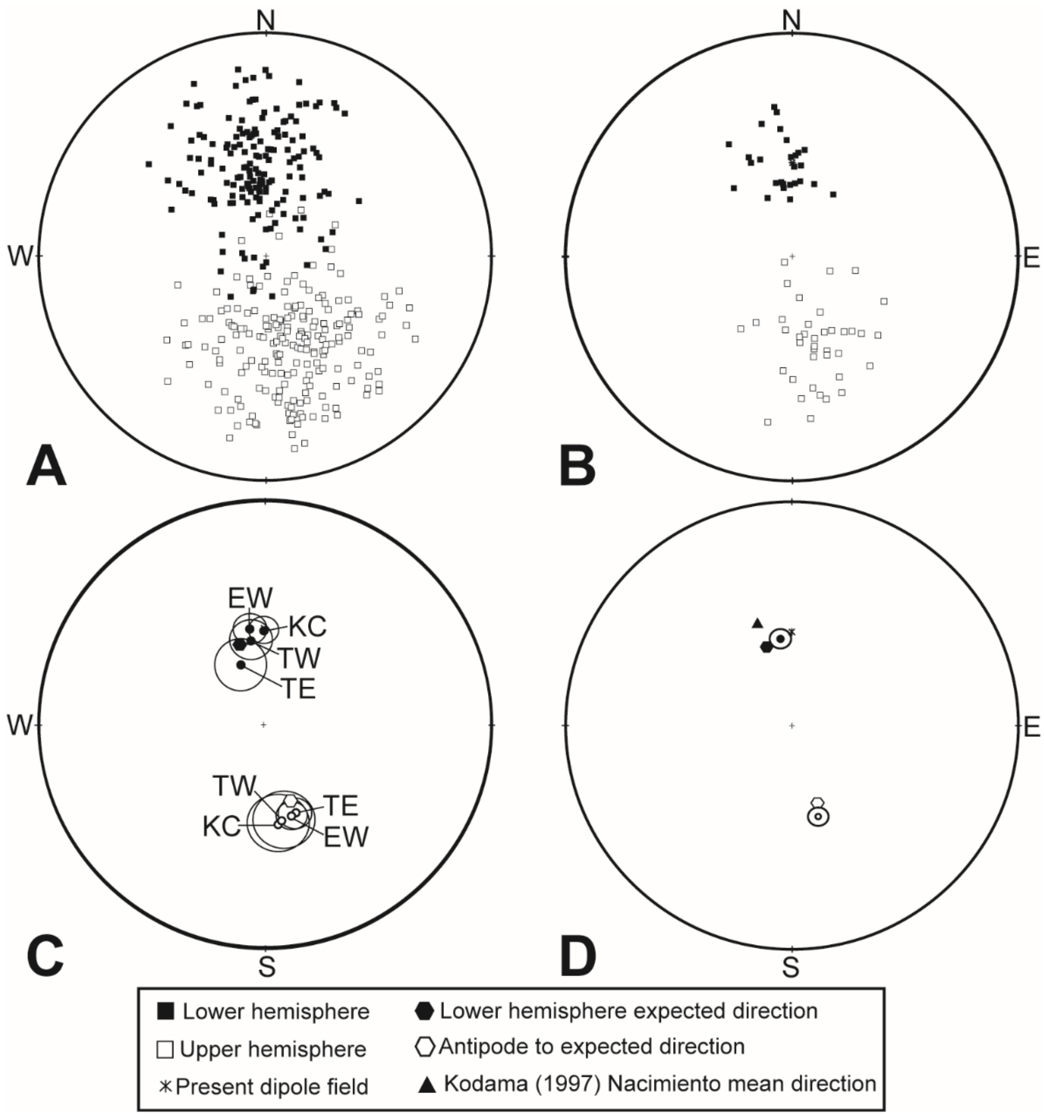

Figure 2.5. A) Equal-area plot of all characteristic magnetization directions obtained from this study. B) Equal-area plot of normal and reversed site-mean directions from all sections. C) Equal-area plot of normal and reversed site-mean directions averaged by section, and plotted alongside the present-day field position, the early Paleocene direction recalculated from Torsvik and others (2008) (see text for details), and the antipode to the early Paleocene direction. The ellipse around the mean direction represents the 95% confidence cone (Fisher, 1953). TW: Torreon West, TE: Torreon East, KC: Kutz Canyon, EW: Escavada Wash. D) Upper Nacimiento Formation normal and reversed formation-mean directions plotted alongside the present-day field position, the early Paleocene direction recalculated from Torsvik and others (2008), the antipode to the early Paleocene direction, and the mean Nacimiento Formation direction reported by Kodama (1997). The ellipse around the mean direction represents the 95% confidence cone (Fisher, 1953).

Table 2.2 Mean paleomagnetic directional data from the upper Nacimiento Formation.

Subset	*n*	D (°)	I (°)	k	a95 (°)	Pole (°N)	Pole (°E)	K	A95 (°)
Kutz Canyon normal sites	*9*	359.3	55.2	57.0	5.3	89.6	203.6	47.3	7.6
Kutz Canyon reversed sites	*6*	169.5	-53.7	12.3	19.9	79.5	174.8	9.3	23.1
Escavada Wash normal sites	*13*	349.7	54.6	20.1	9.5	81.9	174.4	12.2	12.4
Escavada Wash reversed sites	*13*	164.3	-55.3	30.4	7.6	77.6	168.3	18.6	9.9
Torreon West normal sites	*5*	351.2	58.8	116.3	7.1	82.1	195.1	83.0	8.4
Torreon West reversed sites	*3*	168.4	-54.2	38.1	20.3	81.5	162.0	28.6	23.5
Torreon East normal site	*1*	337.3	66.5	--	9.3	--	--	--	--
Torreon East reversed sites	*16*	161.6	-55.4	19.2	8.6	75.1	172.8	12.5	10.9
C27r- sites	*16*	166.7	-53.2	24.8	7.6	79.0	161.5	19.3	8.6
C27n - sites	*28*	352.8	56.1	32.5	4.9	84.1	184.3	20.8	6.1
C26r - sites	*22*	162.5	-56.3	20.4	7.0	75.6	178.5	12.6	9.1
C26r + C27r - sites	*38*	164.4	-55.0	22.3	5.0	77.2	171.0	14.9	6.2

Note. n – number of site-mean directions used to calculate the section and formation averages (see text for details); D – declination; I – inclination; k – Fisher's (1953) precision parameter; a95 – radius of 95% confidence cone around mean (Fisher, 1953); pole N and E – mean of virtual geomagnetic poles calculated from each line or site mean; K and A95 – Fisher statistics of paleomagnetic pole.

The mean VGP latitude and longitude calculated from all reversed (C26r and C27r) polarity sites is 77.2°N, 171.0°E (n=38; A_{95}=6.2), and that calculated from the normal polarity sites (C27n) is 84.1°N, 184.3°E (n=28; A_{95}=6.1), and can be compared to the expected paleopole of 74.9°N, 7.6°E recalculated from Torsvik et al. (2008).

Figures 3.2 and 3.3 show the local polarity stratigraphy for each section including each specimen and site mean polarity and VGP latitude. At Kutz Canyon, the lower reversal is constrained within a 1 m interval while the upper reversal is constrained within a 4.5 m interval. Lower resolution on the latter is due to the presence of coarse grained sandstone at the top of the section that was not sampled (Fig. 2.2, Table 2.3). The presence of coarse grained sandstones and friable paleosols near the reversals at Escavada Wash resulted in poorer resolution. The lower reversal is constrained within an 8 m interval and the upper reversal is constrained within a 6.5 m interval (Fig. 2.2, Table 2.3). At Torreon West, the lower and upper reversals occur within 1.2 m and 0.4 m intervals, respectively (Fig. 2.3, Table 2.3). We assumed that the underlying deposits were reversed, based on the results of Taylor and Butler (1980). The lower and upper reversals at Torreon East are constrained within 0.5 m and 1 m intervals, and the underlying deposits were assumed to be reversed (Fig. 2.3, Table 2.3).

Rock Magnetism

Rock magnetic analyses show that the upper Nacimiento Formation has a mixed magnetic mineralogy. Low temperature magnetometry for a representative sample of a black slickensided paleosol shows a two-fold increase on cooling of the RTSIRM and the magnetite Verwey transition (~120 K), indicating that goethite and magnetite coexist in the same specimen (e.g. Fig. 2.6A, 2.6B).

High temperature susceptibility curves for representative red calcareous paleosol specimens decreased until ~125°C and subsequently dropped at ~550°C, suggesting the

Table 2.3. Stratigraphic position of polarity zone boundary.

Local polarity zone	Chron	Location	Lowermost sample in chron	Uppermost sample in chron	Stratigraphic position of base (m)	Stratigraphic position of top (m)	Chron thickness (m)	Uncertainty (m)
A-	C27r	Kutz Canyon	KC45A	KC13A	0.0	29.0	29.0	± 0.5
		Escavada Wash	EM01A	EM20C	0.0	38.0	38.0	± 4.0
		Torreon West	TW01A	TW14A	0.0	36.7	36.7	± 0.6
		Torreon East	ET02A	ET11D	0.0	31.8	31.8	± 0.25
B+	C27n	Kutz Canyon	KC15A	KC39D	29.0	64.5	35.5	± 2.75
		Escavada Wash	EM21A	EM42C	38.0	72.3	34.3	± 7.25
		Torreon West	TW15B	TW23D	36.7	72.2	35.5	± 0.8
		Torreon East	ET12A	ET40C	31.8	57.5	26.0	± 0.75
C-	C26r	Kutz Canyon	KC41A	KC44D	64.5	69.0	4.5	± 2.25
		Escavada Wash	EM45B	EM50C	72.3	77.6	5.3	± 3.25
		Torreon West	TW24A	TW38C	72.2	78.4	6.2	± 0.2
		Torreon East	ET18C	ET35C	57.5	74.0	16.5	± 0.5

Note. Uncertainty is the number of meters between samples of opposing polarity.

presence of goethite and titanomagnetite (Fig. 2.6C, 2.6I). Low temperature magnetic measurements for these specimens also reveal a hematite Morin transition (~260 K) and a diffuse Verwey transition between ~130-90 K, indicating the presence of magnetite in different oxidation states (maghemite).

Low temperature magnetometry measurements from a brown, weakly-developed paleosol specimen reveal a magnetite Verwey transition and a ~two-fold increase of magnetic remanence upon cooling, indicating the presence of goethite (Fig. 2.6E). A goethite test performed on the same specimen (Fig. 2.6F) shows that remanence is lost when warming to 400 K as goethite is demagnetized through its Néel ordering temperature. However, some magnetic remanence persists upon subsequent cooling to 20 K indicating the presence of a high coercivity phase that is not demagnetized at low temperature, nor up to 400 K, likely indicating the presence of titanohematite.

RTSIRM curves for a representative specimen of a tan paleosol suggests both magnetite and goethite from the presence of the Verwey transition and an increase of remanence upon cooling (Fig. 2.6G). FC-ZFC-LTSIRM curves converge at 190 K, which indicates Al-substituted or nano-goethite (Fig. 2.6H). RTSIRM curves for a tan, silty weakly-paleosol sample have a separation at 90 K indicating maghemite and a slight Morin transition indicating hematite (Fig. 2.6J).

Triaxial-IRM Lowrie tests were performed to determine the relative abundance of magnetic carriers in each sample. For all samples analyzed the majority of the IRM is held by grains whose coercivities are greater than 1 T (Fig. 2.7). The largest remanence drop occurs between 100-150°C suggesting goethite is the most abundant mineralogy in the samples. Some samples also show a decrease in remanence between 150-200°C

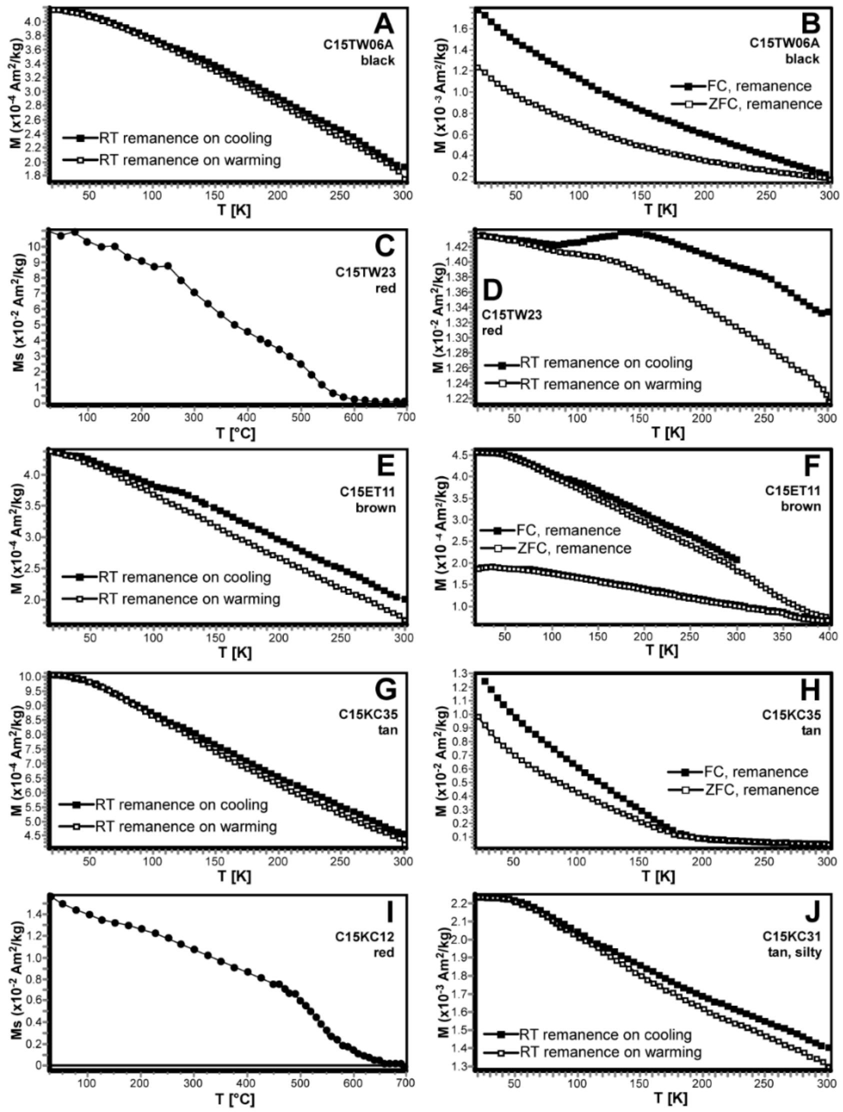

Figure 2.6. Rock magnetic analysis results including low temperature magnetization curve of representative samples and high temperature VSM (vibrating sample magnetometer) curves of saturation magnetization. Room temperature (RT) plots show magnetization measurements upon cooling and warming between 20K and room temperature (300K) following the application of saturation isothermal remanent magnetization (SIRM) at room temperature. FC (field-cooled) and ZFC (zero field-cooled) plots show magnetization during warming following a sustained direct current field of 2.5 T during cooling (FC), and magnetization during warming following a SIRM imparted at low temperature (ZFC). (A) RT curves for a black, slickensided paleosol sample indicating goethite and magnetite. (B) FC/ZFC curves for a black, slickensided paleosol sample indicating goethite. (C) High temperature VSM curve for a red, calcareous paleosol sample indicating goethite, titanomagnetite, and hematite. (D) RT curves for a red, calcareous paleosol sample indicating maghemite. (E) RT curves for a brown paleosol sample indicating magnetite and goethite. (F) FC/ZFC curves from the goethite test for a brown paleosol sample indicating goethite and titanohematite. (G) RT curves for a tan paleosol sample indicating magnetite and goethite. (H) FC/ZFC curves for a tan paleosol sample indicating Al-substituted goethite. (I) High temperature VSM curves for a red, calcareous paleosol indicating goethite, titanomagnetite, magnetite, and hematite. (J) RT curves for a tan, silty weakly-developed paleosol sample indicating titanomagnetite and magnetite (see text for details).

suggesting titanohematite may also be present. Remanence remaining after 200°C is likely held by pigmentary hematite for samples TW23 and KC12, supported by the loss of remanence between 600-650°C, red coloring, and the low temperature rock magnetometry experiments. In all other samples, the remaining remanence is likely maghemite that inverted to hematite upon heating above ~450°C. All samples, except TW06A, also show remanence held by the 300 mT curve up to ~300°C, indicating the presence of magnetite/maghemite.

Detrital Sanidine Dating

The age probability plot for sample HJ16-SJ-11 from Escavada Wash is shown in Figure 2.8. The sample is dominated by Paleocene grains where 66 of the 86 crystals give a weighted mean age of 62.48±0.02 Ma. Older grains concentrate around 68 and 70 Ma with 8 crystals giving apparent ages >200 Ma. The dominance of a high proportion of grains near 62.5 Ma suggests that this sample may be a minimally reworked tephra layer such that the maximum deposition age closely approximates the actual deposition age.

Discussion

Magnetic Mineralogy

The upper Nacimiento Formation has a mixed magnetic mineralogy with titanohematite and maghemite as the characteristic remanent magnetization carriers. Goethite is also present in all lithologies and dominates the low-temperature magnetic measurements, however it does not contribute to the characteristic remanence direction. Titanohematite is likely present in most samples, supported by the drop in remanence between 150-200°C in the orthogonal IRM measurements and low temperature

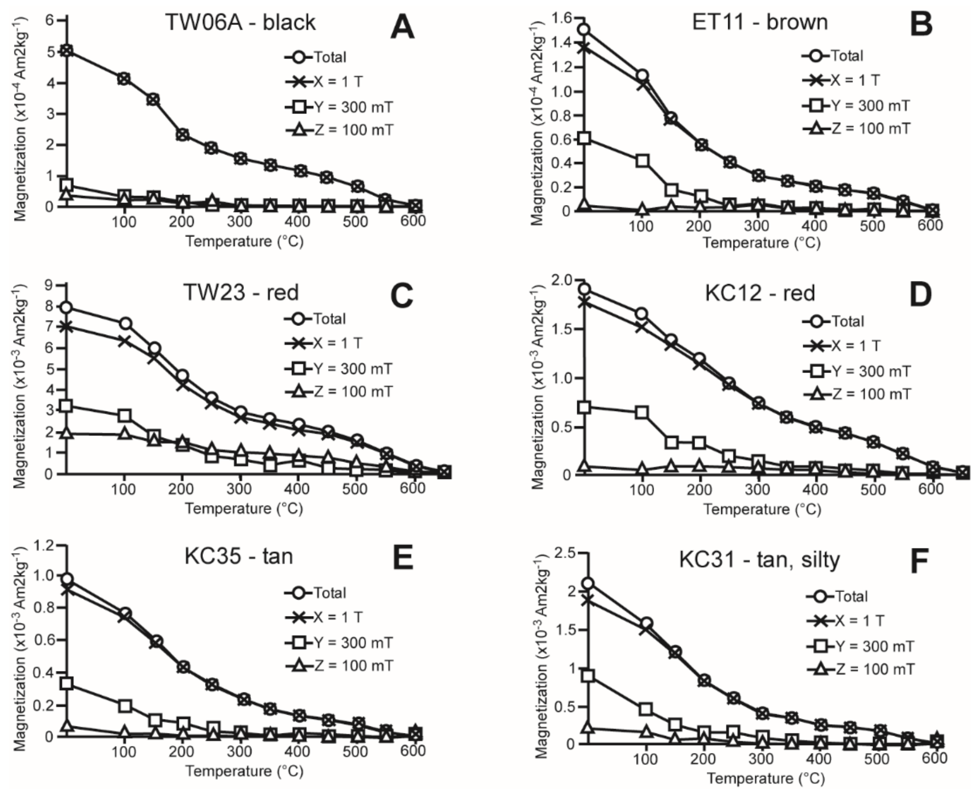

Figure 2.7. Thermal demagnetization of orthogonal isothermal remanent magnetization (IRM) imparted along X, Y, and Z axes for six specimens following Lowrie (1990) indicating a mixed magnetic mineralogy with goethite as the dominant carrier.

magnetometry measurements. Figure 2.6F shows that during the goethite test, there is a**n** increase in remanence from room temperature to low temperatures after goethite is removed. The phase must be high coercivity because it persists after the goethite test and the 1T orthogonal demagnetizations (Fig. 2.7) and must have an ordering temperature above 400 K since it survives heating to that point (Fig. 2.6F). These characteristics collectively indicate titanohematite as a characteristic remanent magnetization carrier, in agreement with the observations of Butler and Lindsay (1985). However, although titanohematite along with maghemite constitute the primary magnetic mineralogy, titanohematite does not appear to be the most abundant remanence carrier as suggested by Butler and Lindsay (1985). It is possible that given the broad sample spacing in Butler

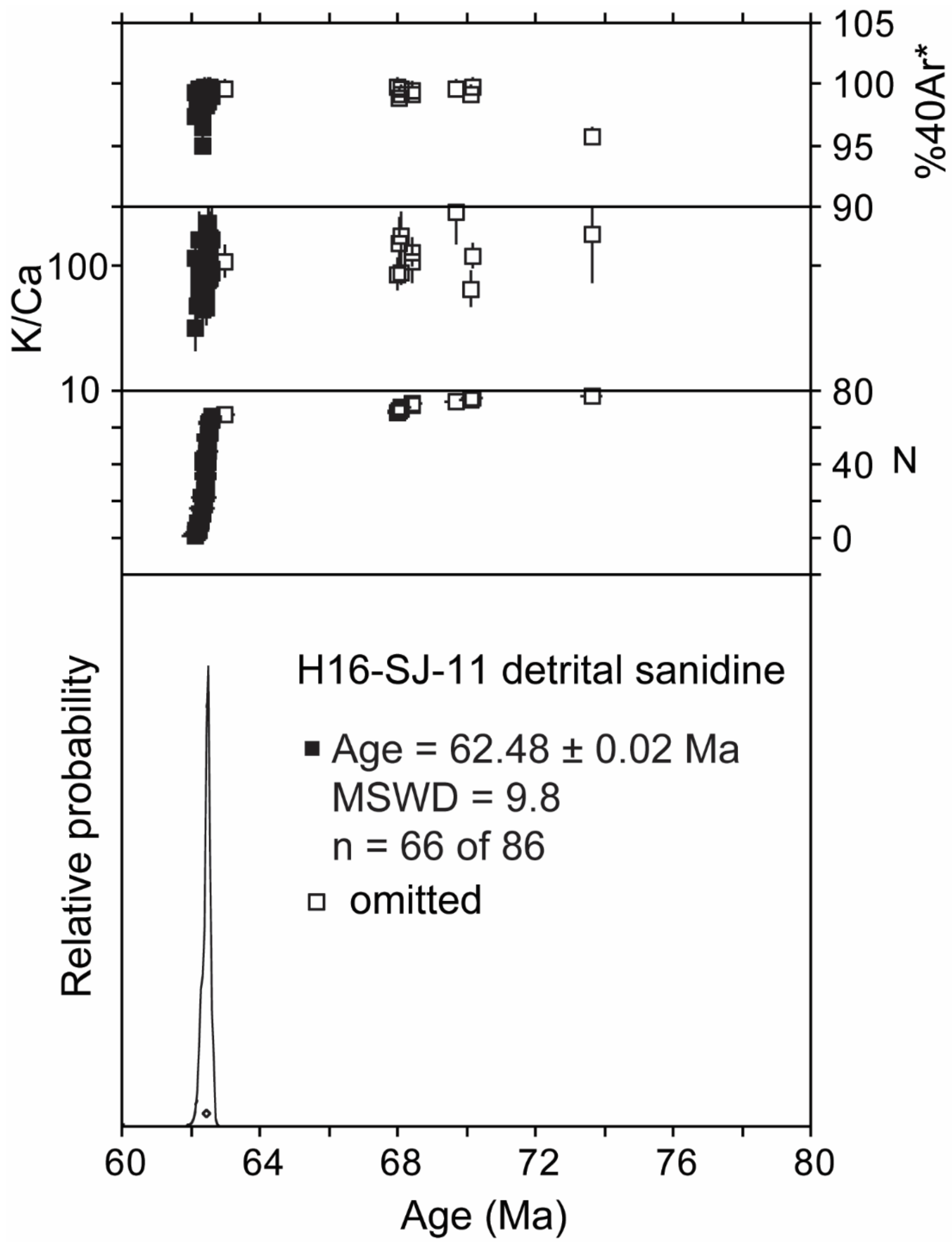

Figure 2.8. Age probability diagram for the analyzed sample, H16-SJ-11. The plot shows, from bottom to top, the age probability distribution spectrum for the data shown with solid squares, distribution of individual single-crystal ages with 2σ errors, K:Ca ratios, and percentage of radiogenic ^{40}Ar.

and Lindsay (1985), our samples do not overlap. Nonetheless, the presence of detrital titanohematite does support their conclusion that sediments were derived from the volcanic San Juan Mountains to the north. Goethite is the most abundant magnetic mineral and likely an alteration product, whereas the titanohematite is likely detrital. Agreement of the characteristic remanent directions obtained in this study to those reported by Kodama (1997) for the Nacimiento Formation confirm the primary nature of the magnetizations residing in maghemite and titanohematite. Kodama (1997) performed an inclination-correction study of the Formation, and reported a 7 to 8° inclination bias, however, it should be noted that any inclination shallowing would not affect a reversal stratigraphy.

Relationship of Polarity Stratigraphy to GPTS

Taylor and Butler (1980) reconstructed the magnetic polarity stratigraphy at Torreon West, Torreon East, and Kutz Canyon and correlated the strata to C26r-C25r based on previous work by Lindsay et al. (1978) and Taylor (ms, 1977). Butler and Lindsay (1985) revised the correlation of the polarity zones to the GPTS to correlate the late To2-To3 deposits at Torreon Wash and Kutz Canyon with C27r through C26r. We use the Butler and Lindsay (1985) interpretations for the base of the Nacimiento Formation and correlate the A-, B+, and C- magnetozones from the sections in our study to C27r-C26r (Figs. 2.2, 2.3). The polarity stratigraphy of the To2-To3 strata of Escavada Wash has not been previously published. This section also contains A-, B+, and C- magnetozones. A detrital sanidine age of 62.48±0.02 Ma from 64 meters in the section, within the B+ magnetozone, indicates correlation to C27n (Ogg, 2012). Thus we can correlate the underlying A- interval to C27r and the overlying C+ interval to C26r.

Sediment Accumulation Rates and Section Durations

Given that the entire C27n polarity zone (local polarity B+) occurs in each section and the temporal duration of the corresponding polarity chron has been estimated (Ogg, 2012), we were able to calculate mean sediment accumulation rates for each section shown in Table 2.4. Uncertainty associated with the duration of C27n (Ogg, 2012) was taken from Cande and Kent (1992), where the uncertainty in the time scale was assumed to be the same as the uncertainty in the width of the magnetic anomaly for C27n, which was ±6.9%. Uncertainties for the calculated sediment accumulation rates are asymmetrical because different stratal thicknesses and durations for C27n were used. The maximum sediment accumulation rate was calculated by dividing the maximum thickness of C27n strata by the minimum duration of C27n. The minimum sediment accumulation rate was calculated by dividing the minimum thickness of C27n strata by the maximum duration of C27n. Kutz Canyon, Torreon West, and Escavada Wash have similar mean sediment accumulation rates ranging from 115.7-119.9 m/myr and the rates are indistinguishable when factoring in their uncertainties. Torreon East has a lower sediment accumulation rate of 87.0 m/myr (-8.0, +9.0 m/myr). Large channel bodies within the C27n interval of this section suggest that erosion into the landscape occurred, reducing the overall preserved sediment thickness and resulting in a lower calculated accumulation rate. As a result, application of the calculated mean sediment accumulation rate to the remainder of the section may overestimate the amount of time the section spans if less erosion or more sediment accumulation occurred over the C27r and C26r intervals. The similarity of sediment accumulation rates at Kutz Canyon, Escavada Wash, and Torreon West suggests that sedimentation was similar across the basin as sampled sections are located both near the basin center (Kutz Canyon) and southern edges (Torreon West and Escavada Wash). This similarity is important because the Nacimiento Formation thins from north to south in the basin. The work of Taylor (ms, 1977) indicates that the entire C27r through C27n section is nearly twice as thick in Kutz Canyon (150 m) as in Torreon West (58 m). Consequently, sediment accumulation rates at Kutz Canyon for the lower part of the Nacimiento Formation (i.e., early in C27r) must have been much greater than in Torreon Wash, but equalize higher in the section (Taylor, ms, 1977). This interpretation is supported by sediment accumulation rates calculated for C27r in Kutz Canyon based on the magnetostratigraphy of Taylor (ms, 1977), which suggest mean rates of ~120-150 m/myr compared to preliminary mean accumulation rates for C27r-C28n from Kutz Canyon of ~180 m/myr (Peppe, unpublished data).

The duration of each section and the ages of all of the mammal fossil localities within each section was determined by extrapolating each section's C27n calculated sediment accumulation rate to the top and the bottom of each section (Fig. 2.9, Table 2.1, 2.4). Uncertainties for the duration of each section are also asymmetrical because the maximum and minimum sediment accumulation rates were used to calculate the uncertainties. Kutz Canyon is estimated to span the least amount of time, 580 kyr (-90, +100 kyr), from 62.76-62.18 Ma. Escavada Wash spans 750 kyr (-190, +280 kyr) from 62.85-62.10 Ma. Torreon West spans 650 kyr (-80, +80 kyr) from 62.82-62.17 Ma. Torreon East is calculated to span 870 kyr (-100, +100 kyr) from 62.88-62.01 Ma, but as noted above, the presence of large channel bodies within the C27n interval suggests that erosion occurred and the calculated sediment accumulation rate may be an

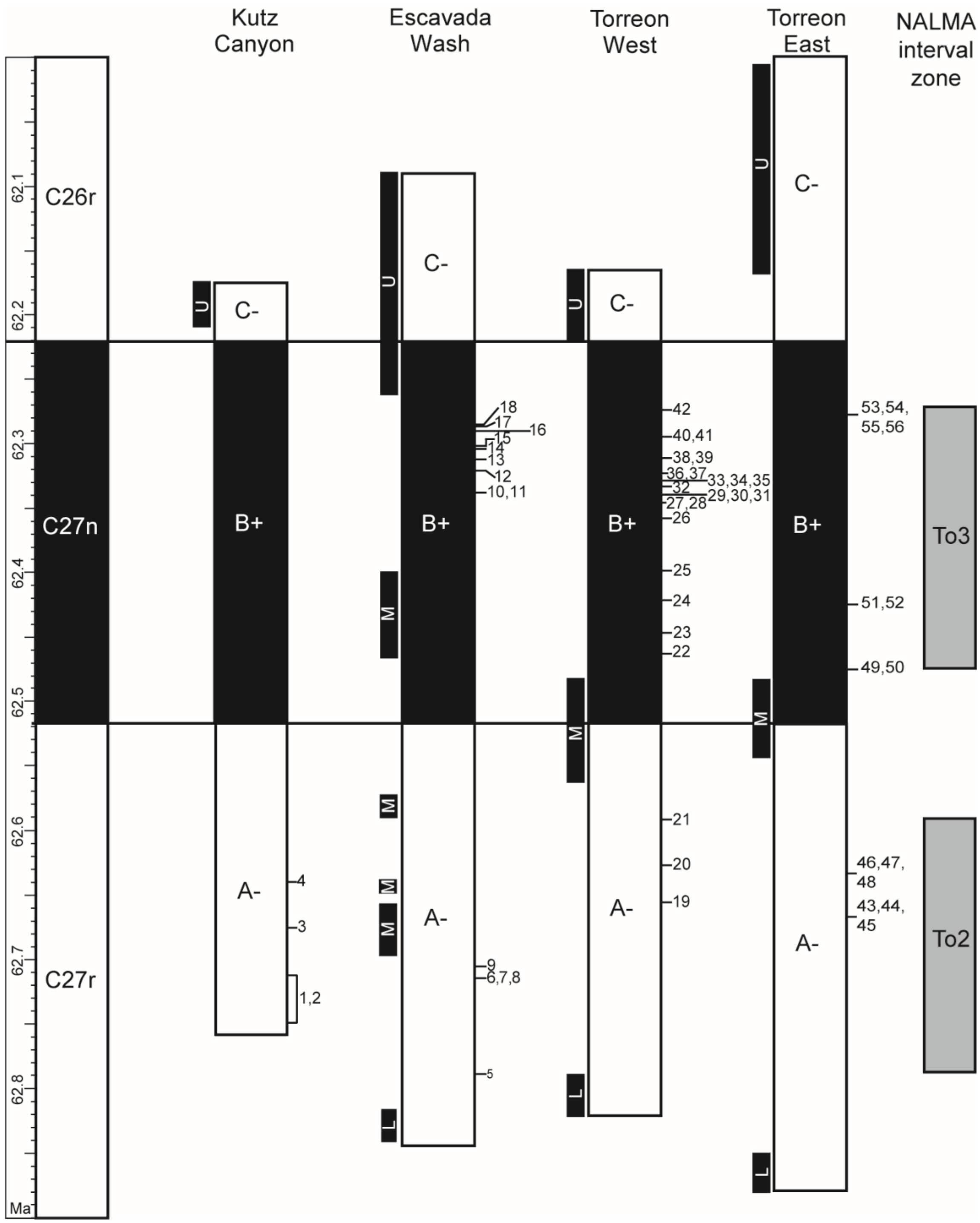

Figure 2.9. Chronostratigraphy of the Upper Nacimiento Formation showing the age and calculated duration of the Kutz Canyon, Escavada Wash, Torreon West, and Torreon East sections. Time scale from Ogg (2012) is shown to the left. Lithologies are highlighted for each section along with fossil localities. Fossil localities 1-4 from Kutz Canyon, 5-18 from Escavada Wash, 19-42 from Torreon West, and 43-56 from Torreon East are described in Table 3.1.

Table 2.4. Calculated sediment accumulation rates and durations of polarity zones.

	Kutz Canyon	Escavada Wash	Torreon West	Torreon East
C27n duration* (myr)	0.296 ± 0.02	0.296 ± 0.02	0.296 ± 0.02	0.296 ± 0.02
Calculated sediment accumulation rate (m/myr)	119.9 (-16.3, +18.7)	115.7 (-30.3, +34.7)	119.9 (-10.1, +11.6)	87.0 (-8.0, +9.0)
Calculated duration of C27r strata (myr)	0.24 (-0.03, +0.04)	0.33 (-0.10, +0.16)	0.30 (-0.03, +0.04)	0.36 (-0.04, +0.04)
Calculated duration of C26r strata (myr)	0.04 (-0.02, +0.02)	0.12 (-0.05, +0.08)	0.05 (-0.01, +0.01)	0.21 (-0.02, +0.03)
Calculated age of section base (Ma)	62.76 (-0.05, +0.06)	62.85 (-0.12, +0.18)	62.82 (-0.05, +0.06)	62.88 (-0.06, +0.06)
Calculated age of section top (Ma)	62.18 (-0.04, +0.04)	62.10 (-0.10, +0.07)	62.17 (-0.03, +0.02)	62.01 (-0.05, +0.04)
Calculated total section duration (myr)	0.58 (-0.09, +0.10)	0.75 (-0.19, +0.28)	0.65 (-0.08, +0.08)	0.87 (-.10, +.10)

Note. *C27n duration from Ogg (2012), uncertainty was taken from Cande and Kent (1992), where the uncertainty in the time scale was assumed to be the same as uncertainty in the width of the magnetic anomaly for C27n, which was ± 6.9%. Uncertainties associated with the sediment accumulation rates, strata durations, section ages, and section durations are shown in parentheses. Sediment accumulation uncertainties are asymmetrical because different stratal thicknesses and durations for C27n were used. The maximum sediment accumulation rate was calculated by dividing the maximum thickness of C27n strata by the minimum duration of C27n. The minimum sediment accumulation rate was calculated by dividing the minimum thickness of C27n strata by the maximum duration of C27n. The maximum and minimum sediment accumulation rates were used to calculate uncertainties for durations and ages, also resulting in asymmetrical uncertainties.

underestimation for the remainder of the section, which results in an overestimate of the duration of deposition in the Torreon East section.

Evolution of the San Juan Basin

The calculated sediment accumulation rates for C27n, which are considerably lower than those for C27r, suggest that the basin was probably mostly filled prior to the end of C27r (late To2) and sedimentation equalized across the basin during the end of C27r through the start of C26r. These findings support the three phase subsidence model proposed by Cather (2004) which determined a phase of subsidence from ~74-67 Ma resulted in the deposition of the Nacimiento Formation. Following this phase of subsidence, the space available for sediments to fill likely decreased with time throughout the early Paleocene so that during the late part of C27r through early in C26r (~63-62 Ma) there was little accommodation space in the basin. This lack of accommodation space likely caused the unconformity between the upper Nacimiento Formation and the overlying Eocene San Jose Formation. Sedimentation resumed in the Eocene once additional accommodation space was created, the third phase of subsidence documented by Cather (2004).

This interpretation of equalized accommodation space in the San Juan Basin plausibly explains the dominance of sheet sands rather than channels throughout the top of C27r-C26r interval in all four sections (Figs. 2.2, 2.3) and the similar sediment accumulation rates from basin center to basin margin (Table 2.3). If accommodation was low in the basin during this time, the sediment transport capacity of a channel was likely frequently exceeded, resulting in unconfined flow and deposition of laterally continuous sheet sands. This evidence for unconfined flow also suggests that the Nacimiento Formation records the progradation and/or aggradation of a distributive fluvial system (DFS), characterized by a radial channel pattern and aggradational deposition below the point where flow becomes unconfined (Weissmann et al., 2010; Hobbs, ms, 2016). Low accommodation and fan progradation could also explain the presence of better drained soils embodied by red, calcareous paleosols. Well-developed soils are expected during accommodation minimums and fan progradation because the distance to the water table increases and distance to the source decreases (Atchley et al., 2013; Weissmann et al., 2010). However, it is important to note that variations in climate may have also been an important contributing factor in generating these features.

Mammalian Biostratigraphy

The Nacimiento Formation contains the only deposits in North America where mammalian turnover between To2-To3 can be constrained, and temporal constraint of this turnover may provide a better understanding of possible driving mechanisms. Using estimated sediment accumulation rates (Table 2.4), an age was assigned to each To2 and To3 mammal locality in each section (Table 2.1, Fig. 2.9). Our magnetostratigraphy for the upper Nacimiento Formation corroborates the interpretation of Lofgren et al. (2004) that the To2 NALMA interval zone occurs within C27r and the To3 NALMA interval zone occurs within C27n. Additionally, there is no evidence that the turnover is diachronous across the San Juan Basin.

Both late To2 and To3 mammals are found at Escavada Wash, Torreon West, and Torreon East, and thus these areas are the best locations to determine the timing of the To2-To3 turnover. At Escavada Wash the youngest To2 locality (e.g., L-10350) occurs at

62.71 Ma (-0.07, +0.08 myr) and the oldest To3 localities (e.g., L-09981 and L-10444) occur at 62.35 Ma (-0.10, +0.05 myr), which indicates the turnover occurred over 360 kyr (-120, +180 kyr). At Torreon West, the youngest To2 locality (L-08180) occurs at 62.59 Ma (-0.02, +0.03 myr) and the oldest To3 locality (L-09173) occurs at 62.46 Ma (-0.02, +0.03 myr) for a duration of 130 kyr (-50, +50 kyr) between NALMA interval zones. At Torreon East the youngest To2 localities (L-07583, L-04954, and L-04950) occur at 62.63 Ma (-0.02, +0.04 myr) and the oldest To3 localities (L-10013 and L-10432) occur at 62.47 Ma (-0.02, +0.04 myr) for a duration of 160 kyr (-60, +60 kyr) between the interval zones. When using the youngest To2 locality in the basin, which is a locality in Torreon West (L-08180), and the oldest To3 localities, which are localities in Torreon East (L-10013 and L-10432), the duration between the To2-To3 NALMA interval zones is 120 kyr (-60, +50 kyr) and occurred between 62.59-62.47 Ma. This indicates that To2-To3 turnover occurred over a relatively short period of time and suggests that the To2-To3 transition was probably not driven exclusively by typical patterns of origination and extinction. Instead, they may be due to very rapid rates of speciation, migration of new taxa into the basin, or both. The driver of an increase in mammalian speciation rates and/or dispersal of taxa into the basin is uncertain, but we posit that it was driven by external factors such as environmental change associated with changes in basin dynamics or regional/global changes in climate. Further work focused on reconstructing the environment and climate of this interval will help resolve this question.

Conclusions

The polarity stratigraphy for the four sections in this study, Kutz Canyon, Escavada Wash, Torreon West, and Torreon East, can be correlated to chrons C27r-C26r of the geomagnetic polarity time scale. This study is the first published polarity stratigraphy for the Escavada Wash section, and a $^{40}Ar/^{39}Ar$ detrital sanidine age further constrains the age of the section. Rock magnetic analyses indicate that although goethite is the most abundant magnetic mineral, titanohematite and maghemite carry the characteristic remanent magnetization. The age model for the upper Nacimiento Formation presented here has important implications for the evolution of the San Juan Basin and the timing and nature of the To2-To3 mammalian turnover. Our results indicate that sediment accumulation rates near the basin center were similar to those near the basin edge, which signals that from the end of C27r through the start of C26r sediment accumulation rates had equalized across the basin. This suggests that the deposition of the upper Ojo Encino Member occurred during a basin accommodation minimum, which was associated with the progradation of a distributive fluvial system across the basin. The later unconformity between the Paleocene Nacimiento Formation and the lower Eocene San Jose Formation was likely driven by a lack of accommodation in the San Juan Basin and sedimentation could not resume until additional accommodation space was created in the Eocene. This is consistent with Cather's (2004) three phase model of basin subsidence.

Estimates of sediment accumulation rates for strata in the Escavada, Torreon West and East, and Kutz Canyon sections were used to determine the age to each To2-To3 fossil locality in those sections, and in turn constrain the duration of the To2-To3 turnover. These results indicate that the To2-To3 turnover was rapid and occurred over ~120 kyr (-60, +50 kyr) between 62.59 and 62.47 Ma. The rapid nature of the mammalian turnover suggests that there was likely an external forcing factor, such as an environmental change driven by the progradation of the distributive fluvial system across the basin and/or changes in regional or global climate.

Acknowledgments

This work was supported by SEPM (CL), National Science Foundation EAR-132552 (DP), -1325612 (RS), -0207750 and -1325544 (TEW), American Chemical Society Petroleum Research Fund (PRF#52822-DN18) (DP), Baylor University Department of Geosciences' Dixon Fund (CL, TL), and the University of Minnesota Institute for Rock Magnetism visiting student fellowship (CL). This is IRM publication #1706. We thank K. Kodama, D. Lofgren, and one anonymous reviewer for their helpful comments and P. Gingerich and D. Rye for the editorial assistance. Thanks to A. Flynn, A. Davis, J. Milligan, and A. Baumgartner for assistance with sample collection and section measuring.

CHAPTER FOUR

Modeling the Upper Nacimiento Formation, San Juan Basin, New Mexico as a Distributive Fluvial System

This chapter published as: Leslie, C.E., Peppe, D.P., and Atchley, S.C., *in review*, Modeling the upper Nacimiento Formation, San Juan Basin, New Mexico as a distributive fluvial system: *Journal of Sedimentary Research.*

Abstract

The Nacimiento Formation of the San Juan Basin contains early Paleocene terrestrial deposits that composed a large fluvial fan. Previous work has shown that from base to top the Nacimiento Formation grain size coarsens, paleosol drainage increases, and accommodation decreases while grain size fines from north to south. This evidence has been used to suggest that the fan system prograded through the basin during the early Paleocene. However, these analyses are from different sections across the basin that span different intervals in time making it difficult to assess how the fan evolved through time spatially and temporally. In this study, we focus on four sections of the upper Nacimiento Formation that were deposited over approximately the same interval in late C27r – C26r (~62.0-62.9 Ma) and sample a transect from the basin center to basin margin: Kutz Canyon, Escavada Wash, Torreon East, and Torreon West. We use the distributive fluvial system (DFS) model to assess the position of the four sections within a depositional fan and then test whether the strata were deposited by a prograding DFS. To do this, we categorize the paleosols into pedotypes and assign a maturity and drainage index value. We then classify the deposits into fluvial facies and determine the corresponding proximal or distal floodplain location. These analyses demonstrate that the Kutz Canyon

(basin center) and Escavada Wash (near basin margin) sections represent a medial fan position whereas the Torreon East (basin margin) and Torreon West (basin margin) sections were deposited in a distal fan position. Within the upper Nacimiento Formation sections there are no discernable trends with respect to grain size, floodplain location, or paleosol drainage and maturity within each section. These findings, coupled with petrographic analyses of sandstones, suggest that the sections record autocyclic migration and fan aggradation, rather than progradation. Though there is no convincing evidence for progradation in the sampled interval, an assessment of the entire Nacimiento Formation indicates an increase in paleosol drainage, pedogenic carbonate, sandstone abundance, and decrease in sediment accumulation rates that are equalized from basin margin to center, which may represent progradation of a DFS on a much longer time scale than sampled in this study. Findings from this study suggest the duration of deposition should be considered when applying the DFS model to assess depositional trends.

Introduction

Distributive fluvial systems (DFS), characterized by a radial channel pattern and aggradational deposition below the point (apex) where flow becomes unconfined, have been recognized and studied in modern settings (Weissmann et al., 2010; Hartley et al., 2010; Buehler et al., 2010; Davidson et al., 2013). DFS have been identified in modern extensional, compressional, and strike-slip tectonic settings and in varying climatic settings. The term DFS has been used to describe more traditional terms such as megafan, alluvial fan, and fluvial fans with distinctions based on area and gradient (Hartley et al., 2010). Work generating the depositional facies model for these systems from modern settings (Hirst, 1991; DeCelles and Cavazza, 1999; Shukla et al., 2001; Horton and DeCelles, 2001; Nichols and Fisher, 2007; Cain and Mountney, 2009, 2011; Weissmann et al., 2011; Davidson et al., 2013) has led to recognition of these systems in the rock record (Pietsch et al., 2013; Trendell et al., 2013; Weissmann et al., 2013; Gulliford et al., 2014; Lawton et al., 2014; Hobbs, 2016).

Assessments of modern and fossil DFS has allowed the development of a DFS model for depositional facies that predicts that depositional facies will change in an expected way spatially and temporally as sedimentary accommodation fills (e.g., Hartley et al., 2010; Weissmann et al., 2010, 2013; Davidson et al., 2012). At the first order, it is expected that there will be a trend of decreasing grain size and increasing soil development from the proximal to distal portions of a DFS (Davidson et al., 2012; Hartley et al., 2013; Weissman et al., 2013). This has been demonstrated by flume experiments and digital models that show that downstream fining occurs in fans that are supported by outcrop descriptions of ancient fan deposits (Price, 1974; Paola et al., 1992; Chakraborty and Ghosh, 2010), and by satellite image analysis of DFS that indicates that the water table shallows downstream resulting in a change from well drained floodplains in the proximal region to poorly drained floodplains in the distal regions (Davidson et al., 2012; Hartley et al., 2013; Weissman et al., 2013). This change in grain size and soil development can be further divided by position on the DFS. Proximal portions of the DFS have the highest stream power due to the highest gradient along the system; consequently, coarser particles are transported (Davidson et al., 2012). Sediments in the proximal portion of the DFS are immature, and typically include sand through pebble grain size and intraclasts (Chakraborty and Ghosh, 2010). In cross-section amalgamated channel complexes dominate. Soils are typically more well-drained, but less mature (Hartley et al., 2013). Moving further from the apex to the medial portion of the system, grain size becomes finer. Sediments are more mature and the proportion of overbank to channel deposits increases (Davidson et al., 2013). At the distal point of the system, sediments are the finest and most mature, and the transport capacity of the system is at its lowest and the proportion of overbank to channel deposits are at a maximum. The most well-developed soils are likely to occur here (Hartley et al., 2013). The down dip portion of the fan is also closest to the water table and as a result may have ponding of water, wetlands, and poorly drained soils.

In addition to interpreting the spatial distribution of depositional facies, the distributive fluvial system model predicts that accommodation will decrease if the rate of sedimentation exceeds the rate of accommodation gain, which in turn will influence depositional facies across the DFS. If accommodation is low, channels are expected to migrate laterally and avulse. Lateral migration and avulsion is most likely to occur proximal to the apex because accommodation is filled most rapidly here. Consequently, a cross-section of this area through time would show amalgamated channels in more proximal positions, and more isolated channels and associated overbank mudrock in more distal positions. DFS deposits are also expected to coarsen upwards due to fan progradation as accommodation is filled.

In this study, we focus on the early Paleocene upper Nacimiento Formation in the San Juan Basin, New Mexico (Fig. 3.1). The Nacimiento Formation accumulated from approximately 65.7 to 61.5 Ma and represents a large, evolving fluvial system. Previous work indicates that grain size fines from north to south in the basin, and that

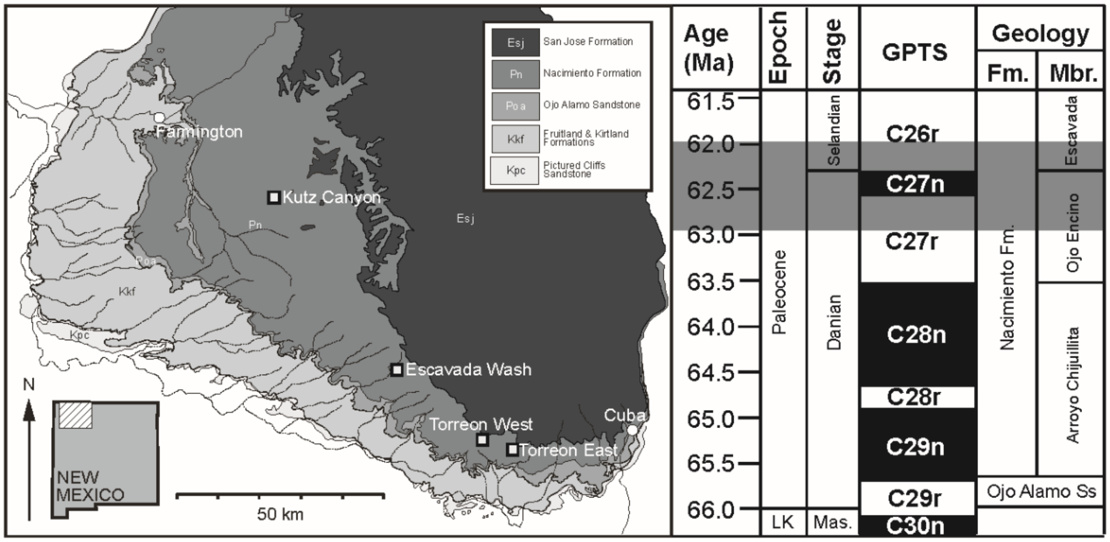

Figure 3.1. Geologic map of the San Juan Basin, New Mexico showing the location of Cretaceous through Eocene lithostratigraphic units and four sections collected in this study, i.e., Kutz Canyon, Escavada Wash, Torreon West, and Torreon East, indicated by white squares (modified from Williamson et al., 2008). Chronostratigraphic chart with age constraints (Butler and Lindsay 1985; Ogg 2012; Peppe et al. 2013, 2015), GPTS (Ogg 2012) stratigraphy (Williamson 1996). Study interval highlighted in gray.

accumulation rates through time that equalize between basin center and basin margin, and paleosols that become increasingly better drained (Baltz, 1967; Williamson et al., 1996; Leslie et al., in press). These findings suggest the fluvial system in the San Juan Basin prograded and/or aggraded during the early Paleocene and represents an ideal location to use the distributive fluvial system model to determine the spatial distribution on the fan and test the prograding fan hypothesis.

We use the distributive fluvial system model to reconstruct the fan geomorphology and associated stratigraphy based on four contemporaneous sections of the upper Nacimiento Formation across the basin: Kutz Canyon, Escavada Wash, Torreon West, and Torreon East (Fig. 3.1). We classify the deposits into fluvial facies, categorize paleosols into pedotypes and assign a maturity and drainage index, and analyze sandstone thin sections to evaluate compositional variations. We then use these data to determine floodplain location and assess landscape evolution for comparison with trends predicted by the DFS model.

Previous Work

The San Juan Basin, a Laramide foreland basin, is located in northwestern New Mexico and contains Upper Cretaceous through lower Eocene deposits (Fig. 3.1) (Chapin and Cather, 1983). Previous work by Cather (2004) indicates there were three phases of subsidence in the San Juan Basin: the first phase during the late Campanian-early Maastrichtian, a second phase during the latest Maastrichtian-early Paleocene, and a third phase during the Eocene. The second phase of subsidence spans from ~74-67 Ma, and provided the accommodation for the later deposition of the early Paleocene Nacimiento Formation. Baltz (1967) found that grain size in the Nacimiento Formation decreases from north to south and interpreted this trend to represent basin-wide fluvial fan deposition during the early Paleocene. The strata of the Nacimiento Formation are interpreted to have been deposited by south-flowing fans and/or fluvial systems sourced from the San Juan Uplift to the north (Baltz, 1967; Donahue, 2016).

The Nacimiento Formation is subdivided into three members: the Arroyo Chijuillita, the Ojo Encino, and the Escavada Members (Fig. 3.1; Williamson and Lucas, 1992; Williamson, 1996). This study focuses on the upper portion of the Ojo Encino Member of the Nacimiento Formation, which contains variegated red and drab paleosols, sheet and channel sandstone bodies, and three persistent “black” paleosols that function as marker beds referred to as the “lower black”, “middle black”, and “upper black” in this paper (Williamson and Lucas, 1992; Leslie et al., in press). The underlying Arroyo Chijuillita Member is dominated by sandstone beds and drab colored mudstones

(Williamson, 1996; Davis et al., 2016), suggesting an overall increase in paleosol drainage throughout Nacimiento deposition. The overlying Escavada Member is dominated by a high proportion of sandstones and silcretes indicating a grain size increase up section in the Nacimiento Formation (Williamson and Lucas, 1992; Williamson, 1996). Hobbs (2016) analyzed the geochemistry, mineralogy, and morphology of the paleosols of the three members of the Nacimiento Formation and concluded that the trend towards better-drained paleosols up section is associated with the progradation of a fluvial system.

The four sections of focus are distributed along a northwest-southeast trend through the basin and span from basin center to basin margin (Fig. 3.1). Kutz Canyon, the northernmost section, is near the center of the basin, Escavada Wash is near the basin margin approximately 48 km southeast of Kutz Canyon, and Torreon West and East, the southernmost sections, are approximately 32 km southeast of Escavada Wash near the basin margin. Torreon West and East are separated by about 10 km. Taylor (1977) and Williamson (1996) produced generalized stratigraphic sections for the four study areas and documented the stratigraphic position of fossil mammal localities. Leslie et al. (in press) produced detailed measured sections in conjunction with a high-resolution age model for sections of the Ojo Encino Member at Kutz Canyon, Escavada Wash, Torreon West, and Torreon East based on sediment accumulation rates. Using the sediment accumulation rates for each section, Kutz Canyon spans 580 kyr (-90, +100 kyr) from 62.76-62.18 Ma, Escavada Wash spans 750 kyr (-190, +280 kyr) from 62.85-62.10 Ma, Torreon West spans 650 kyr (-80, +80 kyr) from 62.82-62.17 Ma, and Torreon East spans 870 kyr (-100, +100 kyr) from 62.88-62.01 Ma. Interestingly, the calculated sediment accumulation rates for Kutz Canyon, Torreon West, and Escavada Wash were indistinguishable when factoring in uncertainty, ranging from 115.7-119.9 m/myr. Torreon East had a lower sediment accumulation rate of 87.0 m/myr (-8.0, +9.0 m/myr). The sediment accumulations rates for C27n (Ojo Encino Member) were lower than those for C27r (Arroyo Chijuillita Member), suggesting the San Juan Basin was probably mostly filled prior to deposition of the Ojo Encino Member. As a result, little accommodation was available which resulted in equalized sedimentation rates from basin center to basin margin during deposition of the Ojo Encino Member.

Methodology

Measured sections

Four sections were measured across the basin: a 70 m section at Kutz Canyon, a 87 m section at Escavada Wash, a 79 m section at Torreon West, and a 76 m section at Torreon East (Figs. 3.2, 3.3, and 3.4; Leslie et al., in press). The lower black marker bed is the base of the Torreon West and Torreon East measured sections, and the lowest black marker bed present is the base of the Escavada Wash. The Kutz Canyon section was measured from a known mammal locality (Bab's Basin) whose age ensures overlap with the other sections as it does not contain the lower or middle black marker beds (Williamson, 1996; Leslie et al., in press). Each section was correlated using the stratigraphic position of the C27r-C27n reversal (Figs. 3.2, 3.3, and 3.4; Leslie et al., in press).

At each section, the outcrop was trenched to remove weathered material and document the lithologic contacts. The paleosols were described at the centimeter scale documenting the texture, color, ped structure, and shrink-swell features using the

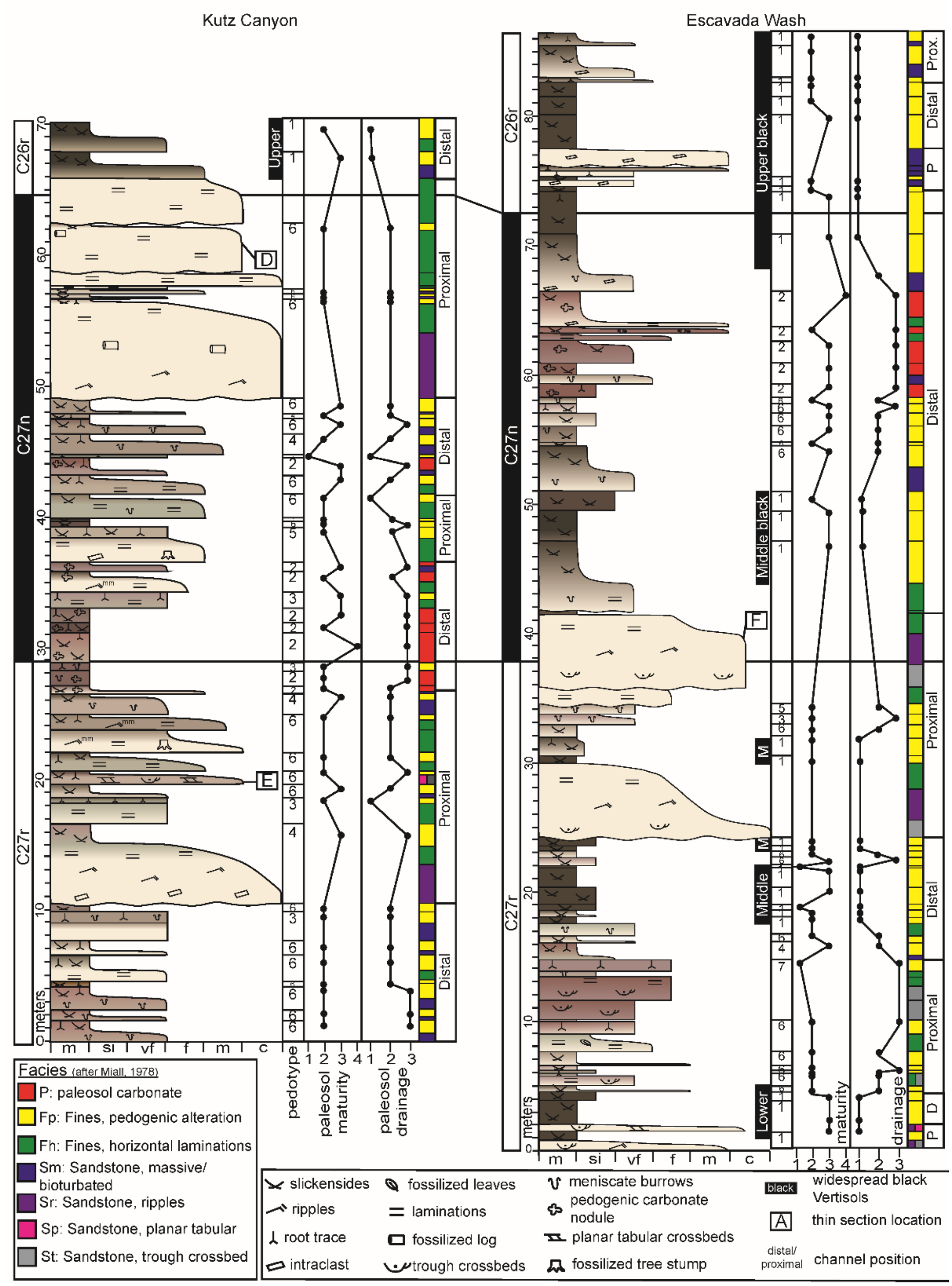

Figure 3.2. Detailed measured sections for Kutz Canyon and Escavada Wash documenting grain size, pedogenic features, sedimentary structures, paleosol color, thin section location, pedotype, maturity index (values 1-4 with 1 representing very weakly developed paleosols and 4 representing strongly developed paleosols), drainage index (values 1-3 with 1 representing poorly drained and 3 representing well drained paleosols), fluvial facies after Miall (1978; 1985), and proximal or distal floodplain location interpreted from fluvial facies.

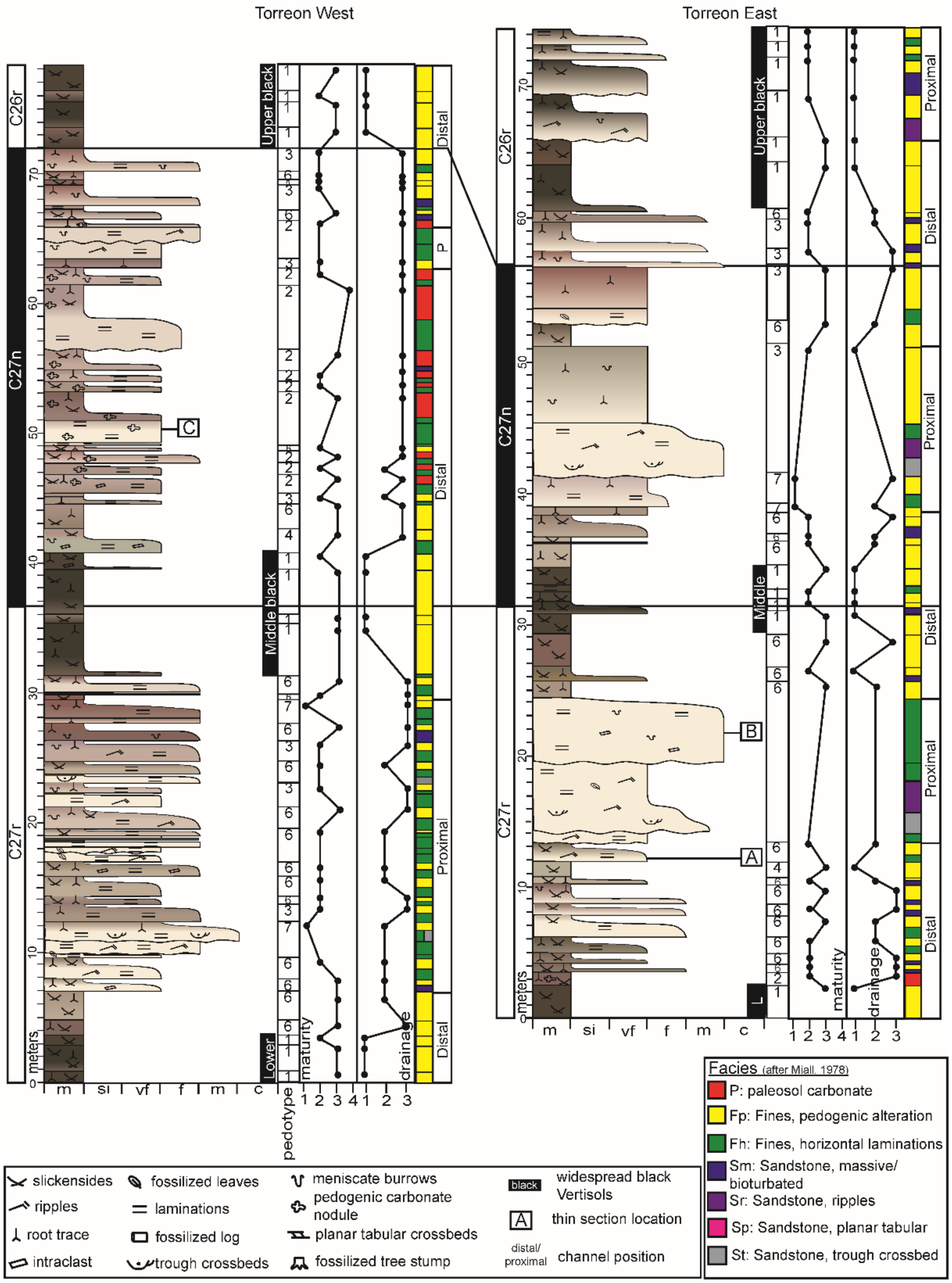

Figure 3.3. Detailed measured sections for Torreon West and Torreon East documenting grain size, pedogenic features and sedimentary structures, paleosol color, thin section location, pedotype, maturity index (values 1-4 with 1 representing very weakly developed paleosols and 4 representing strongly developed paleosols), drainage index (values 1-3 with 1 representing poorly drained and 3 representing well drained paleosols), fluvial facies after Miall (1978; 1985), and proximal or distal floodplain location interpreted from fluvial facies.

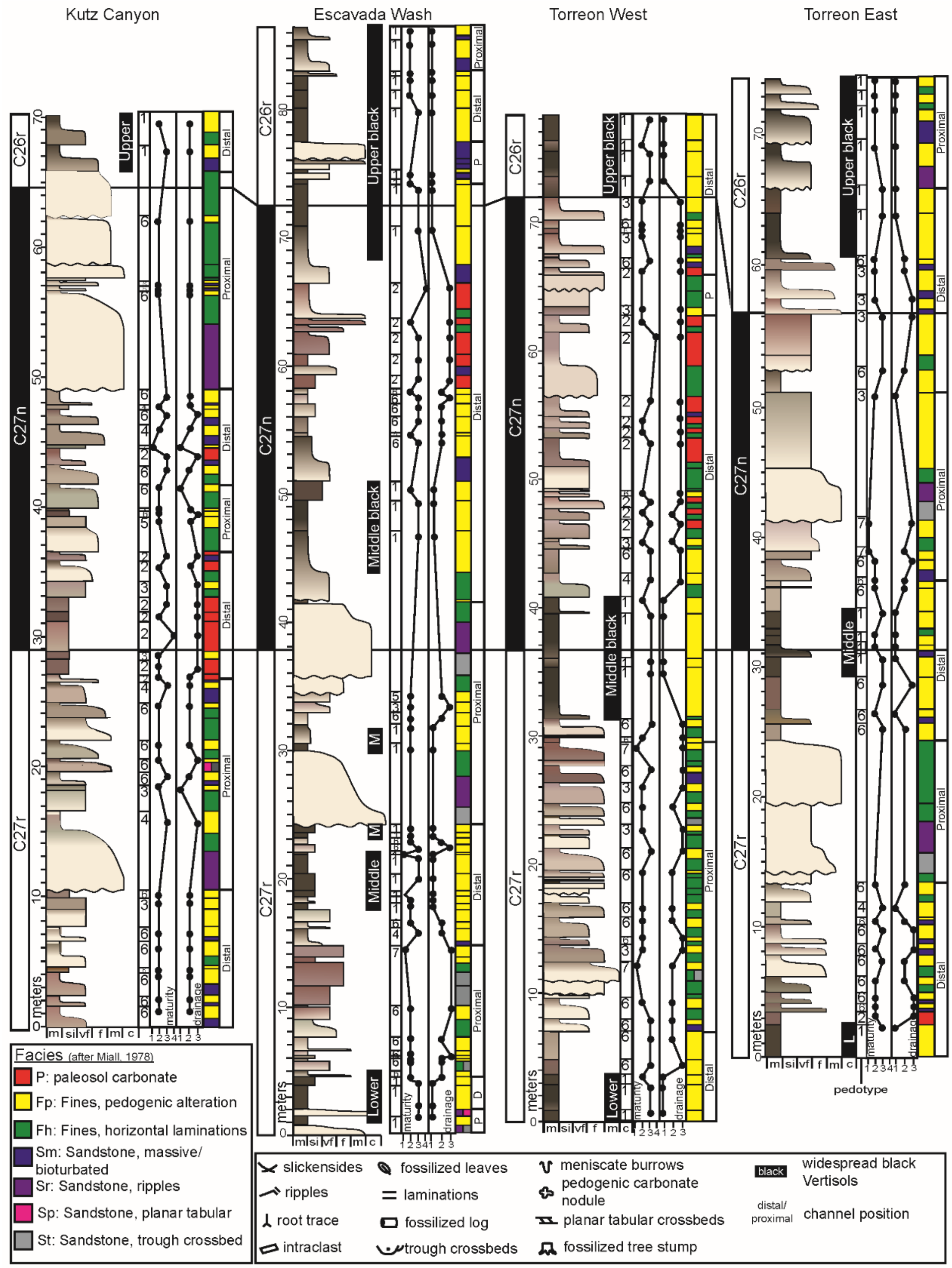

Figure 3.4. Composite figure highlighting the grain size, paleosol color, pedotype, maturity index (values 1-4 with 1 representing very weakly developed paleosols and 4 representing strongly developed paleosols), drainage index (values 1-3 with 1 representing poorly drained and 3 representing well drained paleosols), fluvial facies after Miall (1978; 1985), and proximal or distal floodplain location for all four measured sections.

guidelines of Soil Survey Staff (1999). For sandstones, the grain size and relationship to underlying strata was characterized. Deposits were classified within the fluvial facies scheme of Miall (1978, 1985) (Table 3.1). The fluvial facies were evaluated to determine floodplain location, i.e., proximal or distal. Proximal was assigned where Sr, St, and/or Sp were dominant and distal was assigned where P, Fp, Fh, and/or Sm were dominant.

Paleosol analysis

Paleosols were categorized into seven pedotypes based on similar characteristics and master and subordinate horizon designations (*sensu* Retallack, 1994; Soil Survey Staff, 1999). The pedotypes were defined using a modified version of the USDA modern soil classification (Soil Survey Staff, 1999). A qualitative maturity index was assigned to each paleosol based on its pedotype, B horizon quantity, and thickness (Retallack, 1988; Trendell et al., 2012) (Table 3.2). This index is a relative measure of landscape stability assuming increased thickness and horizonation require increased weathering (Retallack, 1988). The maturity index values range from 0 to 4 with 0 representing 0 cm of B horizon (very weakly developed) and 4 representing over 200 cm of B horizons (strongly developed). A drainage index value was also assigned to each paleosol based on paleosol color and hydromorphic features ranging from poorly drained (index =1) to well drained (index = 3) (Table 3.2).

Point count analysis

Samples were collected for thin sections from sandstone bodies throughout each measured section. Thin sections preparation was contracted to National Petrographics and were stained to better identify potassium feldspar grains. Thin sections were point

Table 3.1. Upper Nacimiento Fluvial Facies.

Facies	Lithology	Description	Interpretation
P	Mud to silt	Pedogenic alteration, carbonate nodules or rhizocretions present, slickensides or rooting may be present	Floodplain, soil
Fp	Mud to silt	Pedogenic alteration, rooting and slickensides common	Floodplain, soil
Fh	Mud to very fine sand	Horizontal laminations	Floodplain, abandoned channel, or waning flood deposit
Sm	Very fine to medium sand	Massive, faint laminations may be present	Floodplain or waning flood deposit
Sr	Very fine to medium sand	Ripple cross laminations	Channel deposits
St	Very fine to coarse sand	Trough crossbeds	Channel deposits
Sp	Very fine to coarse sand	Planar crossbeds	Channel deposits

counted (300 counts) using a PELCON Automatic Point Counter to determine the constituents. The normalized proportions of quartz, feldspar, and lithic fragments for each thin section are plotted on ternary diagrams to determine compositional classifications (McBride, 1963) and possible sediment provenance regimes (Dickinson and Suczek, 1979). The total quartz in the QFL diagrams includes monocrystalline, polycrystalline, and chert.

Table 3.2. Paleosol drainage and maturity indexes.

Value	Drainage or maturity	Description
1	Poorly drained	Gleyed or black subsurface horizons
2	Moderately drained	Brown subsurface horizons
3	Well drained	Red or purple subsurface horizons
1	Very weakly developed	Weak A horizon, no subsurface horizon, bedding visible
2	Weakly developed	Subsurface horizon (e.g. Bw, Bk, Bss) present, thickness < 1 m
3	Moderately developed	Multiple subsurface horizons (e.g. Bw, Bk, Bss) present, thickness 1-2 m
4	Strongly developed	Multiple subsurface horizons (e.g. Bw, Bk, Bss) present, thickness > 2 m

Results

Paleosols

Paleosols were categorized into seven pedotypes based on characteristics and horizonation (Fig. 3.5). Subsurface horizons present include Bw, Bg, Bssg, Bss, Bkss, Bk, and C. Paleosol features include slickensides, root traces, carbonate nodules, and meniscate backfilled burrows. Slickensides were the most common pedogenic feature and both master and minor surfaces were present. Fine root traces (mm thick) were more abundant than thicker (cm scale) roots with organic matter preserved. Drab root halos were also present. Carbonate nodules range from 0.25 mm to 70 mm in maximum diameter. Only Stage I pedogenic carbonate development was present. Meniscate backfilled burrows were common in C horizons and very fine to fine sandstone bodies underlying paleosols. Ped structure varied from fine granular to coarse wedge peds.

Paleosol drainage and maturity index values were plotted along each measured section and compared through and between sections (Figs. 3.2 and 3.3). Within the sections, less mature paleosols are commonly associated with sandstone units whereas more mature paleosols are often stacked on each other to form welded paleosols (Figs. 3.2, 3.3, and 3.4). Within and across all sections there are no distinguishable trends in paleosol maturity or drainage (Fig. 3.4). Red to purple paleosols, representing the most well drained paleosols, are distributed throughout each section and do not appear contemporaneously across the sections. The lower, middle, and upper black paleosols, representing poorly drained paleosols are similar ages across sections (Leslie et al., in press); however, the lower and middle black paleosols are not present at Kutz Canyon, and at Escavada Wash, the middle black has multiple members.

Depositional facies

The four sections contain interbedded mudrocks, siltstones, and sandstones that are categorized into seven fluvial facies (*sensu* Miall, 1978, 1985) based on grain size and mechanical and biological structures (Table 3.1). The general floodplain location (proximal or distal) of the deposits was determined by incorporating the pedotype and fluvial facies (Figs. 3.2 and 3.3). The distal floodplain is characterized by relatively thin, massive or thinly laminated sand bodies (Sm and Fh) representing sheet sands or distal portions of crevasse splays (Fig. 3.6A-D). More mature paleosols such as paleo-Vertisols (Fp) and calcareous paleosols (P) containing multiple B horizons are more likely to be found in the distal floodplain due to long periods of non-deposition and landscape stability allowing for continuous weathering (Fig. 3.6A and D). The proximal floodplain is characterized by thicker sand bodies with higher energy bedforms (Sr, St, and Sp) representing channels or proximal portions of crevasse splays (Fig. 3.6A, B, and D).

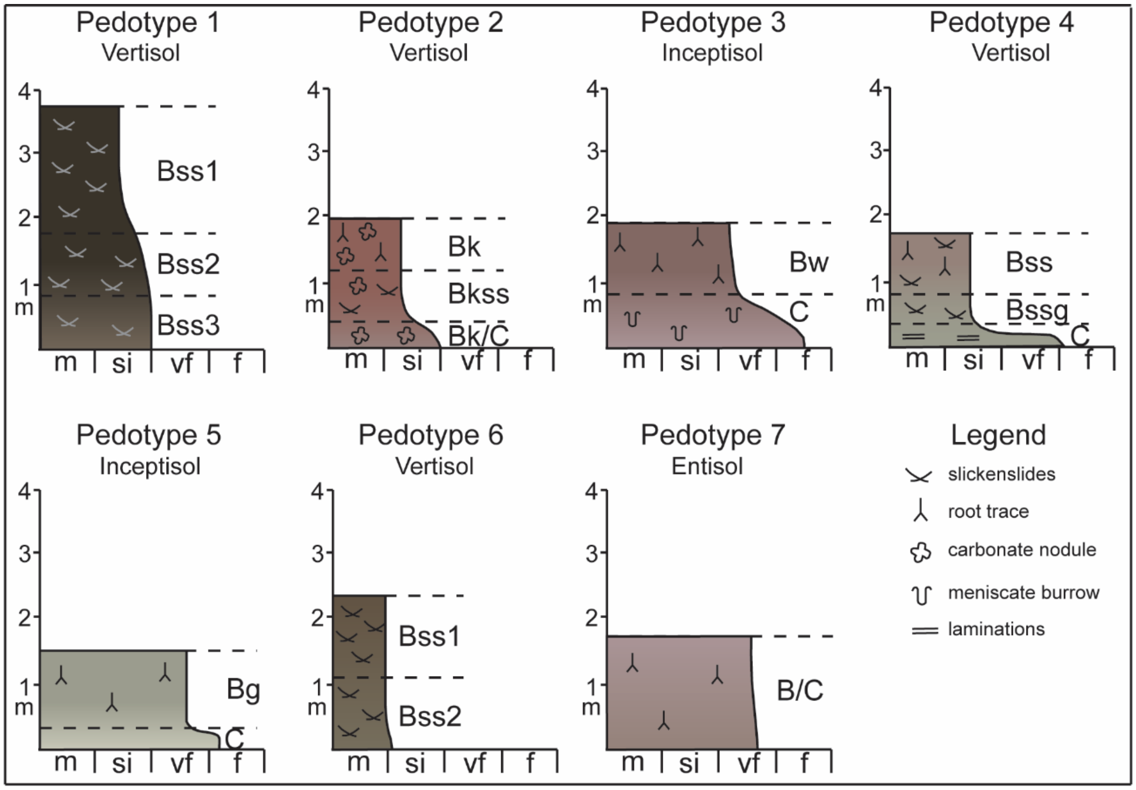

Figure 3.5. Pedotype profiles with interpreted paleosol order. Horizon designations are to the right of each profile. Detailed pedotype descriptions are given in Appendix A.

More weakly-developed soils such as paleo-Inceptisols and Entisols (Fp) are found in the proximal floodplain due to more continual flooding and less weathering.

Kutz Canyon has a higher proportion of proximal floodplain deposits with laterally continuous channel deposits (Figs. 3.2 and 3.6A). Thick (> 4m) sandstone channels composed of Sr and Fh facies are found at the top of both C27r and C27n at Kutz Canyon (Fig. 3.2). Escavada Wash contains approximately an equal distribution of proximal and distal deposits (Figs. 3.2 and 3.6B). Proximal deposits (Sp and Sr) are present at the top of C27r into the base of C27n. Torreon West is more dominated by distal deposits (Fig. 3.3). The proximal deposits are generally finer than the other three sections and contain bedforms indicative of lower flow regime (Figs. 3.3 and 3.6C).

Proximal and distal are present in approximately equal abundance at Torreon East (Fig. 3.3). Proximal floodplain deposits containing Sr and Sp facies are present in both C27r and C27n (Fig. 3.6D). As outlined above, there appears to be no correlation between the presence of distal and proximal floodplain deposits across sections and no section trends toward increased proximal or distal deposits (Fig. 3.4). Calcareous paleosols (P) were present in the lower portion of C27n at Kutz Canyon, the upper portion of C27n at Escavada Wash, through a majority of C27n at Torreon West, and one calcareous paleosol was present near the base of the section in C27r at Torreon East. Well-developed paleosols such as paleo-Vertisols (Fp) are found throughout and across all sections.

Point count analysis

The sandstones contain monocrystalline and polycrystalline quartz (Fig. 3.7A, B, D, and E), feldspar (Fig. 3.7F and E), plutonic rock fragments (Fig. 3.7D), and volcanic rock fragments (Fig. 3.7C and F). Some sandstones also contain calcite cement and/or illuviated clay (Fig. 3.7A and B). The sandstones are classified as feldspathic litharenites and litharenites (Fig. 3.8A). The interpreted provenance is a recycled orogen, with the exception of one sample plotting from a dissected arc (Fig. 3.8B). The samples from the four sections overlap with no discernable trends towards differing composition or provenance across or throughout sections.

Discussion

Applying the DFS model

Weissmann et al. (2010) outlines the major criteria for recognition of DFS deposits in the rock record: 1) a radial pattern of channels from the DFS apex, 2)

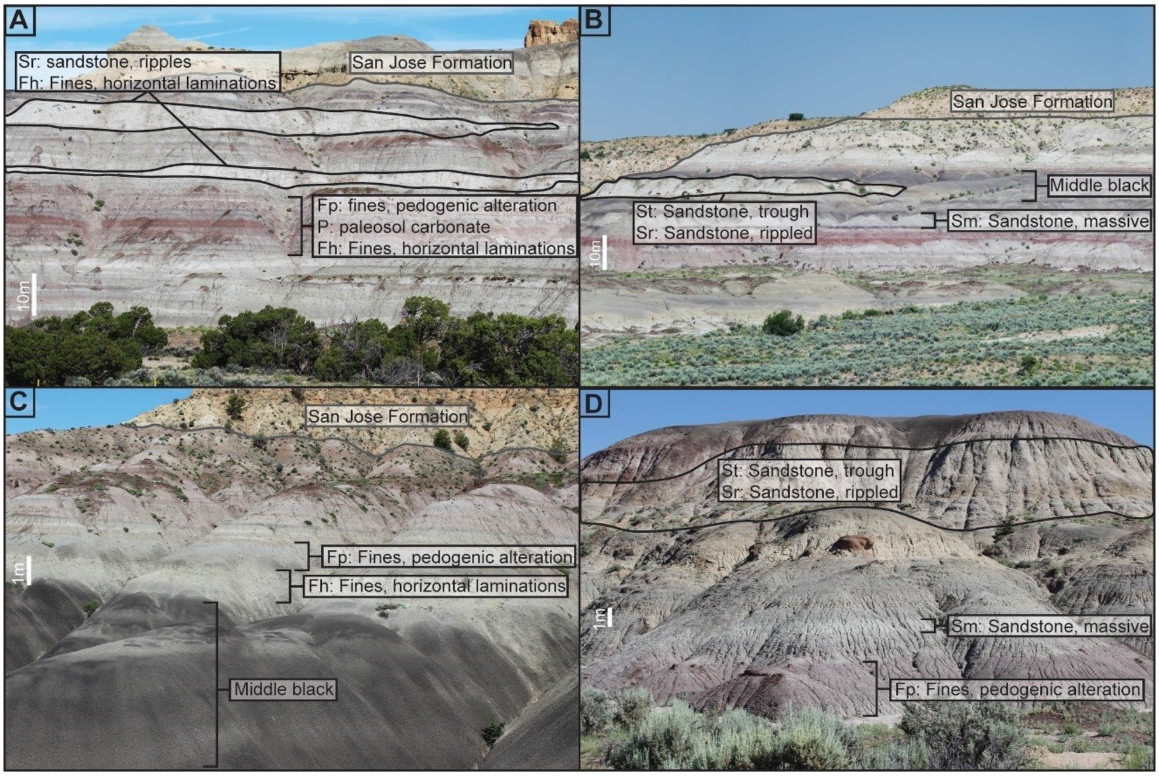

Figure 3.6. Outcrop photos highlighting fluvial facies after Miall (1978, 1985) for A) Kutz Canyon, B) Escavada Wash, C) Torreon West, and D) Torreon East.

common down-DFS channel size decrease, and 3) increased floodplain area/channel area ratios. The Nacimiento Formation exhibits some of these features, supporting the interpretation from Baltz (1967) that the deposits represent a large fluvial fan with its apex to the north. Channel deposits decrease in size and thickness along a general north-south basin transect from Kutz Canyon (Figs. 3.2 and 3.6A) to Torreon East (Figs. 3.3 and 3.6D). Proximal floodplain deposits dominate at Kutz Canyon whereas distal floodplain deposits dominate at Torreon West (Fig. 3.4), indicating floodplain area/channel area ratios increase down the fan. The DFS model can be used to further constrain the spatial distribution of the measured sections on the fan, because the fluvial facies present at each site, and the facies variability between sites, can be compared to those predicted by the DFS model. In the proximal portion of the fan, a high proportion

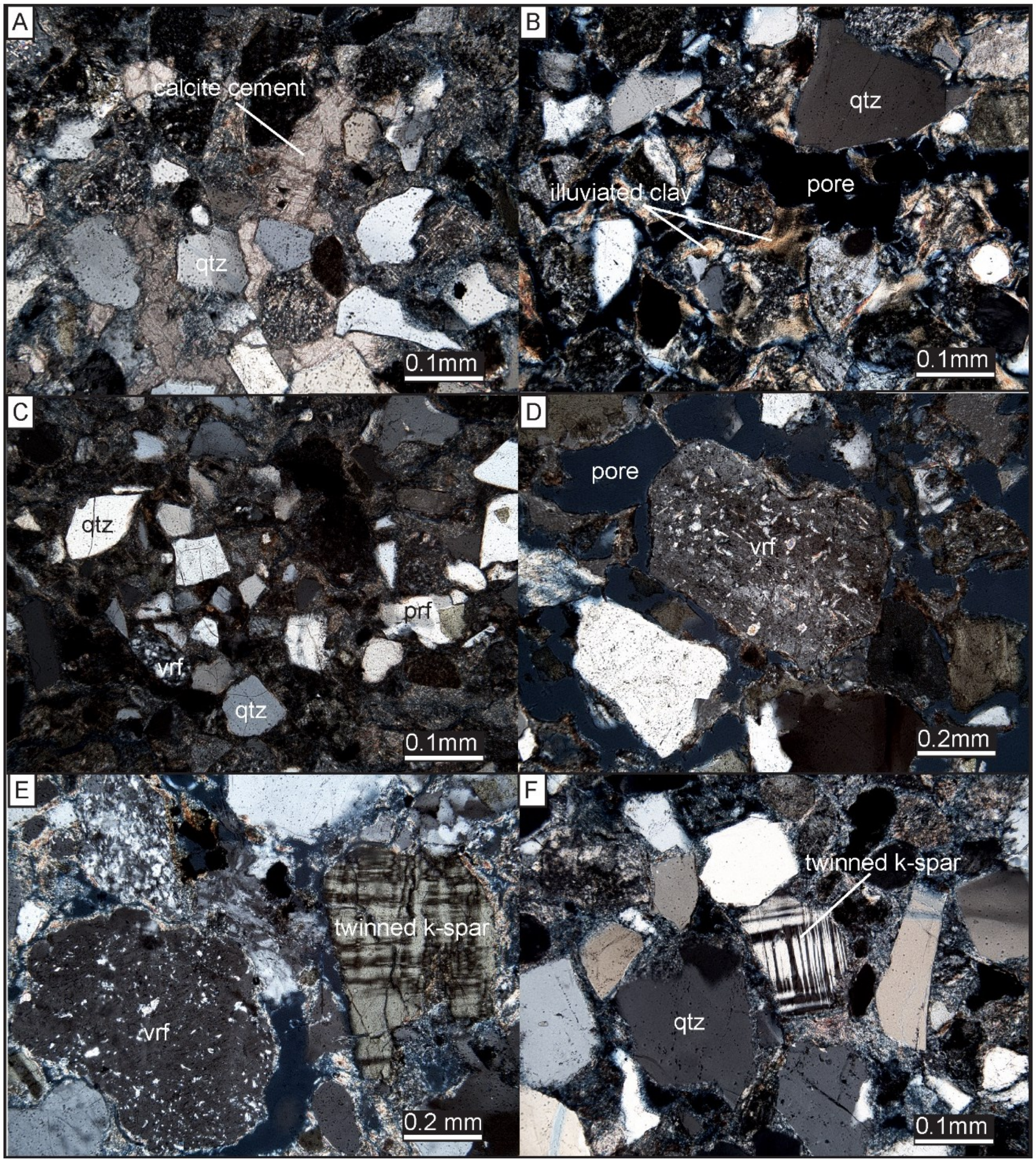

Figure 3.7. XPL photomicrographs of representative samples. See Figures 3 and 4 for location of thin sections within measured sections. A) Sample ESS01 from Torreon East with quartz grains surrounded by calcite cement. B) Sample SS04 from Torreon East with quartz grains and illuviated clay infilling pore spaces. C) Sample WSS19U from Torreon West with quartz grains, volcanic rock fragment, and plutonic rock fragment. D) Sample KSS19 from Kutz Canyon with a volcanic rock fragment surrounded by pore space. E) Sample KSS04 from Kutz Canyon with a volcanic rock fragment and potassium feldspar grain that exhibits microcline twinning. F) Sample VSS11 from Escavada Wash with quartz grains and potassium feldspar grain that exhibits microcline twinning.

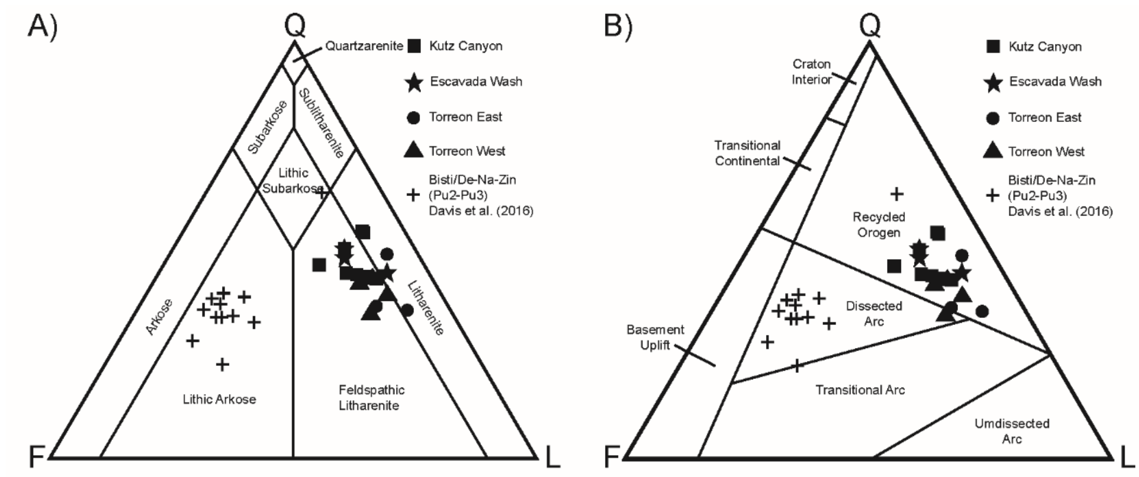

Figure 3.8. A) QFL classification modified from McBride (1963). B) Provenance modified from Dickinson and Suczek (1979). Both diagram use normalized estimations of quartz, feldspar, and lithic fragments. Quartz includes monocrystalline polycrystalline and chert.

of channels and immature sediments are expected (Davidson et al., 2013). In the medial portion of a DFS, the proportion of overbank to channel deposits is expected to increase and grain size decrease. In the distal portion of a DFS, channel are increasingly rare and overbank deposits dominate. Groundwater seeps may also be present.

The Kutz Canyon and Escavada Wash sections are interpreted to represent the medial portion of the DFS and the Torreon West and East sections are interpreted to represent the distal portion of the DFS (Fig. 3.9). Kutz Canyon contains laterally continuous, medium- to coarse-grained channel deposits composed of Sr and Fh facies interpreted to be proximal floodplain deposits (Figs. 3.2 and 3.6A). Intervals of distal floodplain deposits are also present and are characterized by Fh, Fp, and P facies. A variety of pedotypes are present within the P facies but Pedotype 6, a moderately developed and moderately drained Vertisol, is the most common. A higher proportion of proximal floodplain facies with a high density of channels and well-drained soils would be expected if Kutz Canyon was in a proximal portion of the fan. However, given the abundance of proximal deposits, we interpret the Kutz Canyon section to have been the closest section to the proximal portion of the fan and that the proximal portion of the fan must have been located to the north in the Farmington area (Fig. 3.9).

Escavada Wash contains approximately an equal distribution of proximal and distal floodplain deposits (Figs. 3.2 and 3.6B). Proximal deposits are composed of coarse-grained sandstone channels classified as St, Sr, and Fh facies. Distal deposits are dominated by the P and Fp facies, composed of a range of pedotypes including Pedotype 1 (poorly drained Vertisol), Pedotype 2 (calcareous Vertisol), and Pedotype 6 (moderately drained and moderately developed Vertisol). Escavada Wash is also interpreted to be in the medial portion of the fan due to the approximately equal proportion of proximal and distal floodplain deposits and the presence of channels portion of proximal deposits would be expected if this section was located in the proximal portion, and conversely, a higher proportion of finer-grained distal deposits would be expected if this section was located in the distal portion.

Torreon West is interpreted to be located in the distal portion of the fan due to the dominance of distal floodplain deposits (P, Fp, and Fh facies) and the presence of proximal deposits that are generally finer than the other sections and contain lower flow regime bedforms (Fh and Sm) (Figs. 3.3, 3.6C, and 3.9). Pedotype 2 (calcareous Vertisol) and Pedotype 6 (moderately drained and moderately developed Vertisol) are the most common pedotypes within the distal floodplain deposits.

Proximal and distal floodplain deposits are present in approximately equal abundance at Torreon East. The channels within the proximal deposits are composed of fine- to medium-grain sand (St, Sr, and Fh facies) that is finer than those present at

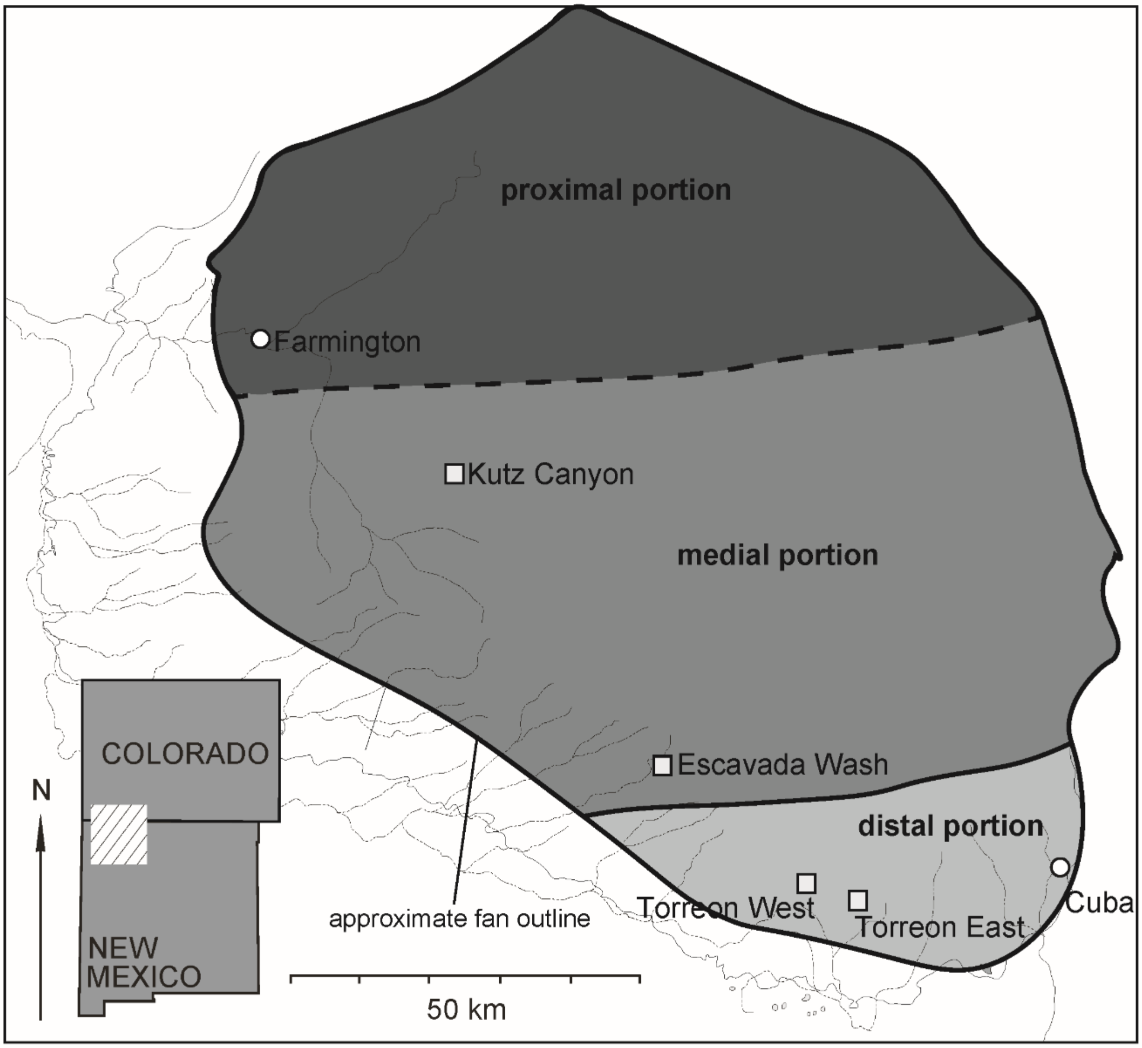

Figure 9. Schematic diagram illustrating the approximate fluvial fan outline for the Nacimiento Formation with the proximal, distal, and medial portions highlighted.

Escavada Wash and Kutz Canyon. As a result, Torreon East is also interpreted to be located within the distal portion of the fan (Fig. 3.9). A higher proportion of coarser-grained proximal deposits would be expected if Torreon East was located in the medial portion of the fan.

The continuous black marker beds at all four sections are interpreted to be poorly drained soils representing groundwater seeps that extended over portions of the basin. These paleosols are similar ages across the sections (Leslie et al., in press), suggesting the basin experienced widespread groundwater seeps. The lack of the lower and middle black at Kutz Canyon suggests a position closer to the apex of the fan where groundwater seeps are not common or later cannibalization of the these paleosols by channels. Based on the interpretation of each section's location within the fan, the proximal portion of the DFS was likely north of the Kutz Canyon section during C27r-C26r (Fig. 3.9).

Following the determination of the location of each section on the fan, the DFS model can be used to test the hypothesis that upper Nacimiento Formation represents a prograding DFS. The presence of paleosol carbonate, lower sediment accumulation rates that are equalized from basin center to basin margin in the upper Nacimiento deposits (Leslie et al., in press), and the overall trend of increasing paleosol drainage from base to top of the Nacimiento Formation suggests progradation and/or aggradation during the early Paleocene. Consequently, we expect to see evidence for the predicted depositional trends of the distributive fluvial system model in the upper portion of the Nacimiento Formation. Overall the sections should coarsen upward and amalgamated channels should be present, and if the entire basin was experiencing progradation of a DFS, we would expect to see the same pattern everywhere. However, the coarsening upwards trend and increased abundance of amalgamated channels is only present in the Kutz Canyon section (Fig. 3.4). Instead, sandstone bodies become less abundant up section in Escavada Wash, and there are no discernable grain size trends at Torreon West and East. We interpret the deposits of the upper Nacimiento Formation record fan aggradation and local autocyclic migration of the fluvial system across the landscape that is different in each location. Thus, the deposits of the upper Nacimiento Formation likely represent the terminal portion of a large-scale DFS and the study interval appears to be too fine a stratigraphic scale to detect progradation of the fan.

Given the evidence that suggest the entire Nacimiento Formation represents a prograding fan, a more complete assessment of the entire Nacimiento Formation, such as, characterizing the features and grain size throughout the entire formation, might be necessary. As outlined above, paleosol drainage increases up section. The Arroyo Chijuillita Member, the oldest member of the Nacimiento Formation, is characterized by drab colored mudstones (Williamson, 1996; Davis et al., 2016) whereas the Ojo Encino Member studied in this paper and overlying Escavada Member (Williamson, 1996) contain red paleosols. Strongly developed soils are documented in the Arroyo Chijuillita Member suggesting maturity does not also increase up section (Davis et al., 2016). The overlying Escavada Member of the Nacimiento Formation contains a higher abundance of sandstone bodies (Williamson, 1996) suggesting an overall coarsening trend in the Nacimiento Formation at the larger scale, which would support progradation of the fluvial system throughout the early Paleocene. However, detailed stratigraphic analyses of the Escavada Member would be needed to test this hypothesis.

Additionally, comparison of point count analysis of sandstones from the Arroyo Chijuillita and Ojo Encino Members presented in this paper suggests sedimentation changes up section in the Nacimiento Formation supporting the interpretation that the entire formation represents a prograding DFS. Point count analysis by Davis et al. (2016) of an outcrop of the lower portion of the Arroyo Chijuillita Member (C29n; 66.2-65.3 Ma) classified the sandstones as lithic arkoses originating from a dissected arc with one exception; the youngest sandstone analyzed was classified as a lithic arkose originating from a recycled orogen (Fig. 3.8). In contrast, point count analysis from the upper Nacimiento Ojo Encino Member (C27r-C26r; 62.9-62.1 Ma) in this paper suggests a higher proportion of lithics with the sandstones classified as feldspathic litharenites and litharenites sourced from a recycled orogen (Fig. 3.8). The change in sandstone provenance through time supports the interpretation that the San Juan Basin was mostly filled by 63 Ma, and sediments were recycled and reworked throughout the basin during deposition of the Ojo Encino Member (Leslie et al., in press). Sediment accumulation rates calculated for the four sections from Leslie et al. (in press) indicate that sedimentation had equalized across the basin from 63-62 Ma. The three-phase subsidence model of Cather (2004) determined a phase of subsidence from ~74-67 Ma generated the accommodation for the subsequent deposition of the Nacimiento Formation. The subsidence generated a steep gradient from which sediments weathered from the uplifts to the north were transported into the basin (Baltz, 1967; Donahue, 2016). We interpret the oldest member of the Nacimiento Formation, the Arroyo Chijuillita Member, to represents deposition of material sourced from outside the basin during this period of high accommodation, supported by the dissected arc origin of the sandstones. Accommodation in the basin decreased with time throughout the early Paleocene so that during the latter part of C27r through early in C26r (~63-62 Ma) there was little accommodation remaining. As a result, the gradient decreased and sediments within the basin were likely recycled and reworked by channels migrating across the landscape supporting the conclusion that the upper Nacimiento deposits record autocyclic migration across the landscape.

Landscape evolution

The lack of trends in the presence of calcareous paleosols across the four sections suggests that the pedogenic carbonate is more likely attributed to landscape position rather than climate, although further work reconstructing paleo-precipitation and temperatures is needed to demonstrate this conclusively (Fig. 3.4). Progradation of the fluvial system during the early Paleocene would have resulted in the upper Nacimiento deposits being located further from the water table than the underlying deposits. As a result, pedogenic carbonate was more likely to be preserved. Pedogenic carbonate is not found in the underlying Arroyo Chijuillita Member of the Nacimiento Formation suggesting the water table may have been higher during this interval. If climate were the driving factor behind the pedogenic carbonate, we would expect to see the carbonate appear at close to the same age in all four sections, which we do not observe. Instead, pedogenic carbonate occurs in different intervals in each section (Fig. 3.4). Additionally, the lack of apparent trends in paleosol drainage also supports this hypothesis. Well drained paleosols, characterized by red to purple colors, are present throughout all four upper Nacimiento sections, with no trends of increasing or decreasing drainage up section. This further supports that landscape position was the controlling factor of pedogenic carbonate preservation and that it varied spatially across the basin during this interval.

Conclusions

We characterized pedotype, paleosol maturity, paleosol drainage, fluvial facies, and floodplain position for four sections of the upper Nacimiento Formation across the San Juan Basin, then applied the DFS model to determine location within the fan and test the hypothesis that the upper Nacimiento Formation records a prograding fluvial system. Kutz Canyon and Escavada Wash represent deposits on the medial portion of the fan based on the abundance of coarse-grained proximal deposits along with the presence of distal deposits dominated by paleosols. Torreon West and East contain finer grained proximal deposits and an abundance of paleosol-dominated distal deposits suggesting sediment accumulation on the distal portion of the fan. This suggests that the proximal portion of the DFS was close to the basin center north of our study area.

Across all four sections, there are no discernable trends in grain size, paleosol maturity, or drainage which does not follow the expected progradational trends of the DFS model. However, the entire Nacimiento Formation may represent a prograding fan as grain size and paleosol drainage increases from the oldest Arroyo Chijuillita Member to the youngest Escavada Member. Petrographic analysis of sandstones lends support to this hypothesis. Previously published point counts from the underlying Arroyo Chijuillita Member indicate input of fresh, extrabasinal material whereas sandstones from the upper Nacimiento Formation indicate sediment recycling as accommodation decreased and sedimentation equalized from basin center to basin margin. Lastly, pedogenic carbonate appearance is diachronous across the four sections suggesting landscape position was the dominant factor in appearance and preservation rather than climate, although more work needs to be done reconstructing the climate over this interval. This work demonstrates the utility of the DFS model for determining location within a fan, but highlights that the time scale examined is an important factor to consider when applying the model.

Acknowledgments

This work was supported by SEPM, National Science Foundation (EAR-132552 to DP and SA), American Chemical Society Petroleum Research Fund (PRF#52822-DN18 to DP), Baylor University Department of Geosciences' Dixon Fund, the Colorado Scientific Society, and the Fort Worth Geological Society. Thanks to T. Leggett, T. Williamson, R. Secord, L. Mace, M. Donahoo, A. Flynn, A. Davis, J. Milligan, and A. Baumgartner for assistance with sample collection and section measuring, and S. Dworkin and S. Driese for assistance with thin section analysis.

CHAPTER FIVE

Conclusions

The Dawson Creek Section of Big Bend National Park correlates to C32n-C31n, C29r, and C27r of the GPTS. The three large hiatuses documented correspond to falling stage and lowstand systems tract terrestrial equivalents, whereas deposition coincides with transgressive and highstand system tract equivalents (Miller et al., 2005) and indicate that eustatic sea level change was the primary depositional driver. Rock magnetic analyses suggest the overprint interval surrounding the K-Pg boundary was likely a result of titanohematite that was reset by burial or overlying basaltic flows. The generated age model indicates the Javelina Formation dinosaur fauna is limited to C29r and equivalent in age to the dinosaur fauna of the Hell Creek Formation in the Northern Great Plains, supporting the hypothesis of dinosaur provinciality in the latest Cretaceous. The mammalian fauna that was previously identified as Puercan by Standhardt (1986) is reidentified as Torrejonian taxa and allows for future mammalian diversity comparisons to other basins. The age constraints also indicate the mid-Maastrichtian and late Maastrichtian greenhouse events documented by Nordt et al. (2003) represent rapid (<200 k.y.) changes in climate during the end-Cretaceous and correlate closely with the marine record.

The four upper Nacimiento Formation sections of the San Juan Basin, Kutz Canyon, Escavada Wash, Torreon West, and Torreon East, correlate to chrons C27r-C26r of the geomagnetic polarity time scale. Rock magnetic analyses indicate that although goethite is the most abundant magnetic mineral, titanohematite and maghemite carry the characteristic remanent magnetization. Calculated sediment accumulation rates near the basin center were similar to those near the basin edge which indicates from late C27r-C26r sediment accumulation rates had equalized across the basin. As a result, deposition of the upper Ojo Encino Member likely occurred during a basin accommodation minimum associated with the progradation of a fluvial system across the basin. Sediment accumulation rates were used to determine the age of Torrejonian 2 – Torrejonian 3 fossil localities at each section and constrain the duration of the Torrejonian 2 – Torrejonian 3 turnover. Findings indicate that the To2-To3 turnover was rapid and occurred over ~120 kyr (-60, +50 kyr) between 62.59 and 62.47 Ma. The rapid nature of this turnover suggests that the presence of an external forcing factor, such as an environmental change driven by the progradation of the distributive fluvial system across the basin and/or changes in regional or global climate.

The pedotype, paleosol maturity, paleosol drainage, fluvial facies, and floodplain position for four sections of the upper Nacimiento Formation across the San Juan Basin was characterized. Following this characterization, the DFS model was applied to determine each sections' location within the fan and test the hypothesis that the upper Nacimiento Formation records a prograding fluvial system. Results indicate Kutz Canyon and Escavada Wash represent medial fan deposits and Torreon West and Torreon East represent distal deposits. Across all four sections, there are no discernable trends in grain size, paleosol maturity, or drainage which does not follow the expected progradational trends of the DFS model and indicate the deposits record fan aggradation and autocyclic migration. However, the entire Nacimiento Formation likely represents a prograding fan as grain size and paleosol drainage increases from base to top. As a result, the sections studied likely document too thin a stratigraphic interval to capture progradation. Previously published petrographic analysis from the underlying Arroyo Chijuillita Member indicate input of fresh, extrabasinal material whereas sandstones from the upper Nacimiento Formation indicate sediment recycling supporting the interpretation that the entire Nacimiento Formation represents a prograding fan with decreasing accommodation up section. The appearance of pedogenic carbonate is diachronous across the four sections signaling landscape position was the dominant factor in appearance and preservation rather than climate.

This work demonstrates the utility of well-constrained age models. High-resolution age constraints allow for calibration of the biotic and climatic records within and between regions and interpretations about the timing of events. Detailed sedimentologic work can be used to assess environmental change. When used in conjunction with each other, they ultimate allow us to better understand the biotic and climatic record in deep time.

APPENDICES

APPENDIX A

Dawson Creek Area Systematic Paleontology

Infraclass METATHERIA Huxley, 1880

Family PERADECTIDAE Trouessart, 1879

Genus PERADECTES Matthew and Granger, 1921

Peradectes sp.

Fig. 1.8A-D

Peratherium sp., Standhardt, 1986, p. 210, fig. 68.

Material.— LSU V-895, right partial M?; and LSU V-705, left m? from TMM locality 42327.

Description.—A small metatherian mammal is represented by a partial upper molar and a lower molar, both from TMM locality 42327(Fig. 1.8A-D). The upper molar fragment, probably an M1 (Fig. 1.8A), consists of a distobuccal fragment of a molar preserving the metacone and the distal portion of the stylar shelf. It lacks any indication of an ectoflexus or a sharp indentation in the buccal margin demarcating the limits of Stylar cusp C on M2s and M3s of that taxon, supporting the conclusion that it represents an M1. M1s and M2s of *P. coproxeches* sometimes bear doubled stylar cusp Cs (Williamson and Taylor, 2011).

The lower molar (LSU V-705; Fig. 1.8B-D) represents either m2 or m3. The apex of the protoconid is damaged, but is larger and evidently would be taller than the metaconid. The paraconid is shorter than the metaconid and projects mesiolingually. The cristid obliqua intersects the distal wall of the trigonid buccal to the protocristid notch. The hypoconid is damaged, missing much of the enamel. The entoconid and hypoconulid are twinned, with the hypoconulid situated near the distolingual margin of the tooth and projecting distally. The entoconid is tall and bladelike. It is larger (length = 1.73; mesial width = 1.00; distal width = 0.99) than corresponding teeth of *Peradectes coprexeches* and falls within the size range of *P. minor* (Clemens, 2006; Williamson et al., 2012).

Remarks.—Unfortunately, there is insufficient material to allow a specific identification of this taxon. *Peradectes* is a wide-ranging genus present in the Puercan, early Paleocene through Eocene of western North America (Williamson et al., 2012).

Order CIMOLESTA McKenna, 1975

Family CIMOLESTIDAE Marsh, 1889

Genus and Species indeterminate

Fig. 1.8E-G

Gelastops sp., Standhardt, 1986, p. 213, fig. 69.

Material.— LSU V-708, left P3; and LSU V-841, partial right M2 from TMM locality 42327.

Description.—A small cimolestid is represented by a complete crown of a poorly preserved and abraded left P3 (LSU V-708; Fig. 1.8E-F) and a partial M2 (LSU V-841; Fig. 1.8G) that includes the mesial and lingual portion of the tooth including part of the paracone and a complete parastylar lobe and the protocone and talon basin.

The P3 (LSU V-708; Fig. 1.8E-F) is triangular in shape in occlusal view (length = 1.95; width = 1.39), with a small parastyle and a lingually-positioned protocone. A small, distinct cusp distal to the protocone, high on the metacrista represents the metacone.

The parastylar lobe of the M2 (LSU V-841; Fig. 1.8G; mesial width = 4.5) is large and projects mesiobuccally, supporting two closely appressed distinct cusps which probably correspond to a parastyle and a stylocone. A significant stylar shelf with a marked ectoflexus was evidently present. The paracristid is low, but sharp. The paracone is conical. The protocone is mesiodistally compressed. The paraconule is situated close to the protocone on the preprotocone crest and is separated from it by a deep notch. A postparaconule crista is absent. A postprotocone crest is straight. Basal cingulae are absent.

Remarks.—Standhardt (1986) referred these specimens to *Gelastops*. However, *Gelastops* is a relatively poorly known taxon and represented by few upper teeth making comparison difficult. For example, the P3 of *Gelastops* remains unknown. We find that the upper molar fragment is essentially indistinguishable from corresponding parts of *Acmeodon secans*, a taxon originally described form the Torrejonian of the Nacimiento Formation, San Juan Basin, New Mexico and which is considered to be close to *Gelastops* (Simpson, 1935). Certain identification is not possible given the fragmentary nature of the tooth. Moreover, the isolated P3 (LSU V-708) resembles that of *Acmeodon*, but differs in that the protocone is smaller and situated directly lingual to the paracone rather than distolingual to it. We are unable to identify these specimens to genus or species.

Cimolestids are usually rare components of Paleocene faunas (e.g., Williamson et al., 2011) that decreased in taxonomic diversity from the Puercan through the Tiffanian of western North America.

Legion CARNIVORAMORPHA Wyss and Flynn, 1993

Family VIVERRAVIDAE Wortman and Matthew, 1899

Genus BRYANICTIS MacIntyre, 1966

Bryanictis new species

Fig. 1.8H-L

Protictis (Bryanictis) terlinguae, Standhardt, 1986, p. 218, figs. 71, 72. [nomen nudum]

Material.— TMM 41400-10, left p4 from TMM locality 41400, and LSU V-709, incomplete P3 from TMM locality 42327.

Description.—A small viverravid carnivoramorph representing a new species of *Bryanictis* is represented by at least two isolated teeth, an incomplete P3 (LSU V-960; Fig. 1.8H-I) from TMM locality 42327 and a p4 (TMM 41400-10; Fig. 1.8J-L) from TMM locality 41400. Standhardt (1986) referred an additional specimen to this taxon consisting of an isolated p2 (LSU V-960). However, this specimen could not be located for this study.

The P3 (LSU V-960; Fig. 1.8H-I; length = 2,38; width = 1.65) is triangular in occlusal view with a large and distally-leaning paracone flanked distally by a smaller metacone. The tooth is encircled by a basal cingulum. A small protocone rises from the lingual cingulum lingual to the paracone.

The p4 (TMM 41400-10; Fig. 1.8J-L; length = 2.38; width = 1.65) is buccolingually narrow with a tall and slightly recurved protoconid, a low, mesially projecting, bladelike paraconid, and a relatively wide talonid. The talonid bears a low hypoconid that is in line with the paraconid and metaconid. A low hypoconulid is positioned distolingual to that line, forming a distolingual wall to a small talonid basin.

Remarks.—The p4 is similar in length, but a bit smaller than that of *Simpsonictis tenuis* and has a relatively more buccolingually expanded talonid. The p4 resembles that of *Intyrictis* from the Torrejonian of the Nacimiento Formation, San Juan Basin, New Mexico in having a relatively low protoconid and wide talonid. However, unlike *Intyrictis*, the Black Peaks carnivoramorph lacks a metaconid.

We refer these specimens to the genus *Bryanictis*, a poorly known taxon represented by two species, *B. microlestes* and *B. paulus* (Gingerich and Winkler, 1985; MacIntyre, 1966; Meehan and Wilson, 2002) from the middle Torrejonian of the Fort Union Formation, Montana and the Nacimiento Formation, New Mexico, respectively, because it shares a broadening of the p4 talonid and lacks a metaconid as is found in *Intyrictis*. The Black Peaks taxon is smaller than either species of *Bryanictis* and undoubtedly represents a new taxon.

The oldest unambiguous carnivoramorphs are Torrejonian in age. Puercan carnivoramorphs have been reported from the Puercan of Saskatchewan, Canada based on isolated teeth. However, we do not find their referral of *Ravenictis* and additional isolated lower molars to Carnivoramorpha to be certain. Regardless, these specimens do not include a P3 or p4 so direct comparison with the Black Peaks taxon is not possible.

The Dawson Creek *Bryanictis* represents a new species and represents among the smallest early Paleocene carnivoramorph. Only the putative Puercan carnivoramorph *Ravenictis krausei* is smaller.

Order Dermoptera Illiger, 1811

Family Mixodectidae Cope, 1883

Genus MIXODECTES Cope, 1883

Mixodectes malaris Cope, 1883

Fig. 1.8M

Indrodon malaris Cope, 1883, p. 60.

Mixodectes malaris Cope, 1883 [see Szalay, 1969 for synonymy]; Rigby, 1980, p. 63, table 16; Taylor, 1984, p. 147, table 10; Standhardt, 1986, p. 222, fig. 73; Williamson, 1996, p. 38.

Material.— LSU V-924, partial left M3; and LSU V-928, partial left M2 from TMM locality 41400.

Description.—The mixodectid *Mixodectes malaris* is represented by two fragmentary upper molars, a partial left M3 (LSU V-924; Fig. 9M) and a partial left M2 (LSU V-928) from TMM locality 41400. Unfortunately, the partial left M2 was not available for this study. The partial left M3 consists of the distal half of the crown. It includes a pronounced mesostyle, metacone, and the distal portion of the protocone and talon basin. The mesostyle is well developed and projects buccally as a blade shaped crest. The protocone is rounded lingually and bordered by a low distal basal cingulum.

Remarks.—The preserved portion of the tooth (distal width = 3.73) is essentially indistinguishable from the M3 of *Mixodectes malaris*, a taxon known from the middle Torrejonian of the Fort Union Formation, Washakie Basin, southern Wyoming (Rigby,

1980) and the Nacimiento Formation, San Juan Basin, New Mexico (Szalay, 1969). *Mixodectes* is easily recognized by its salient mesostyle and *M. malaris* is distinguished from *M. pungens*, which is known only from the late Torrejonian of New Mexico, by its smaller size.

Order PRIMATES Linnaeus, 1758

Family 'PALAECHTHONIDAE' Szalay, 1969

Genus PLESIOLESTES Jepsen, 1930

Plesiolestes nacimienti Wilson and Szalay, 1972

Fig. 1.8N-R

Palaechthon nacimienti Wilson and Szalay, 1972, p. 5, figs. 2-9; Taylor, 1984, p. 164, table 13; Standhardt, 1986, p. 225, fig. 74; Williamson and Lucas, 1993, p. 121, Williamson, 1996, p. 39.

Plesiolestes nacimienti (Wilson and Szalay, 1972). Gunnell, 1989, p. 24; Silcox and Williamson, 2012, p. 810, fig. 4.

Material.— LSU V-921, right P4; TMM 41400-17, left M2; and LSU V-923, right m3 from TMM locality 41400.

Description.—*Plesiolestes nacimienti* is represented by three isolated teeth including a right P4 (LSU V-921; Fig. 1.8N), left M2 (LSU V-923; Fig. 1.8O), and right partial m3 (LSU V-923; Fig. 1.8P-R).

The P4 (LSU V-921; length = 2.18; width = 2.41; Fig. 1.8N) possesses a large paracone, a smaller metacone, and a minute parastyle. The protocone is subequal in size to the paracone and is positioned linguomesially. A preprotocone crest is present, but a distinct postprotocone crest is absent. Conules are absent, but a small, distinct postparaconule crest extends from the preprotocone crest to the lingual base of the paracone.

A left M2 (TMM 41400-17; Fig. 1.8O; length = 2.13; mesial width = 3.41; distal width = 3.13) is relatively poorly preserved and appears to be abraded. The tooth is transverse with subequal and widely-separated paracone and metacone and a small parastyle. The stylar shelf is narrow. The paraconule is positioned near the base of the paracone with short pre- and postparaconular cristae. The metaconule is similarly positioned close to the base of the metacone and small and short pre-and postmetaconular cristae are present. The protocone is large and attended mesially by a basal precingulum that extends buccally to the base of the paraconule. A postprotocingulum extends distally from the apex of the protocone and joins the postcingulum that proceeds buccally to near the base of the metaconule.

The m3 (LSU V-923; mesial width = 1.42; distal width = 1.46; Fig. 1.8P-R) is broken into two fragments: one preserving most of the trigonid and the other preserving most of the talonid. It is incomplete, missing portions of the crown between the two fragments. The trigonid is short and includes the subequal protoconid and metaconid. The metaconid is positioned nearly directly lingual to the protoconid. The paraconid is small and is positioned close and mesial to the metaconid, but is separated from it by a narrow cleft. The mesial edge of the trigonid is bordered by a narrow paracristid. The talonid is wider and much longer than the trigonid. The hypoconid is the largest of the talonid cusps followed by the hypoconulid, which is unfissured, and then the entoconid. The cristid obliqua probably met the trigonid between the protoconid and metaconid. A swelling on the cristid obliqua probably represents a small mesoconid. Buccal and lingual cingulids are not present, but a distinct precingulid extends from the mesial base of the tooth to wrap partway round the buccal side of the protoconid.

Remarks.—The teeth are all similar to those referred to *Plesiolestes nacimienti* from the Nacimiento Formation, San Juan Basin, New Mexico (Wilson and Szalay, 1972; Silcox and Williamson, 2012). We follow Gunnell (1989) in including the species in the genus *Plesiolestes*.

As discussed by Silcox and Williamson (2012), *Plesiolestes nacimienti* is an exceedingly rare taxon in the Nacimiento Formation, San Juan Basin, New Mexico, but appears to have a relatively long stratigraphic ranging, extending from Tj3 to Tj6 (from near the base of chron C27r to at least the middle of chron C27n; see Silcox and Williamson, fig. 14). Gunnell (1989) also assigned two isolated teeth from the North Horn Formation, Dragon Canyon, Utah, to *P. nacimienti*, and at least one of these specimens was collected from near the top of a normal polarity zone correlated with C28n (Tomida and Butler, 1980). Thus, *P. nacimienti* has a stratigraphic range extending through most of the Torrejonian.

Order ‘CONDYLARTHRA’ Cope, 1881b

Family PERIPTYCHIDAE Cope, 1882b

Genus HAPLOCONUS Cope, 1882a

Haploconus sp.

Fig. 1.9A-E

Haploconus inopinatus, Standhardt 1986, p. 248, fig. 82.

Material.— LSU V-710, partial right M1; LSU V-711, partial right M2; and LSU V-835, left m2 from TMM locality 42327.

Description.—The periptychids "condylarth" *Haploconus* is represented by three partial teeth. Two isolated teeth represent a partial M1 (LSU V-710; Fig. 1.9A; length = 3.81*) and a partial M2 (LSU V-711; Fig. 1.9B; length = 3.96) that likely come from a single individual. Both teeth are missing a portion of their crowns, buccal to the apices of the paracones and metacones. They possess the distinctive close convergence of the para- and metacone, protocone, and conules with the protocone and conules being transversely compressed to form a continuous crescentic, cuspidate arc centered on the protocone and a hypertrophied hypocone that extends lingually beyond the base of the protocone. A mesial cingulum terminates lingually in a distinct cusp lingual to the apex of the protocone: the protostyle. Small crests extend between both the bases of the protostyle and the hypocone to the base of the protocone.

A partial fragment of a lower molar (LSU V-835; Fig. 1.9C-E; mesial width = 3.01) preserves the trigonid, mesial to the apices of the metaconid and protoconid. The paraconid is bladelike and projects mesially as is distinctive of *Haploconus*. A strong mesiolingual cingulid is present mesial to the metaconid.

Remarks.—Standhardt (1986) referred these specimens to *Haploconus inopinatus*, a poorly known taxa from the early Torrejonian of the North Horn Formation, Dragon Canyon, Utah, based partly on the presence of a protostyle. However, a protostyle is sometimes present in other species of *Haploconus* including the middle Torrejonian *H. angustus* and *H. corniculatus* from the Nacimiento Formation, San Juan Basin, New Mexico. The Dawson Creek specimens differ significantly from the only Puercan species of *Haploconus*, *H. elachistus* in being larger and having less transverse upper molars and having less transversely-compressed trigon. All three specimens are within the size range of *H. angustus*, but we refrain from making a certain specific identification because of the incomplete nature of the available specimens.

Genus PERIPTYCHUS Cope, 1881a

Periptychus carinidens Cope, 1881a

Fig. 1.9F-H

Periptychus carinidens Cope, 1881a, p. 337 [see Taylor, 1984 for synonymy], Rigby, 1980, p. 111, pl. XIV, figs. 7-9, table 42, Archibald, 1998, p. 312, fig. 20.3c; Williamson and Lucas, 1992, fig. 15i-k; Williamson and Lucas, 1993, p. 125; Williamson, 1996, p. 45.

Periptychus gilmorei Gazin, 1939, p. 272, fig. 3; Archibald, 1998, p. 313.

Carsioptychus coarctatus Standhardt, 1986, p. 243, fig. 81.

Material.— LSU V-888, right m3; LSU V-873, right dentary fragment with partial m?; and LSU V-1554, right partial M? from TMM locality 42327.

Description.—*Periptychus carinidens* is represented by a dentary fragment with a partial and highly abraded lower molar, an isolated partial right upper molar (LSU V-1554), and a nearly complete m3 (LSU V-888; Fig. 1.9G-F; length = 11.91; mesial width = 8.18; distal width = 7.36), all from TMM locality 42327. All fragmentary teeth show highly distinctive apico-basal ridges on tooth margins or on major tooth cusps.

A complete m3 is represented by LSU V-888 (Fig. 1.9G-F). It is approximately rectangular in occlusal view. The talonid is slightly narrower than the trigonid and the tooth narrows distally to a rounded distal margin. The occlusal surface is highly worn through attrition, so that it is nearly flat, with the apices of all cusps removed, exposing the interior dentin. The trigonid occupies the mesial half of the tooth. It is only slightly elevated compared to the talonid. The protoconid is the largest cusp, followed by the metaconid. The metaconid is well separated from the protoconid. The paraconid is positioned mesiobuccal to the metaconid. The paracristid is weak and indistinct. A strong crest descends from the lingual side of the paracristid and curves lingodistally to the mesiolingual base of the metaconid. The postcristid is weak and V-shaped, with the legs of the V spreading mesially to attach to the distal sides of the metaconid and protoconid. The apex of the V represents the protocristid notch. The talonid supports three cuspids, the hypoconid, hypoconulid, and entoconid. The cuspids are approximately conical and well-separated. The hypoconulid and entoconid are subequal, the hypoconulid is larger and positioned near the midline of the tooth and at the distal margin. The cristid oblique extends nearly mesially from the hypoconid to the protocristid notch. A continuous crest connects the hypoconid and hypoconulid. A crest between the hypoconulid and entoconid is thin and notched midway between the two cusps. A crest also connects the metaconid and the entoconid. A swelling is present below this crest midway between the two cuspids. An ectocingulid is present between the buccal face of the protoconid and the distal margin of the hypoconulid. It consists of an irregular, cuspidate ridge. A short cuspidate ridge is also present on the lingual side of the tooth between the lingual sides of the hypoconulid and the entoconid (remnants of a lingual cingulid). A weaker cristid, with single notch, extends along a line drawn between the centers of the hypoconulid and entoconid. A strong crenulated ridge also connects the entoconid and metaconid. The perimeter of the tooth is marked by strong apicobasal plications that originate near the base of the major cusps. The enamel at the base of the tooth is crenulated with fine, apicobasally-aligned ridges around the entire basal margin of the tooth.

Remarks.—Standhardt (1986) originally identified this specimen as the Puercan taxon *Carsioptychus coarctatus*. However, we find that the fragmentary teeth are probably not certainly identifiable. The m3 (LSU V-888) however, can be confidently referred to *P. carinidens*. It is larger than the m3 of *C. coarctatus* and falls within the size range of *P. carinidens* from the Nacimiento Formation, San Juan Basin. It also resembles *P. carinidens* and differs from *C. coarctatus* in the following features: 1) the talonid is relatively longer and more rectangular in shape as seen in occlusal view with an enlarged and distally extended hypoconulid 2) the trigonid is lower relative to the talonid 3) the apices of the primary molar cusps are not strongly convergent as in *C. coarctatus*, but are generally erect as in *P. carinidens* 4) the postcristid is V-shaped, rather than straight and 5) segments of the buccal and lingual cingulids are strongly developed.

Schiebout (1974) tentatively considered all the *Periptychus* specimens from the Big Bend National Park then known to be referable to *P. superstes*. The m3 (LSU V-888) differs from that of *Periptychus superstes* in having a relatively smaller and shorter talonid with a less-expanded hypoconulid.

Periptychus carinidens is an index taxon for the Torrejonian Land Mammal Age (Lofgren et al., 2004) and the first appearance of *P. carinidens* is used to define the base of the Torrejonian.

Family MIOCLAENIDAE Osborn and Earle, 1895

Genus PROMIOCLAENUS Trouessart, 1904

Promioclaenus cf. *P. lemuroides* Matthew, 1897

Fig. 1.9I-J

Promioclaenus sp., Standhardt, 1986, p. 256, fig. 84.

Ellipsodon priscus in part, Standhardt, 1986, (in part) p. 251, fig. 83a.

Material.— LSU V-875, right P3; and LSU V-920, partial left M3 from TMM locality 41400.

Description.—An isolated P3 (LSU V-875; Fig. 1.9I; length = 3.28; width = 2.48) approximates a triangle with rounded apices in occlusal view with a large, central, and swollen paracone. A small parastyle is located mesially and a metastyle is present distally. A basal cingulum is not continuous around the entire margin of the tooth, but is absent from mesiolingual side of the tooth, and is discontinuous along its buccal margin.

A basal cingulum is accentuated near the lingual apex of the tooth, where it forms a low elongate ridge, representing an incipient protocone. The basal cingulum becomes more pronounced as it approaches the para- and metastyles. A ridge rises from the parastyle at the mesial side of the paracone. It is convex in buccal view. The lingodistal face of the paracone is flat to concave and recessed between ridges that ascent to the apex of the paracone from the protocone and metastyle.

A partial M3 (LSU V-920; Fig. 1.9J) is complete, but for the mesiobuccal, or parastylar, region and the distobuccal corners of the crown. The enamel surface is crenulated. The tooth is approximately oval in occlusal view with a large paracone. The metacone is missing, but it is clear that the tooth decreased in transverse width distally. A large protocone dominates the lingual side of the tooth. A paraconule is present approximately midway between the paracone and protocone. A short postparaconule crista extends from the paraconule to the lingual base of the paracone. The metaconule is circular and a premetaconular crista extends to near the lingual base of the metacone. A post protocingulum extends from the apex of the protocone to a postcingulum. A week and irregular precingulum is also present.

Remarks.—*Promioclaenus* spans the Torrejonian and is widely geographically distributed in western North America where it is represented by several species. The specimens from Dawson Creek are close in size to *P. lemuroides*. However, because of their incomplete nature, they are only tentatively referred to that species.

Genus MIOCLAENUS Cope, 1881d

Mioclaenus new species.

Fig. 1.9K-U

Nexus plexus, Standhardt, 1986, p. 258, fig. 85. [nomen nudum]

Material.— LSU V-890, left M2; LSU V-891, left M1; LSU V-833, left P4; LSU V-703, right partial dentary with erupting m2; LSU V-839, V-840, partial right m2; and LSU V-881, left m3 from TMM locality 42327.

Description.—A small mioclaenid “condylarth” represents a new species of *Mioclaenus, M. lehmani*, which represents, the most complete taxon reported from TMM locality 42327.

An isolated, and poorly preserved P4 (LSU V-833; Fig. 1.9K-L; length = 4.49; width = 5.18) is highly pitted and discolored by weathering, but the salient features are readily visible. It is approximately triangular in occlusal view with a highly inflated and subequal paracone and protocone. A small parastyle is present mesial to the paracone and a distinct separate swelling distal to the paracone represents a metacone. A distinct metaconule is present between near the distal margin of the tooth, approximately midway between the protocone and paracone. Both a mesial and a distal cingulum is present, but these do not meet lingually. An ectocingulum appears to be absent.

An isolated M1 (LSU V-891; Fig. 1.9M-N; length = 4.62; mesial width = 5.91; distal width = 5.76), is well-preserved and relatively unworn. A portion of enamel is missing from the distal margin of the tooth, distal to the protocone. The tooth is roughly rectangular in shape, with subequal and widely spaced paracone and metacone and a large and inflated protocone. The surface of the enamel is smoothly-wrinkled, most evident over the wide and rounded lingual face of the protocone. The paraconule is indistinct and positioned approximately midway between the paracone and protocone and is mesial to a line drawn between the two cusps. A short preparaconule crista is short and not contiguous with a strong precingulum that extends from the mesial side of the protocone to the parastyle. A short, but strong postparaconule crista extends bucally from the paraconule to the base of the paracone. A weak preparacrista connects the paracone and a small, but prominent parastyle, which is situated mesial and slightly buccal to the paracone. The metaconule is relatively larger than the paraconule. A thick and short premetaconule crista descends mesiobuccally towards the center of the trigon basin. Narrow and deep clefts delimit the metaconule lingually and buccally, separating the cusp from the protocone and metacone, respectively. Between the paracone and metacone is a slightly V-shaped centrocrista. It approaches, but does not intersect, the ectocingulum which forms a strong border close to the bases of the paracone and metacone. A strong postcingulum extends from midway up the distal side of the protocone (it is positioned closer to the apex of the protocone than is the precingulum) to the distobuccal corner of the tooth where it becomes confluent with the ectocingulum. A weak metacrista descends from the distal face of the metacone to the postcingulum. No hypocone is present.

An isolated left M2 (LSU V-890; Fig. 1.9O-P; length = 4.52; mesial width = 6.32; distal width = 5.74), resembles the M1 (LSU V-891), but is relatively wider (transversely) with a relatively large paracone and metacone and the tooth narrows distally so that the buccal margin of the tooth is obliquely angled relative to the anterior margin of the tooth. As in the M1, the centrocrista is V-shaped, but does not meet the ectocingulum. The ectocingulum is thickened between the metacone and paracone and terminates at the buccal face of the metacone. A distinct mesostyle is absent.

Lower teeth are represented only by three specimens; LSU V-703, a partial right dentary with an erupting m2, LSU V-839 (Fig. 1.9Q-R), LSU V-840, a partial right m2, and LSU V-881 (Fig. 1.9S-U), a left m3. The m2 (LSU V-703; Fig. 1.9Q-R) is erupting from the crypt and virtually unworn. The low, large, and inflated protoconid and metaconid are subequal in size and oriented approximately side-by-side in a transverse line. The metaconid is somewhat larger and higher than the protoconid. The paraconid is small, but distinct and closely appressed to the mesiobuccal face of the metaconid. A curved paracristid connects the protoconid and paracristid. A weak, straight protocristid connects the metaconid and protoconid. The talonid is subequal in size (both length and width) to the trigonid. The hypoconid is the largest and most distinct of the talonid cusps. The cristid obliqua is straight and intersects the postcristid below the protocristid notch. The distal and lingual wall of the talonid is formed by a continuous curved crest that extends from the hypoconid to a position at the distolingual base of the metaconid. A short postmetaconid crest is separate and distinct from the lingual wall of the talonid. A small cuspid on this crest at the distal midline appears to represent the hypoconulid. There is no distinct entoconid. The talonid basin is shallow and a low crest descends into it from the lingual side of the hypoconid.

An isolated m3 (LSU V-881; Fig. 1.9S-U; length = 5.18; mesial width = 3.36; distal width = 2.85), is similar to the m2 (LSU V-703). The trigonid is essentially identical to that of the m2, but the m3 possesses minor attritional wear on the protoconid and metaconid. The talonid is mesiodistally elongated and significantly longer than the trigonid. It narrows distally. The hypoconid is a prominent cusp and the only distinct cusp present on the talonid. The cristid extending from the hypoconid distally and enclosing the talonid lingually is weakly cuspidae, though no distinct hypoconulid or entoconid is visible. As in the m2, a low crest descends mesiolingually from the hypoconid into the talonid basin. A mesial cingulid is present. A short and weak postcingulid is present distal to the hypoconid on the buccal side of the tooth and two small cusps are present within the hypoflexid.

Remarks.—The P4 of *Mioclaenus* new species (Fig. 1.9K-L) resembles that of *Mioclaenus turgidus* in the relative size and shape and positioning of most of the cusps. It differs from *Mioclaenus turgidus* in having less inflated cusps and a larger, more mesially-positioned metacone. The P4 metacone is variable in *M. turgidus*, and it varies from being a small cusp at the distal margin of the tooth at the base of the paracone, to a small distinct cusp, part-way up the distal slope of the paracone, mesial to, and distinct from, a distal cingulum (e.g., NMMNH P-15988), and the presence of a distal cingulum is also variable. However, in no specimens of *M. turgidus* is the P4 metacone as large, relative to the paracone, as it is in LSU V-833.

The M1-2 of the *Mioclaenus* new species (Fig. 1.9M-P) closely resemble those of *M. turgidus*, although they are smaller in size and have less inflated cusps. The upper molars of *M. turgidus* sometimes possesses a centrocrista between the paracone and metacone that sometimes bears a strong and distinct mesostyle or forms an acute V-shape that, in some specimens, intersects the ectocingulum. The M1 of *M. turgidus* also usually bears a small hypocone on the postcingulum, distal to the apex of the protocone. The M2 is very similar in morphology to that of *M. turgidus*. The metacone is similarly small relative to the paracone and the tooth declines in width distally. This suggests that the M3 of the *Mioclaenus* new species is similarly small in size relative to the other molars.

The lower molars of *Mioclaenus* new species (Fig. 1.9Q-U) are also similar to those of *M. turgidus*. Differences are: 1) The cusps in the *M.* new species but the cusps are less inflated; 2) the lower molars of *M. turgidus* similarly possess more pronounced cusps of the distal and lingual walls of the talonid; 3) the cristid obliqua of *M. turgidus* intersects the trigonid below the apex of the protoconid rather than at the more lingual position, below the protocristid notch in the Big Bend species; 4) in *M. turgidus*, there is not a distinct crest entering the talonid basin from the hypoconid as there is in the Big Bend species, thought the m3 talonid of *M. turgidus* sometimes bears a distinct and isolated cusp within the basin; 5) some specimens of *M. turgidus* sometimes possess a weak, discontinuous, and cuspidae buccal cingulid; and 6) the m2 of *M. turgidus* typically possesses an enlarged basal buttress over the root that extends mesially from the mesiolingual corner of the tooth.

Mioclaenus turgidus is a relatively common taxon in the Torrejonian of the Nacimiento Formation, San Juan Basin, New Mexico, but has only been reported from one other area; the latest Torrejonian or early Tiffanian Grayson Ridge fauna of the Hanna Formation, Carbon Basin, Wyoming (Secord, 1998). This report, therefore documents a southern geographic range extension for the genus *Mioclaenus*.

Genus ELLIPSODON Scott, 1892

Ellipsodon cf. *E. inaequidens* Cope, 1884

Fig. 1.9V-Z

Ellipsodon priscus, Standhardt, 1986, p. 251, (in part), fig. 83B-H.

Material.— LSU V-706, left M1; and LSU V-701, right m1 from TMM locality 42327.

Description.—*Ellipsodon inaequidens* is represented by two teeth; a left M1 (LSU V-706; Fig. 1.9V-W), and a right m1 (LSU V-701; Fig. 1.9X-Z).

The left M1 (LSU V-706; Fig. 1.9V-W; length = 3.70; mesial width = 4.85; distal width = 4.85) in occlusal view resembles an isosceles triangular with rounded apices. The tooth is inflated and dominated by a large protocone and smaller, round and subequal para- and metacones. A small parastyle is present mesial and closely appressed to the paracone. A distinct metaconule as well as pre- and postmetaconule cristae are absent. Instead, a postprotocrista extends directly to the metacone as a notched crest. In contrast, a large and circular paraconule is present, positioned approximately midway between the protocone and paracone, and offset mesially from a line drawn between the two cusps. The preprotocrista terminates at the paraconule. The postparaconule crista is short and the paraconule and paracone are divided by a deep cleft mesially. A week preparaconular crista curves distally and buccally and attaches to the lingual face of the paracone. Mesially, a precingulum extends from the distal side of the protocone and extends buccally and uninterrupted to the a distinct parastyle which is closely appressed to the mesial base of the paracone. A strong postcingulum extends from the distal side of the protocone to the distal base of the metacone. A hypocone is absent, though a low ridge descends from the apex of the protocone to the postcingulum. The postcingulum is higher on the protocone than the precingulum. A distinct metastyle is also absent. A paracrista is weak and directed nearly mesially. The centrocrista are straight. A short, but sharp metacrsita descends buccal to the metastyle. An ectocingulum is absent, but for a low remnant that forms a small, distinct cusp, a mesostyle, nestled between the buccal basal margins of the para- and metacones.

The occlusal surface is somewhat worn through attrition so that the apices of all the major cusps (i.e., para- and metacones, protocone, and metastyle) bear flat and circular wear facets exposing dentin bordered by relatively thick enamel. The surface of the tooth is nearly smooth with low, coarse, wavy, and apicobassaly-aligned ridges.

A right m1 (LSU V-701; Fig. 1.9X-Z; length = 3.67; mesial width = 3.1; distal width = 3.15) is approximately rectangular in occlusal view and highly inflated and rounded. The metaconid is the largest cusp and it is swollen and broadly convex over its lingual surface. It is subequal in preserved height to the protocone, which is positioned mesial and buccal to the metacone. The two cusps are strongly conjoined at their bases and their apices are positioned close together but they are separated apically by a low and sharp, mesiodistally-aligned cleft continuous with the protocristid notch. The protocristid is low and indistinct. A low and circular paraconid is positioned mesial to the apex of the metacone, but because the metacone is highly inflated, the apex of the paraconid is well-removed from the lingual margin of the tooth. A distinct paracristid curves mesiolingually from the protoconid and is separated from the paraconid by a sharp notch. A narrow crest descends from the metaconid to the paraconid. The talonid is subequal in width to the trigonid, but shorter, occupying only about one third the length of the tooth.

Only two distinct cusps can be discerned, the hypoconid and entoconid. The hypoconid is the larger of the two and it occupies the distobuccal corner of the tooth. The cristid oblique extends diagonally from the hypoconid to the apex of the metaconid, lingual to the protocristid notch. A deep hypoflexid separated the hypoconid from the protoconid and a distinct notch is present in the cristid oblique at the base of the trigonid. The entoconid is positioned at the lingual side of the trigonid, opposite the hypoconid. It is smaller and lower than the hypoconid. The distal side of the talonid is bordered by a low and curved crest which connects the hypoconid and entoconid. No distinct cuspids can be discerned within this crest. The talonid basin is smooth and concave marked only by a low ridge extending mesially and lingually from the apex of the hypoconid. A narrow and sharp postmetacristid descends from the distal side of the metaconid and it meets a short entocristid to close off the lingual side of the talonid basin. A small sharp notch marks the intersection of the two cristids. The major cusps of the tooth (i.e., metaconid, protoconid, and hypoconid) have apical wear similar to what is present in the M1 (LSU V-706). The tooth has a similar surface ornamentation with weak, coarse, and wavy ridges that are apicobasally-aligned.

Remarks.—Standhardt (1986) originally referred these specimens to the *Ellipsodon priscus,* a taxon known with certainty only from the Puercan of the Nacimiento Formation, San Juan Basin, New Mexico (Williamson and Carr, 2007). Van Valen (1978) erected the genus *Bomburia* for “*E*.” *priscus*. However, because the name *Bomburia* was later found to be preoccupied, a new name, *Bomburodon*, was subsequently proposed as a replacement (Williamson and Carr, 2012). Regardless, the Big Bend specimens differ markedly from *B. priscus* and closely resemble species of

Ellipsodon. The upper teeth of *Bomburodon* are unknown with certainty, but are likely represented by teeth referred to *Platymastus palantir* Van Valen, 1978, a probable subjective junior synonym of *B. priscus* (Williamson and Carr, 2007). Upper molars of *P. palantir* differ from the M1 (LSU V-706) of the Big Bend species in a number of prominent features such as presence of an ectocingulum, presence of a metaconule, and presence of a distinct hypocone. Lower molars of *B. priscus* differ from the m1 of the Big Bend taxon in being distinctly less inflated and having a relatively larger talonid. In addition, the relative positions of the talonid cusps of m1 and m2 differ between genera. In Bomburia, the metaconid is nearly directly lingual to the protoconid, but in *Ellipsodon*, the metaconid is positioned distal to the protoconid, a condition considered to be an autapomorphy for *Ellipsodon* by Williamson and Carr (2007).

The two teeth are here tentatively referred to the middle Torrejonian *E. inaequidens*. The M1 (LSU V-706) lacks an ectocingulum, but for a small area that forms a small mesostyle between the para-and metacones, a feature considered to be one of the diagnostic characters of *Ellipsodon* (Williamson and Carr, 2007). The m1 (LSU V-701) is also similar to that of *Ellipsodon* in being similarly inflated with a distally positioned metaconid (Williamson and Carr, 2007). Williamson and Carr (2007) recognized three species of *Ellipsodon*, *E. inaequidens* (Cope, 1884), *E. granger* (Wilson, 1956), and *E. yotankae* (Van Valen, 1978) which are distinguished by size, the relative proportions of upper molar length and width, and the relative width of the lower molar talonids (Williamson and Carr, 2007). The Big Bend taxon most closely resembles *E. inaequidens*, although both specimens fall below the size range of specimens known from the Nacimiento Formation of New Mexico. *Ellipsodon inaequidens* is extremely rare in the Nacimiento Formation, and m1 measurements are known for only two to three specimens that preserve m1. In measurements of length and width (MW and DW), Big Bend specimens are less than 11% smaller than those documented from the Nacimiento Formation. In addition, the Big Bend taxon differs from other specimens of *Ellipsodon* in that the M1 (LSU V-706) lacks a metaconule, and a metaconule is present on all other known specimens of *E. inaequidens* that preserve a relatively unworn M1, though for some specimens, it is small and relatively indistinct (e.g., NMMNH P-20680, Fig. G.2).

Standhardt referred an isolated tooth that she identified as a right P3 (LSU V-875) to "*E.*" *priscus*. This specimen does not closely resemble premolars of *Bomburodon priscus* or *Ellipsodon inaequidens*. Among other differences, LSU V-875 lacks a distinct protocone and large parastyle that is present in *B. priscus* and does not possess the distinctive, broadly convex occlusal surface mesial and lingual to the paracone and shallowly concave distally as in *E. inaequidens* (Williamson and Carr, 2007). It is tentatively referred to *Promioclaenus* sp. (below).

Family 'TRIISODONTIDAE' Scott, 1892

Genus GONIACODON Cope, 1888

cf. *Goniacodon levisanus* Cope, 1883

Fig. 1.9AA-BB

Eoconodon sp., Standhardt, 1986, p. 238, fig. 84.

Material.— LSU V-704, left M3 from TMM locality 42327.

Description.—An isolated left M3, LSU V-704 (Fig. 1.9AA-BB) is an approximately oval occlusal outline (length = 4.71; mesial width = 7.30; distal width = 5.81). The enamel surface is rugose. The paracone and metacone are conical and the metacone is smaller than the paracone corresponding to a transverse narrowing of the tooth distally. The cones are widely separated, but connected by a straight centrocrista. The paracrista and metacrista are straight and in line with the centrocrista. The buccal margin of the tooth is bordered by a narrow ectocingulum that borders a relatively wide stylar region. The parastylar region is broadly rounded in occlusal view and there is a slight ectoflexus between the para- and metastylar regions. The protocone is large and erect with strong pre- and postprotocristae. The paraconule is situated approximately midway between the metacone and protocone and is represented by an elongate expansion along the preprotocrista with at least two swellings. The premetaconule crista continues in a straight line to the mesiobuccal corner of the tooth. A postparaconule crista is lacking. The metaconule is situated on the postprotocrista. A premetaconule crista is lacking. The postmetaconule crista continues to the distal margin of the tooth where it joins a postcingulum distal to the metacone. The pre- and postcingulum are strong and wrap around the lingual base of the protocone to form a continuous lingual cingulum. The precingulum terminates buccally below and mesial to the paracone without joining the preparaconule crista.

Remarks.—Standhardt (1986) referred this tooth to the “triisodontid” “condylarth” *Eoconodon*, a taxon known only from the Puercan of western North America. However, it differs from the M3 described for any *Eoconodon* species, where known. It is too small to be referable to *E. coryphaeus*. It is closest in size to *E. gaudrianus*, which is poorly known and represented by only two M3s (e.g., AMNH 3200 and NMMNH P-72366) and differs in having a relatively larger stylar shelf. All other *Eoconodon* species are too small to be conspecific (see Clemens and Williamson, 2005; Clemens, 2011).

The tooth probably represents a "triisodontid" based on the rugose enamel texture, the large conical paracone and metacone that appear to be partially merged at their base and the alignment of their associated crests. It closely resembles the M3 of the Torrejonian "triisodontid" "condylarth" *Goniacodon levisanus*. *G. levisanus* is relatively rare and poorly known taxon and the M3 is represented by only a few specimens (e.g., NMMNH P-21906, 59393), some of which are incomplete (e.g., NMMNH P-59393). However, these are similar in size and morphology to LSU V-704, with a similar rugose enamel surface, and large, conical paracone and metacone. However, it differs somewhat from the specimens on hand to make comparison. The M3 of NMMNH P-21906 lacks a lingual cingulum. Both NMMNH P-21906 and 59393 have a paracone and metacone that are more closely appressed more completely conjoined at their base and have a narrower stylar region, without an extoflexus. Based on the similarities and differences, we can only tentatively refer LSU V-704 to *Goniacodon levisanus*.

The genus *Goniacodon* ranges from the late Puercan to the early Tiffanian of western North America. The species *G. levisanus* is restricted to the middle Torrejonian to early Tiffanian of New Mexico, Wyoming, and Montana.

Genus TRIISODON Cope, 1881c

Triisodon quivirensis Cope, 1881c

Fig. A1

Triisodon quivirensis Cope, 1881c, p. 485; Van Valen, 1978, p. 58; Williamson and Lucas, 1993, p. 123; Williamson, 1996, p. 41.

Triisodon antiquus Cope, 1882, p. 193 [see Taylor, 1984 for synonymy]; Tomida, 1981, p. 230, pl. 10.2, figs 1-2.

Eoconodon coryphaeus Standhardt, 1986, p. 232, fig. 77.

Material.— LSU V-1156, partial right M2; and LSU V-1157, partial left m1 or m2 from LSU locality VL-107.

Description.—The taxon *Triisodon quivirensis* is represented by fragments of two teeth (Fig. A1), portions of a dentary, and postcranial fragments. These were found in close association and likely represent a single individual. However, some of the individual fragments were given different specimen numbers.

A portion of a right M2, LSU V-1156 (Fig. A1A-B), includes the occlusal surface of the protocone. It is weathered through attritional wear so that the apex of the protocone is beveled. The preparaconule crista is similarly positioned, the precingulum, the base of the metaconule is expanded distally and separated from the distal face of the protocone by a groove, the postcingulum ascends the distal face of the protocone and is at a similar position, though a hypocone is more developed in V-1156 and in that specimen, the postcingulum does not extend lingually past the hypocone. In V-1156, remnants of the original surface texture are present adjacent to the postcingulum and are similarly rogues and pebbly.

LSU V-1157 is a partial left m1 or m2 (Fig. A1E-F). The tooth is more heavily worn, but the distinctive cleft separating the metaconid and protoconid is present. The paracristid on the mesial face of the protoconid projects mesially. The cusps are of similar size and exhibit a similar pebbly enamel surface texture.

Remarks.—Standhardt (1986) referred fragments of an edentulous left dentary with tooth roots (LSU V-1158) and postcranial fragments consisting of a right proximal radius (LSU V-1151), and a right femoral head (LSU V-1159) to "*Eoconodon coryphaeus*" (Table DR1). However, the dentary fragments exceed the depth of the dentary of any specimen of *E. coryphaeus* and closely match those of mature representatives of *T. quivirensis* from the Nacimiento Formation (e.g., NMMNH P-2676, 21982 and 44608) and is consistent with an identification of T. quivirensis for the other specimens from this locality.

This report of *Triisodon quivirensis* from the Big Bend National Park represents the first from outside of the San Juan Basin, New Mexico. *T. quivirensis* is restricted to the early and middle Torrejonian (To1-To2) of the Nacimiento Formation, San Juan Basin, New Mexico (*Periptychus carinidens – Protoselene opisthacus* zone [Tj1] through *Arctocyon ferox – Mixodectes pungens* zone [Tj5] and thus this represents a significant geographic range extension for this taxon.

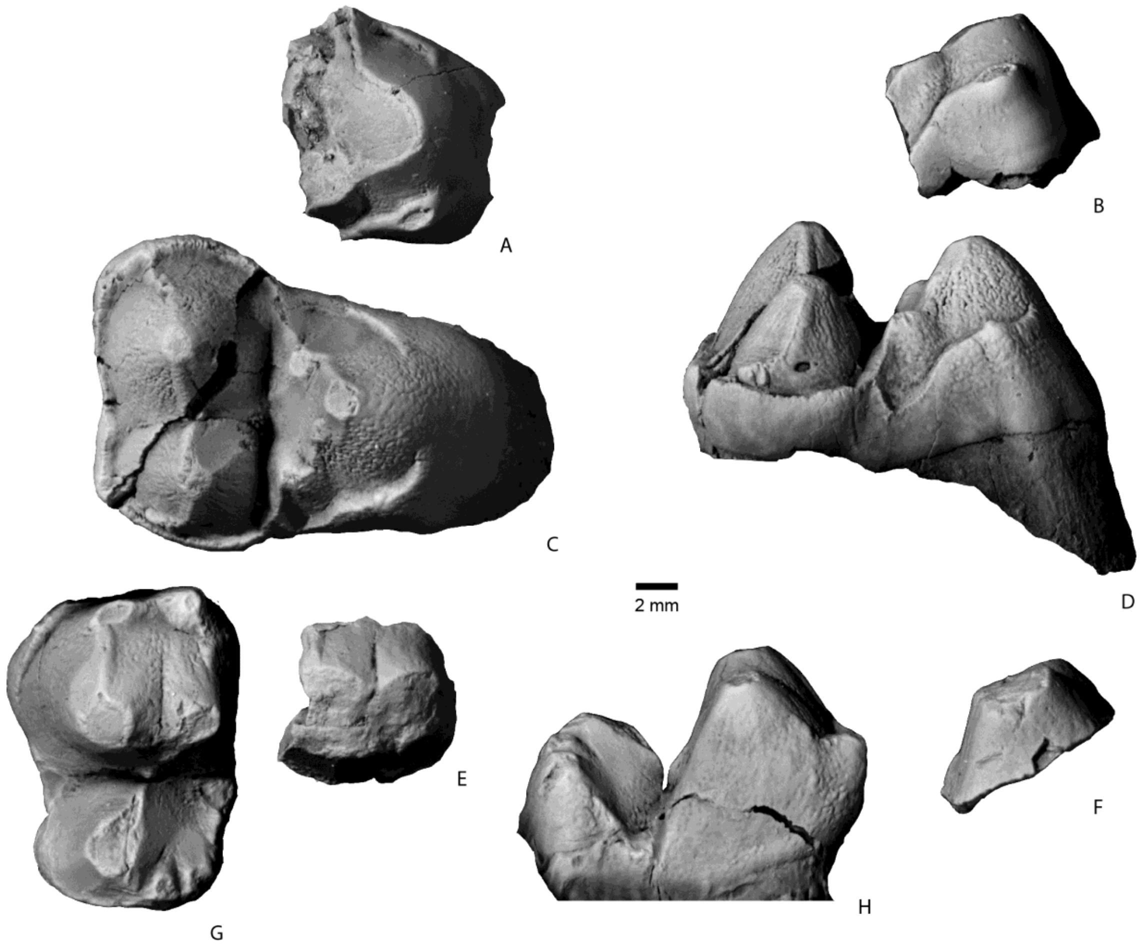

Figure A1. *Triisodon quivirensis* from LSU locality V-111 ("Glen Eleven") compared to *T. quivirensis* from the Nacimiento Formation, San Juan Basin, New Mexico. A-B, trigonid fragment of a left m2 (LSU V-1157) in occlusal (A) and lingual (B) views; C-D, left m2 (NMMNH P-51329) in occlusal (C) and lingual (D) views; E-F, partial right M2 (LSU V-1156) in occlusal (E) and distal (F) views; G-H, right M2 (NMMNH P-20918) in occlusal (G) and distal (H) views. Specimens have been dusted with magnesium oxide to increase visibility of surface features.

Table A.1. Therian mammals "Glen Eleven".

Standhardt (1986)	This paper
LSUMG V-107, "Glen Eleven"	
"Condylarthra"	"Condylarthra"
Arctocyonidae	"Triisodontidae"
Eoconodon coryphaeus	*Triisodon quivirensis*

Table A.2. Dawson Creek summary of $^{40}Ar/^{39}Ar$ results.

Sample	Location (m)	L#	Irrad	min	analysis	n	MSWD	K/Ca	±	2s	Age(Ma)	±	1s
SS02	19	63612	NM-276C	san+	Mean	6	1	43	±	50.3	76.28	±	0.06
SS07	103	63614	NM-276C	mostly san	Mean	4	1.8	7.5	±	28.6	68.83	±	0.13
SS08	135	63616	NM-276C	mostly san	Mean	11	0.7	4.9	±	16.7	68.08	±	0.03
SS13	196	63618	NM-276C	mostly san	Mean	4	4.7	0.4	±	0.8	70.58	±	0.44

Table A.3. Dawson Creek argon data.

ID	^{40}Ar/^{39}Ar	^{38}Ar/^{39}Ar	^{37}Ar/^{39}Ar	^{36}Ar/^{39}Ar (x 10^{-3})	^{39}Ar$_K$ (x 10^{-15} mol)	K/Ca	^{40}Ar* (%)	Age (Ma)	±1s (Ma)
SS02, sanidine&plagioclase, J=0.0039178±0.02%, IC=1.03222±0.00130, NM-276C, Lab#=63612									
59	13.59	0.0064	0.0173	9.374	0.261	29.5	79.6	75.95	0.38
36	10.93	0.0090	0.0084	0.3619	0.512	60.5	99.0	76.00	0.18
27	11.19	0.0128	0.0086	1.135	0.492	59.6	97.0	76.18	0.18
32	11.02	0.0183	0.0128	0.5403	0.540	39.7	98.6	76.20	0.18
61	14.87	0.0258	0.5990	13.73	0.084	0.85	73.0	76.3	1.1
29	10.96	0.0120	0.0075	0.2640	1.499	67.8	99.3	76.352	0.066
62	13.60	0.0172	0.0274	6.610	0.495	18.6	85.6	81.60	0.22
06	18.36	0.0157	0.0060	3.966	2.757	85.0	93.6	119.243	0.061
35	23.07	0.0150	0.0062	8.320	0.497	82.4	89.3	142.12	0.28
28	23.10	0.0149	0.0034	2.964	1.370	148.6	96.2	152.74	0.11
19	25.77	0.0126	0.0019	1.103	2.628	267.1	98.7	173.866	0.071
12	27.34	0.0146	0.0019	1.681		263.5	98.2	183.01	0.11
05	27.23	0.0126	0.0024	1.294	3.111	213.4	98.6	183.014	0.068
14	31.49	0.0138	0.0053	11.10	1.666	97.0	89.6	191.83	0.15
17	29.68	0.0131	-0.0034	2.289	0.629	-	97.7	196.97	0.27
48	31.59	0.0155	0.0027	2.996	0.891	185.6	97.2	207.87	0.19
16	32.04	0.0120	0.0032	1.530	1.451	160.6	98.6	213.49	0.13
18	34.29	0.0178	0.0021	3.153	0.399	248.2	97.3	224.81	0.45
10	35.25	0.0139	0.0017	1.041	5.760	303.7	99.1	234.791	0.050
23	40.67	0.0152	0.0037	3.740	0.940	139.5	97.3	263.75	0.22
40	40.02	0.0126	0.0013	1.246	1.132	407.0	99.1	264.29	0.20
46	59.74	0.0060	-0.0064	3.307	0.216	-	98.4	379.2	1.1
Mean age ± 1s			n=6	MSWD=0.99				76.3	0.1

Table A.3. Dawson Creek argon data.

ID	$^{40}Ar/^{39}Ar$	$^{38}Ar/^{39}Ar$	$^{37}Ar/^{39}Ar$	$^{36}Ar/^{39}Ar$ (x 10^{-3})	$^{39}Ar_K$ (x 10^{-15} mol)	K/Ca	$^{40}Ar^*$ (%)	Age (Ma)	±1s (Ma)
SS07, sanidine&plagioclase, J=0.0039193±0.02%, IC=1.03378±0.00143, NM-276C, Lab#=63614									
16	10.20	-0.0147	1.721	2.740	0.045	0.30	93.4	67.1	1.0
14	10.31	0.0175	1.373	2.534	0.075	0.37	93.8	68.12	0.63
47	9.904	0.0151	0.0176	0.4041	0.529	29.0	98.8	68.840	0.097
01	10.95	0.0311	1.571	4.059	0.084	0.32	90.2	69.52	0.60
05	12.17	0.0049	1.647	7.505	0.070	0.31	82.9	71.01	0.74
04	11.13	0.0131	3.004	4.108	0.049	0.17	91.3	71.56	0.97
21	11.47	-0.0401	2.320	4.828	0.036	0.22	89.2	72.0	1.3
23	10.44	0.0109	0.0096	0.2665	0.799	53.3	99.3	72.813	0.066
38	11.78	-0.1124	2.188	4.970	0.037	0.23	89.0	73.8	1.3
24	12.97	0.0035	3.261	9.310	0.038	0.16	80.8	73.8	1.3
25	20.77	0.0229	6.674	36.53	0.019	0.076	50.6	74.2	2.7
30	14.76	0.0070	3.454	15.00	0.017	0.15	71.8	74.7	3.0
19	12.01	0.0914	4.305	5.636	0.046	0.12	89.0	75.3	1.1
12	11.38	0.0177	2.244	2.763	0.054	0.23	94.4	75.57	0.90
34	12.49	-0.0086	1.294	3.219	0.044	0.39	93.2	81.7	1.2
Mean age ± 1s			n=4	MSWD=1.81				68.8	0.1
SS08, sanidine&plagioclase, J=0.0039123±0.02%, IC=1.03378±0.00143, NM-276C, Lab#=63616									
36	24.67	0.0618	10.98	54.09	0.025	0.046	38.8	67.8	2.3
46	14.91	-0.0498	4.291	18.98	0.065	0.12	64.7	67.95	0.86
37	12.40	0.0582	5.358	10.79	0.049	0.095	77.8	67.99	1.00
13	11.31	0.0614	7.484	7.726	0.038	0.068	85.2	68.0	1.3
30	9.841	0.0134	0.0283	0.5344	1.204	18.0	98.4	68.023	0.047
40	9.745	0.0121	0.0241	0.1775	1.683	21.1	99.5	68.089	0.032
43	9.873	0.0139	0.0369	0.6095	0.824	13.8	98.2	68.101	0.062

Table A.3. Dawson Creek argon data.

ID	$^{40}Ar/^{39}Ar$	$^{38}Ar/^{39}Ar$	$^{37}Ar/^{39}Ar$	$^{36}Ar/^{39}Ar$ (x 10^{-3})	$^{39}Ar_K$ (x 10^{-15} mol)	K/Ca	$^{40}Ar^*$ (%)	Age (Ma)	±1s (Ma)
10	10.60	0.0021	3.273	3.979	0.141	0.16	91.4	68.21	0.37
41	10.60	0.0221	2.761	3.672	0.104	0.18	91.9	68.52	0.48
23	10.91	0.0182	3.517	4.044	0.144	0.15	91.6	70.36	0.36
14	13.10	0.0191	4.665	11.46	0.052	0.11	77.0	71.0	1.0
48	10.62	0.0191	0.1400	1.663	0.750	3.6	95.5	71.183	0.077
15	10.76	0.0177	3.513	2.604	0.152	0.15	95.5	72.26	0.34
19	12.90	0.3995	7.350	10.86	0.050	0.069	79.8	72.6	1.1
42	11.77	0.0245	4.218	5.966	0.083	0.12	87.9	72.78	0.67
38	15.25	0.0122	3.974	17.44	0.027	0.13	68.3	73.3	1.9
08	10.54	0.0119	0.0274	0.2974	1.141	18.6	99.2	73.338	0.048
34	10.74	0.0544	2.036	1.499	0.070	0.25	97.4	73.50	0.70
07	12.19	0.0156	3.231	6.634	0.114	0.16	86.0	73.73	0.47
24	11.94	0.0342	2.400	3.725	0.081	0.21	92.4	77.45	0.65
18	12.30	0.0196	0.1300	3.859	0.595	3.9	90.8	78.22	0.12
17	12.20	0.0048	0.2288	3.434	0.108	2.2	91.8	78.48	0.47
04	13.37	0.0670	3.057	8.103	0.021	0.17	83.9	78.8	2.5
44	12.17	0.0138	0.0043	2.577	0.806	119.0	93.7	79.894	0.088
21	33.93	0.2098	2.073	73.87	0.043	0.25	36.2	85.9	1.7
49	13.71	0.0236	4.440	3.185	0.073	0.11	95.7	91.91	0.74
32	17.16	0.0170	0.0122	5.551	1.320	41.9	90.4	107.84	0.21
Mean age ± 1s			n=11	MSWD=0.69				68.1	0.0
SS13, sanidine&plagioclase, J=0.0039009±0.02%, IC=1.03222±0.00130, NM-276C, Lab#=63618									
84	13.43	0.0321	3.262	14.58	0.240	0.16	69.9	65.92	0.43
34	18.90	0.0304	0.4991	30.51	0.389	1.0	52.5	69.51	0.37
56	15.93	0.0146	3.524	20.83	0.289	0.14	63.1	70.59	0.41

Table A.3. Dawson Creek argon data.

ID	$^{40}Ar/^{39}Ar$	$^{38}Ar/^{39}Ar$	$^{37}Ar/^{39}Ar$	$^{36}Ar/^{39}Ar$ (x 10^{-3})	$^{39}Ar_K$ (x 10^{-15} mol)	K/Ca	$^{40}Ar^*$ (%)	Age (Ma)	±1s (Ma)
29	14.87	0.0086	1.713	16.37	0.321	0.30	68.4	71.23	0.35
07	16.23	0.0128	3.098	21.27	0.194	0.16	62.8	71.46	0.59
39	10.55	0.0129	0.0071	0.6060	3.924	71.7	98.3	72.548	0.029
18	11.45	0.0178	1.965	3.946	0.652	0.26	91.2	73.12	0.16
04	12.40	0.0144	0.0149	5.698	1.798	34.1	86.4	74.921	0.090
57	11.29	0.0136	0.0095	1.488	3.537	54.0	96.1	75.849	0.037
55	11.20	0.0131	0.0067	1.168	3.630	76.1	96.9	75.874	0.036
58	23.40	0.0284	5.976	44.21	0.095	0.085	46.2	75.9	1.2
35	11.82	0.0146	1.159	3.275	0.504	0.44	92.6	76.57	0.19
79	11.15	0.0106	0.0101	0.2971	3.502	50.7	99.2	77.262	0.030
05	11.76	0.0148	0.0119	2.327	4.929	42.9	94.2	77.345	0.034
21	11.75	0.0134	0.0077	1.761	2.919	66.6	95.6	78.457	0.049
28	12.36	0.0162	0.0084	3.400	1.720	61.1	91.9	79.259	0.073
30	11.92	0.0136	0.0066	1.804	4.459	77.6	95.5	79.535	0.035
60	11.58	0.0168	0.0084	0.5838	6.110	60.9	98.5	79.615	0.023
45	12.04	0.0150	0.0063	2.090	2.887	81.1	94.9	79.722	0.050
62	11.96	0.0128	0.0118	1.806	2.106	43.2	95.5	79.747	0.059
13	12.42	0.0125	0.0064	1.471	6.893	80.3	96.5	83.614	0.024
61	12.58	0.0126	0.0197	0.2522	6.854	25.9	99.4	87.162	0.020
69	21.44	0.0138	0.0008	7.555	5.716	603.1	89.6	132.218	0.052
36	51.28	0.0365	2.283	99.08	0.076	0.22	43.3	152.2	1.9
71	23.25	0.0112	0.0010	1.346	1.500	525.7	98.3	156.242	0.098
27	24.86	0.0223	0.0053	6.795	1.403	96.6	91.9	156.28	0.13
41	23.87	0.0126	0.0026	2.803	1.690	196.6	96.5	157.49	0.10
70	24.50	0.0129	0.0009	2.539	1.784	547.3	96.9	162.153	0.093
15	29.76	0.0161	0.0136	19.08	1.794	37.5	81.1	164.59	0.15

Table A.3. Dawson Creek argon data.

ID	$^{40}Ar/^{39}Ar$	$^{38}Ar/^{39}Ar$	$^{37}Ar/^{39}Ar$	$^{36}Ar/^{39}Ar$ (x 10^{-3})	$^{39}Ar_K$ (x 10^{-15} mol)	K/Ca	$^{40}Ar^*$ (%)	Age (Ma)	±1s (Ma)
01	28.63	0.0136	0.0027	3.566	4.418	190.2	96.3	186.991	0.059
48	33.72	0.0138	0.0014	4.976	7.957	367.4	95.6	216.846	0.045
10	34.77	0.0122	0.0032	4.677	1.860	157.8	96.0	224.04	0.11
47	35.64	0.0131	0.0029	1.660	7.100	175.4	98.6	235.171	0.047
24	36.99	0.0133	0.0026	1.352	8.376	195.0	98.9	244.21	0.11
38	37.65	0.0139	0.0054	2.401	5.607	95.3	98.1	246.359	0.052
25	37.88	0.0127	0.0040	2.523	4.661	127.8	98.0	247.568	0.071
42	38.40	0.0153	0.0037	3.830	1.501	137.7	97.1	248.42	0.15
83	54.55	0.0395	0.1644	54.89	0.252	3.1	70.3	255.11	0.92
16	62.98	0.0586	0.0746	77.26	0.130	6.8	63.8	266.3	1.8
81	57.98	0.0126	0.0022	2.188	2.814	232.8	98.9	369.45	0.11
64	61.92	0.0134	0.0042	2.003	4.953	121.1	99.0	392.577	0.083
37	85.56	0.0128	0.0016	1.979	3.585	309.9	99.3	524.00	0.13
08	170.4	0.0659	0.2780	213.5	0.088	1.8	63.0	640.5	4.5
51	519.9	0.2198	1.280	75.03	0.254	0.40	95.8	1976.5	3.3
Mean age ± 1s			n=4	MSWD=4.71				70.6	0.4

Note. Isotopic ratios corrected for blank, radioactive decay, and mass discrimination, not corrected for interfering reactions. Errors quoted for individual analyses include analytical error only, without interfering reaction or J uncertainties. Mean age is weighted mean age of Taylor (1982). Mean age error is weighted error of the mean (Taylor, 1982), multiplied by the root of the MSWD where MSWD>1, and also incorporates uncertainty in J factors and irradiation correction uncertainties. Isotopic abundances after Steiger and Jäger (1977). Ages calculated relative to FC-2 Fish Canyon Tuff sanidine interlaboratory standard at 28.201 Ma (Kuiper et al., 2008). IC = detector intercalibration; Measured $^{40}Ar/^{36}Ar/295.5$. - No detectable ^{37}Ar above blank values. Decay Constant (LambdaK (total)) = 5.463e-10/a (Min et al., 2000). Correction factors: $(^{39}Ar/^{37}Ar)_{Ca} = 0.0007064 \pm 0.000004$, $(^{36}Ar/^{37}Ar)_{Ca} = 0.0002731 \pm 0.0000005$, $(^{40}Ar/^{39}Ar)_K = 0.00808 \pm 0.00041$

Table A.4. Dawson Creek paleomagnetic data: lines.

Formation	Paleosol number	Strat. level (m)	Sample prefix	Sample number	Temperature steps	Strat. Declination	Strat. Inclination	MAD*	Strat. VGP latitude	Strat. VGP longitude
Aguja	P42	0.3	C14BB	01A	460-500	6.4	33	14	77.3	48
Aguja	P42	0.3	C14BB	01C	480-520	11.8	35.5	10.1	75.6	26.2
Aguja	P42	0.3	C14BB	01D	300, 360,380	21.1	25.5	7.1	64.8	21.4
Aguja	ss	7.5	C14BB	126B	250-300	187.4	-22.8	8.9	-71.3	233.7
Aguja	ss	26.0	C14BB	128B	430-480	118.4	-54.9	20.7	-38.4	10.5
Aguja	P39	30.0	C14BB	04C	480-520	223.8	-45.7	20.6	-51.6	159
Javelina	P01	57.5	C14BB	16B	250-300	192.6	-35.8	16.5	-75.2	203.5
Javelina	P01	57.5	C14BB	16C	250-300	193.0	-16.7	12.7	-65.9	223.7
Javelina	P01	59.0	C14BB	17B	150-250	195.3	-31.2	4.1	-71.2	205
Javelina	P02	61.0	C14BB	18A	150-250	214.0	-37.3	4.9	-58.2	174.2
Javelina	P02	61.0	C14BB	18B	150-250	163.0	-66.8	18.3	-66.1	48.7
Javelina	P02	61.0	C14BB	18D	150-250	162.3	-36.6	11.5	-71.7	321.7
Javelina	P03	67.0	C14BB	122B	150-250	179.9	-35.4	4.7	-80.3	257.3
Javelina	P03	67.0	C14BB	122C	250-300	203.9	-22.4	7.6	-61.6	200.2
Javelina	P03	68.0	C14BB	123A	150-250	187.9	-38.7	9.3	-79.7	211.3
Javelina	P03	68.0	C14BB	123B	200-300	220.2	-27.2	4.5	-50.1	179.8
Javelina	P04	69.5	C14BB	36A	300-360	135.7	-27.2	17.7	-46.6	336.5
Javelina	P04	69.5	C14BB	36C	250-300	125.2	-25.9	8.7	-37.2	341.8
Javelina	P05	70.5	C14BB	37A	250-275,500	188.6	-14.8	10.7	-66.8	234.7
Javelina	P05	72.0	C14BB	38A	430-460,500	262.1	-72.2	13	-28.5	114.3
Javelina	P05	74.0	C14BB	39A	400-460	86.0	-75.8	20.8	-24.2	47.2
Javelina	P05	76.0	C14BB	40A	380-430	186.2	-62.1	13.5	-75.1	94.5
Javelina	P06	77.0	C14BB	21C	430-480	158.0	-24.4	16.5	-63.7	312.4

Table A.4. Dawson Creek paleomagnetic data: lines.

Formation	Paleosol number	Strat. level (m)	Sample prefix	Sample number	Temperature steps	Strat. Declination	Strat. Inclination	MAD*	Strat. VGP latitude	Strat. VGP longitude
Javelina	P06	77.0	C14BB	21D	430-480	158.8	-62.9	20	-67.5	34.3
Javelina	P06	80.0	C14BB	24A	480, 520-540	174.6	-78.8	12.9	-50.8	73.6
Javelina	P06	80.0	C14BB	24C	380-430	149	-40.1	7.3	-61.5	341
Javelina	P07	81.0	C14BB	25B	360, 400-430	338.6	11.1	3.1	58.9	121.3
Javelina	P07	81.0	C14BB	25C	250-300	19.5	33.5	12.2	69.1	14.1
Javelina	P07	82.3	C14BB	26A	460-500	325.7	26.1	9.7	54.7	148.1
Javelina	P07	82.3	C14BB	26C	250-300	8.5	18.6	6.6	68.7	53.1
Javelina	P07	82.3	C14BB	26D	275-330	16.8	19.5	8.1	65.1	34.1
Javelina	P07	83.5	C14BB	27A	360-400	31.0	26.8	6.3	57.6	7.9
Javelina	P07	83.5	C14BB	27B	480-520	344.1	47.8	14.9	76.1	168.9
Javelina	P07	83.5	C14BB	27C	150-250	355.7	11.6	9.4	66.2	87.4
Javelina	P07	84.8	C14BB	28A	480-520	0.4	26.5	15	74.7	75.3
Javelina	P07	84.8	C14BB	28B	480-520	24.8	32.8	7.1	64.6	8
Javelina	P07	84.8	C14BB	28D	500-540	21.9	31.7	8.7	66.6	13.1
Javelina	P07	86.5	C14BB	29B	460, 500-520	12.9	30.5	9.3	72.5	31.4
Javelina	P07	86.5	C14BB	29C	360-400	357.8	57.2	8	81.3	245.2
Javelina	P07	86.5	C14BB	29D	330, 380-400	358.1	33	18.7	78.6	85.9
Javelina	P07	88.0	C14BB	30D	150-250	19.1	28.8	9.3	67.6	21
Javelina	P08	89.0	C14BB	31B	300-360	63.8	33.5	12.1	31.3	342.1
Javelina	P08	89.0	C14BB	31C	200-275	38.7	45.3	2.4	55.9	341.4
Javelina	P08	89.0	C14BB	31D	360-400	349.3	25.5	16.6	71.3	111
Javelina	P08	89.5	C14BB	32A	275-330	22.3	30.0	11.6	65.6	14.7
Javelina	P08	89.5	C14BB	32B	480-520	23.8	47.6	19.9	69.2	342.5

Table A.4. Dawson Creek paleomagnetic data: lines.

Formation	Paleosol number	Strat. level (m)	Sample prefix	Sample number	Temperature steps	Strat. Declination	Strat. Inclination	MAD*	Strat. VGP latitude	Strat. VGP longitude
Javelina	P09	90.5	C14BB	33B	250-275, 330	304.0	74.3	9.2	41.7	223.8
Javelina	P09	90.5	C14BB	33D	200-250, 300	344.2	29.2	7.3	70	126.9
Javelina	P09	92.5	C14BB	34A	100-200	24.9	43.6	3.4	67.6	350.6
Javelina	P09	92.5	C14BB	34B	100-300	25.6	42.1	5.6	66.7	353
Javelina	P09	95.0	C14BB	35A	150-300	17.3	41.9	7.6	73.7	1.1
Javelina	P09	95.0	C14BB	35B	360-380,480	29.2	36.7	6.3	62.2	358.6
Javelina	P09	95.0	C14BB	35C	TT100-250	24	54.3	14.1	69	325.3
Javelina	ss	102.0	C14BB	125B	430,480,520	152.5	-17.5	12.3	-57.2	314.0
Javelina	P10	104.0	C14BB	41D	520-560, 600	170.3	-18.5	4.5	-68.3	282.8
Javelina	P10	103.0	C14DC	02B	460,480,560	143.4	-43.8	5.5	-57.4	349.2
Javelina	P10	103.0	C14DC	02C	150-250	178.8	-18.8	7.2	-70.3	260.3
Javelina	P11a	106.0	C14BB	42D	560-600	163.0	-23.9	4.7	-67.0	303.0
Javelina	P12	113.5	C14BB	43A	480-560	161.5	-18.3	1.7	-63.6	301.5
Javelina	P12	113.5	C14BB	43C	540-580	176.7	-43.2	3.3	-85.0	292.6
Javelina	P13	114.0	C14BB	44A	460-500	169.6	-27.0	3.2	-72.2	291.1
Javelina	P13	114.0	C14BB	44C	250, 360-380	176.2	-21.2	4.1	-71.4	267.9
Javelina	P13	114.0	C14BB	44D	500-560	188.0	-67.4	17.7	-68.2	089.9
Javelina	P13	115.0	C14BB	46A	400, 460, 500	182.5	-37.3	11	-81.3	240.4
Javelina	P13	115.0	C14BB	46B	400-430, 500	179.9	-21.8	11	-72.1	256.4
Javelina	P13	115.0	C14BB	46C	430-460, 500	167.2	-18.0	18.9	-66.7	289.6
Javelina	P13	116.0	C14BB	47B	400-460	173.7	-23.2	9.6	-71.9	276.3
Javelina	P13	116.0	C14BB	47C	330-380	103.0	-38.1	13.3	-21.2	000.1
Javelina	P13	116.0	C14BB	47D	480, 520, 600	155.9	-40.3	8.9	-67.5	335.6

Table A.4. Dawson Creek paleomagnetic data: lines.

Formation	Paleosol number	Strat. level (m)	Sample prefix	Sample number	Temperature steps	Strat. Declination	Strat. Inclination	MAD*	Strat. VGP latitude	Strat. VGP longitude
Javelina	P13	117.0	C14BB	48A	200-300, 360-380	173.2	-26.4	15.4	-73.5	279.9
Javelina	P13	117.0	C14BB	48C	360-400	174.3	-41.6	7.7	-82.7	301.3
Javelina	P14	119.0	C14BB	49C	330,360,430	178.0	-24.9	12.7	-73.7	263.1
Javelina	P14	119.5	C14BB	50B	150-250	151.5	-20.9	9.4	-57.6	317.8
Javelina	P14	119.5	C14BB	50C	250, 300-330	156.9	-32.1	12.3	-65.8	322.0
Javelina	P14	119.5	C14BB	50D	250-200,480	160.2	-13.8	11.3	-60.9	300.5
Javelina	P14	120.2	C14BB	52A	150-250	221.4	-77.3	15.9	-45.6	098.9
Javelina	P14	120.2	C14BB	52B	300,330,380	185.7	-42.9	13.5	-83.3	205.1
Javelina	P14	120.2	C14BB	52C	100, 300-360	181.4	-32.4	16	-78.3	249.5
Javelina	P15	121.0	C14BB	53A	360, 460-480	188.7	-14.2	5.4	-66.5	234.0
Javelina	P15	121.0	C14BB	53C	250-330	168.2	-34.6	8.1	-75.2	305.2
Javelina	P15	121.0	C14BB	53D	300, 380-400	186.8	-16.3	11.8	-68.1	237.8
Javelina	P15	123.0	C14DC	03A	250-330	188.4	-13.6	13.2	-66.2	235.7
Javelina	P15	123.0	C14DC	03D	200-300	186.2	-24.8	4.6	-72.7	236.0
Javelina	P16	124.0	C14BB	54B	300, 400, 500	189.5	-17.2	5.5	-67.7	230.6
Javelina	P16	124.0	C14BB	54C	360-380, 580	179.6	-18.4	2.2	-70.2	257.3
Javelina	P16	124.0	C14BB	54D	400-430,480	176.1	-13.4	8.7	-067.2	266.8
Javelina	P17	125.5	C14BB	55D	250-330	182.7	-26.0	6.1	-74.3	246.4
Javelina	P17	132.0	C14BB	56A	200-300	170.2	-37.8	7.9	-78.0	306.1
Javelina	P17	132.0	C14BB	56C	200-330	179.7	-30.8	9.8	-77.4	257.4
Javelina	P17	132.0	C14BB	56D	330,400,480	194.7	-62.5	5.5	-71.3	110.8
Javelina	P17	133.0	C14BB	57A	330, 380-400	89.0	-55.3		-15.9	019.3
Javelina	P19	144.0	C14BB	120C	480,540-560	96.2	-50.8	3.8	-19.6	012.6

Table A.4. Dawson Creek paleomagnetic data: lines.

Formation	Paleosol number	Strat. level (m)	Sample prefix	Sample number	Temperature steps	Strat. Declination	Strat. Inclination	MAD*	Strat. VGP latitude	Strat. VGP longitude
Javelina	P19	146.0	C14BB	59A	430,520,540	189.8	-19.3	4.7	-68.6	228.7
Javelina	P19	146.0	C14BB	59B	520,580,600	214.3	-40.2	4.6	-58.7	169.6
Javelina	P19	146.0	C14BB	59C	430,480,500	182.5	-21.6	9.3	-71.8	248.2
Javelina	P19	147.5	C14DC	04A	430,550,560	208.1	-62.7	13	-63.3	125.5
Javelina	P19	149.0	C14BB	60B	300, 330, 460, 480	278.4	-58.3	14.4	-12.0	127.9
Javelina	P20	162.0	C14DC	05A	380,400,480	194.6	-52.1	2.7	-77.0	147.8
Javelina	P20	162.0	C14DC	05B	560,580,590	193.6	-38.5	6.5	-75.6	195.5
Javelina	P20	162.0	C14DC	05D	360-400	193.3	-41.8	5.7	-77.0	187.3
Javelina	P20	160.0	C14BB	62A	250-330	205.1	-49.9	16.4	-68.3	155.9
Javelina	P20A	163.5	C14BB	92A	250, 330, 360, 500	197.3	-14.6	11.6	-62.8	216.0
Javelina	P20A	163.5	C14BB	92C	500,560,580	192.1	-31.8	7.3	-73.7	210.7
Javelina	P20A	163.5	C14BB	92D	330,380,430	192.6	-39.0	5	-76.6	195.6
Javelina	P21	169.0	C14DC	06D	430, 460, 580	108.6	-30.4	9.9	-23.9	352.8
Javelina	P22	175.0	C14DC	07A	460-500	149.8	-55.7	18.3	-63.8	010.0
Javelina	P22	175.0	C14DC	07C	330,360,430	150.6	-37.9	11.7	-62.3	336.7
Javelina	P22	175.0	C14DC	07D	460-500	149.9	-22.8	19	-57.0	321.2
Black Peaks	P24	181.0	C14BB	102A	150-200, 380	149.1	-32.7	13.5	-59.5	331.5
Black Peaks	P28	193.0	C14BB	68A	300, 350-380	117.2	-47.7	16.2	-35.8	002.8
Black Peaks	P28	193.0	C14BB	68D	150-200	201.2	-58	12.7	-70.1	132.2
Black Peaks	P29	201.0	C14BB	70C	250-300	223.7	-27.9	16.4	-47.3	356.8
Black Peaks	P29	202.0	C14BB	72A	100-200	195.2	-17.0	11.3	-65.0	218.3
Black Peaks	P31	205.5	C14BB	76C	400-460	249.5	-31.9	15.8	-25.9	160.0
Black Peaks	P32	208.0	C14BB	77C	430,460,500	184.6	-41.2	9.1	-83.1	218.7

Table A.4. Dawson Creek paleomagnetic data: lines.

Formation	Paleosol number	Strat. level (m)	Sample prefix	Sample number	Temperature steps	Strat. Declination	Strat. Inclination	MAD*	Strat. VGP latitude	Strat. VGP longitude
Black Peaks	P34	213.0	C14BB	79D	150-200, 300	155.4	-37.1	18.8	-66.2	331.3
Black Peaks	P34	215.0	C14BB	80C	150-200	197.5	-59.1	18.6	-72.1	124.9
Black Peaks	P35	217.0	C14DC	09B	300-360	159.2	-24.6	7	-64.7	310.8
Black Peaks	P35	217.0	C14DC	09C	500-540	156.5	-7.3	16.9	-56	302.2
Black Peaks	plug	220.0	C14BB	107B	150,200,300	184.7	-21.4	18.3	-71.3	241.5
Black Peaks	plug	220.0	C14BB	107C	150-200, 275	185.1	-16.2	13	-68.5	242.2
Black Peaks	P36	226.5	C14BB	83D	150-200,275	195.5	-26.0	7.9	-68.9	210.1
Black Peaks	P36	228.0	C14BB	85C	100-200	213.4	-34.4	16.6	-57.9	177.3
Black Peaks	P37	232.0	C14BB	86A	480, 520-540	355.1	-80.9	20.1	-11.6	78.3
Black Peaks	P37	232.0	C14BB	86C	275-330	221.4	-25.1	8.1	-48.5	179.9
Black Peaks	P37	233.0	C14BB	87A	300-360	188.0	-39.5	5.5	-80	208.7
Black Peaks	P37	233.0	C14BB	87C	250-300	176.0	-67.0	7.3	-69.4	69.4
Black Peaks	P37	233.0	C14BB	87D	300-360	216.6	-36.6	5.5	-55.8	173.4
Black Peaks	P38	236.0	C14BB	89C	AF100-150	186.1	-12.4	13.7	-66.3	241.5
Black Peaks	P38	242.0	C14BB	91A	100-200	124.5	-65.4	7	-44	26.1
Black Peaks	P38	242.0	C14BB	91B	100-200	231.4	-72.9	11.1	-44.6	111.8
Black Peaks	P38	242.0	C14BB	91D	100-200	198.7	-36.9	3.4	-71	189.8

Note. Strat. – stratigraphic, *mean angular deviation.

Table A.5. Dawson Creek paleomagnetic data: circles.

Formation	Paleosol number	Strat. level (m)	Sample prefix	Sample number	Temp. step	Strat. dec. of temp. step	Strat. inc. of temp. step	MAD* of temp. step	Strat. VGP lat. of temp. step	Strat. VGP long. of temp. step	Temp. steps for great circle	Strat. dec. of great circle	Strat. inc. of great circle	MAD* of great circle
Aguja	mud	10.0	C14BB	07A	500	209.5	-74.4	9.1	-53.2	99.6	430, 460, 500	119.2	3.1	15.3
Aguja	mud	10.0	C14BB	07B	460	174.1	-38.5	7.8	-80.7	293	400, 430, 460	96.5	32	18.3
Aguja	mud	10.0	C14BB	07C	480	231.5	-56.7	10	-46.8	142.1	430, 460, 480	340.4	-13.6	3.9
Aguja	mud	12.0	C14BB	08A	480	154.3	-25.9	14.2	-61.5	318.9	430, 460, 480	195.5	51.8	12.8
Aguja	mud	12.0	C14BB	08B	500	173.1	-57.3	9.6	-79.7	44.9	460, 480, 500	94.8	4.8	3.9
Aguja	mud	13.5	C14BB	10C	520	209.0	-4.6	4.9	-79.7	44.9	430, 480, 520	127.3	52.8	10.8
Aguja	mud	15.5	C14BB	09A	460	153.7	-2.0	8.3	-52.2	303	400, 430, 460	64	28.9	11.4
Aguja	mud	15.5	C14BB	09B	330	246.8	-23.2	380	-26	167.1	275, 300, 330	98.9	-22.4	13.5
Aguja	mud	25.0	C14BB	127B	460	120.7	5.9	6.5	-24.8	327.8	400, 430, 460	213.3	69.6	9.5

Table A.5. Dawson Creek paleomagnetic data: circles.

Formation	Paleosol number	Strat. level (m)	Sample prefix	Sample number	Temp. step	Strat. dec. of temp. step	Strat. inc. of temp. step	MAD* of temp. step	Strat. VGP lat. of temp. step	Strat. VGP long. of temp. step	Temp. steps for great circle	Strat. dec. of great circle	Strat. inc. of great circle	MAD* of great circle
Aguja	P39	32.0	C14BB	13D	380	127.6	5.2	2.1	-30.6	323.6	275, 300, 380	225.6	56.8	0.9
Aguja	P40	34.0	C14BB	06B	400	167.5	-21.4	8.8	-68.4	291.9	360, 380, 400	92.4	56.8	16.9
Aguja	P40	34.0	C14BB	06D	520	175.5	39.8	7.9	-37.9	262	460, 500, 520	121.9	-22.5	17.2
Aguja	P40	38.5	C14BB	11C	200	140.2	37.7	14.8	-26.7	298.7	100, 150, 200	83.7	-33	17.3
Aguja	P40	38.5	C14BB	11D	200	114.3	20.1	13.2	-15.4	325.1	100, 150, 200	217.9	30.2	15.6
Aguja	P41	49.5	C14BB	12A	460	139.3	42.0	14.8	-23.7	297.2	275, 300, 460	59.1	-12.3	10.7
Aguja	P41	49.5	C14BB	12B	380	142.5	-6.5	7.7	-45.9	317.7	300, 330, 380	51	-23.6	9.4
Aguja	P41	49.5	C14BB	12C	480	112.2	-6.2	5.3	-20.8	338.3	430, 460, 480	24.4	-10.2	5.8
Aguja	ss	56.5	C14BB	130C	430	179.9	-25.5	8.8	-74.1	257.1	380, 400, 430	121.6	46.7	5.3
Javelina	P01	59.0	C14BB	17A	200	185.2	-4.3	6.5	-62.4	245.5	100, 150, 200	88.1	-10.2	19.4

Table A.5. Dawson Creek paleomagnetic data: circles.

Formation	Paleosol number	Strat. level (m)	Sample prefix	Sample number	Temp. step	Strat. dec. of temp. step	Strat. inc. of temp. step	MAD* of temp. step	Strat. VGP lat. of temp. step	Strat. VGP long. of temp. step	Temp. steps for great circle	Strat. dec. of great circle	Strat. inc. of great circle	MAD* of great circle
Javelina	P02	62.2	C14BB	19A	250	209.6	16.7	9.1	-42.6	215.1	150, 200, 250	130.7	-15.9	11.6
Javelina	P02	62.2	C14BB	19B	250	132.8	3.6	8.3	-34.3	317.4	150, 200, 250	41.9	12.5	3.3
Javelina	P02	62.2	C14BB	19D	380	127.3	-70.3	5.4	-44.9	35.9	330, 360, 380	72.9	23.6	19.7
Javelina	P03	64.5	C14BB	20B	500	191.5	-52.2	6.6	-79.6	144.3	460, 480, 500	22	-36.3	5.4
Javelina	P03	67.0	C14BB	122A	250	190.4	-22.6	13	-70	225.7	150, 200, 250	158.2	63.8	5.6
Javelina	P03	68.0	C14BB	123C	150	219.5	21.4	4.5	-34.5	207.5	AF100, 100, 150	134.4	-15.4	6.3
Javelina	P04	69.5	C14BB	36B	250	209.1	-16.9	7.5	-55.8	198.0	100, 150, 200, 250	128.9	25.7	16
Javelina	P05	72.0	C14BB	38B	330	232.3	-15.2	6.2	-36.5	179.6	275, 300, 330	167.2	59.1	17.3
Javelina	P05	76.0	C14BB	40D	460	233.0	-8.6	12	-34.1	182.7	380, 430, 460	333.3	-45.3	5.5
Javelina	P06	78.0	C14BB	22C	360	259.6	-44.3	12.5	-20.9	147.8	250, 300, 360	34	-42.1	16.3

Table A.5. Dawson Creek paleomagnetic data: circles.

Formation	Paleosol number	Strat. level (m)	Sample prefix	Sample number	Temp. step	Strat. dec. of temp. step	Strat. inc. of temp. step	MAD* of temp. step	Strat. VGP lat. of temp. step	Strat. VGP long. of temp. step	Temp. steps for great circle	Strat. dec. of great circle	Strat. inc. of great circle	MAD* of great circle
Javelina	P06	79.0	C14BB	23A	480	148.7	23.8	6	-38.5	297.1	400, 460, 480	56.5	3.9	3.8
Javelina	P06	79.0	C14BB	23B	500	190.3	10.5	5.8	-54	239.1	430, 460, 500	91.2	43	4.9
Javelina	P06	79.0	C14BB	23C	400	211.9	-75.3	14	-51	99.7	330, 360, 400	10.2	-12.3	5.2
Javelina	P06	80.0	C14BB	24D	500	198.3	-71.2	11.1	-60.5	97.8	380, 480, 500	321	-22.4	19.3
Javelina	ss	102.0	C14BB	125C	520	121.1	-23.1	14.0	-32.9	342.3	400, 480, 500, 520	17.8	-24.6	17.4
Javelina	ss	102.0	C14BB	125A	500	162.3	38.7	10.6	-36.1	277.2	400, 460, 500	113.3	-39.5	2.6
Javelina	P10	104.0	C14BB	41B	460	168.4	2.2	3.6	-57.6	278.8	380, 400, 430, 460	77.2	26.2	6.5
Javelina	P11a	106.0	C14BB	42A	600	173.9	-30.3	6.8	-075.8	281.4	560, 580, 600	67.3	-24.5	8
Javelina	P11a	106.0	C14BB	42C	600	201.7	-15.4	5.0	-060.4	208.9	560, 580, 600	103.5	-26.9	9.5
Javelina	P11	108.0	C14BB	45A	580	145.6	22.5	8.5	-037.3	300.8	540, 560, 580	264.1	48.3	5.4

Table A.5. Dawson Creek paleomagnetic data: circles.

Formation	Paleosol number	Strat. level (m)	Sample prefix	Sample number	Temp. step	Strat. dec. of temp. step	Strat. inc. of temp. step	MAD* of temp. step	Strat. VGP lat. of temp. step	Strat. VGP long. of temp. step	Temp. steps for great circle	Strat. dec. of great circle	Strat. inc. of great circle	MAD* of great circle
Javelina	P14	119.0	C14BB	49A	540	167.4	31.1	13.0	-042.3	273.2	500, 520, 540	70.1	14.2	18.1
Javelina	P14	120.0	C14BB	51D	430	155.9	-40.6	5.9	-67.6	336.6	380, 400, 430	66.5	7.6	9.4
Javelina	P15	123.0	C14DC	03B	560	112.9	-8.5	16.3	-22.0	339.0	430, 540, 560	112.9	-8.5	16.3
Javelina	P17	126.0	C14BB	55B	580	112.1	43.7	9.1	-004.9	313.8	540, 560, 580	41.8	-14.3	15.1
Javelina	P17	125.5	C14BB	55C	600	176.3	-2.8	5.2	-61.9	264.6	560, 580, 600	83.8	-31.3	9.8
Javelina	P19	145.0	C14BB	58A	600	171.4	4.5	3.4	-057.4	272.8	540, 580, 600	81.1	7.7	2.9
Javelina	P19	145.0	C14BB	58C	580	211.8	48.1	9.2	-24.2	226.5	520, 560, 580	90.9	26.7	11
Javelina	P19	147.5	C14DC	04B	480	147.3	-19.5	5.5	-53.9	321.3	400, 430, 480	193.6	62.3	8.4
Javelina	P20	159.0	C14BB	61A	560	311.8	-61.9	14.7	05.2	109.9	300, 380, 560	29.1	6.8	19.6
Javelina	P20	160.0	C14BB	62B	580	11.3	-69.9	5.1	006.3	70.1	250, 300, 580	36.5	17.8	3.7

Table A.5. Dawson Creek paleomagnetic data: circles.

Formation	Paleosol number	Strat. level (m)	Sample prefix	Sample number	Temp. step	Strat. dec. of temp. step	Strat. inc. of temp. step	MAD* of temp. step	Strat. VGP lat. of temp. step	Strat. VGP long. of temp. step	Temp. steps for great circle	Strat. dec. of great circle	Strat. inc. of great circle	MAD* of great circle
Javelina	P20	160.0	C14BB	62C	300	32.6	-74.3	3.4	-003.8	61.4	200, 250, 300	52.9	14.7	4.5
Javelina	P21	167.0	C14BB	93C	550	318.2	-61.6	10.7	08.3	106.4	520, 540, 550	43.7	0.4	3.5
Javelina	P22	176.0	C14BB	94A	460	158.9	23.6	9.2	-43.7	285.8	400, 430, 460	92.9	-30.2	12.1
Javelina	P22	176.0	C14BB	94C	330	148.0	25.8	14.6	-20.1	339.2	275, 300, 330	78.4	-29.9	12.5
Javelina	P22	176.0	C14BB	94D	480	109.2	9.4	2.7	-14.2	332.9	430, 460, 480	14.5	14.6	5.9
Javelina	P23	177.0	C14BB	95C	520	173.6	-4.8	4.9	-62.4	270.7	480, 500, 520	76.7	-31.2	20.3
Javelina	P23	177.0	C14BB	95D	520	96.7	68.2	0.8	18.6	297.6	480, 500, 520	109.8	-20.1	2.8
Javelina	P23	177.5	C14BB	96A	480	148.6	27.3	7	-36.8	295.8	430, 460, 480	73	-29.8	15.1
Javelina	P23	177.5	C14BB	96B	250	115.8	18.0	11.2	-17.2	325.2	150, 200, 250	220.7	37.9	10.1
Javelina	P23	177.5	C14BB	96D	400	108.3	-19.1	3	-20.7	346.6	300, 360, 400	28.5	19.6	5.6

Table A.5. Dawson Creek paleomagnetic data: circles.

Formation	Paleosol number	Strat. level (m)	Sample prefix	Sample number	Temp. step	Strat. dec. of temp. step	Strat. inc. of temp. step	MAD* of temp. step	Strat. VGP lat. of temp. step	Strat. VGP long. of temp. step	Temp. steps for great circle	Strat. dec. of great circle	Strat. inc. of great circle	MAD* of great circle
Javelina	P23	178.0	C14BB	97C	480	73.1	-18.6	5.3	09.7	003.6	380, 400, 480	340	-4.5	9.3
Javelina	P23	179.0	C14BB	99C	540	188.2	28.6	12.9	-44.8	245.6	480, 500, 520, 540	107.1	-27.1	10.2
Javelina	P23	179.0	C14BB	99D	500	101.2	-14.8	14.9	-13.4	347.9	450, 480, 500	129.7	69.3	14.5
Javelina	P23	179.5	C14BB	100B	400	191.3	5.3	1.5	-56.3	236.1	300, 360, 400	103	-13	2.2
Black Peaks	P24	181.0	C14BB	102C	300	188.5	59.0	6.7	-20.5	249.8	150, 200, 300	57.2	26.2	13.8
Black Peaks	P24	181.0	C14BB	102D	300	168.9	-3.0	2.2	-60.3	279.6	150, 200, 300	78.3	-30.2	19.7
Black Peaks	P24	182.0	C14BB	103A	300	54.9	-53.2	13.2	08.3	033.3	150, 200, 300	89.5	30.6	12.9
Black Peaks	P26	187.0	C14BB	64A	580	102.8	13.7	3.8	-07.6	334.3	520, 560, 580	24.9	-42.3	4.8
Black Peaks	P26	187.6	C14BB	65C	480	241.6	-24.5	5.9	-30.9	169.0	380, 430, 480	180	44.3	12.4
Black Peaks	P27	189.5	C14BB	66B	540	137.0	-40.4	10.8	-51.1	347.9	500, 520, 540	176.4	40.8	3.1

Table A.5. Dawson Creek paleomagnetic data: circles.

Formation	Paleosol number	Strat. level (m)	Sample prefix	Sample number	Temp. step	Strat. dec. of temp. step	Strat. inc. of temp. step	MAD* of temp. step	Strat. VGP lat. of temp. step	Strat. VGP long. of temp. step	Temp. steps for great circle	Strat. dec. of great circle	Strat. inc. of great circle	MAD* of great circle
Black Peaks	P27	189.5	C14BB	66C	540	133.2	-13.6	5.8	-40.6	329.3	460, 500, 540	111.3	75.4	0.4
Black Peaks	P28	191.0	C14BB	67A	520	91.4	-32.9	4.4	-09.8	001.9	480, 500, 520	345.7	-24.5	3.3
Black Peaks	P28	191.0	C14BB	67B	520	95.8	-33.9	4.5	-13.9	000.5	460, 480, 520	103.5	55.7	0.4
Black Peaks	P28	191.0	C14BB	67D	250	85.9	-30.3	8.8	-04.4	003.0	150, 200, 250	103.8	58.4	2.2
Black Peaks	P28	193.0	C14BB	68C	250	156.5	27.8	13.5	-40.4	287.2	150, 200, 250	61.3	5.1	6.1
Black Peaks	P29	201.0	C14BB	70A	360	153.4	-25.8	11.7	-60.8	319.9	300, 330, 360	51.1	-11.8	13.6
Black Peaks	P29	202.0	C14BB	72B	200	175.8	-1.6	7.7	-61.2	265.5	100, 150, 200	178.6	-8.6	7.6
Black Peaks	P30	203.0	C14BB	73B	150	249.7	-36.2	12.3	-26.9	157.7	NRM, 100, 150	2.2	-24.5	9.9
Black Peaks	P30	203.0	C14BB	73C	275	210.8	-18.1	10.1	-54.9	195.2	150, 200, 275	114.4	-18.9	2.1
Black Peaks	P30	203.0	C14BB	73D	400	252.6	-49.1	8.6	-28.1	146.2	330, 360, 400	348.1	-8.9	19.7

Table A.5. Dawson Creek paleomagnetic data: circles.

Formation	Paleosol number	Strat. level (m)	Sample prefix	Sample number	Temp. step	Strat. dec. of temp. step	Strat. inc. of temp. step	MAD* of temp. step	Strat. VGP lat. of temp. step	Strat. VGP long. of temp. step	Temp. steps for great circle	Strat. dec. of great circle	Strat. inc. of great circle	MAD* of great circle
Black Peaks	P31	205.5	C14BB	76A	330	48.4	-76.3	8.8	-10.7	57.3	275, 300, 330	80.5	13.5	16.1
Black Peaks	P31	205.5	C14BB	76B	250	159.3	6.6	6.8	-51.8	291.6	150, 200, 250	72.8	43.6	19
Black Peaks	P32	208.0	C14BB	77A	460	106.9	-0.8	10.1	-14.9	338.6	400, 430, 460	198.6	58.6	8.5
Black Peaks	P32	208.0	C14BB	77B	300	179.4	1.5	5.1	-59.9	257.9	200, 250, 300	88.1	-2.1	20
Black Peaks	P33	211.0	C14BB	78A	550	170.6	21.8	9.4	-48.4	270.7	480, 540, 550	85.2	-12.5	1.6
Black Peaks	P33	211.0	C14BB	78C	380	120.2	10.4	7	-23.1	326.1	330, 360, 380	35.1	-44.8	6.7
Black Peaks	P33	213.0	C14BB	79B	430	191.2	-73.8	8.4	-58.5	087.5	360, 400, 430	105.2	-0.7	3.4
Black Peaks	P34	215.0	C14BB	80B	300	169.3	-24.9	14.6	-71.0	290.4	250, 275, 300	99.3	47.6	11.4
Black Peaks	P34	215.0	C14BB	80D	250	143.0	-49.0	8.3	-58	357.2	150, 200, 250	3.2	-34.7	15.5
Black Peaks	P35	217.0	C14DC	09D	360	138.9	-35.6	15.4	-51.6	341.8	100, 300, 360	6.6	-45.9	19.2

Table A.5. Dawson Creek paleomagnetic data: circles.

Formation	Paleosol number	Strat. level (m)	Sample prefix	Sample number	Temp. step	Strat. dec. of temp. step	Strat. inc. of temp. step	MAD* of temp. step	Strat. VGP lat. of temp. step	Strat. VGP long. of temp. step	Temp. steps for great circle	Strat. dec. of great circle	Strat. inc. of great circle	MAD* of great circle
Black Peaks	P36	225.0	C14BB	82A	300	168.0	-42.3	12.1	-78.3	325.2	200, 275, 300	112.5	33.9	4.5
Black Peaks	P36	226.5	C14BB	83C	150	268.1	-78.0	8.5	-27.5	102.9	AF100, 100, 150	322.1	1.5	9.6
Black Peaks	P36	227.0	C14BB	84C	200	237.1	12.1	9.5	-24.8	189.9	100, 150, 200	324	-14	2.6
Black Peaks	P36	227.0	C14BB	84D	300	191.5	-1.5	6.4	-59.4	233.7	250, 275, 300	104.2	-18.3	10.1
Black Peaks	P36	228.0	C14BB	85B	300	197.5	-40.4	8.3	-73.1	184.4	150, 250, 300	202.5	51.5	5.6
Black Peaks	P37	232.0	C14BB	86D	330	104.6	8.4	7.5	-10.6	335.8	100, 300, 330	16.4	-9.1	2.8
Black Peaks	P37	233.5	C14DC	10B	330	232.2	-37.9	7.7	-42.5	163.9	250, 300, 330	8.6	-45.2	11.7
Black Peaks	P37	233.5	C14DC	10C	430	113.4	-66.2	6.8	-36.6	27.6	380, 400, 430	94.4	22	2.4
Black Peaks	P37	233.5	C14DC	10D	430	161.3	14.6	6.8	-49.1	285.8	300, 380, 430	74.5	-11.6	11.7
Black Peaks	P38	234.0	C14BB	88A	200	159.7	-1.1	3.2	-55.3	294.3	AF100, 150, 200	64.4	-33.8	12

Table A.5. Dawson Creek paleomagnetic data: circles.

Formation	Paleosol number	Strat. level (m)	Sample prefix	Sample number	Temp. step	Strat. dec. of temp. step	Strat. inc. of temp. step	MAD* of temp. step	Strat. VGP lat. of temp. step	Strat. VGP long. of temp. step	Temp. steps for great circle	Strat. dec. of great circle	Strat. inc. of great circle	MAD* of great circle
Black Peaks	P38	234.0	C14BB	88B	300	162.3	4.2	5.9	-54.3	288.1	150, 200, 300	74	-24.5	3.1
Black Peaks	P38	234.0	C14BB	88D	200	211.9	17.5	6.3	-40.9	213	100, 150, 200	115.5	10.6	9
Black Peaks	P38	236.0	C14BB	89B	300	232.1	-31.5	13.5	-41	169.2	100, 200, 300	318.8	-2	17.9
Black Peaks	P38	240.0	C14DC	11B	330	191.5	-54.8	13.4	-78.6	132	250, 300, 330	47.8	-25.4	12.1

Note. Strat. - stratigraphic, temp. – temperature, dec. – declination, inc. – inclination, *mean angular deviation, lat. – latitude, long. – longitude.

Table A.6. Dawson Creek paleomagnetic data: site means.

Formation	Paleosol number	Strat level (m)	Sample prefix	Sample number	n*	Stratigraphic Declination	Stratigraphic Inclination	alpha-95	Stratigraphic VGP latitude	Stratigraphic VGP longitude
Aguja	P42	0.3	C14BB	1	3	13.3	31.5	12.7	72.7	29
Javelina	P02	61.0	C14BB	18	3	182.7	-49.6	34.5	-87.4	140.2
Javelina	P07	82.3	C14BB	26	3	357.9	22.9	33.6	72.5	83.6
Javelina	P07	84.8	C14BB	28	3	15.4	30.8	18.5	71	25.3
Javelina	P07	86.5	C14BB	29	3	341.5	32.6	25.1	69.5	136.5
Javelina	P13	115.0	C14BB	46	3	176.2	-25.8	19.4	-73.9	270.2
Javelina	P14	120.0	C14BB	50	3	156.2	-22.3	15.5	-61.6	313.1
Javelina	P15	121.0	C14BB	53	3	181.9	-21.9	23.4	-72.0	250.7
Javelina	P16	124.0	C14BB	54	3	181.7	-16.4	10.9	-069.0	252.0
Javelina	P17	132.0	C14BB	56	3	179.4	-44	28.8	-86.4	265.5
Javelina	P19	146.0	C14BB	59	3	194.2	-27.6	28.5	-70.3	211.9
Javelina	P20	162.0	C14DC	5	3	193.8	-44.1	10.9	-77.3	179.2
Javelina	P20A	163.5	C14BB	92	3	194.2	-28.5	19.7	-70.8	210.8
Javelina	P22	175.0	C14DC	7	3	150.1	-38.8	26	-62.1	338.3
Black Peaks	P37	233.0	C14BB	87	3	197.3	-48.8	33.9	-75	160.8

Note. *number of samples used for site mean calculation

APPENDIX B

Upper Nacimiento Formation Paleomagnetic data

Table B.1. Upper Nacimiento Formation paleomagnetic data: lines.

Location	Paleosol #	Strat. level (m)	Sample	Temp. steps	Strat. Declination	Strat. Inclination	MAD*	Strat. VGP latitude	Strat. VGP longitude
Kutz	P34	1	C15KC45A	200,250,275	174.3	-39.3	19.1	-74.9	272
Kutz	P34	1	C15KC45B	250-300	197.2	-68.1	18.1	-70.9	106.5
Kutz	P34	1	C15KC45C	250-300	163.8	-26	4	-63	288.7
Kutz	P35	2	C15KC46C	250-300	136.3	-29.2	11.7	-46	325.5
Kutz	P35	2	C15KC46D	200-250	146	-33.8	8.3	-55.2	320.3
Kutz	P36	2	C15KC47A	225,250,300	127.6	-73.2	16.6	-49.7	32.8
Kutz	P37	4.5	C15KC48A	250-300	178	-64.2	9.9	-80.4	63.7
Kutz	P37	4.5	C15KC48B	250-300	157.4	-69.8	8.3	-66.8	36.8
Kutz	P37	4.5	C15KC48C	150,225,250	125.3	-65	12.6	-48.7	14.5
Kutz	P1	15.5	C15KC01B	225-275	171.9	-41.5	9.3	-75.6	283.2
Kutz	P1	15.5	C15KC01D	250-300	189.4	-24.1	18.8	-64.7	230.2
Kutz	P1	16	C15KC02A	175, 250, 275	251.3	-56.2	20	-34.2	138.7
Kutz	P1	16	C15KC02B	150-225	173.1	-58.2	5.4	-84	7.8
Kutz	P1	16	C15KC02D	250-275	129.6	-62.3	5.8	-51.4	8.7
Kutz	P2	18.5	C15KC03A	150-200	217.7	-29.9	9.8	-50.9	183.5
Kutz	P3	19	C15KC04A	175, 200, 250	65.9	-62.5	8.3	-10.1	30.1
Kutz	P3	19.5	C15KC05A	150-200	167.8	-28.6	7.6	-66.1	282.4
Kutz	P4	20.5	C15KC06A	150-200	138.9	-24.8	3.1	-46.4	320.3
Kutz	P5	21.8	C15KC07B	150-200	145.9	-50.5	12.4	-61.4	341.6
Kutz	P5	21.8	C15KC07C	250-300	171.7	-32.9	4.9	-70.0	275.8
Kutz	P5	21.8	C15KC07D	125-175	160.3	-23.6	16.7	-060.0	293.3
Kutz	P6	24.8	C15KC08C	175-225	221.2	-59.4	9.3	-57.8	142.7
Kutz	P7	26.3	C15KC09A	250-300	116.7	-31.1	19.3	-31.2	340.5
Kutz	P7	26.3	C15KC09C	275-325	197	-28.5	14.9	-63.9	212.3

Table B.1. Upper Nacimiento paleomagnetic data: lines.

Location	Paleosol #	Strat. level (m)	Sample	Temp. steps	Strat. Declination	Strat. Inclination	MAD*	Strat. VGP latitude	Strat. VGP longitude
Kutz	P7	26.5	C15KC10A	250-300	183.7	-25.9	11.1	-66.9	242.9
Kutz	P7	26.5	C15KC10B	250-300	191.1	-18.1	11	-61	229
Kutz	P7	26.5	C15KC10D	250-300	190.9	-35	19.1	-70.3	220.1
Kutz	P8	27.8	C15KC11B	225-300	171.6	-13.9	12.3	-59.6	268.7
Kutz	P8	27.8	C15KC11D	150-200	220.7	-46.4	7.7	-54.7	164.6
Kutz	P9	27.5	C15KC12A	250-300	176.7	-46.2	4	-80.6	270.3
Kutz	P9	27.5	C15KC12C	250-300	182.7	-40.4	10.1	-76.4	241.5
Kutz	P9	27.5	C15KC12D	250-300	186.5	-46.9	9.2	-79.3	245.8
Kutz	P10	28.5	C15KC13A	250-300	141.9	-55.2	14.7	-59.4	352.2
Kutz	P11	29.5	C15KC15A	250-300	103.4	74.8	13.4	25.7	283.1
Kutz	P11	29.5	C15KC15B	NRM, 125, 150	331.7	38.5	4.1	61.3	138.8
Kutz	P11	29.5	C15KC15D	NRM, 125, 150	355.3	44.4	7.5	78.8	94.5
Kutz	P11	30.5	C15KC16A	NRM, 125, 150	22.4	73.4	7.3	63.1	277.6
Kutz	P11	30.5	C15KC16B	NRM, 125, 150	350.6	62.3	3.7	79.9	209.7
Kutz	P11	30.5	C15KC16C	125, 225, 275	340.2	47.4	5.3	71.6	142.2
Kutz	P12s	31.5	C15KC17A	150-200	334.7	44.1	15.2	66	143
Kutz	P12	31.5	C15KC17B	250-300	351.6	17	15.8	61.2	89.5
Kutz	P12	31.5	C15KC17D	125-175	355.5	53.2	2.8	85.4	126.7
Kutz	P13	32.5	C15KC18A	250-300	16.9	65.7	3.7	73.1	294.3
Kutz	P13	32.5	C15KC	150-200	2.4	63.2	5.1	81.6	263.8
Kutz	P13	32.5	C15KC18D	225-275	349	58.2	4.5	81	180.7
Kutz	P13	32.8	C15KC19A	250-300	357.1	47.6	2.9	81.8	90.3
Kutz	P13	32.8	C15KC19B	225-275	352.4	45.6	13.8	78.6	108.5
Kutz	P13	32.8	C15KC19C	200-250	24.6	58.3	6.2	70.4	327.3

Table B.1. Upper Nacimiento paleomagnetic data: lines.

Location	Paleosol #	Strat. level (m)	Sample	Temp. steps	Strat. Declination	Strat. Inclination	MAD*	Strat. VGP latitude	Strat. VGP longitude
Kutz	P14	33.5	C15KC20B	175,225,275	1.5	54.7	5.2	88.2	27.9
Kutz	P14	33.5	C15KC20C	125,175,200	347.8	56.7	4.1	80.2	170.3
Kutz	P14	33.5	C15KC20D	125,150,200	5.7	45.6	8.2	79.4	43.4
Kutz	P14	33.8	C15KC21A	200, 275, 325	274.7	74.5	9	33.5	216.7
Kutz	P14	33.8	C15KC21B	150-200	337.6	18.1	20	56	114.4
Kutz	P14	33.8	C15KC21C	NRM, 125, 200	23.6	47	9.7	68.5	358
Kutz	P15	35.5	C15KC22A	125,175,200	2.2	50.7	4.7	84.6	51.7
Kutz	P15	35.5	C15KC22D	NRM, 125, 150	264.5	82.3	15.6	33.6	233.9
Kutz	P16	36.2	C15KC23A	225,250,300	354	31.3	14.3	69.7	88.9
Kutz	P16	36.2	C15KC23D	125-175	14.6	30.3	8.9	66	35.6
Kutz	P16	36.5	C15KC24A	225,250,300	14	54.5	4.4	78.6	345.3
Kutz	P16	36.5	C15KC24C	225-275	354.6	44.5	6.7	78.7	97.6
Kutz	P16	36.5	C15KC24D	225,275,300	11.3	49.9	4.8	49	10.5
Kutz	P17	39.7	C15KC25C	125, 175, 225	4.2	34.4	13.8	72	59.1
Kutz	P18	39.3	C15KC26C	NRM, 125, 175	10.1	36.9	11.4	71.8	40.4
Kutz	P19	39.8	C15KC27D	125-175	341.7	69.4	5.3	69.1	220.2
Kutz	P20	41.5	C15KC28A	125-175	349.3	43.8	11.7	75.8	115.1
Kutz	P20	41.5	C15KC28C	250-300	332.9	40.1	16.5	62.9	139.3
Kutz	P21	43	C15KC29B	125, 200, 225	25.2	27.7	7.3	58.7	19.6
Kutz	P21	43	C15KC29C	125, 175, 325	332.2	59.6	15.2	68	180.9
Kutz	P22	44	C15KC30C	NRM, 125, 250	73.2	69.2	8.8	37.9	299.3
Kutz	P22	44	C15KC30D	NRM, 125, 150	10.8	21.9	13	63	48.2
Kutz	P23	44.6	C15KC31C	125-175	359.4	36.1	13.4	73.5	74.1
Kutz	P24B	46	C15KC32B	125, 200, 225	16	77.7	14.3	58.7	264.3

Table B.1. Upper Nacimiento paleomagnetic data: lines.

Location	Paleosol #	Strat. level (m)	Sample	Temp. steps	Strat. Declination	Strat. Inclination	MAD*	Strat. VGP latitude	Strat. VGP longitude
Kutz	P24	46	C15KC32C	250-300	346	63	12	76.7	203.3
Kutz	P24	46	C15KC32D	125, 175, 200	359.6	65.1	4.8	79.4	250.6
Kutz	P25	47	C15KC33D	100-150	70.3	64.5	9.6	38.1	307.8
Kutz	P26	47.8	C15KC34B	250-300	346.8	12.8	12.8	76.5	131.1
Kutz	P26	47.8	C15KC34C	250-300	12.6	38.4	10	71.5	32.7
Kutz	P26	47.8	C15KC34D	250-300	348.7	51	9.2	79.5	138.2
Kutz	P27	48.5	C15KC35A	100, 275, 300	316.5	61.8	4.3	56.3	186.9
Kutz	P27	48.5	C15KC35D	200, 250, 275	354.4	53	9.9	84.6	131.1
Kutz	P28	56.5	C15KC36B	100-200	2.6	63	6.1	81.8	265.2
Kutz	P28	56.5	C15KC36D	NRM-150	322.6	44.2	13.1	56.6	154.4
Kutz	P29	57.8	C15KC37A	100, 200, 225	18.4	30.2	6.6	64	28.4
Kutz	P30	58.4	C15KC38A	225-275	156.1	-23	14.2	-57.4	299.4
Kutz	P30	58.4	C15KC38C	NRM, 100, 350	322.7	53.1	10.6	59.5	169.4
Kutz	P31	62.3	C15KC39A	NRM, 100, 225	328.5	67.5	5.7	63.5	203.7
Kutz	P31	62.3	C15KC39B	NRM, 100, 250	17.9	51.4	9	74.6	353.6
Kutz	P31	62.3	C15KC39D	NRM-150	45.1	57.9	9.2	54.5	324.8
Kutz	P32	66.8	C15KC41A	200, 300, 325	185.5	-26.3	15.4	-66.9	238.4
Kutz	P32	66.8	C15KC41C	125, 150, 250	84.5	-66.3	9.7	-23.3	26.4
Kutz	P32	67	C15KC42A	125-200	149.9	-68.8	5.8	-63.7	28.2
Kutz	P32	67	C15KC42C	150-225	128.9	-70.1	12	-51.1	25.5
Kutz	P32	67	C15KC42D	150-225	37.3	-69	10	-4.7	50.4
Kutz	P33	68.5	C15KC43A	200-275	122.4	-49.7	9.9	-42.3	352.5
Kutz	P33	69	C15KC44A	250-300	208.5	-62.2	15.9	-67.2	135.4
Kutz	P33	69	C15KC44C	250-300	168.2	-66.2	16.9	-75.2	40.2

Table B.1. Upper Nacimiento paleomagnetic data: lines.

Location	Paleosol #	Strat. level (m)	Sample	Temp. steps	Strat. Declination	Strat. Inclination	MAD*	Strat. VGP latitude	Strat. VGP longitude
Kutz	P33	69	C15KC44D	225-275	148.6	-49	8	-63	337.1
Torreon West	P22	29.4	C15TW01A	225-275	178.3	-63.2	1.3	-81.2	64.7
Torreon West	P22	29.4	C15TW01B	225-275	198.6	-61.8	3.9	-74.1	130.9
Torreon West	P22	29.4	C15TW01C	225-275	179.6	-64.4	2.7	-79.8	71
Torreon West	P24	31.5	C15TW02A	225-275	167.3	-65.8	1.7	-74.7	38.7
Torreon West	P24	31.5	C15TW02C	225-275	163.3	-55.6	3.8	-76.5	348.1
Torreon West	P24	31.5	C15TW02D	225-275	169.7	-44.9	3.3	-77.1	298.2
Torreon West	P24	31.7	C15TW03B	300, 350-375	167.4	-18.8	13.7	-61.3	279.2
Torreon West	P24	31.7	C15TW03C	225-275	195	-54	3.6	-77.7	165
Torreon West	P24	31.7	C15TW03D	225-275	172.2	-53.1	2.1	-83.2	324.8
Torreon West	P24	31.9	C15TW04A	225-275	180.3	-50.9	11.6	-85.6	249.3
Torreon West	P24	32.1	C15TW05C	225, 250, 325	171.2	-26.5	8.7	-66.6	274.6
Torreon West	P24	32.3	C15TW06A	225-275	125.6	-77.4	11.2	-46.8	43.6
Torreon West	P24	32.8	C15TW07A	125, 150, 225	167	-32.9	6.3	-68.6	288.5
Torreon West	P24	32.8	C15TW07C	225-275	147.8	-40	11	-59.2	326.1
Torreon West	P24	33.3	C15TW08A	NRM, 150, 175	170.5	-31.8	7.3	-69.4	279.2
Torreon West	P24	33.3	C15TW08B	715, 225, 275	132.9	-36.9	5.2	-46.2	335.1
Torreon West	P24	35.2	C15TW11C	200-250	219.6	-37.1	4.7	-52.3	175.6
Torreon West	P24	35.2	C15TW11D	225-275	221.4	-45.6	13.4	-53.9	165
Torreon West	P25	35.5	C15TW12B	125-275	203.9	-37.2	9.8	-64.2	192.2
Torreon West	P25	35.8	C15TW13D	100-150	38.2	72.8	6.8	56.6	288.8
Torreon West	P26	36.1	C15TW14A	125, 200, 300	174.8	-36.5	19.8	-73.7	270.2
Torreon West	P26	37.3	C15TW15B	225-275	1	20.8	7	64.7	70.3
Torreon West	P26	38.2	C15TW16D	125, 250, 225	296.2	51.7	13.2	38	178.3

Table B.1. Upper Nacimiento paleomagnetic data: lines.

Location	Paleosol #	Strat. level (m)	Sample	Temp. steps	Strat. Declination	Strat. Inclination	MAD*	Strat. VGP latitude	Strat. VGP longitude
Torreon West	P26	39	C15TW17B	150, 200, 250	353.6	45.1	17.5	79.2	104.6
Torreon West	P27	40	C15TW18C	150, 200, 225	12.3	31.5	9.4	68.1	39.5
Torreon West	P29	43.2	C15TW19A	100, 125, 175	8	39.2	4.8	74.5	43.7
Torreon West	P29	43.2	C15TW19B	100-150	342.2	59.7	4	75.3	186
Torreon West	P29	43.2	C15TW19C	225-275	309.9	48.7	9.9	47.9	168.8
Torreon West	P39	56.7	C15TW20A	225-275	355.2	63.6	1.5	80.1	232.5
Torreon West	P39	56.7	C15TW20C	225-275	358.7	60	3.4	85	241.2
Torreon West	P39	56.7	C15TW20D	225-275	359.6	66.5	3	77	251.4
Torreon West	P40	61.4	C15TW21A	125, 175, 200	16	52.7	3.9	76.6	349.6
Torreon West	P40	61.4	C15TW21B	225-275	353.2	58	8.8	84	190.9
Torreon West	P40	61.4	C15TW21C	175-225	296	72.5	5.2	43.3	211.4
Torreon West	P43	66.7	C15TW22A	225-275	0.2	80.5	5	54.5	252.7
Torreon West	P43	66.7	C15TW22B	125, 150, 225	350	55.7	1	81.9	167.3
Torreon West	P43	66.7	C15TW22D	175-225	341.2	50	4.1	73.5	149.6
Torreon West	P49	72	C15TW23A	125, 250, 275	5.2	43.3	2.4	78.3	48.7
Torreon West	P49	72	C15TW23C	100-150	355.2	42.8	4.1	78.1	94.2
Torreon West	P49	72	C15TW23D	100-150	349.6	67.3	4.5	74	227.7
Torreon West	P49	72.4	C15TW24A	100-150	5.2	-74.6	4.8	-7.2	70.1
Torreon West	P50	72.7	C15TW25C	225-275	131	-49.5	13.4	-49	349.3
Torreon West	P50	73.3	C15TW27D	125, 275, 200	152.8	-75.2	15.3	-58.9	48.2
Torreon West	P50	73.8	C15TW28A	175, 200, 250	230.1	-51.2	10.1	-48.7	153.3
Torreon West	P50	73.8	C15TW28B	175, 275, 325	302.4	-79.7	19.9	-23.9	91
Torreon West	P50	74	C15TW29B	100-150	160.3	-42.9	10.7	-69.8	314.8
Torreon West	P51	74.6	C15TW30A	250, 275, 325	196.7	-36.8	14.2	-68.7	204.8

Table B.1. Upper Nacimiento paleomagnetic data: lines.

Location	Paleosol #	Strat. level (m)	Sample	Temp. steps	Strat. Declination	Strat. Inclination	MAD*	Strat. VGP latitude	Strat. VGP longitude
Torreon West	P51	74.6	C15TW30B	175-225	7.5	73.5	8.4	66.1	262.1
Torreon West	P52	75.9	C15TW32A	300, 325, 375	173.2	-25.7	18.4	-66.7	269.5
Torreon West	P52	76.8	C15TW36C	150-200	149.1	-48.9	15.6	-63.5	338.1
Torreon West	P53	77.4	C15TW37B	225-275	170.4	-28.6	7.2	-67.5	277.5
Torreon West	P53	77.4	C15TW37C	250, 275, 325	140.2	-36.6	17.8	-51.9	329.3
Torreon West	P53	77.4	C15TW37D	200-250	168.6	-59.2	8.1	-80.2	10
Torreon West	P53	78.4	C15TW38B	125, 300, 325	119.5	-25.1	5	-31.5	336
Torreon West	P53	78.4	C15TW38C	225, 250, 300	128.7	-51.9	19.2	-47.9	353.4
Torreon East	P7	27.5	C15ET02A	175-225	153.3	-43	6.8	-64.6	324.5
Torreon East	P7	27.8	C15ET03A	NRM-125	203.5	-47.7	8.3	-69	176
Torreon East	P7B	27.8	C15ET03B	200, 250, 275	142.4	-64.5	7.4	-60.2	14.8
Torreon East	P7	27.8	C15ET03D	150, 200, 250	233.4	-76.9	9	-47.4	102.7
Torreon East	P7	28	C15ET04A	275-325	144.3	-24.4	7.3	-50.4	316
Torreon East	P7	28	C15ET04B	200-250	121.4	-50.7	10.4	-41.8	355.1
Torreon East	P7	28.5	C15ET05C	125-175	124.6	-37.8	11.5	-39.9	341.3
Torreon East	P8	29.8	C15ET07A	225-275	208.1	-68.3	9.4	-64.7	116.1
Torreon East	P8	29.8	C15ET07B	125-175	117.8	-41.5	10	-35.7	348.1
Torreon East	P8	29.8	C15ET07C	125, 175, 275	154.9	-54.8	15.3	-69.7	348.2
Torreon East	P9	31.5	C15ET11D	225, 250, 300	105	-38.8	12.9	-24.4	352.9
Torreon East	P10	32	C15ET12A	225-275	9.6	80.2	1	54.7	258.1
Torreon East	P10	32	C15ET12B	100-150	12.9	46	4.9	76.1	17.3
Torreon East	P10	32	C15ET12D	150, 300, 325	220.4	70.6	0.6	7.2	230.6
Torreon East	OVBK	32.5	C15ET13A	125-175	261.9	85.8	1.2	34.4	242.7
Torreon East	OVBK	32.5	C15ET13B	100, 125, 200	170.4	75	4.5	8.1	257.3

Table B.1. Upper Nacimiento paleomagnetic data: lines.

Location	Paleosol #	Strat. level (m)	Sample	Temp. steps	Strat. Declination	Strat. Inclination	MAD*	Strat. VGP latitude	Strat. VGP longitude
Torreon East	OVBK	32.5	C15ET13C	100-150	200.1	76.5	3.5	11.6	244
Torreon East	P11	33	C15ET14B	100-150	355.4	30.6	13.2	70	85.7
Torreon East	P11	33	C15ET14C	100-150	59.1	50.4	17.4	41.3	330.4
Torreon East	P11	33	C15ET14D	175-225	4.2	50.9	7.4	84.4	33.1
Torreon East	P12	35	C15ET16C	NRM-150	44.3	70.5	14.4	54.5	296.8
Torreon East	P17	46	C15ET44A	200-250	340.9	64.1	12.3	72.6	203
Torreon East	P17	46	C15ET44C	100-150	353.7	69.8	12.2	71.8	240.7
Torreon East	P17	48	C15ET43B	100-150	250.6	72.8	7.9	21	220.6
Torreon East	P17	48	C15ET43C	150-200	350.5	68.6	7.9	72.7	232.7
Torreon East	P17	48	C15ET43D	NRM-125	41.7	60.6	3.5	57.3	319.9
Torreon East	P17	50	C15ET42B	NRM-125	51.9	74.5	16.5	49.1	288.4
Torreon East	P17	50	C15ET42C	150, 175, 225	345.1	36.4	10.2	69.5	116.3
Torreon East	P17	50	C15ET42D	150-200	335.6	61.5	12	70.1	189.6
Torreon East	P19	55	C15ET41C	NRM-125	340.5	76	13.7	60	235.3
Torreon East	P19	55	C15ET41D	150, 175, 225	346.2	63.7	7.7	76	208.8
Torreon East	P19	55.5	C15ET17A	125-175	332.9	24.5	3.7	56.4	126.1
Torreon East	P19	55.5	C15ET17B	100, 225, 275	353.6	21.9	4.3	64.7	87.5
Torreon East	P19	57	C15ET40A	125, 150, 200	331.1	65.2	6.2	65.8	199.4
Torreon East	P19	57	C15ET40B	100-150	354.3	65.8	3.5	77.2	235.2
Torreon East	P19	57	C15ET40C	125, 150, 275	326.4	67.1	5.7	62.1	202.9
Torreon East	P20	58	C15ET18C	225, 275, 300	110.2	-33	13.9	-26.6	346.3
Torreon East	P21	60	C15ET39C	225-275	191.3	-69.5	8.2	-71.1	93.9
Torreon East	P21	60	C15ET39D	250-300	33.1	-81.4	18.2	-21.5	62.9
Torreon East	P22	61	C15ET38A	150, 175, 275	168.5	-15.4	9.5	-59.9	275.9

Table B.1. Upper Nacimiento paleomagnetic data: lines.

Location	Paleosol #	Strat. level (m)	Sample	Temp. steps	Strat. Declination	Strat. Inclination	MAD*	Strat. VGP latitude	Strat. VGP longitude
Torreon East	P22	61	C15ET38C	NRM, 100, 175	164	-36.2	6.1	-68.8	298.4
Torreon East	P22	61	C15ET38D	250-300	189.3	-32.3	0.8	-69.8	226.2
Torreon East	P22	61.5	C15ET37B	175, 200, 275	172.8	-46	2.7	-79.4	290
Torreon East	P22	61.5	C15ET37C	NRM-125	181.6	-60.1	11.5	-84.8	86.2
Torreon East	P22	61.5	C15ET37D	200, 250, 275	143.4	-60	4.3	-61.1	3.7
Torreon East	SS10	61.8	C15ET36A	175, 225, 250	173.2	-50.3	15.7	-82.5	303.5
Torreon East	SS10	61.8	C15ET36B	125-175	171.7	-20.3	13.8	-63.4	271.2
Torreon East	SS10	61.8	C15ET36D	175, 200, 275	162.1	-40.9	4.4	-70.1	308.5
Torreon East	P23	62	C15ET19A	200, 225, 300	214.8	-40.4	4	-57.3	176.3
Torreon East	P23	62	C15ET19C	200-250	141.2	-78	13	-52	49.3
Torreon East	P23	63	C15ET21A	200, 250, 275	135	-39.8	13.6	-48.9	336.4
Torreon East	P23	63	C15ET21B	225-275	145	-68.1	13.3	-60.8	25.2
Torreon East	P23	63	C15ET21D	125-175	141.2	-78	7.3	-55.1	345.7
Torreon East	P23	63.5	C15ET22A	125-175	171.8	-29.6	7.6	-68.6	274.8
Torreon East	P23	63.5	C15ET22B	125, 150, 250	191.5	-45.6	15.9	-76.7	202
Torreon East	P23	63.5	C15ET22D	200, 225, 275	169.3	-34.4	11.9	-70.5	284.4
Torreon East	P23	64	C15ET23A	150, 175, 300	182.1	-48.8	7.7	-83.5	236.4
Torreon East	P23	64	C15ET23B	250-300	164.3	-33.3	11.4	-67.4	294.7
Torreon East	P23	64.5	C15ET24B	225-275	205.4	-61.7	6.2	-69.3	135.5
Torreon East	P23	64.5	C15ET24C	225-275	218.9	-64.3	4.5	-59.3	131.3
Torreon East	P23	64.5	C15ET24D	225-275	204	-61.7	7.1	-70.3	134.9
Torreon East	P23	65	C15ET25B	100, 125, 175	187.7	-50.9	8.9	-82.2	195
Torreon East	P23	65	C15ET25C	250-300	143.6	-49.4	12.4	-59.2	342.6
Torreon East	P23	65	C15ET25D	125, 225, 250	170.3	-63.3	6.4	-78.5	35.9

Table B.1. Upper Nacimiento paleomagnetic data: lines.

Location	Paleosol #	Strat. level (m)	Sample	Temp. steps	Strat. Declination	Strat. Inclination	MAD*	Strat. VGP latitude	Strat. VGP longitude
Torreon East	P24	65.2	C15ET26A	125-175	175	-57.8	10.2	-85.3	15.8
Torreon East	P24	65.2	C15ET26B	150, 250, 300	176.2	-36.8	3.7	-74.2	265.8
Torreon East	P24	65.2	C15ET26C	125-175	203	-46.6	5.7	-68.9	178.9
Torreon East	P24	65.8	C15ET27A	150-200	155.6	-59.3	12.5	-70.4	2.2
Torreon East	P24	65.8	C15ET27C	225-275	214.8	-79.7	2.7	-51.2	90.8
Torreon East	P24	65.8	C15ET27D	250-300	174.8	-82.5	3	-50.7	70.6
Torreon East	P24	66.3	C15ET28B	225-275	155.4	-42.8	7.3	-66.1	321.7
Torreon East	P24	66.3	C15ET28C	150, 175, 250	158.3	-33	5.4	-63.7	305.2
Torreon East	P24	66.3	C15ET28D	150-200	119.4	-42	4.4	-37.1	347.7
Torreon East	P24	66.8	C15ET30A	125-175	124.7	-52	16.1	-44.8	355.3
Torreon East	P24	66.8	C15ET30B	200-250	131.3	-60	8.7	-52	5.3
Torreon East	P24	66.8	C15ET30D	125-175	139.8	-30	14.6	-49.2	324.2
Torreon East	P24	67	C15ET31A	150-200	129.1	-65.6	7.5	-51.1	16.6
Torreon East	P24	67	C15ET31C	150, 175, 250	154.8	-46	20.4	-67	327.8
Torreon East	P24	67	C15ET31D	150-200	134.9	-53.5	9.1	-53.3	353.2
Torreon East	P25	70	C15ET32A	225-275	172.6	-67.3	4.8	-74.9	54.2
Torreon East	P25	70	C15ET32C	225-275	147.3	-55	5.9	-63.6	351.4
Torreon East	P25	70	C15ET32D	225-275	157.5	-57.9	4.2	-72	357.6
Torreon East	P26	71.5	C15ET33A	225-275	163.2	-62.6	4	-74.9	19.7
Torreon East	P26	71.5	C15ET33B	225-275	139.6	-57.4	4.2	-57.9	358.6
Torreon East	P26	71.5	C15ET33D	150-200	155.8	-58.3	8.6	-70.6	358.9
Torreon East	P26	72.5	C15ET34A	175, 275, 300	101.8	-72.6	8.9	-35.9	32.8
Torreon East	P26	72.5	C15ET34B	175, 200, 250	103.4	-62.2	6.5	-32.7	15.7
Torreon East	P26	72.5	C15ET34D	175, 200, 250	100	-66.2	5.4	-32.3	22.3

Table B.1. Upper Nacimiento paleomagnetic data: lines.

Location	Paleosol #	Strat. level (m)	Sample	Temp. steps	Strat. Declination	Strat. Inclination	MAD*	Strat. VGP latitude	Strat. VGP longitude
Torreon East	ss13m	74	C15ET35B	150, 175, 225	192.6	-29.8	3.4	-67	220.2
Torreon East	ss13m	74	C15ET35C	200-250	157	-66.1	6.8	-69	26.3
Escavada Wash	P1	1	C15EM01A	100, 150, 175	213.5	-49.6	4.2	-61.6	164.1
Escavada Wash	P1	1	C15EM01B	125-175	233.2	-67.9	7.6	-49.6	123.8
Escavada Wash	P2	2.6	C15EM02B	150-200	155.6	-25.9	15.1	-58.7	303.2
Escavada Wash	P3	4.3	C15EM03B	225, 275, 300	118.4	-55.8	3.9	-41.2	2.3
Escavada Wash	P3	4.3	C15EM03C	200-250	122.1	-58.7	4	-44.9	5.2
Escavada Wash	P3	4.3	C15EM04B	275-325	109.1	-43.9	4.3	-29.6	354.4
Escavada Wash	P5	5.9	C15EM04B	275-325	149	-64.3	4.4	-64.7	15.8
Escavada Wash	P5	5.9	C15EM04C	150-200	133.1	-53.3	4.8	-51.9	353.5
Escavada Wash	P5	5.9	C15EM04D	250-300	156.9	-52.3	4.8	-70.7	340.1
Escavada Wash	P8	7.2	C15EM05B	275-325	142.8	-26.4	6.2	-50.1	318.7
Escavada Wash	P8	7.2	C15EM05D	275-325	167.4	-26.9	4.3	-65.5	283.2
Escavada Wash	SS05	8.5	C15EM06B	275-325	112.1	-40.6	10.7	-30.8	350.3
Escavada Wash	SS05	8.5	C15EM06D	350-400	181.1	-19	16.7	-63.7	250.2
Escavada Wash	SS06	10	C15EM07B	125-175	1.2	50.7	4.7	85.3	60
Escavada Wash	SS06	10	C15EM07C	125-175	19.6	49	2.9	72.5	357.4
Escavada Wash	SS06	10	C15EM07D	225-275	347.3	66.2	2.1	74.3	220
Escavada Wash	P9	12.5	C15EM08A	275-325	183.9	-60.4	2.1	-83.8	101
Escavada Wash	P9	12.5	C15EM08C	275-325	150.8	-68.3	6.1	-64.1	28.5
Escavada Wash	P9	12.5	C15EM08D	275-325	161.1	-65.9	5.8	-71.5	29.7
Escavada Wash	SS07	13. 8	C15EM09A	275-325	173.9	-53.6	7.5	-84.7	324
Escavada Wash	SS07	13.8	C15EM09B	275-325	160.9	-54.1	2.3	-74.4	343.2
Escavada Wash	SS07	13.8	C15EM09C	225-275	149.9	-47.6	1.8	-63.7	335.2

Table B.1. Upper Nacimiento paleomagnetic data: lines.

Location	Paleosol #	Strat. level (m)	Sample	Temp. steps	Strat. Declination	Strat. Inclination	MAD*	Strat. VGP latitude	Strat. VGP longitude
Escavada Wash	P10	15	C15EM10A	275-325	134.7	-47.8	6	-75.3	318
Escavada Wash	P10	15	C15EM10C	200-250	196.3	-62.1	4.5	-75.5	127.2
Escavada Wash	P10	15	C15EM10D	250-300	180.2	-39.6	5.1	-76.5	251.8
Escavada Wash	P11	16.6	C15EM11A	250-300	184.8	-28.9	4.2	-69	239.6
Escavada Wash	P11	16.6	C15EM11C	250-300	139.7	-48.4	4.7	-55.7	343.2
Escavada Wash	P11	16.6	C15EM11D	225, 300, 325	169.4	-24.4	11	-64.9	277.6
Escavada Wash	P14	17.6	C15EM12A	150-200	183.1	-25.4	13.2	-67.2	244.8
Escavada Wash	P18	19.1	C15EM13A	250-300	173	-53	5	-83.8	321.7
Escavada Wash	P18	19.1	C15EM13B	200-250	159.6	-46.9	1.8	-71	323.8
Escavada Wash	P18	19.1	C15EM13D	275-325	146.4	-58.7	2.2	-63.4	0.2
Escavada Wash	P19	20.5	C15EM14A	225-275	164.5	-61.4	4.1	-76.4	15.9
Escavada Wash	P19	20.5	C15EM14B	275-325	175.2	-34.5	6	-72.4	267.8
Escavada Wash	P19	20.5	C15EM14C	275-325	171.8	-26.4	7.2	-66.7	273.1
Escavada Wash	P21	22	C15EM15B	275-325	189.9	-48.4	2.8	-79.4	198.3
Escavada Wash	P21	22	C15EM15C	225-275	149.2	-63.3	6.5	-65.1	12.9
Escavada Wash	P21	22	C15EM15D	250-300	179.7	-67.1	4.3	-76.2	71.8
Escavada Wash	P24	23.5	C15EM16A	100-150	140.3	-22.6	7.6	-46.8	318.6
Escavada Wash	P24	23.5	C15EM16C	125-175	171.5	-64.6	2.8	-77.7	44
Escavada Wash	P24	23.5	C15EM16D	125-175	151.9	-34	7	-59.8	315.1
Escavada Wash	P26	30.9	C15EM18C	225-275	158.7	-28	13	-61.6	300.1
Escavada Wash	P27	32.3	C15EM19A	250-300	215.6	-66.1	2.2	-61.2	125.8
Escavada Wash	P27	32.3	C15EM19B	250-300	161.5	-38.4	7	-68.4	305.9
Escavada Wash	P27	32.3	C15EM19D	150, 200, 275	225.1	-57.4	6.3	-54.3	145.5
Escavada Wash	P29	34	C15EM20B	275-325	166.8	-45.3	5.6	-75.5	307

Table B.1. Upper Nacimiento paleomagnetic data: lines.

Location	Paleosol #	Strat. level (m)	Sample	Temp. steps	Strat. Declination	Strat. Inclination	MAD*	Strat. VGP latitude	Strat. VGP longitude
Escavada Wash	P29	34	C15EM20C	275-325	154.1	-49.8	4.8	-67.8	336.1
Escavada Wash	SS12	42	C15EM21A	175-225	329.7	50.6	5	64.5	160.9
Escavada Wash	SS12	42	C15EM21B	100, 125, 200	325.4	46.4	5.5	59.6	156.7
Escavada Wash	SS12	42	C15EM21C	100-150	335.7	27.4	6	59.5	124.2
Escavada Wash	SS12	43.3	C15EM22B	100-150	346.4	56.7	4.9	79	173.3
Escavada Wash	SS12	43.3	C15EM22C	100-150	322.5	51.3	3.5	58.8	166.2
Escavada Wash	SS12	43.3	C15EM22D	100-150	341.3	46.2	2.2	72	139.8
Escavada Wash	P30	45	C15EM23B	100-150	330.5	49.3	8.6	64.7	157.8
Escavada Wash	P30	45	C15EM23C	100-150	310.6	54.7	5.3	50.3	176.6
Escavada Wash	P30	46.3	C15EM24A	150-200	360	18.1	4.7	63.3	72.6
Escavada Wash	P31	48	C15EM25B	125, 200, 250	42.1	58.3	9.2	56.8	324.5
Escavada Wash	P32	49.5	C15EM26A	275-325	327.3	38.7	2.8	58.3	145.1
Escavada Wash	SS13	51	C15EM27A	250-300	28.1	48.6	3.8	65.6	349.8
Escavada Wash	SS13	51	C15EM27B	250-300	7.7	39.5	4.3	74.8	44.3
Escavada Wash	SS13	51	C15EM27C	100-150	315.7	63.4	7.3	55.6	191.6
Escavada Wash	P33	52.5	C15EM28A	100, 125, 175	3.9	43.9	9.3	79.2	53.6
Escavada Wash	P33	52.5	C15EM28B	NRM-125	17	68.7	15.1	69.9	284.2
Escavada Wash	P33	52.5	C15EM28D	100-150	351.6	43.2	15.2	77	108.5
Escavada Wash	P33	54	C15EM29C	100-150	25.8	47.5	4.4	67.1	354
Escavada Wash	P33	54	C15EM29D	125, 150, 200	12.1	70.7	18.3	69.3	272.5
Escavada Wash	P35	55.5	C15EM30A	NRM-125	23.8	26.4	7.1	59.3	22.5
Escavada Wash	P35	55.5	C15EM30C	150, 200, 225	28.7	28.2	5.4	56.9	14.5
Escavada Wash	P37	57	C15EM31B	NRM-125	350.1	23.9	4	64.9	95.9
Escavada Wash	P37	57	C15EM31C	NRM, 100, 200	336.7	27.6	5.1	60.2	122.9

Table B.1. Upper Nacimiento paleomagnetic data: lines.

Location	Paleosol #	Strat. level (m)	Sample	Temp. steps	Strat. Declination	Strat. Inclination	MAD*	Strat. VGP latitude	Strat. VGP longitude
Escavada Wash	P37	57	C15EM31D	NRM, 100, 250	16.9	43.6	9.7	72.1	14
Escavada Wash	P39	58.5	C15EM32A	275-325	353.6	69.3	2.9	72.5	239.7
Escavada Wash	P39	58.5	C15EM32C	NRM, 125, 175	324	29.2	6.1	52.1	139.6
Escavada Wash	P39	58.5	C15EM32D	125-175	343.9	48.1	3.8	74.8	140.3
Escavada Wash	P40	59.5	C15EM33A	150-200	20.8	55.2	7.3	73.2	337.4
Escavada Wash	P40	59.5	C15EM33B	150-200	354.5	66.5	3.5	76.4	237.1
Escavada Wash	P40	59.5	C15EM33C	150-200	355.9	62.3	2.5	81.8	231.4
Escavada Wash	P42	59	C15EM34A	NRM, 100, 150	309.2	52	6.9	48.4	173.3
Escavada Wash	P42	59	C15EM34B	NRM, 100, 150	333.8	54.3	4.8	68.7	167.2
Escavada Wash	P42	59	C15EM34D	NRM-125	317.4	62.2	7.8	56.8	188.9
Escavada Wash	SS15	59.5	C15EM35A	225-275	351.4	64.9	1	77.4	224.7
Escavada Wash	SS15	59.5	C15EM35B	125-175	348.9	60.4	2.9	79.8	197.7
Escavada Wash	SS15	59.5	C15EM35D	200-250	357	62.6	3.8	81.7	237.5
Escavada Wash	SS15	59.8	C15EM36B	100-150	338.4	67	7.4	69.2	210.4
Escavada Wash	SS15	59.8	C15EM36D	100-150	340.7	59.7	2.5	74.2	185.2
Escavada Wash	SS16	61.5	C15EM37A	NRM-125	355.9	21.2	13.3	64.7	82.1
Escavada Wash	SS16	61.5	C15EM37B	NRM-125	358.4	38.6	4	75.7	78.6
Escavada Wash	SS16	61.5	C15EM37D	NRM-125	346	44.6	7.4	74.6	127.3
Escavada Wash	P45	63	C15EM38B	NRM-125	348.4	41.7	4.4	74.4	115.6
Escavada Wash	P45	63	C15EM38C	100-150	359.9	53.1	5	87.7	74.6
Escavada Wash	P45	63	C15EM38D	100-150	356.1	30.4	4.9	70	83.6
Escavada Wash	P47	64.5	C15EM39B	200-250	16.2	59.5	5.8	76.6	318.9
Escavada Wash	P47	64.5	C15EM39C	100-150	353.7	49.3	5.5	82.1	116.5
Escavada Wash	P47	64.5	C15EM39D	200-250	354.7	59.6	3.4	83.9	211

Table B.1. Upper Nacimiento paleomagnetic data: lines.

Location	Paleosol #	Strat. level (m)	Sample	Temp. steps	Strat. Declination	Strat. Inclination	MAD*	Strat. VGP latitude	Strat. VGP longitude
Escavada Wash	P47	66	C15EM40A	100-150	8.8	44.4	4.9	77.6	33
Escavada Wash	P47	66	C15EM40B	100, 175, 200	32.4	65	6.8	63.6	307.9
Escavada Wash	P47	66	C15EM40C	NRM-125	83.6	68.3	6	31.1	298.9
Escavada Wash	P48	67.5	C15EM41A	125-175	194.8	86.1	4.2	28.5	250.4
Escavada Wash	P48	67.5	C15EM41B	225, 275, 300	179.6	87.6	12	31.2	252.6
Escavada Wash	P48	67.5	C15EM41D	125, 150, 200	276.6	81.5	7.1	36.1	232
Escavada Wash	P48	69	C15EM42A	NRM, 150, 175	349	75	3.6	63.3	241
Escavada Wash	P48	69	C15EM42C	125-175	308.4	34.4	2.7	41.7	156.2
Escavada Wash	SS21	75.5	C15EM45B	100-150	153.6	-50.3	2.7	-67.5	337.6
Escavada Wash	SS21	75.5	C15EM45C	200, 250, 275	146.2	-52.9	15.8	-62.2	347.4
Escavada Wash	SS21	75.5	C15EM45D	225-275	164.3	-48.7	3.5	-75.4	321.3
Escavada Wash	P52	78	C15EM46B	225-275	207	-77.8	5.9	-55.6	91.2
Escavada Wash	P52	79	C15EM47A	225-275	159.5	-53.5	7.4	-73.1	342
Escavada Wash	P52	79	C15EM47B	150-200	200.3	-59.1	7.7	-73.5	141.7
Escavada Wash	P52	79	C15EM47D	250-300	169.9	-60	15	-80.7	17.4
Escavada Wash	P53	81	C15EM48B	125-175	192	-60.7	12.1	-79.1	127.5
Escavada Wash	P53	81	C15EM48C	100-150	152.4	-57.1	5.3	-67.9	355.3
Escavada Wash	P53	81	C15EM48D	100, 150, 175	155.1	-56.3	7.7	-70	352.5
Escavada Wash	P54	82	C15EM49A	200, 250, 275	191	-78.7	3.7	-57.2	80.1
Escavada Wash	P54	82	C15EM49C	150-200	207.3	-50.2	4.8	-66.8	167.2
Escavada Wash	P54	82	C15EM49D	100-150	229.4	-41.9	16.5	-46.1	164.1
Escavada Wash	P56	84	C15EM50A	150-250	167.4	-57.2	16.7	-79.8	356.5
Escavada Wash	P56	84	C15EM50C	125, 150, 200	207.6	-55.2	7.7	-67.7	155.1

Note. Strat – stratigraphic, *mean angle of deviation.

Table B.2. Upper Nacimiento paleomagnetic data: site means.

Location	Paleosol #	Strat level (m)	Sample #	n*	Strat. Declination	Strat. Inclination	alpha-95	Strat. VGP latitude	Strat. VGP longitude
Kutz	P37	4.5	C15KC48	3	153.7	-67.9	17.1	-66.4	28
Kutz	P5	21.75	C15KC7	3	160.5	-36	26.2	-066.2	303.3
Kutz	P7	26.5	C15KC10	3	188.6	-26.4	14.2	-66.2	231.1
Kutz	P9	27.5	C15KC12	3	180.1	-44.5	6.3	-79.7	251.6
Kutz	P11	30.5	C15KC16	3	351.8	62	24.7	80.8	211.6
Kutz	P12	31.5	C15KC17	3	347.3	38.5	32.3	71.5	112.3
Kutz	P13	32.5	C15KC18	3	1.6	62.9	11.4	82.1	260.4
Kutz	P13	32.75	C15KC19	3	2.9	51.2	19.2	84.8	43.9
Kutz	P14	33.5	C15KC20	3	359	52.9	12.5	86.9	87.5
Kutz	P16	36.5	C15KC24	3	6	50	13	82.4	29.2
Kutz	P24	46	C15KC32	3	357.1	68.9	14.3	74	245.7
Kutz	P26	47.8	C15KC34	3	357	46.3	18.7	80.8	88.9
Kutz	P31	62.25	C15KC39	3	15.9	62.1	30.4	76	307.8
Kutz	P32	67	C15KC42	3	110	-75.9	29.3	-40.9	38.2
Kutz	P33	69	C15KC44	3	171.6	-61.6	27.9	-81	28.8
Escavada Wash	P3	4.3	P16EM03	3	115.8	-52.9	13.6	-38.2	359.8
Escavada Wash	P5	5.9	P16EM04	3	146.2	-57.1	14.7	-63	356.4
Escavada Wash	SS06	10	P16EM07	3	5	55.9	19.9	85.9	334.8
Escavada Wash	P9	12.5	P16EM08	3	167	-65.5	12.7	-74.9	37.1
Escavada Wash	SS07	13.75	P16EM09	3	161	-52.2	12.7	-74	336.6
Escavada Wash	P10	15	P16EM10	3	168.5	-52.6	35.7	-80.1	329.4
Escavada Wash	P11	16.6	P16EM11	3	167	-35.2	34.6	-69.9	290.7
Escavada Wash	P18	19.1	P16EM13	3	160.2	-53.3	14.9	-73.7	340.9
Escavada Wash	P19	20.5	P16EM14	3	171.5	-40.7	29.2	-75.3	284.9

Table B.2. Upper Nacimiento paleomagnetic data: site means.

Location	Paleosol #	Strat level (m)	Sample #	n*	Strat. Declination	Strat. Inclination	alpha-95	Strat. VGP latitude	Strat. VGP longitude
Escavada Wash	P21	22	P16EM15	3	175.3	-60.8	22.3	-83.1	41.9
Escavada Wash	SS12	42	P16EM21	3	330.8	41.6	20	62.1	145.1
Escavada Wash	SS12	43.3	P16EM22	3	336.5	51.8	14.3	70.3	159
Escavada Wash	P33	52.5	P16EM28	3	1.6	52.3	25	86.6	49.1
Escavada Wash	P37	57	P16EM31	3	353	32.7	30.8	70.8	93.2
Escavada Wash	P39	58.5	P16EM32	3	336.5	49.5	35.1	69.6	153.3
Escavada Wash	P42	59	P16EM34	3	320.1	56.6	13.7	58.2	176.8
Escavada Wash	P40	59.5	P16EM33	3	5.4	61.9	14.2	81.8	281.2
Escavada Wash	SS15	59.5	P16EM35	3	352.4	62.7	4.5	80	219.3
Escavada Wash	SS16	61.5	P16EM37	3	353.8	34.9	20.4	72.4	92.3
Escavada Wash	P45	63	P16EM38	3	354.5	41.8	18.6	77.2	95.8
Escavada Wash	P47	64.5	P16EM39	3	0.8	56.6	13.9	88.7	281.1
Escavada Wash	P47	66	P16EM40	3	32.5	62.7	34.8	64	314.4
Escavada Wash	P48	67.5	P16EM41	3	241.4	86.4	8	32.3	245.1
Escavada Wash	SS21	75.5	P16EM45	3	154.9	-50.8	9.4	-68.7	337.7
Escavada Wash	P52	79	P16EM47	3	175.6	-58.7	18.1	-85.1	28.5
Escavada Wash	P53	81	P16EM48	3	165.4	-59.2	17.7	-77.8	6.1
Escavada Wash	P54	82	P16EM49	3	215.7	-57.6	33.5	-61.6	147.3
Torreon West	P22	29.4	C15TW01	3	185.8	-63.4	8.1	-80	97
Torreon West	P24	31.5	C15TW02	3	167	-55.5	16.3	-79.5	346.6
Torreon West	P29	43.2	C15TW19	3	341.7	51.9	34.6	74.5	155
Torreon West	P39	56.7	C15TW20	3	357.8	63.4	5.2	80.9	242.7
Torreon West	P40	61.4	C15TW21	3	352.4	64.3	30.8	78.4	225.4
Torreon West	P43	66.7	C15TW22	3	347.1	62.1	25.8	77.7	203.2
Torreon West	P49	72	C15TW23	3	358	51.2	22.8	85.6	95.1

Table B.2. Upper Nacimiento paleomagnetic data: site means.

Location	Paleosol #	Strat level (m)	Sample #	n*	Strat. Declination	Strat. Inclination	alpha-95	Strat. VGP latitude	Strat. VGP longitude
Torreon West	P53	77.4	C15TW37	3	159	-42.3	32.1	-68.6	315.8
Torreon East	P7	27.75	C15ET03	3	189.7	-67	34.2	-74.6	97
Torreon East	P19	57	C15ET40	3	337.3	66.5	9.3	69	207.9
Torreon East	P22	61	C15ET38	3	173.8	-28.4	24.9	-68.4	269.2
Torreon East	P22	61.5	C15ET37	3	166.8	-56.4	20.6	-79.4	351.8
Torreon East	SS10	61.75	C15ET36	3	169	-37.3	24.9	-72.1	288.1
Torreon East	P23	63	C15ET21	3	138.4	-52.5	22.6	-55.9	350.2
Torreon East	P23	63.5	C15ET22	3	176.7	-36.9	19.2	-74.3	264.2
Torreon East	P23	64.5	C15ET24	3	209.1	-62.7	6.1	-66.4	133.7
Torreon East	P23	65	C15ET25	3	166.6	-56	23.8	-79.2	349.6
Torreon East	P24	65.2	C15ET26	3	184.9	-47.8	23.2	-81.8	221.2
Torreon East	P24	65.75	C15ET27	3	170.7	-75.2	23	-63.2	63.1
Torreon East	P24	66.25	C15ET28	3	145.1	-40.6	27	-57.3	329.4
Torreon East	P24	66.75	C15ET30	3	133	-47.6	25.5	-50	346
Torreon East	P24	67	C15ET31	3	141.6	-55.5	19.4	-59.1	354.3
Torreon East	P25	70	C15ET32	3	157.5	-60.4	13.5	-71.7	6.5
Torreon East	P26	71.5	C15ET33	3	152.3	-59.8	10.2	-67.9	3.3
Torreon East	P26	72.5	C15ET34	3	101.8	-67	8.1	-33.7	23.1

Note. Strat. – stratigraphic, *number of samples used for site means calculations.

Table B.3. Upper Nacimiento summary of $^{40}Ar/^{39}Ar$ results.

ID	Power (watts)	$^{40}Ar/^{39}Ar$	$^{37}Ar/^{39}Ar$	$^{36}Ar/^{39}Ar$ (x 10^{-3})	$^{39}Ar_K$ (x10^{-15} mol)	K/Ca	$^{40}Ar^*$ (%)	Age (Ma)	±1σ (Ma)
H16-SJ-11, Detrital Sanidine, J=0.0018728±0.03%, IC=1.010695±0.0017517, NM-291D, Lab#=65815, Argus VI									
39	4.5	18.96	0.0162	1.725	0.309	31.5	97.3	62.16	0.12
65	4.5	18.60	0.0045	0.4969	0.794	113.3	99.2	62.174	0.047
83	4.5	18.84	0.0110	1.252	0.819	46.3	98.0	62.231	0.048
44	4.5	18.64	0.0032	0.5331	0.926	158.8	99.2	62.269	0.041
80	4.5	18.58	0.0056	0.3124	0.986	91.0	99.5	62.272	0.039
46	4.5	18.66	0.0052	0.5740	0.920	98.6	99.1	62.280	0.041
08	4.5	18.70	0.0088	0.7001	0.861	58.2	98.9	62.286	0.043
79	4.5	18.57	0.0072	0.2567	1.423	71.3	99.6	62.290	0.029
72	4.5	18.66	0.0055	0.5750	0.699	92.1	99.1	62.300	0.052
85	4.5	18.69	0.0045	0.6524	0.846	113.1	99.0	62.311	0.045
06	4.5	18.73	0.0051	0.7722	1.257	99.7	98.8	62.340	0.032
61	4.5	18.70	0.0098	0.6443	0.907	52.0	99.0	62.342	0.041
04	4.5	18.84	0.0060	1.122	1.524	85.0	98.2	62.348	0.028
09	4.5	18.60	0.0066	0.3011	1.438	77.2	99.5	62.356	0.029
07	4.5	19.52	0.0055	3.361	0.802	93.5	94.9	62.394	0.050
27	4.5	19.23	0.0115	2.397	0.592	44.5	96.3	62.399	0.066
17	4.5	19.07	0.0045	1.853	1.214	114.6	97.1	62.400	0.034
05	4.5	18.72	0.0046	0.6558	1.235	109.9	99.0	62.411	0.032
03	4.5	18.62	0.0052	0.3196	2.411	98.7	99.5	62.414	0.018
32	4.5	18.70	0.0073	0.5564	1.063	70.3	99.1	62.426	0.036
52	4.5	18.76	0.0045	0.7667	0.577	114.5	98.8	62.427	0.061
31	4.5	18.79	0.0089	0.8474	0.535	57.0	98.7	62.435	0.072
24	4.5	18.62	0.0048	0.2894	1.283	106.8	99.5	62.439	0.030

Table B.3. Upper Nacimiento summary of $^{40}Ar/^{39}Ar$ results.

ID	Power (watts)	$^{40}Ar/^{39}Ar$	$^{37}Ar/^{39}Ar$	$^{36}Ar/^{39}Ar$ (x 10^{-3})	$^{39}Ar_K$ (x10^{-15} mol)	K/Ca	^{40}Ar* (%)	Age (Ma)	±1σ (Ma)
35	4.5	18.61	0.0071	0.2380	1.160	71.8	99.6	62.444	0.031
77	4.5	18.60	0.0052	0.2157	1.745	98.5	99.7	62.446	0.023
87	4.5	18.61	0.0061	0.2470	1.430	84.1	99.6	62.449	0.027
54	4.5	18.73	0.0058	0.6516	0.903	88.4	99.0	62.456	0.042
64	4.5	18.63	0.0046	0.2954	2.033	111.1	99.5	62.456	0.020
67	4.5	18.72	0.0100	0.6020	1.038	50.8	99.1	62.459	0.039
88	4.5	18.73	0.0111	0.6328	0.883	45.9	99.0	62.462	0.043
66	4.5	18.78	0.0052	0.7859	1.447	97.5	98.8	62.464	0.027
59	4.5	18.68	0.0065	0.4706	1.032	78.4	99.3	62.468	0.039
71	4.5	18.67	0.0076	0.4394	0.986	67.3	99.3	62.469	0.040
43	4.5	18.77	0.0037	0.7539	1.056	137.2	98.8	62.475	0.037
56	4.5	18.91	0.0108	1.214	0.543	47.2	98.1	62.484	0.068
26	4.5	18.67	0.0055	0.4128	2.265	92.6	99.3	62.484	0.019
78	4.5	18.70	0.0053	0.5131	1.087	95.5	99.2	62.487	0.038
12	4.5	18.69	0.0031	0.4843	1.988	164.7	99.2	62.490	0.021
74	4.5	18.69	0.0040	0.4660	1.423	126.1	99.3	62.490	0.028
23	4.5	18.75	0.0041	0.6532	1.549	124.3	99.0	62.494	0.027
33	4.5	18.69	0.0051	0.4473	1.920	100.7	99.3	62.496	0.021
19	4.5	18.73	0.0072	0.6112	0.991	71.1	99.0	62.500	0.039
29	4.5	18.67	0.0032	0.3961	1.452	158.1	99.4	62.500	0.027
25	4.5	18.78	0.0048	0.7506	2.293	106.6	98.8	62.501	0.019
53	4.5	18.73	0.0057	0.5935	1.160	89.5	99.1	62.502	0.034
82	4.5	18.82	0.0058	0.9105	1.509	87.8	98.6	62.502	0.029
48	4.5	18.70	0.0051	0.4923	0.738	99.7	99.2	62.509	0.052
34	4.5	18.67	0.0054	0.3885	1.140	94.2	99.4	62.512	0.035

Table B.3. Upper Nacimiento summary of $^{40}Ar/^{39}Ar$ results.

ID	Power (watts)	$^{40}Ar/^{39}Ar$	$^{37}Ar/^{39}Ar$	$^{36}Ar/^{39}Ar$ (x 10^{-3})	$^{39}Ar_K$ (x10^{-15} mol)	K/Ca	$^{40}Ar^*$ (%)	Age (Ma)	±1σ (Ma)
60	4.5	18.67	0.0027	0.3785	1.064	190.2	99.4	62.513	0.035
22	4.5	18.67	0.0024	0.3638	0.885	216.5	99.4	62.516	0.042
84	4.5	18.69	0.0068	0.4535	1.402	74.6	99.3	62.519	0.028
86	4.5	18.63	0.0057	0.2374	1.349	88.8	99.6	62.524	0.029
58	4.5	18.71	0.0048	0.4906	1.204	105.5	99.2	62.546	0.033
30	4.5	18.85	0.0049	0.9480	1.043	104.5	98.5	62.555	0.039
15	4.5	18.77	0.0047	0.6691	1.537	107.7	98.9	62.556	0.027
41	4.5	18.69	0.0045	0.4059	1.698	113.2	99.4	62.557	0.024
62	4.5	18.76	0.0031	0.6351	1.190	163.5	99.0	62.561	0.034
63	4.5	18.75	0.0040	0.5922	1.375	126.9	99.1	62.563	0.029
21	4.5	18.73	0.0044	0.5220	1.249	115.6	99.2	62.570	0.034
18	4.5	18.74	0.0054	0.5593	1.357	94.3	99.1	62.577	0.029
89	4.5	18.64	0.0055	0.2137	2.039	92.5	99.7	62.584	0.020
68	4.5	18.74	0.0066	0.5386	1.298	77.4	99.2	62.603	0.030
76	4.5	18.72	0.0033	0.4339	1.266	155.8	99.3	62.613	0.031
45	4.5	18.73	0.0059	0.4501	1.904	87.1	99.3	62.647	0.022
47	4.5	18.80	0.0032	0.6781	0.680	158.6	98.9	62.653	0.057
38	4.5	18.73	0.0056	0.4189	2.099	91.8	99.3	62.665	0.021
69	4.5	18.79	0.0048	0.2733	1.730	105.5	99.6	63.018	0.024
70	4.5	20.30	0.0062	0.2579	1.206	82.4	99.6	68.007	0.035
51	4.5	20.48	0.0034	0.8047	1.137	149.2	98.8	68.075	0.036
13	4.5	20.43	0.0059	0.6202	1.859	86.9	99.1	68.112	0.023
73	4.5	20.36	0.0030	0.3138	1.392	169.0	99.5	68.156	0.031
40	4.5	20.50	0.0040	0.4815	2.593	126.3	99.3	68.454	0.019
57	4.5	20.55	0.0048	0.6314	0.965	105.3	99.1	68.473	0.044

Table B.3. Upper Nacimiento summary of $^{40}Ar/^{39}Ar$ results.

ID	Power (watts)	$^{40}Ar/^{39}Ar$	$^{37}Ar/^{39}Ar$	$^{36}Ar/^{39}Ar$ (x 10^{-3})	$^{39}Ar_K$ (x10^{-15} mol)	K/Ca	$^{40}Ar^*$ (%)	Age (Ma)	±1σ (Ma)
49	4.5	20.85	0.0019	0.3680	1.350	269.5	99.5	69.740	0.031
75	4.5	21.06	0.0079	0.6135	0.830	64.5	99.1	70.172	0.049
81	4.5	20.95	0.0044	0.2100	2.826	115.9	99.7	70.228	0.018
55	4.5	22.94	0.0029	3.425	0.422	177.9	95.6	73.66	0.10
02	4.5	32.49	0.0090	0.9612	1.675	56.6	99.1	107.18	0.18
42	4.5	68.99	0.0201	1.217	0.965	25.4	99.5	221.32	0.70
37	4.5	91.91	-0.0548	4.230	0.253	-	98.6	287.0	2.6
11	4.5	109.5	0.0248	1.153	0.802	20.6	99.7	340.4	1.3
10	4.5	130.2	-0.0010	1.411	0.958	-	99.7	398.4	1.5
01	4.5	205.1	0.0556	3.279	0.195	9.2	99.5	592.6	4.4
16	4.5	234.6	0.0151	6.574	0.532	33.8	99.2	662.1	3.9
20	4.5	475.0	0.0112	1.869	0.701	45.5	99.9	1163.8	9.0
50	4.5	501.0	0.0451	1.870	0.517	11.3	99.9	1210.4	9.7
	Mean age ± 1σ		n=66	MSWD=9.8				62.48	0.02

Notes. Isotopic ratios corrected for blank, radioactive decay, and mass discrimination, not corrected for interfering reactions. Errors quoted for individual analyses include analytical error only, without interfering reaction or J uncertainties. Mean age is weighted mean age of Taylor (1982). Mean age error is weighted error of the mean (Taylor, 1982), multiplied by the root of the MSWD where MSWD>1, and also incorporates uncertainty in J factors and irradiation correction uncertainties. Isotopic abundances after Steiger and Jäger (1977). IC = measured $^{40}Ar/^{36}Ar$ of air standard divided by 295.5. Ages calculated relative to FC-2 Fish Canyon Tuff sanidine interlaboratory standard at 28.201 Ma. Decay Constant (LambdaK (total)) = 5.463e-10/a. Correction factors: $(^{39}Ar/^{37}Ar)_{Ca}$ = 0.0007115 ± 0.000009, $(^{36}Ar/^{37}Ar)_{Ca}$ = 0.0002755 ± 0.0000010, $(^{40}Ar/^{39}Ar)_K$ = 0.0088 ± 0.0004

APPENDIX C

Upper Nacimiento Formation pedotypes

Table C.1. Upper Nacimiento description of pedotypes.

Pedotype	Horizon	Depth	Texture	Structure	Colors	Slicks	Ca-features	Biologic	Sed-structures
1: Vertisol	Bss1	0-210	silty clay	3csbk	5YR5/1	cd	--	--	--
	Bss2	210-306	sandy clay	3cwe/sbk	5YR5/2	cd	--	--	--
	Bss3	306-389	sandy clay	2cwe	5YR5/2	cd	--	--	--
2: Vertisol	Bk	0-80	vfs clay	2msbk	10R3/1	--	nodules: 5mm	fine rooting	--
	Bkss	80-159	vfs clay	2msbk	10R3/1	cd	nodules: 1-5 mm	--	--
	Bk/C	159+	vfs clay	m	2.5YR4/2	--	nodules: 10 mm matrix: disseminated	--	--
3: Inceptisol	Bw	0-110	fs clay	3f/msbk	10R4/3	--	--	fine drab root halos	--
	C	110+	fs	m	10R 5/2	--	--	meniscate back filled burrows	--
4: Vertisol	Bss	0-103	silty clay	3cwe	7.5YR4/1	cd	--	fine rooting	--
	Bssg	103-157	silty clay	2cwe	GY1 6/5GY	cd	--	--	--
	Cg	157+	fs	m	GY1 6/5GY	--	--	--	fine horizonal laminations

Table C.1. Upper Nacimiento description of pedotypes.

Pedotype	Horizon	Depth	Texture	Structure	Colors	Slicks	Ca-features	Biologic	Sed-structures
5: Inceptisol	Bg	0-98	vfs clay	1csbk	GY1 6/5GY	--	--	fine rooting	--
	C	98+	vfs			--	--	--	massive
6: Vertisol	Bss1	0-60	clay	3msbk	5Y2.5/1	cd	--	--	--
	Bss2	60-142	clay	3csbk	5Y4/4	cd	--	--	--
7: Entisol	B/C	0-155	vfs	1cabk	10R6/2	--	--	fine rooting	--

BIBLIOGRAPHY

Archibald, J.D., 1998, Archaic ungulates ("Condylarthra"), *in* Janis, C.M., Scott, K.M., and Jacobs, L. L., eds., Evolution of Tertiary Mammals of North America. Terrestrial Carnivores, Ungulates, and Ungulate like Mammals, Volume 1: Cambridge, Cambridge University Press, p. 292–331.

Archibald, J. D., Clemens, W. A., Gingerich, P. H., Krause, D. W., Lindsay, E. H., and Rose, K. D., 1987, First North American land mammal ages of the Cenozoic Era, *in* Woodburne, M. O., ed., Cenozoic mammals of North America: Berkeley, University of California Press, p. 24–76.

Atchley, S.C., Nordt, L.C., and Dworkin, S.I., 2004, Eustatic control on alluvial sequence stratigraphy: A possible example from the Cretaceous-Tertiary transition of the Tornillo Basin, Big Bend National Park, West Texas, USA: Journal of Sedimentary Research, v. 74, p. 391–404, https://doi.org/10.1306/102203740391.

Atchley, S. C., Nordt, L. C., Dworkin, S. I., Cleveland, D. M., Mintz, J. S., and Harlow, R. H., 2013, Alluvial stacking pattern analysis and sequence stratigraphy: concepts and case studies, *in* New Frontiers in Paleopedology and Terrestrial Paleoclimatology. SEPM Special Publication: p. 109–129.

Baltz, E.H., 1967, Stratigraphy and regional tectonic implications of part of Upper Cretaceous and Tertiary rocks, East-Central San Juan Basin, New Mexico: U.S. Geological Survey Professional Paper, v. 552, 101 p.

Bataille, C.P., Watford, D., Ruegg, S., Lowe, A., and Bowen, G.J., 2016, Chemostratigraphic age model for the Tornillo Group: A possible link between fluvial stratigraphy and climate: Palaeogeography, Palaeoclimatology, Palaeoecology, v. 457, p. 277–289, https://doi.org/10.1016/j.palaeo.2016.06.023.

Befus, K.S., Hanson, R.E., Lehman, T.M., and Griffin, W.R., 2008, Cretaceous basaltic phreatomagmatic volcanism in west Texas: maar complex at Pena Mountain, Big Bend National Park: Journal of Volcanology and Geothermal Research, v. 173, p. 245–264, https://doi.org/10.1016/j.jvolgeores.2008.01.021.

Breyer, J.A., Busbey, A.B., III, Hanson, R.E., Befus, K.E., Griffin, W.R., Hargrove, U.S., and Bergman, S.C., 2007, Evidence for Late Cretaceous volcanism in Trans-Pecos Texas: The Journal of Geology, v. 115, p. 243–251, https://doi.org/10.1086/510640.

Brochu, C.A., 2000, *Borealosuchus* (Crocodylia) from the Paleocene of Big Bend National Park, Texas: Journal of Paleontology, v. 74, p. 181–187, https://doi.org/10.1017/S0022336000031358.

Brusatte, S.L., Butler, R.J., Barrett, P.M., Carrano, M.T., Evans, D.C., Lloyd, G.T., Mannion, P.D., Norell, M.A., Peppe, D.J., Upchurch, P., and Williamson, T.E., 2015, The extinction of dinosaurs: Biological Reviews of the Cambridge Philosophical Society, v. 90, p. 628–642, https://doi.org/10.1111/brv.12128.

Buehler, H.A., Weissmann, G.S., Scuderi, L.A., Hartley, A.J., 2011, Spatial and temporal evolution of an avulsion on the Taquari River distributive fluvial system from satellite image analysis: Journal of Sedimentary Research, v. 81, p. 630-640.

Butler, R. F., and Lindsay, E. H., 1985, Mineralogy of Magnetic Minerals and Revised Magnetic Polarity Stratigraphy of Continental Sediments, San Juan Basin, New Mexico: The Journal of Geology, v. 93, p. 535–554.

Butler, R. F., Lindsay, E. H., Jacobs, L. L., and Johnson, N. M., 1977, Magnetic stratigraphy of the Cretaceous-Tertiary boundary in the San Juan Basin: Nature, v. 267, p. 318–323.

Butler, R. F., and Taylor, L. H., 1978, A middle Paleocene paleomagnetic pole from the Nacimiento Formation, San Juan Basin, New Mexico: Geology, v. 6, p. 495–498.

Cande, S. C., and Kent, D. V., 1992, A new geomagnetic polarity time scale for the Late Cretaceous and Cenozoic: Journal of Geophysical Research, v. 97, p. 13917–13951.

Carr, T.D., and Williamson, T.E., 2000, A review of Tyrannosauridae (Dinosauria, Coelurosauria) from New Mexico: New Mexico Museum of Natural History and Science: Bulletin, v. 17, p. 113–146.

Carr, T.D., and Williamson, T.E., 2004, Diversity of late Maastrichtian Tyrannosauridae (Dinosauria: Theropoda) from western North America: Zoological Journal of the Linnean Society, v. 142, p. 479–523, https://doi.org/10.1111/j.1096-3642.2004.00130.x.

Cather, S. M., 2004, Laramide orogeny in central and northern New Mexico and southern Colorado, *in* Mack, G. H., Giles K. A. eds., Geology of New Mexico: a geologic history: New Mexico Geological Society, Special Publication 11, p. 202–248.

Chakraborty, T., Ghosh, P., 2010, The geomorphology and sedimentology of the Tista megafan, Darjeeling Himalaya: Implications for megafan building processes: Geomorphology, v. 115, p. 252-266.

Chapin, C. E., and Cather, S. M., 1983, Eocene tectonics and sedimentation in the Colorado Plateau-Rocky Mountain area: Arizona Geological Society Digest, v. 14, p. 173–198.

Cifelli, R.I., 1995, Therian mammals of the Terlingua Local Fauna (Judithian), Aguja Formation, Big Bend of the Rio Grande, Texas: Contributions to Geology, University of Wyoming, v. 30, p. 117–136.

Cifelli, R.L., Eberle, J.J., Lofgren, D.L., Lillegraven, J.A., and Clemens, W.A., 2004, Mammalian biochronology of the Latest Cretaceous, *in* Woodburne, M.O., ed., Late Cretaceous and Cenozoic Mammals of North America: New York, Columbia University Press, p. 21–42, https://doi.org/10.7312/wood13040-004.

Clemens, W.A., 2006, Early Paleocene (Puercan) peradectid marsupials from northeastern Montana: North American Western Interior: Palaeontographica Abteilung A, v. 27, p. 19–31.

Clemens, W.A., 2011, *Eoconodon* ("Triisodontidae," Mammalia) from the Early Paleocene (Puercan) of northeastern Montana, USA: Palaeontologia Electronica, v. 14, no. 3, 22 p.

Clemens, W.A., and Williamson, T.A., 2005, A new species of *Eoconodon* (Triisodontidae, Mammalia) from the San Juan Basin, New Mexico: Journal of Vertebrate Paleontology, v. 25, p. 208–213, https://doi.org/10.1671/0272-4634(2005)025[0208:ANSOET]2.0.CO;2.

Clyde, W.C., Ramezani, J., Johnson, K.R., Bowring, S.A., and Jones, M.M., 2016, Direct high-precision U-Pb geochronology of the end-Cretaceous extinction and calibration of Paleocene astronomical timescales: Earth and Planetary Science Letters, v. 452, p. 272–280, https://doi.org/10.1016/j.epsl.2016.07.041.

Cobb, J., 2016, Sedimentology of the Cretaceous-Paleogene boundary interval in the Tornillo Group of West Texas [M.S. thesis]: Lubbock, Texas Tech University, 163 p.

Colbert, E.H., and Bird, R.T., 1954, A gigantic crocodile from the Upper Cretaceous beds of Texas: American Museum Novitates, v. 1688, p. 1–22.

Cope, E.D., 1881a, Mammalia of the lower Eocene beds: American Naturalist, v. 15, p. 337–338.

Cope, E.D., 1881b, On some Mammalia of the lowest Eocene beds of New Mexico: Proceedings of the American Philosophical Society, v. 19, p. 484–495.

Cope, E.D., 1881c, The temporary dentition of a new creodont: American Naturalist, v. 15, p. 667–669.

Cope, E.D., 1881d, Mammalia of the lowest Eocene: American Naturalist, v. 15, p. 829–831.

Cope, E.D., 1882a, Two new genera of the Puerco Eocene: American Naturalist, v. 16, p. 417–418.

Cope, E.D., 1882b, The Periptychidae: American Naturalist, v. 16, p. 832–833.

Cope, E.D., 1883, First addition to the fauna of the Puerco Eocene: Proceedings of the American Philosophical Society, v. 20, p. 545–563.

Cope, E.D., 1884, The Tertiary Marsupialia: American Naturalist, v. 18, no. 7, p. 686–697, https://doi.org/10.1086/273711.

Cope, E.D., 1888, Synopsis of the vertebrate fauna of the Puerco series: Transactions of the American Philosophical Society, v. 16, p. 298–361, https://doi.org/10.2307/1005393.

Davidoff, A.J., and Yancey, T.E., 1993, Eustatic cyclicity in the Paleocene and Eocene: Data from the Brazos River Valley, Texas: Tectonophysics, v. 222, p. 371–395.

Davidson, S.K., Hartley, A.J., Weissmann, G.S., Nichols, G.J., Scuderi, L.A., 2013, Geomorphic elements on modern distributive fluvial systems: Geomorphology, v. 180-181, p. 82-95.

Davies, K.L., 1983, Hadrosaurian dinosaurs of Big Bend National Park, Brewster County, Texas [M.S. thesis]: Austin, University of Texas, 235 p.

Davis, A. J., Peppe, D. J., Atchley, S. C., Williamson, T. E., and Flynn, A. G., 2016, Climate and landscape reconstruction of the Arroyo Chijuillita Member of the Nacimiento Formation, San Juan Basin, New Mexico: Providing environmental context to early Paleocene mammal evolution: Palaeogeography, Palaeoclimatology, Palaeoecology, v. 463, p. 27–44.

Dekkers, M.J., 1989, Magnetic properties of natural goethite - II. TRM behaviour during thermal and alternating field demagnetization and low-temperature treatment: Geophysical Journal International, v. 97, p. 341–355, https://doi.org/10.1111/j.1365-246X.1989.tb00505.x.

Dickinson, W.R., and Suczek, C.A., 1979, Plate tectionics and sandstone compositions: AAPG Bulletin, v. 63, p. 2164–2182.

Donahue, M.S., 2016, Episodic uplift of the Rocky Mountains: Evidence from U-Pb detrital zircon geochronolgy and low-temperature thermochronology with a chapter on using mobile technology for geoscience education [Ph.D. thesis]: University of New Mexico: Albuquerque, New Mexico, 1177 p.

Dunlop, D. J., and Ozdemir, O., 1997, Rock Magnetism. Fundamentals and Frontiers: New York, Cambrdige University Press, 573 p.

Dworkin, S., Nordt, L., and Atchley, S., 2005, Determining terrestrial paleotemperatures using the oxygen isotopic composition of pedogenic carbonate: Earth and Planetary Science Letters, v. 237, p. 56–68, https://doi.org/10.1016/j.epsl.2005.06.054.

Erez, J., and Luz, B., 1983, Experimental paleotemperature equation for planktonic foraminifera: Geochimica et Cosmochimica Acta, v. 47, p. 1025–1031, https://doi.org/10.1016/0016-7037(83)90232-6.

Fastovsky, D.E., and Bercovici, A., 2016, The Hell Creek Formation and its contribution to the Cretaceous-Paleogene extinction: A short primer: Cretaceous Research, v. 57, p. 368–390, https://doi.org/10.1016/j.cretres.2015.07.007.

Fastovsky, D.E., and Sheehan, P.M., 2005, The extinction of the dinosaurs in North America: GSA Today, v. 15, p. 4–10, https://doi.org/10.1130/1052-5173(2005)15<4:TEOTDI>2.0.CO;2.

Fisher, R.A., 1953, Dispersion of a sphere: Proceedings of the Royal Society of London, v. A217, p. 295–305, https://doi.org/10.1098/rspa.1953.0064.

Forster, C.A., Sereno, P.C., Evans, T.W., and Rowe, T.B., 1993, A complete skull of *Chasmosaurus mariscalensis* (Dinosauria: Ceratopsidae) from the Aguja Formation (late Campanian) of west Texas: Journal of Vertebrate Paleontology, v. 13, p. 161–170, https://doi.org/10.1080/02724634.1993.10011498.

France, D.E., and Oldfield, F., 2000, Identifying goethite and hematite from rock magnetic measurements of soils and sediments: Journal of Geophysical Research, v. 105, p. 2781–2795, https://doi.org/10.1029/1999JB900304.

Fronimos, J.A., and Lehman, T.M., 2014, New specimens of a titanosaur sauropod from the Maastrichtian of Big Bend National Park, Texas: Journal of Vertebrate Paleontology, v. 34, p. 883–899, https://doi.org/10.1080/02724634.2014.840308.

Gazin, C.L., 1939, A further contribution to the Dragon Paleocene fauna of central Utah: Journal of the Washington Academy of Sciences, v. 29, p. 273–286.

Gingerich, P.D., and Winkler, D.A., 1985, Systematics of Paleocene Viverravidae (Mammalia, Carnivora) in the Bighorn Basin and Clark's Fork Basin, Wyoming: Contributions from the Museum of Paleontology: The University of Michigan, v. 27, p. 87–128.

Gradstein, F.M., Ogg, J.G., Schmitz, M., and Ogg, G., 2012, The geologic time scale 2012: Boston, Elsevier, 1176 p.

Granger, W., 1917, Notes on Paleocene and lower Eocene mammal horizons of northern New Mexico and southern Colorado: Bulletin of the American Museum of Natural History, v. 37, p. 821–830.

Gulliford, A.R., Flint, S.S., and Hodgson, D.M., 2014, Testing applicability of models of distributive fluvial systems or trunk rivers in ephemeral systems: Reconstructing 3-D fluvial architecture in the Beaufort Group, South Africa: Journal of Sedimentary Research, v. 84, p. 1147-1169.

Gunnell, G.F., 1989, Evolutionary history of Microsyopoidea (Mammalia? Primates) and the relationship between Plesiadapiformes and Primates: University of Michigan Papers on Paleontology, no. 27, 157 p.

Guyodo, Y., LaPara, T. M., Anschutz, A. J., Penn, R. L., Banerjee, S. K., Geiss, C. E., and Zanner, W., 2006, Rock magnetic, chemical and bacterial community analysis of a modern soil from Nebraska: Earth and Planetary Science Letters, v. 251, p. 168–178.

Hartley, A.J., Weissmann, G.S., Bhattacharayya, P., Nichols, G.J., Scuderi, L.A., Davidson, S.K., Leleu, S., Chakraborty, T., Parthasarthi, G., and Mather, A.E., 2012, Soil development on modern distributive fluvial systems: preliminary observations with implications for interpretation of paleosols in the rock record: SEPM Special Publication 104, p. 149-158.

Hartley, A.J., Weissmann, G.S., Nichols, G.J., Warwick, G.L., 2010, Large distributive fluvial systems: Characteristics, distribution, and controls on development: Journal of Sedimentary Research, v. 80, p. 167-183.

Hobbs, K.M., 2016, Sedimentation, pedogenesis, and paleoclimate conditions in the Paleocene San Juan Basin, New Mexico, U.S.A. [Ph.D. thesis]: University of New Mexico, Albuquerque, 160 p.

Hunt, R.K., and Lehman, T.M., 2008, Attributes of the ceratopsian dinosaur *Torosaurus*, and new material from the Javelina Formation (Maastrichtian) of Texas: Journal of Paleontology, v. 82, p. 1127–1138, https://doi.org/10.1017/S0022336000055335.

Huxley, T.H., 1880, On the application of the laws of evolution to the arrangement of the Vertebrata and more particularly of the Mammalia: Proceedings of the Zoological Society of London, v. 43, p. 649–662.

Illiger, C., 1811, Prodromus systematis mammalium et avium additis terminis zoographicis utriusque classis, Berlin, C. Salfeld, https://doi.org/10.5962/bhl.title.106965.

Jasinski, S.E., and Sullivan, R.M., 2011, Re-evaluation of Pachycephalosaurids from the Fruitland-Kirtland transition (Kirtlandian, Late Campanian), San Juan Basin, New Mexico, with a description of a new species of *Stegoceras* and a reassessment of *Texacephale langstoni*: New Mexico Museum of Natural History and Science: Bulletin, v. 53, p. 202–215.

Jepsen, G.L., 1930, New vertebrate fossils from the lower Eocene of the Bighorn Basin, Wyoming: Proceedings of the American Philosophical Society, v. 69, no. 1, p. 117–131.

Kirschvink, J.L., 1980, The least-squares line and plane and the analysis of palaeomagnetic data: Geophysical Journal International, v. 62, p. 699–718, https://doi.org/10.1111/j.1365-246X.1980.tb02601.x.

Kodama, K. P., 1997, A successful rock magnetic technique for correcting paleomagnetic inclination shallowing: Case study of the Nacimiento Formation, New Mexico: Journal of Geophysical Research, v. 102, p. 5193–5205.

Kuiper, K.F., Deino, A., Hilgren, F.J., Krijgsman, W., Renne, P.R., and Wijbrans, J.R., 2008, Synchronizing rock clocks of Earth History: Science, v. 320, p. 500–504, https://doi.org/10.1126/science.1154339.

Larson, D.W., and Currie, P.J., 2013, Multivariate Analyses of Small Theropod Dinosaur Teeth and Implications for Paleoecological Turnover through Time: PLoS One, v. 8, p. e54329, https://doi.org/10.1371/journal.pone.0054329.

Lawson, D.A., 1972, Paleoecology of the Tornillo Formation, Big Bend National Park, Brewster County, Texas [M.S. thesis]: Austin, The University of Texas at Austin, 182 p.

Lawson, D.A., 1975, Pterosaur from the Latest Cretaceous of West Texas: Discovery of the largest flying creature: Science, v. 187, p. 947–948, https://doi.org/10.1126/science.187.4180.947.

Lawson, D.A., 1976, *Tyrannosaurus* and *Torosaurus*, Maestrichtian dinosaurs from Trans-Pecos, Texas: Journal of Paleontology, v. 50, p. 158–164.

Lawton, T.F., Schellenbach, W.L., Nugent, A.E., 2014, Late Cretaceous fluvial-megafan and axial-river systems in the southern Cordilleran foreland basin: Drip Tank Member of Straight Cliffs Formation and adjacent strata, southern Utah, U.S.A.: Journal of Sedimentary Research, v. 84, p. 407-434.

Lehman, T.M., 1982, A ceratopsian bone bed from the Aguja Formation (Upper Cretaceous), Big Bend National Park, Texas [M.S. thesis]: Austin, University of Texas, 209 p.

Lehman, T.M., 1985, Stratigraphy, sedimentology, and paleontology of Upper Cretaceous (Campanian-Maastrichtian) sedimentary rocks in Trans-Pecos, Texas [Ph.D. thesis]: Austin, University of Texas, 299 p.

Lehman, T.M., 1986, Late Cretaceous sedimentation in Trans-Pecos Texas, *in* Pause, P.H., and Spears, R.G., eds., Geology of the Big Bend Area and Solitario Dome, Texas: West Texas Geological Society, Fieldtrip Guidebook, no. 86-82, p. 105–110.

Lehman, T.M., 1987, Late Maastrichtian paleoenvironments and dinosaur biogeography in the western interior of North America: Palaeogeography, Palaeoclimatology, Palaeoecology, v. 60, p. 189–217, https://doi.org/10.1016/0031-0182(87)90032-0.

Lehman, T.M., 1989a, Upper Cretaceous (Maastrichtian) paleosols in Trans-Pecos Texas: Geological Society of America Bulletin, v. 101, p. 188–203, https://doi.org/10.1130/0016-7606(1989)101<0188:UCMPIT>2.3.CO;2.

Lehman, T.M., 1989b, *Chasmosaurus mariscalensis*, sp. nov., a new ceratopsian dinosaur from Texas: Journal of Vertebrate Paleontology, v. 9, p. 137–162, https://doi.org/10.1080/02724634.1989.10011749.

Lehman, T.M., 1990, Paleosols and the Cretaceous/Tertiary transition in the Big Bend region of Texas: Geology, v. 18, p. 362–364, https://doi.org/10.1130/0091-7613(1990)018<0362:PATCTT>2.3.CO;2.

Lehman, T.M., 1991, Sedimentation and tectonism in the Laramide Tornillo Basin of West Texas: Geology, v. 18, p. 363–364.

Lehman, T.M., 1997, Late Campanian dinosaur biogeography in the western interior of North America, *in* Wolberg, D., and Stump, E., eds., Dinofest International Proceedings: Philadelphia, The Academy of Natural Sciences, p. 223–240.

Lehman, T.M., 1998, A gigantic skull and skeleton of the horned dinosaur *Pentaceratops sternbergi* from New Mexico: Journal of Paleontology, v. 72, p. 894–906.

Lehman, T.M., 2001, Late Cretaceous Dinosaur Provinciality, *in* Tanke, D., and Carpenter, K., eds., Mesozoic Vertebrate Life: Bloomington and Indianapolis, Indiana University Press, p. 310–328.

Lehman, T.M., 2010, Pachycephalosauridae from the San Carlos and Aguja Formations (Upper Cretaceous) of West Texas, and observations of the frontoparietal dome: Journal of Vertebrate Paleontology, v. 30, p. 786–798, https://doi.org/10.1080/02724631003763532.

Lehman, T.M., and Barnes, K., 2010, Champsosaurus (Diapsida: Choristodera) from the Paleocene of West Texas: paleoclimatic implication: Journal of Paleontology, v. 84, p. 341–345, https://doi.org/10.1666/09-111R.1.

Lehman, T.M., and Busbey, A.B., 2007, Big Bend Field Trip Guidebook, *in* Society of Vertebrate Paleontology: 67th Annual Meeting, Field Trip Guidebook, 69 p.

Lehman, T.M., and Coulson, A.B., 2002, A juvenile specimen of the sauropod dinosaur *Alamosaurus sanjuanensis* from the Upper Cretaceous of Big Bend National Park, Texas: Journal of Paleontology, v. 76, p. 156–172, https://doi.org/10.1666/0022-3360(2002)076<0156:AJSOTS>2.0.CO;2.

Lehman, T.M., Mcdowell, F.W., and Connelly, J.N., 2006, First isotopic (U-Pb) age for the Late Cretaceous Alamosaurus vertebrate fauna of West Texas, and its significance as a link between two faunal provinces: Journal of Vertebrate Paleontology, v. 26, p. 922–928, https://doi.org/10.1671/0272-4634(2006)26[922:FIUAFT]2.0.CO;2.

Leslie, C., Peppe, D., Williamson, T., Bilardello, D., Heizler, M., Secord, R., and Leggett, T., *in press*, High-resolution magnetostratigraphy of the upper Nacimiento Formation, San Juan Basin, New Mexico, USA: Implications for basin evolution and mammalian turnover: American Journal of Science.

Leslie, C.E., Secord, R., Peppe, D.J., Atchley, S., Williamson, T.E., Nordt, L.C., and Brusatte, S., 2016, Climatic and depositional history of the lower Paleocene Upper Nacimiento Formation, San Juan Basin, New Mexico: Geological Society of America Abstracts with Programs, v. 48, no. 7, https://doi.org/10.1130/abs/2016AM-287214

Li, L., and Keller, G., 1998a, Maastrichtian climate, productivity and faunal turnovers in planktic foraminifera in south Atlantic DSDP sites 525 and 21: Marine Micropaleontology, v. 33, p. 55–86, https://doi.org/10.1016/S0377-8398(97)00027-3.

Li, L., and Keller, G., 1998b, Abrupt deep-sea warming at the end of the Cretaceous: Geology, v. 26, p. 995–998, https://doi.org/10.1130/0091-7613(1998)026<0995:ADSWAT>2.3.CO;2.

Linnaeus, C., 1758, Systema naturae per regna tria naturae, secundum classes, ordines, genera, species, cum characteribus, differentiis, synonymis, locis, v. 1: Regnum animale, Stockholm, Laurentii Salvii, Editio decima, reformata.

Lindsay, E., 2003, Chronostratigraphy, biochronology, datum events, land mammal ages, stage of evolution, and appearance event ordination, *in* Flynn, L. J., editor, Vertebrate fossils and their context: contributions in honor of Richard H. Tedford: Bulletin of the American Museum of Natural History, v. 279, p. 212–230.

Lindsay, E. H., Butler, R. F., and Johnson, N. M., 1981, Magnetic polarity zonation and biostratigraphy of Late Cretaceous and Paleocene continental deposits, San Juan Basin, New Mexico: American Journal of Science, v. 281, p. 390–435.

Lindsay, E. H., Jacobs, L. L., and Butler, R. F., 1978, Biostratigraphy and magnetostratigraphy of Paleocene terrestrial deposits, San Juan Basin, New Mexico: Geology, v. 6, p. 425–429.

Lofgren, D.L., Lillegraven, J.A., Clemens, W.A., Gingerich, P.D., and Williamson, T.E., 2004, Paleocene biochronology: The Puercan through Clarkforkian land mammal ages, *in* Woodburne, M.O., ed., Late Cretaceous and Cenozoic Mammals of North America: Biostratigraphy and Geochronology, p. 43–105, https://doi.org/10.7312/wood13040-005.

Lofgren, D.L., Scherer, B.E., Clark, C.K., and Standhardt, B., 2005, First record of *Stygimys* (Mammalia, Multituberculata, Eucosmodontidae) from the Paleocene (Puercan) part of the North Horn Formation, Utah, and a review of the genus: Journal of Mammalian Evolution, v. 12, p. 77–97, https://doi.org/10.1007/s10914-005-4865-9.

Longrich, N.R., 2011, *Titanoceratops ouranos*, a giant horned dinosaur from the Late Campanian of New Mexico: Cretaceous Research, v. 32, p. 264–276, https://doi.org/10.1016/j.cretres.2010.12.007.

Longrich, N.R., Sankey, J., and Tanke, D., 2010, *Texacephale langstoni*, a new genus of pachycephalosaurid (Dinosauria: Ornithischia) from the upper Campanian Aguja Formation, southern Texas, USA: Cretaceous Research, v. 31, p. 274–284, https://doi.org/10.1016/j.cretres.2009.12.002.

Longrich, N.R., Barnes, K., Clark, S., and Millar, L., 2013, Caenagnathidae from the Upper Campanian Aguja Formation of west Texas, a revision of the Caenagnathinae: Bulletin of the Peabody Museum of Natural History, v. 54, p. 23, https://doi.org/10.3374/014.054.0102.

Lowrie, W., 1990, Identification of ferromagnetic minerals in a rock by coercivity and unblocking temperature properties: Geophysical Research Letters, v. 17, p. 159–162.

Lucas, S.G., Sullivan, R.M., Lichtig, A.J., Dalman, S.G., and Jasinski, S.E., 2016, Late Cretaceous dinosaur biogeography and endemism in the Western Interior Basin, North America: A critical re-evaluation: New Mexico Museum of Natural History and Science Bulletin, v. 71, p. 195–213.

MacIntyre, G.T., 1966, The Miacidae (Mammalia, Carnivora), Pt. 1, The systematics of *Ictidopappus* and *Protictis*: Bulletin of the American Museum of Natural History, v. 131, p. 115–210.

Mannion, P.D., and Upchurch, G.R., Jr., 2011, A re-evaluation of the ‘mid-Cretaceous sauropod hiatus’ and the impact of uneven sampling of the fossil record on patterns of regional dinosaur extinction: Palaeogeography, Palaeoclimatology, Palaeoecology, v. 299, p. 529–540, https://doi.org/10.1016/j.palaeo.2010.12.003.

Marsh, O.C., 1889, Discovery of Cretaceous Mammalia: American Journal of Science, v. s3-38, no. 223, p. 81–92, https://doi.org/10.2475/ajs.s3-38.223.81.

Matthew, W.D., 1897, A revision of the Puercan fauna: Bulletin of the American Museum of Natural History, v. 9, p. 259–323.

Matthew, W. D., 1937, Paleocene faunas of the San Juan Basin, New Mexico: Transactions of the Philosophical Society, v. 30, p. 1–510.

Matthew, W.D., and Granger, W., 1921, New genera of Paleocene mammals: American Museum Novitates, v. 13, no. 7, p. 1–7.

McFadden, P. L., and McElhinney, M. W., 1990, Classification of the reversal test in palaeomagnetism: Geophysical Journal International, v. 103, p. 725 New York 729.

McKenna, M.C., 1975, Toward a phylogenetic classification of the Mammalia, *in* Luckett, W.P., and Szalay, F.S., eds., Phylogeny of the Primates: New York, Plenum Press, p. 21–46, https://doi.org/10.1007/978-1-4684-2166-8_2.

Meehan, T.J., and Wilson, R.W., 2002, New viverravids from the Torrejonian (Middle Paleocene) of Kutz Canyon, New Mexico and the oldest skull of the Order Carnivora: Journal of Paleontology, v. 76, p. 1091–1101, https://doi.org/10.1017/S0022336000057899.

Miall, A. D., 1978, Lithofacies types and vertical profile models of braided river deposits: a summary, *in* Miall, A. D., ed., Fluvial Sedimentology: Canadian Society of Petroleum Geologists Memoir, v. 5, p. 598-604.

Miall, A.D., 1985, Architectural-element analysis: a new method of facies analysis applied to fluvial deposits: Earth-Science Reviews, v. 21, p. 261-308.

Miller, K.G., Kominz, M.A., Browning, J.V., Wright, J.D., Mountain, G.S., Katz, M.E., Sugarman, P.J., Cramer, B.S., Christie-Blick, N., and Pekar, S.F., 2005, The Phanerozoic record of global sea-level change: Science, v. 310, p. 1293–1298, https://doi.org/10.1126/science.1116412.

Min, K., Mundil, R., Renne, P.R., and Ludwig, K.R., 2000, A test for systematic errors in $^{40}Ar/^{39}Ar$ geochronology through comparison with U/Pb analysis of a 1.1-Ga rhyolite: Geochimica et Cosmochimica Acta, v. 64, p. 73–98, https://doi.org/10.1016/S0016-7037(99)00204-5.

Nordt, L., Atchley, S., and Dworkin, S., 2003, Terrestrial evidence for two greenhouse events in the latest Cretaceous: GSA Today, v. 13, p. 4–9, https://doi.org/10.1130/1052-5173(2003)013<4:TEFTGE>2.0.CO;2.

Nydam, R., Cifelli, R.I., and Rowe, T.B., 2013, Lizards and snakes of the Terlingua local fauna (late Campanian), Aguja Formation, Texas, with comments on the distribution of paracontemporaneous squamates throughout the western interior of North America: Journal of Vertebrate Paleontology, v. 33, p. 1081–1099, https://doi.org/10.1080/02724634.2013.760467.

Ogg, J.G., 2012, Geomagnetic polarity time scale, *in* Gradstein, F. M., Ogg, J.G., Schmitz, M.D., and Ogg, G.D., eds., The Geologic Time Scale: Oxford, UK, Elsevier, p. 85–114.

Osborn, H. F., 1929, The titanotheres of ancient Wyoming, Dakota, and Nebraska: U.S. Geological Survey, Monograph 55, p. 1–701.

Osborn, H.F., and Earle, C., 1895, Fossil Mammals of the Puerco Beds. Collection of 1892: Bulletin of the American Museum of Natural History, v. 7, p. 1–70.

Paola, C., Heller, P., and Angevine, C.L., 1992, The large-scale dynamics of grain-size variation in alluvial basins, I, Theory: Basin Research v. 4, p. 73-90.

Pearson, D.A., Schaefer, T., Johnson, K.R., Nichols, D.J., and Hunter, J.P., 2002, Vertebrate biostratigraphy of the Hell Creek Formation in southwestern North Dakota and northwestern South Dakota: GSA Special Paper 361, p. 145–167.

Peppe, D.J., Evans, D.A.D., and Smirnov, A.V., 2009, Magnetostratigraphy of the Ludlow Member of the Fort Union Formation (Lower Paleocene) in the Williston Basin, North Dakota, v. 121, p. 65–79.

Peppe, D.J., Heizler, M.T., Williamson, T.E., Masson, I.P., Brusatte, S., Weil, A., Secord, R., 2013, New age constraints on the Late Cretaceous through early Paleocene rocks in the San Juan Basin, New Mexico: Geological Society of America Abstracts with Programs, v. 45, p. 290.

Peppe, D.J., Williamson, T.E., Secord, R., Flynn, A., Davis, A.J., Brusatte, S.L., 2015, Drivers of faunal turnover of early Paleocene mammalian communities in the San Juan Basin: Journal of Vertebrate Paleontology, Program and Abstracts 2015, p. 193.

Pietsch, T.J., Nanson, G.C., Olley, J.M., 2013, Late Quaternary changes in flow-regime on the Gwydir distributive fluvial system, southeastern Australia: Quaternary Science Reviews, v. 69, p. 168-180.

Price, W.E., 1974, Simulation of alluvial fan deposition by a random walk model: Water Resources Research, v. 10, p. 263-274.

Prieto-Márquez, A., 2014, Skeletal morphology of *Kritosaurus navajovius* (Dinosauria: Hadrosauridae) from the Late Cretaceous of the North American south-west, with an evaluation of the phylogenetic systematics and biogeography of Kritosaurini: Journal of Systematic Palaeontology, v. 12, p. 133–175, https://doi.org/10.1080/14772019.2013.770417.

Renne, P.R., Deino, A.L., Hilgen, F.J., Kuiper, K.F., Mark, D.F., and Mitchell, W.S., III, 2013, Time scales of critical events around the Cretaceous-Paleogene Boundary: Science, v. 339, p. 684–687, https://doi.org/10.1126/science.1230492.

Rigby, J.K., 1980, Swain Quarry of the Fort Union Formation, middle Paleocene (Torrejonian), Carbon County, Wyoming: geologic setting and mammalian fauna: University of Chicago, Evolutionary Monographs, 179 p.

Rivera-Sylva, H.E., Hedrick, B.P., and Dodson, P., 2016, A Centrosaurine (Dinosauria: Ceratopsia) from the Aguja Formation (Late Campanian) of Northern Coahuila, Mexico: PLoS One, v. 11, p. e0150529, https://doi.org/10.1371/journal.pone.0150529.

Rowe, T., Cifelli, R.L., Lehman, T.M., and Weil, A., 1992, The Campanian Terlingua local fauna, with a summary of other vertebrates from the Aguja Formation, Trans-Pecos Texas: Journal of Vertebrate Paleontology, v. 12, p. 472–493, https://doi.org/10.1080/02724634.1992.10011475.

Russell, D. E., 1967, Le Paleocene continental d'Amerique du Nord.: Memoires du Museum National d'Histoire Naturelle (Nouvelle Series), Series C, v. 13, p. 1–32.

Sampson, S.D., Loewen, M.A., Farke, A.A., Roberts, E.M., Forster, C.A., Smith, J.A., and Titus, A.L., 2010, New horned dinosaurs from Utah provide evidence for intracontinental dinosaur endemism: PLoS One, v. 5, p. e12292, https://doi.org/10.1371/journal.pone.0012292.

Sankey, J.T., 1998, Vertebrate paleontology and magnetostratigraphy of the upper Aguja Formation (Late Campanian), Talley Mountain area, Big Bend National Park [Ph.D. thesis]: Baton Rouge, Louisiana State University, 251 p.

Sankey, J.T., 2001, Late Campanian southern dinosaurs, Aguja Formation, Big Bend, Texas: Journal of Paleontology, v. 75, p. 208–215, https://doi.org/10.1017/S0022336000031991.

Sankey, J.T., 2008, Vertebrate paleoecology from microsites, Talley Mountain, Upper Aguja Formation, (Late Cretaceous), Big Bend National Park, Texas, USA, *in* Sankey, J.T., and Baszio, S., eds., Vertebrate Microfossil Assemblages: Their Role in Paleoecology and Paleobiogeography: Bloomington, Indiana University Press, p. 61–77.

Sankey, J.T., Standhardt, B.R., and Schiebout, J.A., 2005, Theropod teeth from the Upper Cretaceous (Campanian-Maastrichtian), Big Bend National Park, Texas *in* Carpenter, K., ed., The Carnivorous Dinosaurs: Bloomington, Indiana University Press, p. 127–152.

Schiebout, J.A., 1974, Vertebrate paleontology and paleoecology of Paleocene Black Peaks Formation, Big Bend National Park, Texas: Texas Memorial Museum Bulletin, no. 24, 88 p.

Schiebout, J.A., Rigsby, C.A., Rapp, J.D., Hartnell, J.A., and Standhardt, B.R., 1987, Stratigraphy of Late Cretaceous, Paleocene, and early Eocene rocks of Big Bend National Park, Texas: The Journal of Geology, v. 95, p. 359–375, https://doi.org/10.1086/629135.

Scott, W.B., 1892, A revision of the North American Creodonta: Proceedings. Academy of Natural Sciences of Philadelphia, v. 44, p. 291–323.

Secord, R., 1998, Paleocene mammalian biostratigraphy of the Carbon Basin, southeastern Wyoming, and age constraints on local phases of tectonism: Rocky Mountain Geology, v. 33, no. 1, p. 119–154.

Secord, R., Leslie, C.E., Williamson, T.E., Peppe, D.J., and Brusatte, S., 2016, First recognition of climate hyperthermals in the Lower Paleocene record of the San Juan Basin, New Mexico, USA: Geological Society of America Abstracts with Programs, v. 48, no. 7, https://doi.org/10.1130/abs/2016AM-278979

Shanley, K.W., and McCabe, P.J., 1994, Perspectives on the sequence stratigraphy of continental strata: AAPG Bulletin, v. 78, p. 544–586.

Sheehan, P.M., Fastovsky, D.E., Hoffmann, R.G., Berghaus, C.B., and Gabriel, D.L., 1991, Sudden extinction of the dinosaurs: Family-level patterns of ecological diversity during the latest Cretaceous, upper Great Plains, U.S.A: Science, v. 254, p. 835–839, https://doi.org/10.1126/science.11536489.

Silcox, M.T., and Williamson, T.E., 2012, New discoveries of early Paleocene (Torrejonian) primates from the Nacimiento Formation, San Juan Basin, New Mexico: Journal of Human Evolution, v. 63, no. 6, p. 805–833, https://doi.org/10.1016/j.jhevol.2012.09.002.

Simpson, G.G., 1935, New Paleocene mammals from the Fort Union of Montana: Proceedings of the United States National Museum, v. 83, p. 221, https://doi.org/10.5479/si.00963801.2981.221.

Sinclair, W. J., and Granger, W., 1914, Paleocene deposits of the San Juan Basin, New Mexico: American Museum of Natural History Bulletin, v. 33, p. 297–316.

Sloan, R.E., 1969, Cretaceous and Paleocene terrestrial communities of western North America, *in* E. L. Yochelson, ed., Proceedings of the North American Paleontological Convention: Kansas, Allen Press, p. 427–453.

Soil Survey Staff, 1999, Soil taxonomy: a basic system of soil classification for making and interpreting soil surveys. U.S. Department of Agriculture-NRCS Agriculture Handbook: U.S. Government Printing Office, Washington, 869 p.

Sprain, C.J., Feinberg, J.M., Renne, P.R., and Jackson, M., 2016, Importance of titanohematite in detrital remanent magnetizations of strata spanning the Cretaceous-Paleogene boundary, Hell Creek region, Montana: Geochemistry Geophysics Geosystems, v. 17, p. 660–678, https://doi.org/10.1002/2015GC006191.

Standhardt, B.R., 1986, Vertebrate paleontology of the Cretaceous/Tertiary transition of Big Bend National Park, Texas [Ph.D. thesis]: Louisiana State University, Baton Rouge, Louisiana, 298 p.

Standhardt, B.R., 1995, Early Paleocene (Puercan) vertebrates of the Dogie Locality, Big Bend National Park, Texas, *in* Santucci, V., and McClelland, L., eds., National Park Services Paleontological Research: Natural Resources Publication Office, p. 46–48.

Steiger, R.H., and Jäger, E., 1977, Subcommission on geochronology: Convention on the use of decay constants in geo- and cosmochronology: Earth and Planetary Science Letters, v. 36, p. 359–362.

Sullivan, R.M., Boere, A.C., and Lucas, S.G., 2005, Redescription of the ceratopsid dinosaur *Torosaurus utahensis* (Gilmore, 1946) and a revision of the genus: Journal of Paleontology, v. 79, p. 564–582.

Szalay, F.S., 1969, Mixodectidae, Microsyopidae, and the insectivore-primate transition: Bulletin of the American Museum of Natural History, v. 140, p. 195–330.

Szalay, F. S., and Lucas, S. G., 1996, The postcranial morphology of Paleocene *Chriacus* and *Mixodectes* and the phylogenetic relationships of archontan mammals: New Mexico Museum of Natural History and Science, v. 7, p. 1–47.

Taylor, L. H., ms, 1977, Geochronology of Torrejonian sediments, Nacimiento Formation, San Juan Basin, New Mexico: M.S. thesis, University of Arizona, Tucson, 93 p.

Taylor, L.H., 1984, Review of Torrejonian mammals from the San Juan Basin [Ph.D. thesis]: New Mexico, University of Arizona, 553 p.

Taylor, L. H., and Butler, R. F., 1980, Magnetic-polarity stratigraphy of Torrejonian sediments, Nacimiento Formation, San Juan Basin, New Mexico: American Journal of Science, v. 280, p. 97–115.

Tobin, T.S., Ward, P.D., Steig, E.J., Olivero, E.B., Hilburn, I.A., Mitchell, R.N., Diamond, M.R., Raub, T.D., and Kirschvink, J.L., 2012, Extinction patterns, $\delta^{18}O$ trends, and magnetostratigraphy from a southern high-latitude Cretaceous – Paleogene section: links with Deccan volcanism: Palaeogeography, Palaeoclimatology, Palaeoecology, v. 350–352, p. 180–188, https://doi.org/10.1016/j.palaeo.2012.06.029.

Tomida, Y., 1981, “Dragonian” fossils from the San Juan Basin and the status of the “Dragonian” land mammal “age”, *in* Lucas, S. G., Rigby, J. K., Jr., and Kues, B. S., eds., Advances in San Juan Basin Paleontology: Albuquerque, University of New Mexico Press, p. 222–241.

Tomlinson, S.L., 1997, Late Cretaceous and early Tertiary turtles from the Big Bend region, Brewster County, Texas [Ph.D. thesis]: Lubbock, Texas Tech University, 195 p.

Torsvik, T.H., Müller, R.D., Van der Voo, R., Steinberger, B., and Gaina, C., 2008, Global plate motion frames: Toward a unified model: Reviews of Geophysics, v. 46, p. RG3004 https://doi.org/10.1029/2007RG000227.

Trendell, A.M., Atchley, S.C., Nordt, L.E., 2012, Depositional and diagenetic controls on reservoir attributes within a fluvial outcrop analog: Upper Triassic Sonsela member of the Chinle Formation, Petrified National Park, Arizona: American Association of Petroleum Geologists Bulletin, v. 96, p. 679–707.

Trendell, A.M., Atchley, S.C., Nordt, L.C., 2013, Facies analysis of a probable large fluvial fan depositional system: The Upper Triassic Chinle Formation at Petrified Forest National Park, Arizona, USA: Journal of Sedimentary Research, v. 83, p. 873–895.

Trouessart, E.L., 1879, Catalogue des mammifères vivants et fossiles. Insectivores: Revue et Magasin de Zoologie Pure et Appliquée, v. 3, no. 7, p. 219–285.

Trouessart, E.L., 1904, Catalogus Mammalium. Quinquenale Suplementum: Berlin, Friedlander, 929 p.

Tsentas, C., 1981, Mammalian biostratigraphy of the middle Paleocene (Torrejonian) strata of the San Juan Basin. Notes on Torreon Wash and the status of the *Pantolambda* and *Deltatherium* faunal "zones", *in* Lucas, S. G., Rigby, J. K., Jr., and Kues B. S., editors, Advances in San Juan Basin paleontology: Albuquerque, University of New Mexico Press, p. 262–292.

Tykoski, R.S., and Fiorillo, A.R., 2016, An articulated cervical series of *Alamosaurus sanjuanensis* Gilmore, 1922 (Dinosauria, Sauropoda) from Texas: new perspective on the relationship of North America's last giant sauropod: Journal of Systematic Paleontology, https://doi.org/10.1080/14772019.2016.1183150, 27 p.

Van Valen, L., 1978, The beginning of the age of Mammals: Evolutionary Theory, v. 4, no. 2, p. 46–80.

Wagner, J., 2001, The hadrosaurian dinosaurs (Ornithischia: Hadrosauridae) of Big Bend National Park, Brewster County [M.S. thesis]: Lubbock, Texas Tech University, 417 p.

Wagner, J.R., and Lehman, T.M., 2009, An Enigmatic New Lambeosaurine Hadrosaur (Reptilia: Dinosauria) from the Upper Shale Member of the Campanian Aguja Formation of Trans-Pecos Texas: Journal of Vertebrate Paleontology, v. 29, p. 605–611, https://doi.org/10.1671/039.029.0208.

Watson, G.S., 1956, Analysis of dispersion on a sphere: Monthly Notices of the Royal Astronomical Society, v. 7, p. 153–159, https://doi.org/10.1111/j.1365-246X.1956.tb05560.x.

Weil, A., 1992, The Terlingua local fauna: stratigraphy, paleontology, and multituberculate systematics [M.S. thesis]: Austin, The University of Texas at Austin, 119 p.

Weissmann, G. S., Hartley, A. J., Nichols, G. J., Scuderi, L. A., Olsen, M. E., Buehler, H. A., and Banteah, R., 2010, Fluvial form in modern continental sedimentary basins: distributive fluvial systems: Geology, v. 38, p. 39–42.

Weissmann, G.S., Hartley, A.J., Scuderi, L.A., Nichols, G.J., Davidson, S.K., Owen, A., Atchley, S.C., Bhattacharyya, P., Chakraborty, T., Ghosh, P., Nordt, L.C., Michel, L., and Tabor, N.J., 2013, Prograding distributive fluvial systems – geomorphic models and ancient examples: SEPM Special Publication no. 104, p. 313-137.

Westerhold, T., Röhl, U., Donner, B., McCarren, H.K., and Zachos, J.C., 2011, A complete high-resolution Paleocene benthic stable isotope record for the central Pacific (ODP Site 1209): Paleoceanography, v. 26, p. 1–13, https://doi.org/10.1029/2010PA002092.

Wick, S.L., 2014, New evidence for the possible occurrence of *Tyrannosaurus* in West Texas, and discussion of Maastrichtian tyrannosaurid dinosaurs from Big Bend National Park: Cretaceous Research, v. 50, p. 52–58, https://doi.org/10.1016/j.cretres.2014.03.010.

Wick, S., and Lehman, T., 2013, A new ceratopsian dinosaur from the Javelina Formation (Maastrichtian) of West Texas and implications for chasmosaurine phylogeny: Naturwissenschaften, v. 100, p. 667–682, https://doi.org/10.1007/s00114-013-1063-0.

Wick, S.L., Lehman, T.M., and Brink, A.A., 2015, A theropod tooth assemblage from the lower Aguja Formation (early Campanian) of West Texas, and the roles of small theropod and varanoid lizard mesopredators in a tropical predator guild: Palaeogeography, Palaeoclimatology, Palaeoecology, v. 418, p. 229–244, https://doi.org/10.1016/j.palaeo.2014.11.018.

Wiest, L.A., Lukens, W.E., Peppe, D.J., Driese, S.G., Tubbs, J., 2018, Terrestrial evidence for the Lilluput effect across the Cretacoues-Paleogene (K-Pg) boundary: Palaeogeography, Palaeoclimatology, Palaeoecology, v. 491, p. 161-169. https://doi.org/10.1016/j.palaeo.2017.12.005.

Williamson, T.E., 1996, The beginning of the age of mammals in the San Juan Basin, New Mexico; biostratigraphy and evolution of Paleocene mammals of the Nacimiento Formation: New Mexico Museum of Natural History and Science Bulletin, v. 8, p. 1–141.

Williamson, T.E., Brusatte, S.L., Carr, T.D., Weil, A., and Standhardt, B.R., 2012, The phylogeny and evolution of Cretaceous-Paleogene metatherians: New cladistic analysis and description of new early Paleocene specimens from the Nacimiento Formation, New Mexico: Journal of Systematic Palaeontology, v. 10, p. 625–651, https://doi.org/10.1080/14772019.2011.631592.

Williamson, T.E., and Carr, T.D., 2007, *Bomburia* and *Ellipsodon* (Mammalia: Mioclaenidae) from the early Paleocene of New Mexico: Journal of Paleontology, v. 81, no. 5, p. 966–985, https://doi.org/10.1666/pleo05-116.1.

Williamson, T.E., and Carr, T.D., 2012, *Bomburodon*, a new name for the Paleocene mammal *Bomburia* Van Valen, 1978: Journal of Paleontology, v. 86, no. 3, p. 567, https://doi.org/10.1666/12-013.1.

Williamson, T.E., and Lucas, S.G., 1992, Stratigraphy and mammalian biostratigraphy of the Paleocene Nacimiento Formation, southern San Juan Basin, New Mexico: New Mexico Geological Society Guidebook, v. 43, p. 265–296.

Williamson, T.E., and Lucas, S.G., 1993, Stratigraphy and mammalian biostratigraphy of the Paleocene Nacimiento Formation, southern San Juan Basin, New Mexico: New Mexico Museum of Natural History and Science Bulletin, v. 43, p. 265–296.

Williamson, T. E., Nichols, D. J., and Weil, A., 2008, Paleocene palynomorph assemblages from the Nacimiento Formation, San Juan Basin, New Mexico, and their biostratigraphic significance: New Mexico Geology, v. 30, p. 3–11.

Williamson, T.E., and Taylor, L., 2011, New species of *Peradectes* and *Swaindelphys* (Mammalia; Metatheria) from the early Paleocene (Torrejonian) Nacimiento Formation: San Juan Basin, New Mexico, Palaeontologia Electronica, v. 14, 16 p.

Wilson, R. W., 1956, A new multituberculate from the Paleocene Torrejon fauna of New Mexico: Kansas Academy of Science Transactions, v. 59, p. 76–84.

Wilson, R.W., and Szalay, F.S., 1972, New paromomyid primate from the Middle Paleocene beds, Kutz Canyon area, San Juan Basin, New Mexico: American Museum Novitates, v. 2499, p. 1–18.

Wood, H. E., Chaney, R. W., Clark, J., Colbert, E. H., Jepsen, G. L., Reeside Jr., J. B., and Stock, C., 1941, Nomenclature and correlation of the North American Continental Tertiary: Bulletin of the Geological Society of America, v. 52, p. 1–48.

Woodburne, M.O., ed., 2004, Late Cretaceous and Cenozoic Mammals of North America: Biostratigraphy and Geochronology: New York, Columbia University Press, 376 p. https://doi.org/10.7312/wood13040.

Wortman, J.L., and Matthew, W.D., 1899, The ancestry of certain members of the Canidae, the Viverradae, and Procyonidae: Bulletin of the American Museum of Natural History, v. 12, p. 109–138.

Wright, V.P., and Marriott, S.B., 1993, The sequence stratigraphy of fluvial depositional systems: the role of floodplain sediment storage: Sedimentary Geology, v. 86, p. 203–210, https://doi.org/10.1016/0037-0738(93)90022-W.

Wyss, A.R., and Flynn, J.J., 1993, A phylogenetic analysis and definition of the Carnivora, *in* Szalay, F.S., Novacek, M.J., and McKenna, M.C., eds., Mammal phylogeny: Placentals: New York, Springer, v. 2, p. 32–52, https://doi.org/10.1007/978-1-4613-9246-0_4.